A Systematic Study of The Optical to X-ray Spectral Properties of Active Galactic Nuclei

JIN, CHICHUAN

A Systematic Study of The Optical to X-ray Spectral Properties of Active Galactic Nuclei

by Chichuan Jin

A thesis submitted to the University of Durham
in accordance with the regulations for
admittance to the Degree of Doctor of Philosophy.

Department of Physics
University of Durham
March 2012

A Systematic Study of The Optical to X-ray Spectral Properties of Active Galactic Nuclei

Chichuan Jin

Abstract

In this thesis I present a detailed study of the optical to X-ray spectral properties of Active Galactic Nuclei (AGN). We propose a new broadband SED model which combines the standard accretion disc emission, low and high temperature Comptonisation components by introducing a corona radius. Applying the new models to broadband spectral data, we found that RX J0136.9-3510 and RE J0134+396 have similar *rms* spectra and broadband SEDs, representing a distinct spectral state which can only be attained by super Eddington flows.

A detailed optical and X-ray spectral analysis is then carried out for a big sample of 51 unobscured nearby type 1 AGNs. We find that NLS1s tend to have softer 2-10 keV spectra, lower black hole mass, higher Eddington ratio, higher α_{ox} index and smaller coronal radius. The edge of Balmer continuum is shifted redwards and smoothed by more than predicted by the FWHM of the Balmer emission lines. A new method called 'Correlation Spectra Technique (CST)' is proposed, which is powerful for multi-waveband spectral analysis. We find that among the three Balmer line components, the broad component has the best correlation with hard X-ray emission. Optical oxygen forbidden lines all well correlate with the hard X-ray emission.

We conducted a systematic cross-correlation among the 9 key SED parameters: $\Gamma_{2-10keV}$, $\kappa_{2-10keV}$, κ_{5100A}, λ_{Edd}, FWHM$_{H\beta}$, M$_{BH}$, α_{ox}, L$_{bol}$ and L$_{2-10keV}$, and found the driven parameters to be M$_{BH}$, λ_{Edd} and L$_{bol}$ (or equivalently $\dot{M}$). AGN's intrinsic SEDs exhibit strong diversity and changes similarly with λ_{Edd}, $\kappa_{2-10keV}$, κ_{5100}, $\Gamma_{2-10keV}$, FWHM$_{H\beta}$ and M$_{BH}$. However, the SED shape is not sensitive to L$_{bol}$.

Contents

List of Figures

Declaration

The work presented in this thesis was undertaken between 2008 and 2011 when the author was a research student under the supervision of Prof. Martin Ward and Prof. Chris Done in the Department of Physics at the University of Durham. This work has not been submitted for any other degree at the University of Durham or any other University.

The AGN SED models presented in Chapter 2 are developed by Prof. Chris Done and have been published as:

• Done C., Davis S. W., Jin C., Blaes O., Ward M., 2011, 'Intrinsic disc emission and the Soft X-ray Excess in AGN', *Monthly Notice of the Royal Astronomical Society*, Volume 420, Issue 3, pages 1848-1860

The timing and spectral analysis of RX J0136.9-3510 in Chapter 2 has been published as:

• Jin C., Done C., Ward M., Gierliński M., Mullaney J., 2009, 'The Seyfert AGN RX J0136.9-3510 and the Spectral State of Super Eddington Accretion Flows', *Monthly Notice of the Royal Astronomical Society*, Volume 398, Issue 1, pages L16-L20

The work presented in Chapter 3 has been published as:

• Jin C., Ward M., Done C., Gelbord J., 2012, 'A Combined Optical and X-ray Study of Unobscured Type 1 AGN. I. Optical Spectra and SED Modeling', *Monthly Notice of the Royal Astronomical Society*, Volume 420, Issue 3, pages 1825-1847

The work presented in Chapter 4 has been published as:

• Jin C., Ward M., Done C., 2012, 'A Combined Optical and X-ray Study of Unobscured Type 1 AGN - II. Relation Between X-ray Emission and Optical Spectra', *Monthly Notice of the Royal Astronomical Society*, preprint

The work presented in Chapter 5 has been completed in collaboration with Ward M., Done C. and has been submitted for publication under the title 'A Combined Optical and X-ray Study of Unobscured Type 1 AGN - III. Broadband SED Properties' in *Monthly Notice of the Royal Astronomical Society*.

The sample presented in Chapter 2 is based on a bigger sample provided by Dr. Jonathan Gelbord from the cross-correlation of SDSS and XMM-Newton catalogs. The XMM-Newton data reduction scripts were also written by Dr. Jonathan Gelbord. All spectral fitting scripts were written by myself.

Acknowledgements

I would first like to thank my primary supervisor, Professor Martin Ward, who arranged the meeting 3 years ago during the black hole workshop in Beijing (it was really a surprise and great pleasure!), and then helped me to come to UK through complex procedures. Martin introduced me into the interesting research field of active galactic nuclei and provided constant guidances over the past 3 years. As an international student who went abroad for the first time. I am also very grateful for his great help in my daily life in UK, without which I would not have adapted the new environment so quickly.

Likewise I would like to thank my secondary supervisor, Professor Chris Done, who taught me detailed physics in AGN and various data analysis techniques throughout my study in Durham. Without her guidances the work in this thesis would be impossible to accomplish. I am always impressed and inspired by Chris' intelligence and enthusiasm in science.

Many people have provided valuable supports and advices for my work, which means that it is impossible to mention all of them one by one. However, I would like to particularly thank the following people. I must give my most sincere thanks to Dr. Jonathan Gelbord for providing me with the big sample and XMM-Newton data reduction scripts which sets the footstone of my following work. He also taught me a lot on statistics and science. I would also like to thank Dr. Marek Gierliński for teaching me the XMM-Newton data reduction and providing me with the scripts for producing *rms* spectra and broadband SED figures. I also need to thank Dr. James Mullaney for introducing me to IDL programming. I am so grateful to Dr. Matthew Middleton, who guided me through writing the first telescope proposal in my life which resulted in a 120 ks XMM-Newton observation for PG 1244+026 taken at the *Christmas day* of 2011. I must also thank Prof. Jian-ming Wang and Dr. Hermine Landt for their extremely valuable discussion and suggestions about the work in Chapter 4 and 5.

I would like to give my special thanks to Ms. Lindsay Borrero, our group secretary, who started to help me on various trivial but troublesome things ever since

the first day of my arrival in Durham. I would not be able to focus on my research without her constant help throughout my whole time in Durham.

I am so thankful to my dear friends in United Kingdom, China and United States. I would not made it through the past 3 years without your constant encouragement and support. I always owe a great due to my family members, especially Mom, Dad and grandma, thank you so much for your toleration, support and everything you provided for me on very stage throughout my life.

Finally, I would like to thank Durham University for the financial support through the award of Durham Doctoral Fellowship for the past 3 years, which makes it possible for me to come to Durham and accomplish all the works in this thesis.

Chapter 1 | *Introduction*

1.1 Black Holes

A 'Black hole' is an extreme object predicted by Einstein's general relativity, the name of which suggests that it is totally invisible. During the eighteenth century, Laplace and Michell first postulated the existence of black holes using Newtonian mechanics and the particle theory of light. It was proposed that if an object's mass is so huge that its escape velocity $(2GM/R)^{1/2}$ exceeds the speed of light c, then no light will be observed from it, i.e. totally 'black' to all types of detectors. This concept was ignored because at that time light was considered only as pure electromagnetic wave rather than particles, and so not affected by gravity. In 1915, the establishing of Einstein's special and general relativity theory brought the concept of a 'black hole' back to public attention. Schwarzschild (1916) derived the first analytical solution of Einstein's field equation in the vacuum ($G_{\mu\nu} = 0$), which depicts the gravity field around a static, spherical symmetric point mass. The uniqueness of this solution was proved by Israel (1967). Kerr (1963) derived a more general solution for a static, spherical symmetric point mass with non-zero spinning. However, the name 'black hole' itself was first used *publicly* by John Wheeler in 1967, afterwards this name became popular.

Although there are abundant physical properties related to the progenitor of a black hole, all information will be lost once the black hole forms, except for three properties (i.e. the 'no-hair' theorem): black hole mass (M), charge (Q) and angular momentum (L) which is more often expressed by the black hole spin parameter $\alpha = L/M$. According to the value of these three parameters, black holes can be classified into the following four types: a Schwarzschild black hole ($M \neq 0, Q = 0, \alpha = 0$), a Kerr black hole ($M \neq 0, Q = 0, \alpha \neq 0$), a Reissner-Nordstrom black hole

($M \neq 0, Q \neq 0, \alpha = 0$) and a Kerr-Newman black hole ($M \neq 0, Q \neq 0, \alpha \neq 0$).

A key parameter of a black hole is its gravitational radius (R_g), which is defined as:

$$R_g = GM/c^2 \tag{1.1}$$

R_g serves as a natural unit of distance of the gravitational field around a black hole. In the simplest case of a Schwarzschild black hole, there is a spherical surface called the 'event horizon', whose radius is $R_s = 2R_g$ (also called the Schwarzschild radius). No electromagnetic wave or particles can be emitted from inside R_s. For a Schwarzschild black hole, the 'event horizon' also overlaps with the 'infinite redshift surface', which is defined such that any electromagnetic wave launching from this surface will have its energy approach zero as it propagates further and further away from the black hole. Another typical radius is the 'last stable circular orbit' (R_{lso}), which defines the region within which no stable circular orbit can exist. For a Schwarzschild black hole, $R_{lso} = 6R_g$. But these radii can be different for other types of black hole. For example, a Kerr black hole has $R_s \sim R_g$, $R_{lso} \sim 1.24R_g$, and its 'infinite redshift surface' no longer overlaps with the 'event horizon'. Note that the spin parameter α satisfies the condition $0 \lesssim \alpha \lesssim 0.998GM/c$ (Thorne 1974).

1.1.1 Different Types of Black Hole

The black holes in the observable universe may have the following forms: micro black hole, stellar-mass black hole, supermassive black hole and intermediate-mass black hole.

(i) Micro black holes (MBH)

A micro black hole is a hypothetical type of black hole where quantum mechanical effects are important. The formation of MBH may be due to density fluctuations in the early universe, so they are also referred to as 'primordial black hole (PBH)'. It was first realized by Hawking (1971) that such density perturbations can cause mass collapse to form black holes. There is yet no observational evidence to confirm the existence of such PBH, but some theories suggest that MBH can form in high

energy particle accelerators such as the Large Hadron Collider (LHC) when the energy reaches TeV. However, MBH are not the concern of this thesis and so we will not continue to discuss it.

(ii) Stellar-mass black holes (SBH)

Compared to the PBH, the existence of stellar-mass black holes is much more certain. Although it is not possible to observe a SBH directly, their existence is strongly implied by many X-ray binary systems. Cygnus X-1 is one of the most well-known examples of SBH. It has a companion star in a close orbit, from which one can determine the mass of the companion star to be $8 - 15\ M_{\odot}$ (Axelsson et al. 2011; Orosz et al. 2011). This is higher than the upper limit of mass for a white dwarf ($1.4\ M_{\odot}$: Chandrasekhar mass for a star supported by electron degeneracy pressure) or a neutron star ($2.2\ M_{\odot}$: as proposed by Kalogera & Baym (1996) for a star supported by neutron degeneracy pressure), leaving the only possibility of a SBH. Other examples include LMC X-1, LMC X-3, M33 X-7, NGC 300 X-1, GRS 1915-105 etc.. The formation of SBH is still not clear. A neutron star may continue accreting nearby material, its mass finally exceeds the upper limit so that it collapses into a SBH.

(iii) Super-massive black holes (SMBH)

Strong radio sources such as 3C 48 and 3C 273 were first discovered during 1960s. These sources appear star-like in the optical images, but their optical spectra were confusing since there are very broad emission lines. Then it was realized that those emission lines are actually Hydrogen Balmer lines, and thus the redshift was identified to be 0.158 for 3C 273 (Schmidt 1963), which immediately implies extremely high luminosity of these 'Quasi-stellar objects' (or quasars). To explain the huge energy output, the possible role played by massive black hole in such sources was proposed (e.g. Zel'Dovich & Novikov 1964), but it was not until the accretion process near SMBH was modelled (Shakura & Syunyaev 1973; Shields 1978) that the accretion mechanism and the cosmological distance of quasars were widely accepted.

The most direct evidence for the existence of SMBH is the observation of stellar and gas motion in the centre of our galaxy and nearby galaxies such as M87 and NGC 4528. For example, `Hubble Space Telescope (HST)` observed a disc of gas of Keplerian velocity profile near the centre of M87 galaxy, from which one can

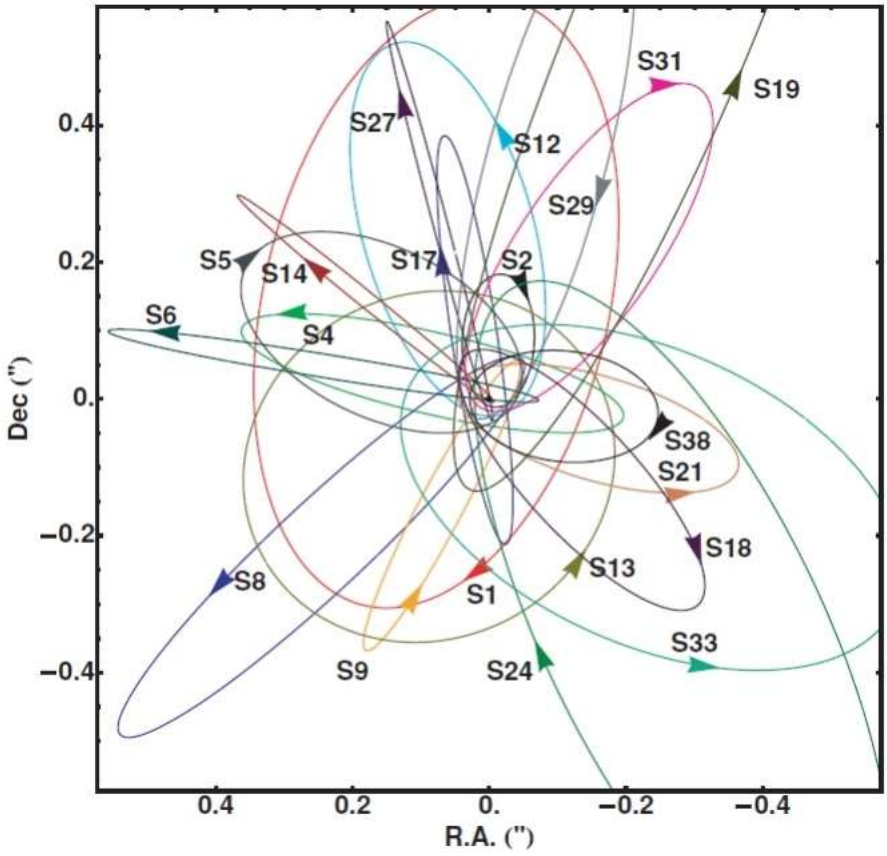

Figure 1.1: The stellar orbits around Sagittarius A* in the centre of the Milky Way. The S2 orbit has a period of 15.2 year and a pericentre distance of 17 light hours, strongly implying a central point mass of $(4.31\pm0.42)\times10^6 M_\odot$. This is one of the most direct evidence for the existence of SMBH. Figure is taken from Gillessen et al. (2009a).

estimate a total mass of 2×10^9 $M_\odot$ within 18 parsec (pc) (Harms et al. 1994), strongly implying a SMBH.

Figure 1.1 shows the stellar orbits around Sagittarious A* in the centre of our Milky Way (Gillessen et al. 2009a). The observation of the whole orbit of S2 star suggests a period of 15.2 year and a pericentre distance of 17 light hours (or at 2100 R_s of a 3×10^6 $M_\odot$ black hole) (Schödel et al. 2002), confirming the existence of a point mass (i.e. a SMBH) in the centre of Milky Way with a refined mass of $(4.31\pm0.42)\times10^6 M_\odot$ (Gillessen et al. 2009b). However, such direct observations can

not be conducted for any other galaxies harboring SMBH due to the limited spacial resolution.

Other less direct, but no less important, techniques can also predict the existence of SMBHs with masses between $10^5 - 10^{10}$ $M_\odot$, such as reverberation mapping techniques (Chapter 1.3.4) and Equation 1.15 where the radius of broad line region (R_{BLR}) and stellar/gas velocity dispersion (σ_{velo}) can both be determined observationally (Chapter 1.3.4).

(iv)Intermediate-mass black hole (IMBH)

The mass of IMBH may fill in the gap of $10^2 - 10^5$ $M_\odot$ between SBH and SMBH, but the existence of IMBH is much less certain than SBH and SMBH. These black holes are suspected to be associated with ultra-luminous X-ray sources (ULXs). Detailed X-ray spectral studies suggest that ULXs are more likely to be super-Eddington and in a new, ultraluminous state, with the black hole mass ranges between $10 - 100$ $M_\odot$ (e.g. Roberts 2007; Gladstone, Roberts & Done 2009; Vierdayanti et al. 2010; Middleton et al. 2011). Further details regarding IMBH are beyond the scope of this thesis. In the following chapters we will focus only on SMBH, and refer to the accretion processes in SBH where relevant.

1.1.2 Black Hole Accretion Processes

The in-fall of material onto a black hole converts gravitational potential energy into kinetic and thermal energy, resulting in strong radiative emission over the entire waveband from radio to hard X-ray. The conversion of gravitational potential energy into radiated energy can be described by the accretion efficiency μ. Thus if the mass accretion rate is $\dot{M}$, then the radiated luminosity is:

$$L = \mu \dot{M} c^2 \tag{1.2}$$

The accretion efficiency is directly related to R_{lso} which in turn depends on the spin of SMBH. μ ranges from 0.06 for a Schwarzschild black hole to 0.31 for an extreme Kerr black hole (Thorne 1974), thus the measurement of μ can be used to determine the spin of black hole. In this thesis we make the simplest assumption of

a Schwarzschild black hole and adopt an overall efficiency of 0.057 (Novikov-Thorne emissivity).

The radiation will also exert a force on the accreting material. Simply considering the accreted material to consist of a proton and an electron, the irradiated photons from the centre may be scattered by both proton and electron. But the Thomson cross-section is $\sigma_T \propto m^{-2}$, which shows that the proton scattering is negligible compared to the electron scattering. The radiation pressure in a radiation field of luminosity L can be expressed as:

$$F_{rad} = \frac{L\sigma_T}{4\pi r^2 c} \tag{1.3}$$

This force is also exerted indirectly on protons due to the Coulomb force between electrons and protons. The gravitational force on an electron-proton pair is:

$$F_{gra} = \frac{GM(m_p + m_e)}{r^2} \simeq \frac{GMm_p}{r^2} \tag{1.4}$$

The critical luminosity satisfies $F_{rad} = F_{gra}$ can be derived from Equation 1.3 and 1.4 as:

$$L_{Edd} = \frac{4\pi GMm_p c}{\sigma_T} = 1.3 \times 10^{38}(M/M_\odot)\ ergs\ s^{-1} \tag{1.5}$$

L_{Edd} is called the 'Eddington luminosity' which simply scales with black hole mass. The ratio between actual bolometric luminosity and Eddington luminosity is called the 'Eddington ratio' (i.e. $\lambda_{Edd} = L/L_{Edd}$), which represents the relative importance between radiation pressure and gravity.

However, the assumption of steady accretion flow, spherically symmetric and accreted material of fully ionized hydrogen may not be valid in a real source, so the above L_{Edd} is only a rough approximation. For example, the accreted material may contain heavier elements than hydrogen, and the material may not be fully ionized, thus the actual cross-section σ_T may be much bigger. Heinzeller & Duschl (2007) suggested that L_{Edd} only weakly depends on the geometry, but the critical luminosity should vary at different radii of accretion disc.

Despite these caveats in L_{Edd}, λ_{Edd} has proved to be one of the most fundamental parameters in the accretion process around black holes, especially in X-ray binaries whose SED state shows dramatic changes with changing Eddington ratio

(e.g. Remillard & McClintock 2006; Done, Gierliński & Kubota 2007). The SED dependence on λ_{Edd} has been proposed in AGNs but not in great detail (e.g. Vasudevan & Fabian 2007). This is one of the main issues studied in this thesis.

One of the most interesting issues concerns sources having *super-Eddington* accretion flows, whose λ_{Edd} is above 1. In such cases the radiation pressure is too high to be overcome by gravity, and so blows away at least part of the accreting material, forming a disc wind. In Chapter 2 I discuss one of the most extreme *super-Eddington* sources, namely RX J0136.9-3510.

1.2 AGN Taxonomy and Unified Model

The term of 'active galactic nuclei (AGN)' describes the luminous central region of galaxies. The huge energy output of AGN over a wide waveband cannot simply be explained as originating a single star or star clusters, although sometimes an AGN at the cosmological distance does appear star-like (i.e. quasar). It is now widely accepted that each AGN harbors a SMBH in its centre, and it is the accretion process around SMBH that generates the powerful multi-frequency radiation.

1.2.1 AGN Taxonomy

The taxonomy of AGN is complex and somewhat confusing because the fundamental physical differences between different types of AGN are not clear. However, there are some generally recognised AGN subsets which are summarised in Table 1.1 and discussed below.

(1) Seyfert Galaxies

The first AGN optical spectrum was observed from a Seyfert galaxy NGC 1068 by E. A. Fath in 1908 at Lick Observatory. Seyfert (1943) realised that there are other sources similar to NGC 1068, whose host galaxy has a compact and bright nuclei emitting strong, high-ionisation lines, including a series of forbidden lines. The hydrogen lines are broader than the forbidden lines. Many more Seyfert galaxies were found after that, whose host galaxies all show spiral morphology. Khachikian & Weedman (1974) realised that there are two sub-types of Seyferts, namely type 1

Classes of AGN

Radio Luminosity	Emission Lines	$L_N \gtrsim L_{gal}$	$L_N \lesssim L_{gal}$	$L_N << L_{gal}$
Radio Quiet $L_R \lesssim 10^{-4} L_{opt}$	Broad + Narrow	RQ QSO	Seyfert 1 1.5	LINER 1.9 LINER/ Seyfert 2
	Narrow Only	[NLQSO]	Seyfert 2	
	None	------	------	
Radio Loud $L_R \gtrsim 10^{-2} L_{opt}$	Broad + Narrow	RL QSO [QSR]	BLRG	PRG Weak lines LINERs
	Narrow Only	------	NLRG	
	None	Blazar [BL Lac] (OVV, HPQ)	------	

RQ-AGN host galaxies are usually: Early type Spirals (often disturbed)

RL-AGN host galaxies are usually: S0 or Ellipticals (often with nuclear dust lanes)

Table 1.1: The summary of different types of AGN. Table adopted from the website of Department of Astronomy, Virginia University (http://www.astro.virginia.edu/class/whittle/astr553/Topic15/Lecture_15.html)

and type 2, depending on the visibility of broad component in the permitted lines (Figure 1.2). Osterbrock (1981) further introduced type 1.5, 1.8 and 1.9 Seyferts, according to the presence of broad base in Hα and Hβ lines. Generally speaking, Seyfert galaxies are lower luminosity AGNs with $M_B > -21.5 + 5log(h_0)$, with quasars defining the higher luminosity AGNs. But the luminosity division between Seyferts and quasars is rather arbitrary.

Narrow Line Seyfert 1 (NLS1) are a special class of Seyfert AGN, whose definition is Seyfert 1 AGN with Hβ FWHM $\leq$ 2000 km s^{-1} and [OIII] λ5007/Hβ $<$ 3 (Goodrich 1989). However, there seems to be more fundamental differences between NLS1s and broad line Seyfert 1s (BLS1s). For example, compared to BLS1s, NLS1s have stronger soft X-ray excess (Done et al. 2011) and more prominent FeII emission (e.g. Komossa 2008). Their central black hole masses were found to be systematically lower than that prediction based on the M-σ_* relation which holds well for BLS1s (Greene & Ho 2006) (Chapter 1.3.4). It is proposed that the central black

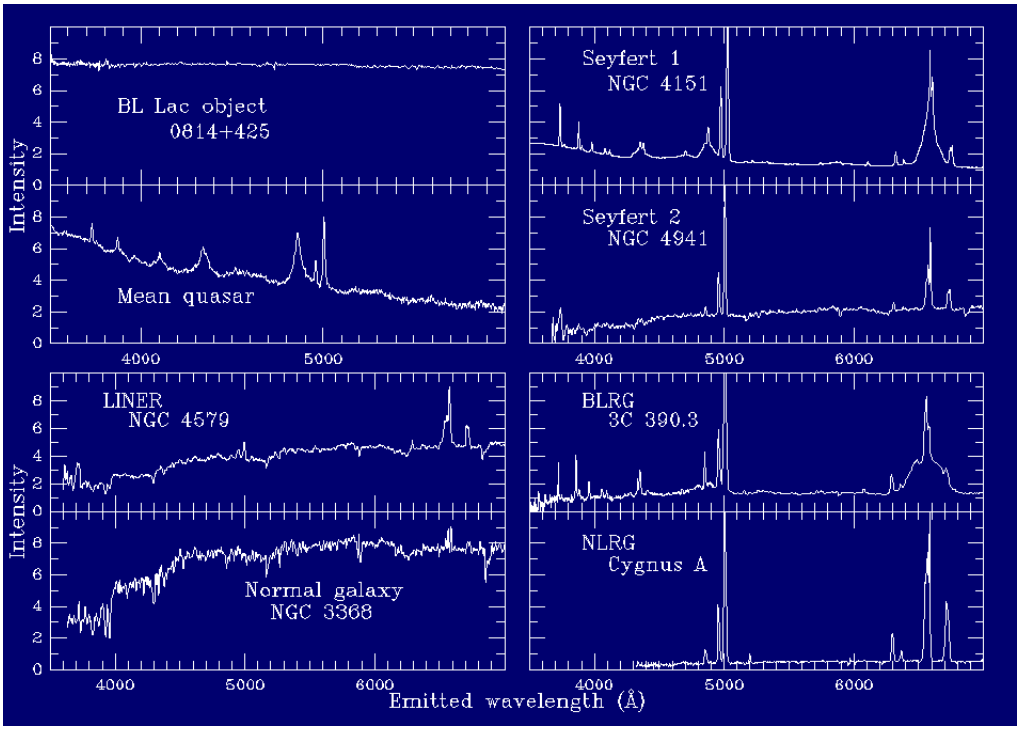

Figure 1.2: Optical spectrum of different types of AGN. Figure adopted from W. Keel's home page (http://www.astr.ua.edu/keel/agn/spectra.html)

hole of NLS1s may still be growing (e.g. Mathur, Kuraszkiewicz & Czerny 2001; Komossa & Mathur 2001; Komossa 2008). It is also found that among all AGNs the highest mass accretion rates in terms of Eddington are in the NLS1s (Casebeer, Leighly & Baron 2006; Middleton et al. 2009; also see Chapter 3). In this thesis, we will examine the differences between NLS1s and other type 1 AGNs.

(2) Quasars

Quasars were first identified in 1950s during the first systematic radio surveys. The optical counterparts of some of these strong radio sources was stellar in appearance rather than a diffused galaxy. The first optically identified quasar was 3C 48, identified by Matthews and Sandage (1963). Later, another quasar 3C 273 was identified by Hazard, Mackey & Shimmins (1963), whose redshift $z = 0.158$ was first determined by Schmidt (1963) from the Hydrogen Balmer lines. The cosmological distance implied by the high redshift of quasars implies extreme luminosity (typically $\geq 10^{45}\ ergs\ s^{-1}$), which could not be explained immediately at that time. But now it is clear that quasars form another class of AGNs lying at high redshift

with higher luminosity than Seyfert galaxies, the radiated energy is also from the accretion onto SMBH.

Although the first quasar was discovered due to its radio emission, most quasars found in optical surveys were not present in radio surveys. In fact 'radio-quiet (RQ)' quasars are 10-20 times more numerous than 'radio-loud (RL)' quasars. The flux ratio between radio (5GHz) and optical (B band or 4400Å) $F_{5GHz}/F_B \geq 10$ is used as the criteria for classifying RL AGNs (Kellermann et al. 1989).

(3) Radio Galaxies

Radio galaxies can be considered as the RL counterpart of Seyfert galaxies, but the morphology of a radio galaxy is elliptical, while the majority of Seyferts have spiral host galaxies. Similar to quasars and Seyfert galaxies, radio galaxies can also be divided into broad line radio galaxy (BLRG) and narrow line radio galaxy (NLRG).

(4) Low-ionisation Nuclear Emission-line Galaxies (LINERs)

LINERs are the least luminous but most common type of AGNs. They were first identified by Heckman (1980). More than 30% of all spiral galaxies are LINERs, thus they are the most common type of AGN. The optical spectrum of LINERs is similar to Seyfert 2's as both types of AGN show low ionisation narrow emission lines, but the Seyfert 2 can also exhibit strong highly ionised species as well. The differences between LINERs and Seyferts can be directly seen in the 'Baldwin-Phillips-Terlevich (BPT)' diagram (Baldwin, Phillips & Terlevich 1981), as shown in Figure 1.3. Compared to Seyferts, LINERs have stronger low-ionisation lines such as [SII] $\lambda\lambda$6717,6731, [NII] λ6584, [OII] $\lambda\lambda$3726,3729 and [OI] λ6300 (Ho, Filippenko & Sargent 1997). They also have [OIII] λ5007/Hβ $\leq$3.

(5) Blazars

Blazars are a different type of AGN which show extreme variability at most frequencies. All blazars have radio emission. Other terms used for this type of AGN are BL Lac objects and 'Optical Violent Variables (OVVs)'. These AGNs have continuum emission which is dominated by a relativistic jet. In the Unified Model (next section) they are believed to be viewed in a direction closely aligned with the jet, hence the emission undergoes relativistic Doppler boosting.

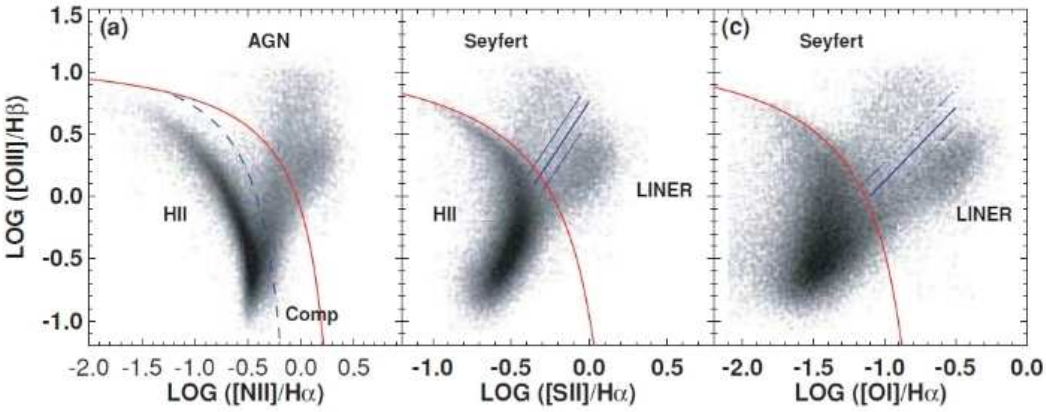

Figure 1.3: Three BPT diagrams used for classifying different galaxies using emission line ratios. Red solid lines are the extreme starburst classification lines from Kewley et al. (2001); Blue dashed line is pure star formation line from Kauffmann et al. (2003); Blue solid lines are the Seyfert-LINER classification lines from Kewley et al. (2006). These lines are used to separate galaxies into HII-region-like, Seyferts, LINERs, and composite HII-AGN types ('Comp'). Figure is from Kewley et al. (2006).

1.2.2 The Unified Model

Osterbrock (1978) suggested that the absence of broad component in the permitted lines could be due to the obscuration of the central region. Convincing evidence was found in the Seyfert 2 AGN NGC 1068 whose polarisation spectrum shows broad hydrogen lines similar as in Seyfert 1 galaxies (Antonucci & Miller 1985). This hidden BLR is also observed in other Seyfert 2 galaxies (e.g. Tran 1995; Heisler, Lumsden & Bailey 1997). Blandford and Rees (1978) recognised that blazars may be normal AGNs except that we are viewing along the relativistic beaming axis. Based on these results, Antonucci & Miller (1985) and Antonucci (1993) proposed the unified model for all the AGNs and introduced the orientation effect to account for different types of AGN in the same scenario.

Figure 1.4 shows a cartoon of unified model. The model includes a SMBH in the centre of AGN, a standard accretion disc forms around the black hole down to a few R_g whose emission dominates the optical/UV bump in AGN's broadband

SED (Shields 1978; Chapter 1.3). A torus of gas and dust at a few parsecs distance surrounds the accretion disc, reprocessing high energy central emission so that it emerges at infrared waveband. Type 2 AGN can be explained as type 1 AGN viewed 'Edge-on' thus the central broad line region (BLR) is obscured by the dusty torus. This model is supported by the observation that the UV spectrum in Seyfert 2 galaxies is similar to that of Seyfert 1 galaxies (Kinney et al. 1991). The narrow line region (NLR) lies up to 10s of kpc from the centre, and so is visible at all viewing angles. Blazars are observed close to the angle of a highly collimated jet, and so they are less common than other types of AGN.

However, orientation alone in the unified model is too simple to explain all the observed differences between the different types of AGN. For example, the radius and covering factor (the fraction of the spherical area covered) of the dusty torus may also depend on the AGN's luminosity (the so-called receding torus model: Lawrence (1991)). The mass of SMBH may also be systematically smaller in NLS1s than in other AGNs. The formation mechanism and mass accretion rates for different AGNs may also be different, resulting in a range of spectral and temporal characteristics (e.g. Shemmer et al. 2006; Brandt, Mathur & Elvis 1997).

1.3 AGN Optical/UV Emission

An AGN's optical/UV emission contains a wealth of information about the physical environment in the core region. A typical AGN's UV/optical spectrum consists of a series of emission lines superposed on the underlying continuum. Figure 1.5 shows a typical quasar composite spectrum over the spectral range between 800Å - 8500Å. All major emission line features are labelled according to the ion species, while the underlying continuum is shown as the dashed and dotted lines.

1.3.1 Accretion Disc Continuum

The optical/near UV emission is considered to be the tail of the big blue bump (BBB) peaking in the UV/soft X-ray region. The optical underlying continuum is attributed to the sum of emission at each radius within the accretion disc. For

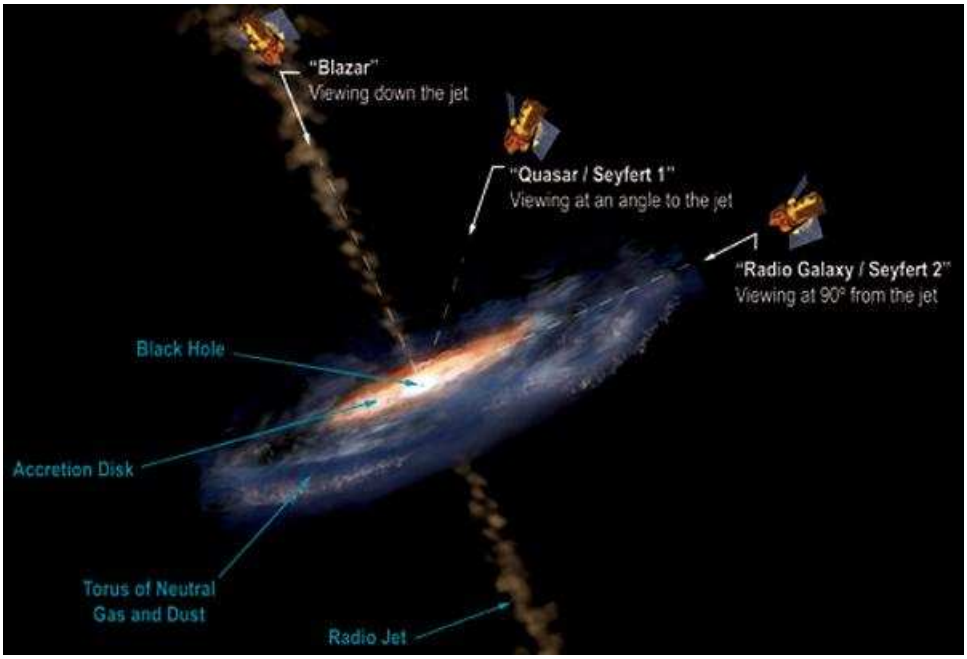

Figure 1.4: The cartoon of unified model of AGN. The physical size of accretion disc is up to a few hundred R_g. The size of dusty torus is between a few parsecs and hundreds of parsecs. The size of the NLR is up to tens of kilo-parsecs. Illustration: Aurore Simonnet/Sonoma State University.

a standard accretion disc which is geometrically thin and optically thick, one can assume local thermal equilibrium at the surface of the accretion disc, thus the energy is dissipated as a local black-body at each radius. Equation 1.6 shows that the surface temperature of the accretion disc changes with the radius roughly as:

$$T \approx T_0 \ (r/R_s)^{-3/4} \tag{1.6}$$

where $k_B T_0 \approx 54 \ (\dot{m}/M_8)^{1/4} \ eV$, with $\dot{m}$ being the mass accretion rate in the unit of the Eddington mass accretion rate, and M_8 the black hole mass in the units of $10^8 \ M_\odot$. This equation implies that the inner region of accretion disc is hotter and emits photons at higher energy (or shorter wavelengths). The sum of all the local black-body emission from the entire accretion disc between the inner radius R_{in}, and outer radius R_{out} forms the spectrum of the standard accretion disc (also called multi-colour accretion disc). Figure 1.6 shows the spectrum of such a disc which consists of a series of black-body components.

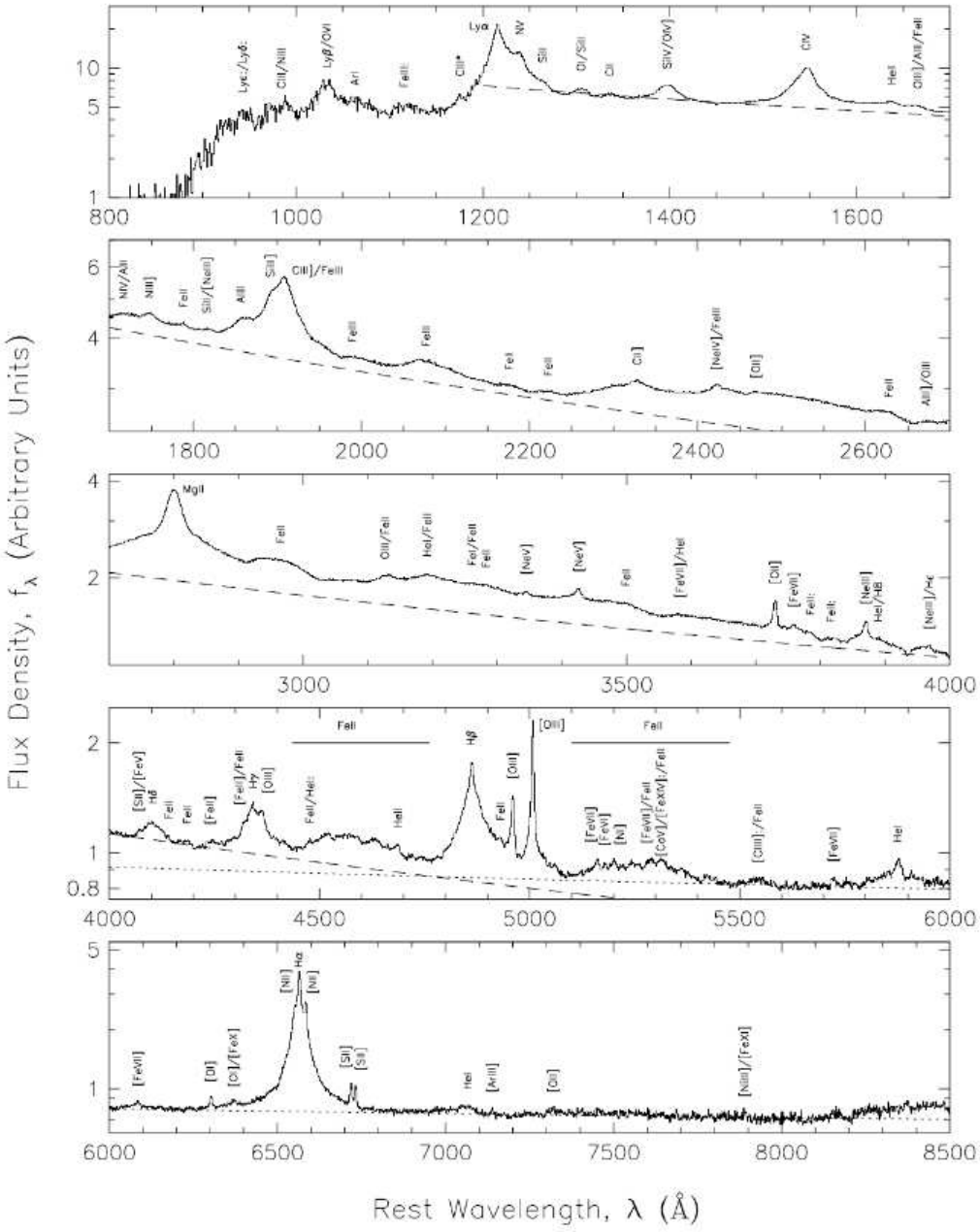

Figure 1.5: Median quasar composite spectrum showing various emission lines. Two power law components are fitted to the underlying continuum (dotted and dashed lines). Figure is taken from Vanden Berk et al. (2001).

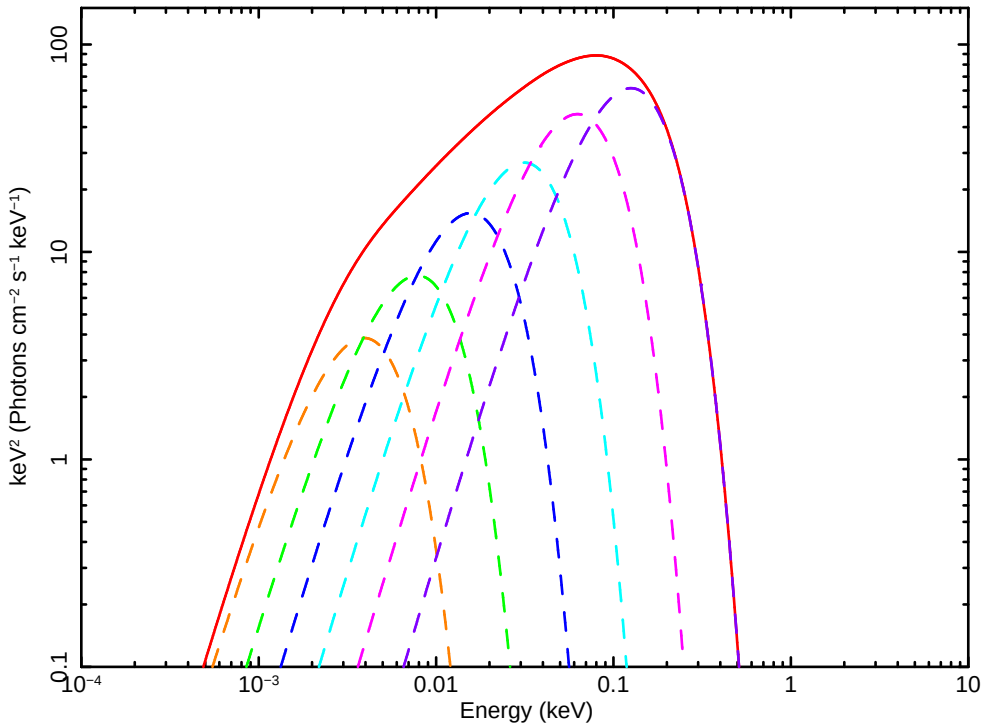

Figure 1.6: A simplified picture of a multi-colour accretion disc spectrum (red solid line), formed by adding the black-body emission at each radius (dash lines).

As mentioned previously the maximum effective temperature of a geometrically thin, optically thick accretion disc is $k_B T_{max} \approx 10\ \dot{m}/M_8\ eV$ (Shakura & Sunyaev 1973; Novikov & Thorne 1973), and the peaking energy of the disc spectrum is $\sim 2.7 k_B T$. So for a $10^7\ M_\odot$ black hole accreting at 10% of the Eddington mass accretion rate, the maximum effective temperature is 10 eV, and the peak energy of the disc spectrum is 30 eV (i.e. $\sim$400Å). So the accretion disc spectrum peaks in the UV region and produces significant continuum emission in the UV/optical spectrum. Taking the outer radius R_{out} of the standard accretion disc to be 500 R_s (outside which the disc may become clumpy due to self-gravity: e.g. Collin & Huré 2001), then the temperature $K_B T$ at R_{out}, calculated from Equation 1.6, is $\sim$0.5 eV (i.e. $\sim$2 μm). Therefore, optical photons with $3000\mathring{A} \lesssim \lambda_{opt} \lesssim 7000\mathring{A}$ have an intermediate photon energy of:

$$k_B T(R_{in}) \gg h\nu_{opt} \gg k_B T(R_{out}) \tag{1.7}$$

Also note that for such a locally thermalised accretion disc, we can write:

$$L(\nu) = 2\pi^2 cos(i) \int_{R_{in}}^{R_{out}} rI(\nu, T)dr \tag{1.8}$$

where i is the inclination angle, $I(\nu, T)$ is the *Planck's* equation for the black-body spectrum:

$$I(\nu, T) = \frac{2h\nu^3}{c^2} \frac{1}{e^{h\nu/kT} - 1} \tag{1.9}$$

Combining Equation 1.6, 1.7, 1.8 and 1.9, one can derive the spectral shape for a standard accretion disc in the optical and near UV region as:

$$L(\nu) \propto \nu^{1/3} \tag{1.10}$$

i.e. the predicted optical continuum emission from the standard accretion disc has the form of $L(\lambda) \propto \lambda^{-7/3}$.

The observed spectrum from accretion disc will be much more complicated than this simple picture if we also consider the rotation, inclination, magnetic field, relativistic effects, etc. (e.g. Czerny & Elvis 1987; Laor & Netzer 1989). For example, the temperature gradient will deviate from a simple power law as r approaches R_{in} where general relativistic effects become important (e.g. Gierliński et al. 1999); the black hole spin determines R_{lso} and thus affects the disc spectrum (e.g. Norikov & Thorne 1973; Zhang et al. 1997); the power index $-3/4$ in Equation 1.6 may increase if the radial advection becomes important (e.g. Mineshige et al. 1994; Kubota et al. 2005); electron scattering inside the accretion disc may also modify disc spectrum considering the vertical disc temperature profile (Done et al. 2011). In order to derive a more accurate accretion disc spectrum, one needs to perform a full radiative transfer calculation and a complete treatment of all the above factors.

1.3.2 Dust Reddening

A typical UV/optical spectrum often appears flatter (redder) than the predicted optical slope of accretion disc spectrum (Chapter 3). One of the main reasons for this apparent flatness is dust reddening. Figure 1.7 gives an example in which strong reddening flattens the intrinsic UV/optical spectrum of NGC 3227.

Dust grains between light emitter and observer will scatter and absorb photons in a wavelength dependent way, according to the size and composition of the grains. It is observed that the dust grains in the interstellar medium scatter more blue optical light than red, resulting in an absorbed optical spectrum that is 'reddened'. The extinction in magnitudes is written as A_λ, so the observed flux f_o is related to the intrinsic flux f_i as:

$$f_o = f_i \times 10^{-0.4 \times A_\lambda} \tag{1.11}$$

The commonly used variable to quantify the reddening level is the 'colour excess' between the `B` band and `V` band: $A_B - A_V$ (i.e. $E(B-V)$), then the reddening curve shown as a R_λ *vs.* λ plot where R_λ is defined as:

$$R_\lambda = \frac{A_\lambda}{A_B - A_V} = \frac{A_\lambda}{E(B-V)} \tag{1.12}$$

Reddening curves can also be determined relative to the `V` band and normalised to $E(B-V)$ (Savage & Mathis 1979) as:

$$\xi(\lambda) = \frac{E_{\lambda - V}}{E(B-V)} = R_\lambda - R_V \tag{1.13}$$

where R_V refers to the R_λ in the `V` band. Its value differs from galaxy to galaxy depending on the grain size (see below).

The dust reddening curve for the Milky Way (MW) has been well studied and constrained (e.g. Seaton 1979; Koornneef 1983; Pei 1992). The model of graphite-silicate grains with a wide size range has been used to depict the Galactic dust (Mathis, Rumpl & Nordsieck 1977; Pei 1992). The Galactic dust reddening in each direction of the sky can be obtained from publicly available databases such as the Leiden/Argentine/Bonn (LAB) map (Kalberla et al. 2005) and Dickey & Lockman (DL) map (Dickey & Lockman, 1990). The typical R_V for the MW is 3.08 (Pei 1992) but may change for a different line of sight.

Figure 1.8 shows the reddening curve of the Milky Way. The strength of absorption increases towards shorter wavelengths, with a stronger absorption feature centred at 2175Å. The origin of this bump is still not clear. Its central wavelength is almost invariant, but its width changes with the line of sight. It is suggested

that the dust grains responsible for this feature may consist of organic carbon and amorphous silicates (Bradley et al. 2005).

While the Galactic reddening has been well measured, the 'intrinsic' reddening for other galaxies (especially the galaxies hosting AGNs) is more difficult to quantify. Figure 1.8 also includes the reddening curves for Large Magellanic Cloud (LMC), Small Magellanic Cloud (SMC) and starburst galaxies (SB). It is clearly seen that the strength of dust absorption differs significantly below 3000Å between the MW, LMC, SMC and SB, while above 3000Å all the curves are quite similar except for the SB. It was also shown by Crenshaw et al. (2001) that the reddening curve of NGC 3227 (a Seyfert 1) is very similar to that of the SMC for wavelengths longer than 4000Å, below which the absorption is stronger in NGC 3227. In contrast, work by Gaskell et al. (2004) based on a large sample of RQ and RL quasars showed that the reddening curve of quasars is flatter than the MW, which may be due to a larger grain size in AGNs than in the MW (Maiolino et al. 2001). The 2175Å feature is also absent in the SMC, NGC 3227 and the quasar reddening curves reported in Gaskell et al. (2004). This may be due to an underabundance of carbon in the interstellar medium (ISM) of these galaxies. Overall all these studies confirm that over the optical range of 4000Å - 7000Å (which I am focusing on in this thesis) adopting a reddening curve of either the MW, LMC or SMC for non-starburst AGNs, is equally acceptable.

1.3.3 Dusty Torus and Host Galaxy Continuum

The emission from a dusty torus and a host galaxy can contribute to the longer wavelength emissions in the optical spectrum, as shown by Figure 1.9. The dusty torus absorbs emission from the AGN and reprocesses it into infrared emission longward of 1 μm. Together with the optical underlying continuum, it produces a local minimum in the SED at 1 μm which is commonly observed in AGNs (Sanders et al. 1989; Landt et al. 2010). The temperature of the dusty torus must be less than 2000 K, because above this dust grains will sublimate. The emission from the hottest part of dusty torus can be approximated by a single blackbody with best-fit

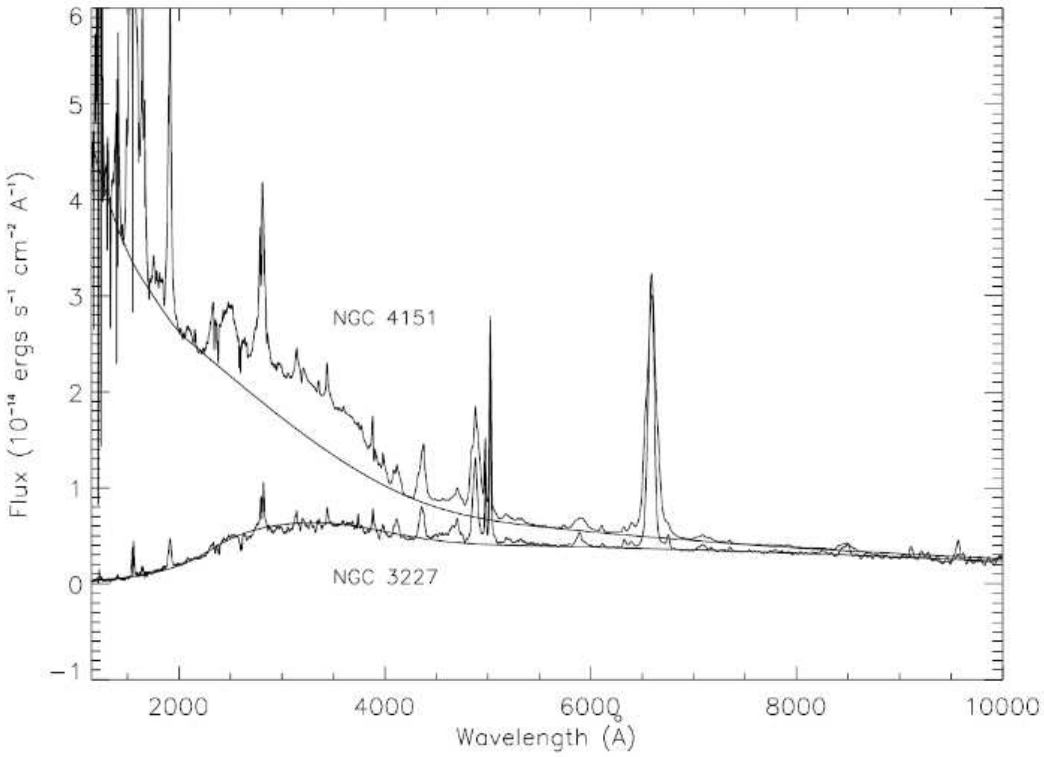

Figure 1.7: The strongly reddened UV/optical spectrum of NGC 3227, compared with the unobscured UV/optical spectrum of NGC 4151. Solid lines show the shape of the underlying continua. Note that the reddened spectrum is much flatter than the intrinsic spectrum. Figure is obtained from Crenshaw et al. (2001).

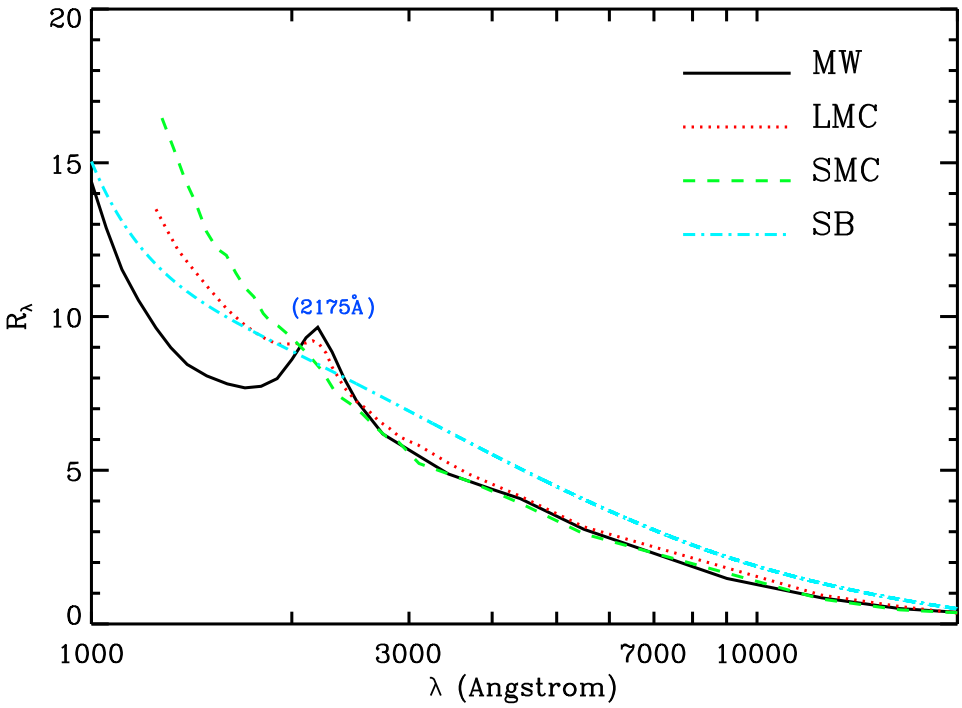

Figure 1.8: The extinction curves for the Milky Way (MW; Pei 1992), Large Magellanic Cloud (LMC; Pei 1992), Small Magellanic Cloud (SMC; Pei 1992) and Starburst Galaxies (SB; Calzetti et al. 2000). R_V = 3.08 (MW), 3.16 (LMC), 2.93 (SMC), 4.05 (SB). The marked position is the 2175Å bump. R_λ is defined in Equaiton 1.12.

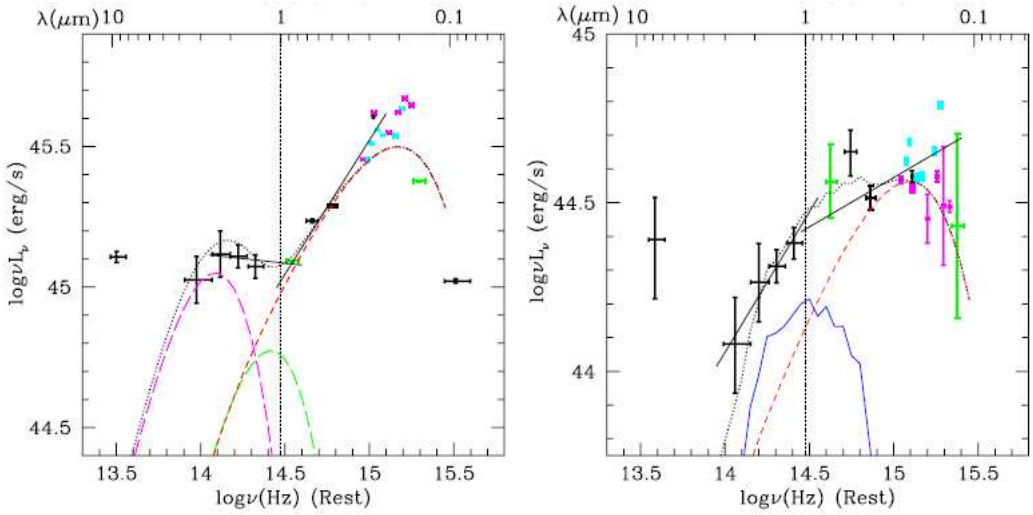

Figure 1.9: Two examples of optical to Infrared SED taken from Hao et al. (2010). Data points are fitted with standard accretion disc model (red dashed), plus a blackbody component representing emission from hot dust (magenta dashed), plus another blackbody component possibly arising from emission from outer region of the accretion disc (green dashed), and emission from the host galaxy (blue solid). The black dotted line is the sum of all the components.

temperature ranging from 1100-1700 K (Landt et al. 2010). The Wien tail of this infrared blackbody emission can extend into the optical region, but its contribution is small as seen in Figure 1.9.

The starlight from the host galaxy may also make a significant contribution to the optical region. However, the spectral shape depends on the stellar population. Figure 1.10 shows stellar spectral templates for different types of host galaxy. It is clear that the star-burst galaxies have strong emission blueward of the optical region. Quiescent galaxies mainly contribute to emission redward of 5000Å. The clearest signatures of host galaxy emission are the strong absorption features of Ca H+K $\lambda\lambda$3969, 3934, CaII $\lambda\lambda$8498, 8542, 8662 triplets and Mg I*b* $\lambda\lambda$5167, 5173, 5184 triplets, etc.. But since the study in this thesis focuses on type 1 AGNs without a star-burst component, only the optical spectrum above 5000Å might be significantly contaminated by the host galaxy.

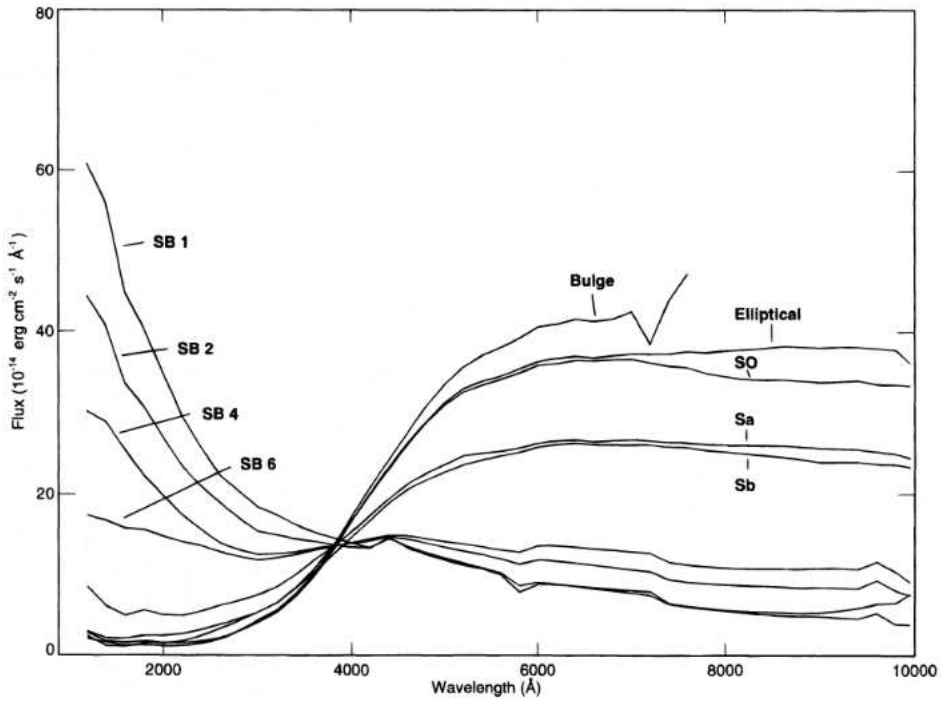

Figure 1.10: Spectral templates (binned in 200Å) for different types of host galaxies, normalised at 4000Å. 'SB' represents starburst galaxy template with different $E(B-V)$: SB 1 for $E(B-V) \leq 0.10$; SB 2 for $0.11 \leq E(B-V) \leq 0.21$; SB 4 for $0.39 \leq E(B-V) \leq 0.50$; SB 6 for $0.61 \leq E(B-V) \leq 0.70$. Figure is taken from Kinney et al. (1996).

1.3.4 Emission Features

One of the main difference between the optical spectrum of an AGN and a galaxy is that the AGN spectrum exhibits abundant emission lines. The most prominent emission lines between 3000-9000Å include hydrogen Balmer line series (Hα, Hβ, Hγ, etc.), HeII λ4686, Li λ6708, FeII emission line series, forbidden lines [OIII] $\lambda\lambda$4959,5007, [NII] $\lambda\lambda$6548,6584, [OI] $\lambda\lambda$6300,6363, [SII] $\lambda\lambda$6718,6732, etc.. There are also many other important and strong emission lines in both UV and infrared wavebands, such as CIV λ1549, MgII λ2799 and the hydrogen Paschen series. These lines are not studied in this thesis because they are not covered by the SDSS spectra of sources in our sample.

Along with strong emission lines, another prominent features in the optical spectrum is the hydrogen Balmer continuum which forms the small blue bump (SBB). The ideal shape of the Balmer continuum is a sharp edge (i.e. the Balmer photon recombination Edge: BPR edge) at 3646Å with an exponentially decreasing blue wing extending toward shorter wavelengths (e.g. Grandi 1982; Wills, Netzer & Wills 1985). I describe the detailed properties of the BPR edge in Chapter 3.

According to their ionisation potential, some forbidden lines are referred to as high ionisation lines (HILs), such as [Fe XIV] λ5303, [Fe X] λ6374 and [Fe XI] λ7892, if their ionization potential is $\geq$100 eV (e.g. Mullaney et al. 2009). Because these lines were first observed in the solar corona, they are also referred to as "coronal lines", in spite of the crucial difference that collision excitation dominates in the solar corona while photon ionisation dominates in an AGN. I do not study these lines in this thesis due to their limited S/N in the SDSS spectra.

The main emission lines studied in this thesis are Hα, Hβ and [OIII] λ5007. As mentioned previously these lines all have complex profiles (Figure 1.11), often including a broad base and a narrow core component, and sometimes also an intermediate component, when fitted by multiple Gaussian profiles (e.g. Hu et al. 2008; Mei, Yuan & Dong 2009; Zhu, Zhang & Tang 2009). The different line components are thought to originate from different regions, i.e. the narrow component from the 'narrow line region' (a low density extended region), broad component from the

'broad line region' (a dense compact region) and intermediate component from the 'intermediate line region' (a transition region in between the previous two). These regions are discussed as below.

Narrow Line Region (NLR)

The NLR is responsible for the narrow lines in the optical/UV spectrum. This region often extends from several hundred parsecs out to above 1 kilo-parsecs (e.g. Schmitt et al. 2003a,b). It is so far the most compact optical/UV structure that can be spatially resolved, which is directly associated with the AGN. The temperature and electron density can be determined from the relative strengths of some forbidden lines (e.g. [OIII] $\lambda\lambda$4363, 4959, 5007 and [SII] $\lambda\lambda$6716, 6731) and has $T_e \sim 10^4\ K$ and $n_e \sim 10^2 - 10^4\ cm^{-3}$ (e.g. Osterbrock 1989; Cai & Pradhan 1993).

The line width of the narrow lines is a few hundred $km\ s^{-1}$, with typical width of $\sim$500 $km\ s^{-1}$. A blue component is often observed to accompany the core component in [OIII] λ5007 profile, as shown in Figure 1.11, which suggests outflows in NLR of a few hundred $km\ s^{-1}$ (e.g. Boroson 2005, Bian, Yuan & Zhao 2005; Komossa et al. 2008). Ruiz et al. (2005) reported HST observations of the NLR in some Seyferts. It is found that the NLR is clumpy with 'knots' of emission extending a few arcseconds (Evans et al. 1991, 1993; Schmitt et al. 2003a). The NLR has various morphologies which may depend on the viewing angle (Schmitt et al. 2003b). The morphology of the NLR appears more axisymmetric than spherical symmetric, which stands out clearly in maps of [OIII] λ5007 as 'ionisation cones' (Pogge 1988), with a typical opening angle of $30°-100°$.

The width of the narrow lines can also be used to infer stellar/gas velocity dispersions. One of the most important results obtained from the study of narrow line emission and absorption features is the M-σ_* relation (Figure 1.12) (Gebhardt et al. 2000; Ferrarese & Merritt 2000) where σ_* is the gas velocity dispersion which can be determined from the width of the [OIII] λ5007 emission line (Boroson 2003; Greene & Ho 2005; Bian et al. 2006; Komossa & Xu 2007; Barth, Greene & Ho 2008), or from the stellar velocity dispersion which can be determined from the width of

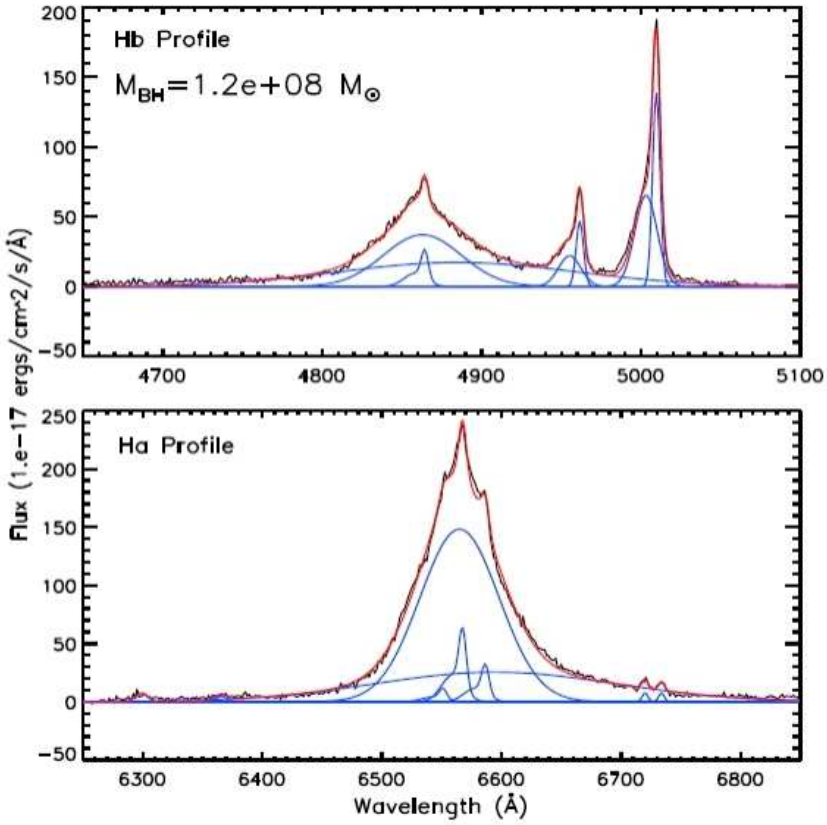

Figure 1.11: An example of broad Hα and Hβ emission lines, along with nearby emission lines such as [OIII] $\lambda\lambda$4959,5007, [NII] $\lambda\lambda$6548,6584 and [SII] $\lambda\lambda$6716,6731, from the SDSS spectrum of RBS 1423, fitted with multiple Gaussian components (blue solid lines). The red solid line is the sum of all the Gaussian components. This figure is reproduced from Jin et al. (2011).

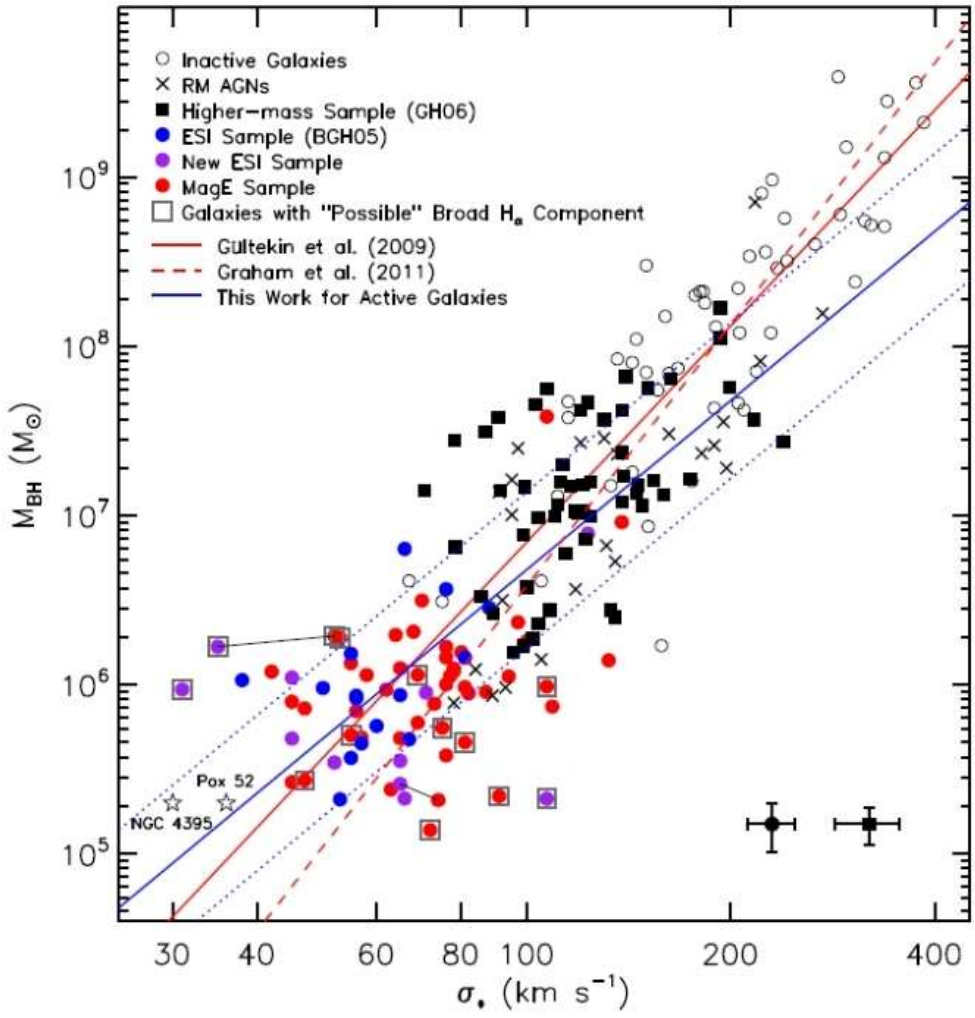

Figure 1.12: The latest M-σ_* relation from Xiao et al. (2011). Different symbols represent different samples as shown in the figure. The solid and dotted lines are the linear regression lines. Strong correlation is seen for the whole mass range of SMBH with $\sim$1 dex dispersion.

absorption lines such as Ca II $\lambda\lambda$8498, 8542, 8662 triplets (CaT), Mg I*b* and Fe λ5270 (e.g. Barth et al. 2002; Barth, Greene & Ho 2005; Greene & Ho 2006; Xiao et al. 2011).

Broad Line Region (BLR)

There are a series of strong broad lines in the optical spectrum, especially Hα and Hβ, as shown in Figure 1.11. The line profile is believed to be broadened by motions of gas within the BLR. So the line width is often quoted in the units of $km\ s^{-1}$. However, it remains controversial which particular estimate of line width best correlates with the mass of the central SMBH. Several possibilities include full width at half maximum (FWHM), full width at zero intensity (FWZI) and second moment of the line profile (Peterson et al. 2004), which is defined as.

$$\sigma^2_{line}(\lambda) = \left[\int \lambda^2 f(\lambda) d\lambda / \int f(\lambda) d\lambda\right] - \lambda_0^2 \tag{1.14}$$

The FWHM of broad lines ranges from a few hundred $km\ s^{-1}$ up to a few $10^4\ km\ s^{-1}$ with typical widths $\sim$5000 $km\ s^{-1}$ (e.g. Boroson & Green 1992; Peterson et al. 2004; Zhu, Zhang & Tang 2009). If thermally broadened, such velocity dispersion requires the temperature of the gas in BLR to be $\sim 10^9\ K$. But such a high temperature is not realistic, so the preferred explanation is that of bulk motions of individual clouds in BLR which is clumpy rather than homogeneous (Baldwin et al. 1995).

The physical properties of the BLR are hard to derive since it is such a compact region and cannot be spatially resolved by any telescopes. However the broad optical/UV emission lines can provide crucial clues. For example, the absence of a broad component to the [OIII] λ4363 line implies that the electron density of BLR is higher than the collision de-excitation density of $10^8\ cm^{-3}$. In fact, the zone of the BLR producing the strong carbon emission lines may have a density close to $10^{11}\ cm^{-3}$ (Ferland et al. 1992).

The total mass of gas in the BLR is estimated to be at least several hundred $M_\odot$ (e.g. Baldwin et al. 2003). It consists of more than 10^4 clouds with a volume filling

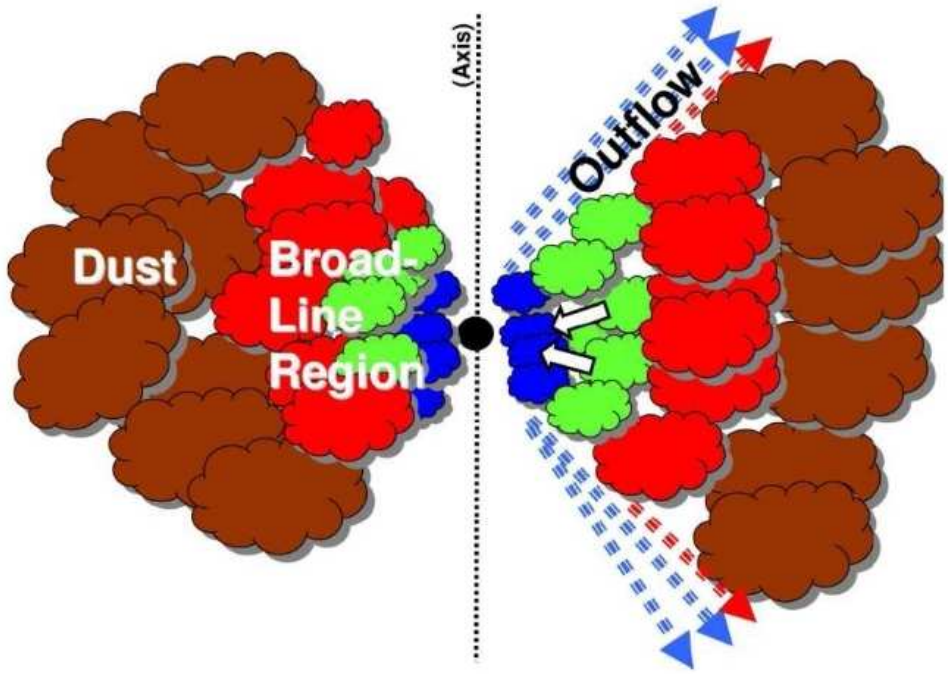

Figure 1.13: A schematic model from Gaskell (2009) showing the flattened BLR and dusty torus. The BLR emission can be observed through the two cones along the axis.

factor (i.e. the ratio between the total volume of all the clouds and the volume of the whole BLR) as small as 10^{-7}. However, if the clouds are distributed uniformly around the central source, then the observed strength of the emission lines implies a high covering factor of 50% (Gaskell, Klimek & Nazarova 2007), which would result in Lyman continuum absorption that has not been observed (MacAlpine 2003). So instead of a uniform distribution, a flattened geometry of the BLR was proposed by Gaskell (2009) as shown in Figure 1.13. Another scenario proposed recently introduces a link between star formation in the self-gravity dominated disc region and the BLR (Wang et al. 2011). In this scenario the star formation in the disc elevates gas above the disc to form the BLR, then the gas cools down to form dust and sinks back to the disc so that BLR disappears. This could explain the metalicity-luminosity correlation observed in the BLR gas (Hamann & Ferland 1999; Warner et al. 2003; Matsuoka et al. 2011) and also various types of broad line profile. In this thesis, I will investigate the density, dust abundance and inflow velocity in the BLR, and

discuss the correlations between BLR emission and various parameters associated with the central continuum.

Reverberation Mapping

The radius of the BLR can be best estimated by using the 'Reverberation Mapping (RM)' technique (e.g. Kaspi et al. 2000; Peterson et al. 2004), the theory of which was established by Blandford & McKee (1982). Using the velocity width of the broad line as the indicator of velocity dispersion in the BLR, the black hole mass can then be determined using the relation,

$$M_{BH} \;=\; f\,\frac{R_{BLR}\,\sigma^2_{velo}}{G} \tag{1.15}$$

(e.g. Peterson et al. 2004; Bentz et al. 2010; Denney et al. 2010; Barth et al. 2011). The essence of this method is to monitor the optical/UV underlying continuum simultaneously with the broad emission lines, then calculate the time lag t required by various broad lines to respond to the variation of the underlying continuum. So the light crossing distance ct is an estimate of R_{BLR}. The exact value of the scaling factor f depends on detailed geometry and kinematics, and its uncertainty remains an open question, e.g. $f = 3$ by assuming an isotropic velocity dispersion and $\sigma_{velo} = FWHM/2$ (Peterson et al. 2004). The most important result from using the RM technique is the correlation found between R_{BLR} and the monochromatic luminosity at 5100Å (i.e. $\lambda L_\lambda(5100\mathring{A})$), i.e. $R_{BLR} \propto (\lambda L_\lambda(5100\mathring{A}))^{0.7\pm0.03}$ (e.g. Kaspi et al. 2000; Woo & Urry 2002). This permits a 'single-epoch Virial mass estimate' using a single optical spectrum, such as the spectra from the Sloan Digital Sky Survey (SDSS), to estimate black hole masses of large samples of AGN (e.g. Baskin & Laor 2005; McGill et al. 2008). In Chapter 4 of this thesis I will discuss the uncertainties in the black hole masses derived from the R_{BLR} - $\lambda L_\lambda(5100\mathring{A})$ relation.

1.4 X-ray Emission from AGN

The X-ray band (0.1-100 keV) is one of the most useful for AGN observation. This is not only because the AGN X-ray emission contributes a high fraction of around ten percent of the total emitted energy, but also because the observed X-ray variability has a time scale of only a few minutes. Considering a black hole of mass $10^8\ M_\odot$, the gravitational radius R_g is $1.5{\times}10^{13}\ cm$, so the time scale of light crossing time is $\sim R_g/c\ =\ 8.2\ min$, which has a similar time scale to the AGN as X-ray variability. This suggests that the X-ray emission originates from the innermost region close to the central SMBH. Note: a few Seyfert galaxies show extended structure in soft X-ray waveband (e.g. Elvis et al. 1990), which may arise from electron scattering of the central X-ray emission and/or the nearby hot gas thermal bremsstrahlung emission. For analysis the X-ray spectrum is often divided into the 'soft' and 'hard' wavebands, referring to 0.1-2 keV and 2-10 keV, respectively.

1.4.1 The Hard X-ray Power Law Spectrum

The hard X-ray spectrum often exhibits the shape of a power law with the following form:

$$F_E = F_0{\times}E^{-\Gamma}(photons/s/cm^2/keV) \tag{1.16}$$

F_0 can be determined from the photon counts at 1 keV, and the index Γ is called the 'photon index'. However, it is more common to show the spectrum in terms of $EF_E\ vs.\ E$, since $EF_E = F_E{\times}h\nu$ directly shows the energy density distribution of the X-ray spectrum. Initially, the 2-20 keV X-ray spectrum was found to be well fitted by a single power law with $\Gamma{\simeq}1.7 \pm 0.2$ (Mushotzky et al. 1980). Later it was shown that the power law shape spectrum can extend to 100 keV. Figure 1.14 shows an example of the entire X-ray spectrum observed for MCG 01-05-047 by XMM-Newton and Swift's BAT. It is clear that the hard X-ray can be well fitted by an absorption modified power law, although an additional component is required in the spectral range below 2 keV (i.e. the 'soft excess', see Chapter 1.4.2). The origin of this hard X-ray power law spectrum is thought to be inverse Compton scattering of accretion disc photons by a hot electron population with temperature of a few

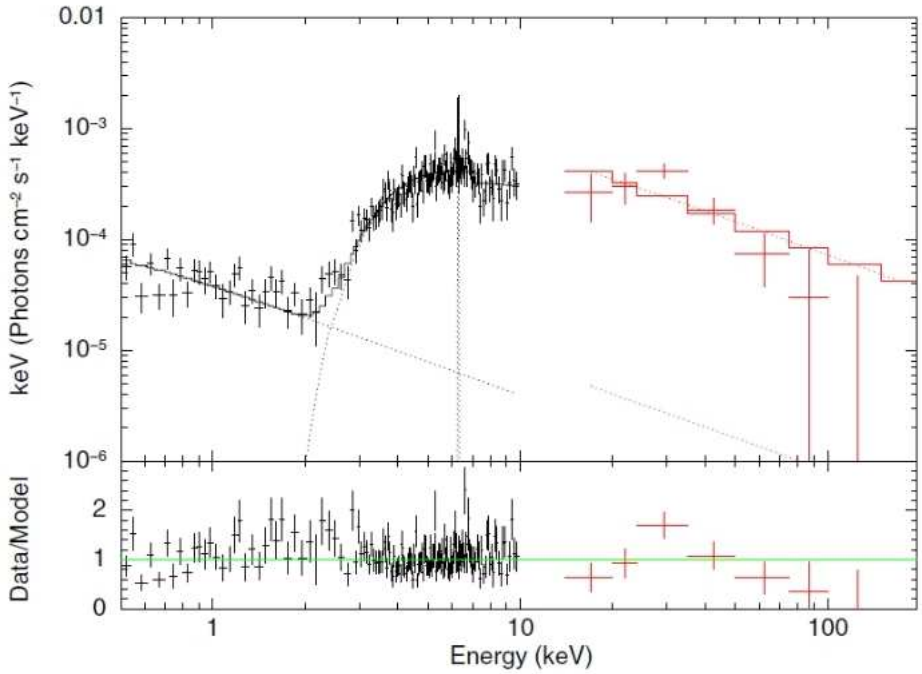

Figure 1.14: The entire X-ray spectrum of MCG 01-05-047 consists of data from XMM-Newton (black) and Swift BAT (red) observations. The figure is taken from Trippe et al. (2011). The fitted model is an absorption modified power law for the hard X-ray, plus another power law for the 'soft excess'. A small Gaussian profile component is also added to fit the iron Kα line emission at $\sim$6.4 keV.

hundred keV, forming a corona surrounding the disc (Zdziarski et al. 1990). This inverse Compton scattering process is referred to as 'Comptonisation'. The photon index Γ is predicted to be only weakly dependent on the temperature and optical depth of this corona (Haardt & Maraschi 1991; Zdziarski et al. 2000). However, the precise nature of this corona and its coupling with the accretion disc remains unclear. At even higher energies above 100 keV, the spectrum will exhibit an exponential cut-off at a few hundred keV. But the cut-off energy varies from AGN to AGN, which may help us to distinguish between different interpretations of X-ray spectra such as reflection, absorption and Comptonisation (Done et al. 2011). The γ ray emission from AGN is often weaker than predicted from extrapolation of a simple power law, which is consistent with the prediction from electron-positron pair production processes.

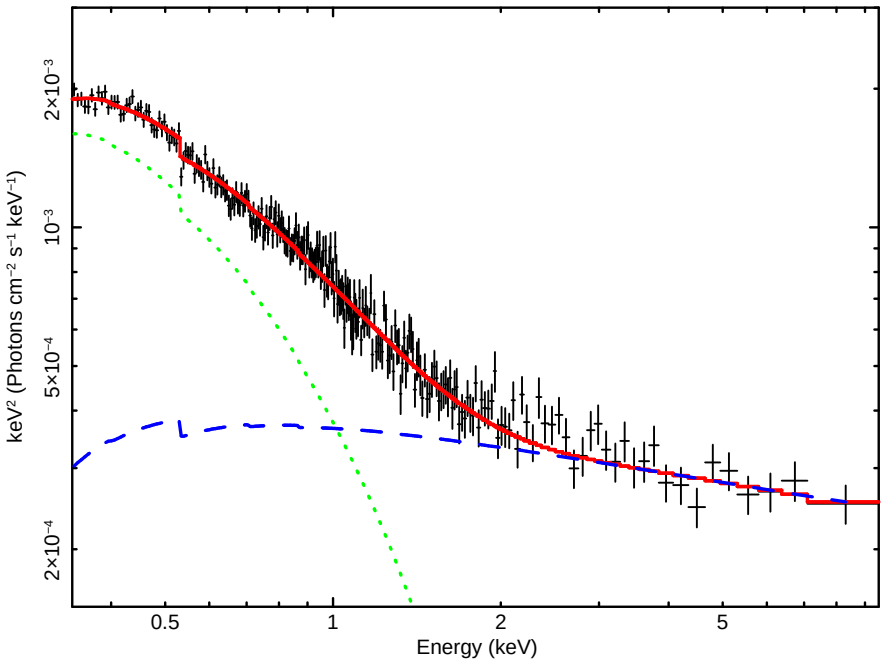

Figure 1.15: The strong soft X-ray excess observed in RX J0136.9-3510. The blue dashed line is the power law fit to the 2-10 keV spectrum observed by XMM-Newton. The green dotted line shows the soft excess which is fitted by a separate Comptonisation component. The red solid line is the sum of both components.

1.4.2 The 'Soft Excess'

A single power law is not sufficient to explain the overall X-ray spectrum. In many cases the soft X-ray spectrum appears much steeper than the hard X-ray spectral slope (e.g. Nandra & Pounds 1994; Middleton, Done & Schurch 2008; Jin et al. 2011), producing a excess flux commonly known as the 'soft X-ray excess'. Figure 1.15 shows another example, the X-ray spectrum of the Seyfert 1 RX J0136.9-3510. A power law is fitted to the 2-10 keV spectrum, then extrapolated below 2 keV. The best-fit photon index is $\Gamma = 2.27 \pm 0.08$. The ratio of the total flux to the power law flux at 0.4 keV is $\sim$4, suggesting a strong soft excess.

The origin of this excess flux is still a source of controversy among the AGN community. Although some simple forms of spectral models are often used to fit the soft X-ray spectrum such as a (broken) power law and blackbody. Although this approach can achieve some success in fitting the spectral shape phenomenologically, it is not based on actual physical scenarios. Physical models capable of explaining

the existence of the 'soft excess' include reflection from a partially ionised disc, partial absorption and Comptonisation (e.g. Crummy et al. 2006; Sobolewska & Done 2007; Done & Nayakshin 2007; Middleton et al. 2009; Done et al. 2011). The accretion disc emission may also make a significant contribution in the soft X-ray region in some low black hole mass, high mass accretion rate sources (Done et al. 2011; Jin et al. 2011). I will discuss the origin of the 'soft-excess' in several sections of this thesis.

1.4.3 Further Modifications to The X-ray Spectrum

The intrinsic X-ray spectrum consists of a hard X-ray power law and a soft X-ray excess, but the actual observed spectra are often much more complicated due to various spectral modification influences such as cold and warm absorption, reflection and iron Kα emission.

Absorption

Photo-ionisation of neutral or partial ionised gas along the line-of-sight may absorb the intrinsic X-ray emission and change the shape of the observed spectrum. The most common origin of absorption is that due to neutral gas in both the AGN's host galaxy and our own Galaxy. Many metal species are responsible for the absorption e.g. Oxygen and Iron, but it is the convention to use the equivalent neutral hydrogen column density n_H to quantify the amount of absorption by assuming a solar metal abundance. Note that the actual metal abundance in AGN may be higher than solar abundance. In that case the evaluated n_H is an over-estimate (Hamann et al. 2002; Nagao et al. 2006a; Nagao et al. 2006b).

The Galactic n_H is of the order of 10^{20} cm^{-2} (Dickey & Lockman 1990), mainly resulting in absorption below 2 keV. However, an AGN's intrinsic n_H can sometimes be above 10^{24} cm^{-2} (such as in NGC 5135, Levenson et al. 2004), resulting in strong absorption below 10 keV which is due to the fact that photoelectric absorption of the X-ray photons becomes more serious. These sources are called 'mildly Compton-

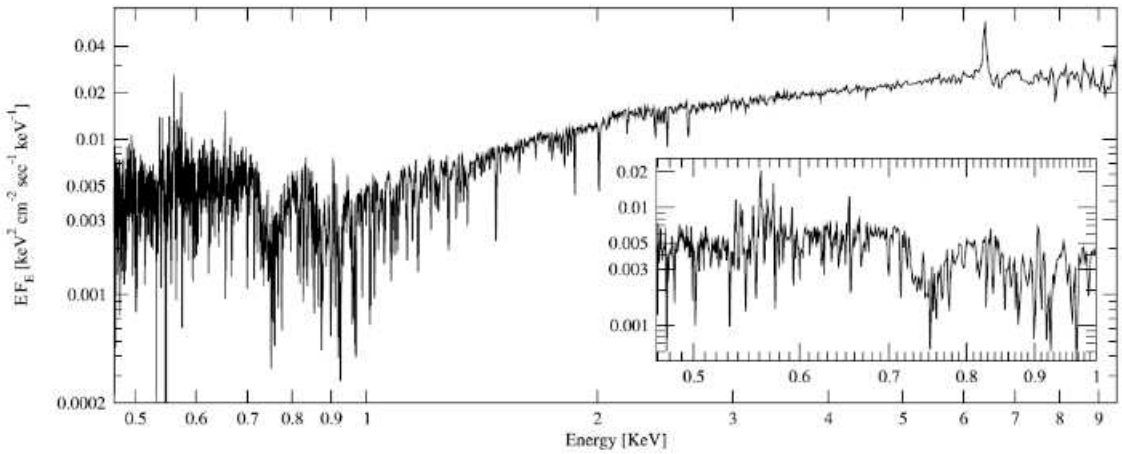

Figure 1.16: The combined Chandra medium-energy grating (MEG) and high-energy grating (HEG) first order 900 ks spectrum of NGC 3783, showing abundant warm absorption features especially in the soft X-ray region below 2 keV. This figure is taken from Kaspi et al. (2002).

thick' sources (Comastri, 2004). Sources with $n_H \geq 10^{25}\ cm^{-2}$ are called 'heavily Compton-thick' since in such cases the entire primary X-ray emission is strongly attenuated (Matt et al. 2000).

Compared to the neutral gas absorption, another type of absorption is due to a 'warm-absorber' composed of gas which is located much closer to the high radiation core and is thus partially ionised (e.g. Nandra & Pounds 1994; Crenshaw, Kraemer & George 2003). The main characteristic of a 'warm-absorber' is the presence of a broad absorption trough at 0.7∼0.8 keV consisting of numerous absorption lines and edges of partially ionised Oxygen and Iron (e.g. Turner et al. 2004), as shown in Figure 1.16.

Reflection and Fe K emission

Another mechanism that may occur in the core region of AGN is the reprocessing of X-ray emission by a partially ionised accretion disc, i.e. 'Reflection' from the disc (e.g. Ross & Fabian 1993; Ross, Fabian & Young 1999; Reynolds 1999; Fabian 2005). An X-ray photon entering the disc is subject to several interactions. It may

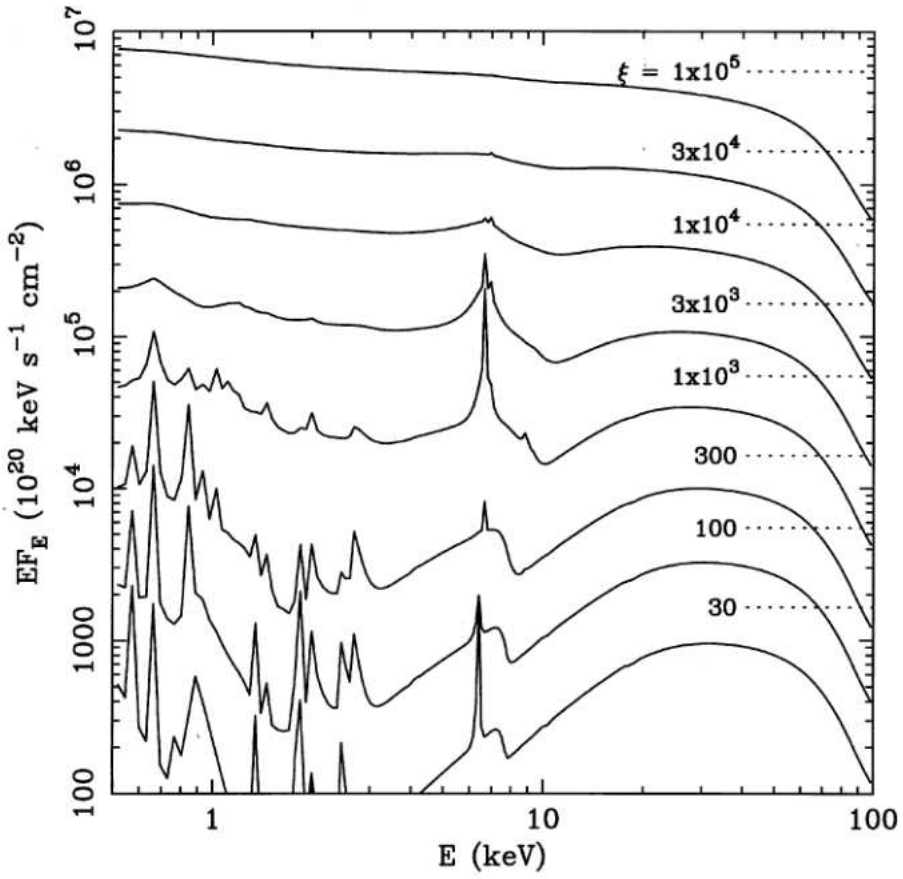

Figure 1.17: Reflection spectra with different ionisation parameter (ξ) values. The incident continua all have a power law shape of $\Gamma = 2$ (dotted lines). The figure is taken from Ross, Fabian & Young (1999).

be Compton down-scattered by electrons within the disc, or be photoelectrically absorbed which is then followed by fluorescent line emission or "Auger" de-excitation.

Taking the incident X-ray continuum to have a power law shape of $\Gamma = 2$, examples of the reflected spectra are shown in Figure 1.17. The shape of the reflected spectrum depends on the ionisation parameter ξ, which is defined as:

$$\xi = \frac{4\pi F}{n_H} \tag{1.17}$$

ξ is sensitive to the mass accretion rate (Ross & Fabian 1993; Ross, Fabian & Young 1999). Although the reflection mechanism can naturally produce a soft-excess by choosing a low value of ξ, the predicted flux can only be a maximum factor of 2-3 above the 2-10 keV continuum (Sobolewska & Done 2007). In addition, it also

predicts sharp atomic features in the spectrum which are difficult to reconcile with the observed smoothness of the soft-excess. It would require extreme relativistic effects to smear out the predicted atomic features (e.g. Crummy et al. 2006). These effects are large even when compared to the expected relativistic smearing from the innermost regions of the accretion disc, and so require some fine-tuning of the ionization state of the reflecting material.

Another form of reflection is the so-called 'cold reflection', which is due to reflection by the cold, Compton-thick medium further out from the core region which strongly absorbs the X-ray emission in Compton-thick sources. However, this reflection component is often difficult to detect since it is two orders of magnitude fainter than the primary emission.

As can be seen in Figure 1.17 that a prominent iron K-α emission line at 6.4 keV is often associated with the reflection spectrum, which is indeed observed in many AGN spectra (e.g. Nandra et al. 2007; Reynolds et al. 2009). Due to different locations of the reflection gas, the iron K-α line often exhibits a narrow component which corresponds to reflection from distant neutral gas, and a broad component which corresponds to reflection from the inner accretion disc. The line does not vary directly with the underlying power law, but it does vary on short timescales (Iwasawa et al. 1996, 1999; Nandra et al. 2000; Fabian et al. 2002; Fabian 2005).

The AGNs studied in this thesis all have 'clean' X-ray spectrum, i.e. without evidence of strong absorption or emission features. Thus the modification effects summarised above should not affect the sources studied in the following chapters.

1.5 Broadband SED of AGN

The spectral energy distribution (SED) of AGN has been modeled for several decades. Initial studies focused on the infrared, optical and ultraviolet continuum. With the inclusion of X-ray data, it was possible to define the continuum on both sides of the ultraviolet/X-ray gap which is due to Galactic and intrinsic photoelectric absorption. It is possible to constrain and model the whole broadband SED from the infrared/optical to hard X-ray, and so constrain properties of the accretion disc (e.g.

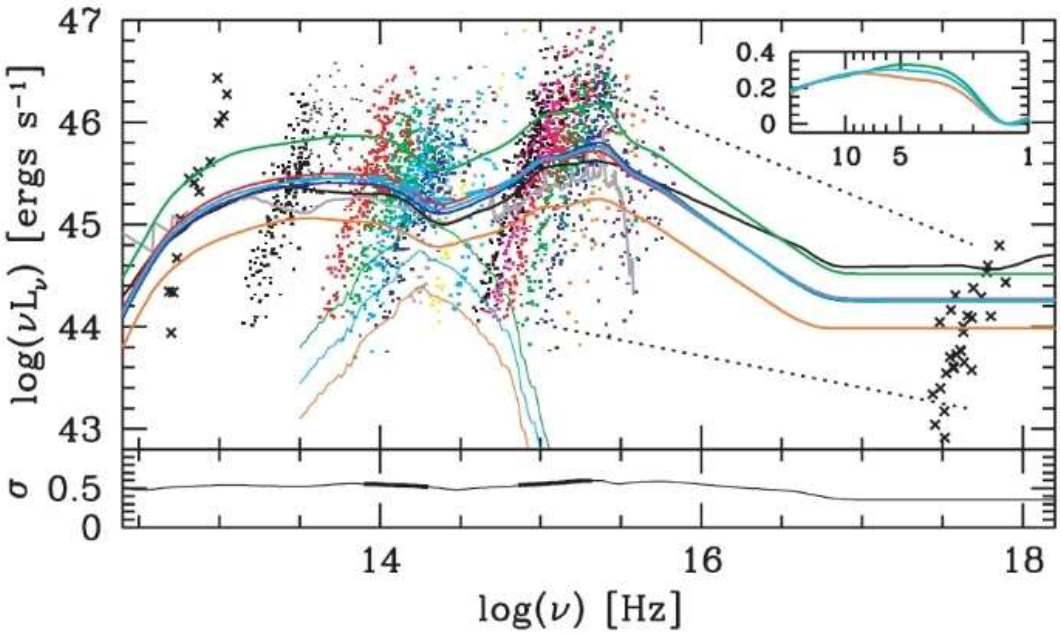

Figure 1.18: Mean quasar SEDs taken from Richards et al. (2006). Each point is an actual observation. The black solid line is the radio-quiet quasar mean SED from Elvis et al. (1994). The thick green, red, blue and orange solid lines show mean quasar SEDs based on SDSS sub-samples classified by their optical luminosity. The thin green, blue and orange solid lines show host galaxy contribution. Dotted lines show the range of α_{ox}.

Ward et al. 1987; Elvis et al. 1994). This is a core goal of the work described in this thesis.

1.5.1 Broadband SED Shape and Parameters

The shape of AGN broadband SEDs exhibit strong diversity across the whole AGN population (e.g. Elvis et al. 1994; Richards et al. 2006; Jin et al. 2011). SEDs can be quite different not only between different types of AGN, but also between individual sources. Figure 1.18 shows some SED for different types of AGN. Some of previous studies of multi-wavelength SEDs are summarised below.

At first it was found that the strength of soft X-ray excess anti-correlates with the velocity width of permitted lines such as Balmer lines (Puchnarewicz et al. 1992; Boller; Brandt & Fink 1996). Later Walter & Fink (1993) combined soft X-ray and

optical data for 58 Seyfert 1s, and showed that their broadband SEDs have a bump peaking in the UV and soft X-ray region, which is now referred to as the big blue bump (BBB) (also confirmed by Grupe et al. 1998, 1999). Elvis et al. (1994) studied 47 quasars in a UV/soft X-ray sample, and derived the mean SEDs for radio-loud and radio-quiet sources (the black solid line in Figure 1.18). Recently, more detailed spectral models have been applied to broadband SEDs. For example, Vasudevan & Fabian (2007, 2009) combined a disc and a broken power law model to fit optical, far UV and X-ray data for 54 AGNs. They found a well-defined correlation between the hard X-ray bolometric correction and the Eddington ratio. Middleton, Done & Gierliński (2007) applied various broadband SED models such as a disc plus power law model, disc reflection model and disc wind absorption model to the sample presented in Crummy et al. (2006). Grupe et al. (2010) used the models of two exponentially cut-off power law and a double broken power laws to describe AGN broadband SEDs. Simultaneous optical/UV and X-ray observations are used more frequently to avoid potential problems related to variability between optical/UV and the X-ray (Brocksopp et al. 2006; Crummy et al. 2006; Vasudevan & Fabian 2009; Grupe et al. 2010). Most of the sources in the sample studied in this thesis have simultaneous XMM-Newton OM optical/UV and EPIC X-ray data (Chapter 3)

Among these SED studies a number of important AGN parameters received intense study, including: black hole mass (MBH), Eddington ratio (L_{Edd}), bolometric luminosity (L_{bol}), 2-10 keV luminosity ($L_{2-10keV}$), 2-10 keV photon index ($\Gamma_{2-10keV}$), Hβ FWHM, etc. In addition, parameters directly related to broadband SED shape were also proposed, such as the optical to X-ray spectral index (α_{ox}, defined as Equation 1.18), 2-10 keV bolometric correction ($\kappa_{2-10keV}$, defined as $L_{bol}/L_{2-10keV}$), 5100Å bolometric correction (κ_{5100}, defined as L_{bol}/L_{5100} where L_{5100} is the monochromatic luminosity at 5100Å, Kaspi et al. 2000).

$$\alpha_{ox} = -\frac{Log(F(2keV)/F(2500\mathring{A}))}{2.605} \tag{1.18}$$

Since the number of sources with both optical/UV and X-ray spectra is relatively small, researchers searched for correlations among these AGN SED parameters, especially for parameters able to predict the shape of broadband SED. In this thesis

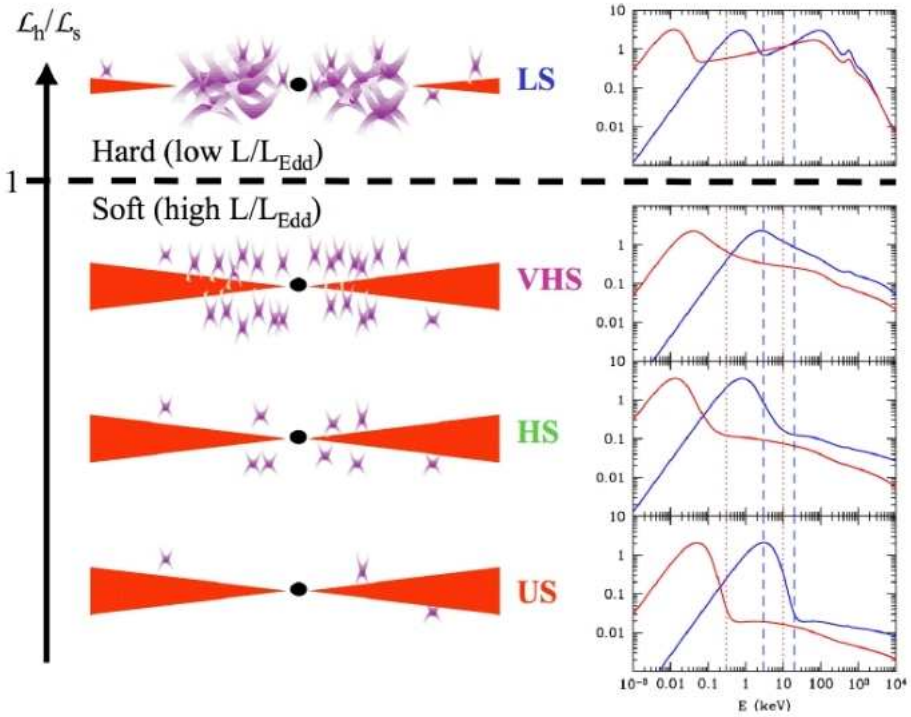

Figure 1.19: Suggested geometries for different spectral states of Black Hole Binary (BHB) systems. Solid lines in the left panels compare the shape of corresponding SEDs between BHB (blue solid) and AGN (red solid). Note that the mass of AGN is much higher than BHB (10^6 ×), so the AGN SED appears much cooler. The dashed and dotted vertical lines on the left panels show the energy ranges for RXTE and XMM-Newton, respectively. This figure is from Done & Gieliński (2005).

I carry out a systematic across-correlation study of all the parameters mentioned above (Chapter 3, 4 and 5).

1.5.2 The Spectral States of AGN

Several distinct spectral states have been identified in BHB systems, namely the 'hard state' (low/hard state), 'thermal state' (high/soft state), 'ultra-soft state' and 'very high' state (SPL-steep power law state), with quasi periodic oscillation (QPO) being most prominent during the 'very high' state (Remillard & McClintock 2006). In this scenario the Eddington ratio is the primary indicator of these accretion states, and changes from high to low Eddington ratios was confirmed as these BHB

sources undergo transitions through the 'very high', 'high/soft' and 'low/hard' states during an outburst. It has been proposed that the accretion processes in AGN may be the scaled up counterparts of those seen in BHB as shown in Figure 1.19 (Done & Gierliński 2005; McHardy et al. 2006; Gierliński et al. 2008; Middleton et al. 2009; Jin et al. 2009). Therefore, the Eddington ratio may also be a good indicator of AGN accretion states, and also determining the shape of the AGN broadband SED (e.g. Vasudevan & Fabian 2009; Done et al. 2011). A BHB can undergo an outburst within tens of days, and exhibit a clear spectral state transition (Remillard & McClintock 2006; Done, Gierliński & Kubota 2007). Clearly it is not possible to observe similar accretion state transitions in an AGN on time scales accessible to our observations. Instead, different SEDs can be looked for representing AGNs in different accretion states. One of the main aims of this thesis is to investigate similar SED states in AGN as seen in BHB, and to explain the many correlations found between the various AGN SED parameters (Chapter 5).

1.6 This Thesis

In this thesis I undertake conduct a systematic study of the characteristics associated with the emission lines and continua in AGN optical/UV and X-ray spectra. In order to probe the intrinsic properties of AGN radiation from and near the disc, this thesis focuses on unobscured type 1 AGNs with high quality spectra. I do not consider AGN with strong jets and focus on radio-quiet sources. The structure of the thesis is as follows. First, a new broadband SED model is described in Chapter 2 and is fitted to the spectral data of a subclass of NLS1s which display the most extreme *super Eddington* accretion flows. Chapter 3 defines a nearby unobscured type 1 AGN sample which is used in the following chapters. Detailed optical/UV and broadband SED fitting is described in this Chapter. Chapter 4 applies the results from Chapter 3 to investigate cross-correlations between optical/UV emission and X-ray emission, including emission line correlations and SED continuum correlations. Chapter 5 reports the correlations between various SED parameters. Different AGN mean SEDs are presented in this Chapter to show the distinct spectral states analogous

to those seen in BHB systems. All the principal results in this thesis are then summarised in Chapter 6, along with a discussion of open questions for future study. The appendix contains the results of spectral fitting for each source in the sample described in Chapter 2. A flat universe model with Hubble constant of $H_0 = 72$ km s^{-1} Mpc^{-1}, $\Omega_M = 0.27$ and $\Omega_\Lambda = 0.73$ is adopted throughout the thesis.

Chapter 2

AGN's SED Model and Super Eddington Accretion State

2.1 Introduction

In this chapter, We propose a new broadband SED model for AGN's optical to hard X-ray spectrum, which is so far the most advanced SED model used for big AGN sample studies and will be used throughout this thesis.

Then we summarize the properties of RE J1034+396. The most unusual feature of RE J1034+396 is its extreme SED shape, which exhibits a peak in the far UV which connects smoothly onto the steep soft X-ray spectrum. These components form a huge 'soft X-ray excess' with respect to the $\Gamma \sim 2.2$ X-ray tail which dominates above ~ 2 keV (Puchnarewicz et al. 1995; Casebeer, Leighly & Baron 2006; Middleton, Done & Gierliński 2007; Middleton et al. 2009). The energy dependence of its variability is also very different to that commonly seen in other AGN. The fractional variability amplitude (as measured by root mean square, hereafter *rms*) rises steeply to ~ 2 keV and then levels off. This is most likely due to the presence of two separate components in the X-ray spectrum, with the variability being associated with the X-ray tail, whilst the soft excess component remains more or less constant (Middleton et al. 2009). This situation contrasts with the flat or falling *rms* spectra seen in other AGN, sometimes with a peak at ~ 2 keV superimposed on this (Vaughan et al. 2003; Vaughan et al. 2004; Fabian et al. 2004; Gierliński & Done 2006; Ponti et al. 2006; Petrucci et al. 2007; Larsson et al. 2008), which

makes it more likely that the apparent soft excess in these objects is due instead to a single spectral component distorted by reflection and/or absorption (Crummy et al. 2006; Gierliński & Done 2006).

We make use of the unusual energy dependence of the X-ray variability in RE J1034+396 to search for potentially similar objects. A survey of all long ($\gtrsim$ 50 ks) XMM-Newton observations of bright and variable AGN yielded a similar *rms* shape only in one object RX J0136.9-3510 (2MASSi J0136544-350952). This AGN also has a similar broadband spectrum to RE J1034+396, suggesting that they may form a subclass of the highest mass accretion rate AGN. Therefore, we apply the new broadband SED models to the spectral data of both RE K1034+396 and RX J1036.9-3510, in order to confirm the accretion rate of Super Eddington in this subclass.

The SED models described in this chapter have been published in Done et al. (2011). The temporal and spectral properties of RX J0136.9-3510 presented in this chapter have been published in Jin et al. (2009).

2.2 Broadband SED Model: *optxagn(f)*

A standard interpretation of the broadband SED is that the emission is dominated by a multi-temperature accretion disc component which peaks in the UV (e.g. Gierliński et al. 1999, `Xspec` model: *diskpn*). This produces the seed photons for Compton upscattering by a hot, optically thin electron population within a corona situated above the disc, resulting in a power law component above 2 keV (e.g. Haardt & Maraschi 1991; Zdziarski, Poutanen & Johnson 2000, `Xspec` model: *bknpl*). However, the X-ray data clearly show that there is yet another component which rises below 1 keV in almost all high mass accretion rate AGNs. The ubiquity of this component can be seen, for example, in the compilation of AGN SEDs presented in Middleton, Done & Gierliński (2007), and one of the strongest cases is the NLS1 RE J1034+396 (Casebeer, Leighly & Baron 2006; Middleton et al. 2009). The origin of this so-called soft X-ray excess is still unclear (e.g. Gierliński & Done 2004; Crummy et al. 2006; Turner et al. 2007; Miller, Turner & Reeves 2008), and so some previous

broadband SED modeling studies have explicitly excluded data below 1 keV. An obvious consequence is that in such studies a soft excess component cannot influence the models, so making it possible to fit the data using just a disc and (broken) power law continuum (Vasudevan & Fabian 2007, here after: VF07; Vasudevan & Fabian 2009, here after: VF09). However, in our current study we include all of the data, and so we require a self-consistent model which incorporates this soft component.

Whatever the true origin of the soft X-ray excess, the simplest model which can phenomenologically fit its shape is the optically thick, low temperature thermal Comptonisation model (*compTT*). But the observed data are used to constrain the three separate components, *diskpn + compTT + bknpl*, which is generally problematic given the gap in spectral coverage between the UV and soft X-ray regions caused by interstellar absorption. So instead, we combine these three components together using a local model in `Xspec`, assuming that they are all ultimately powered by gravitational energy released in accretion. This model can be loaded to `Xspec` v12 as *optxagn* (Done et al. 2011). It is in essence a faster version of the models recently applied to black hole binary spectra observed close to their Eddington limit (Done & Kubota 2006) and to the (possibly super Eddington) Ultra-Luminous X-ray sources (Gladstone, Roberts & Done 2009; Middleton & Done 2010), thus this model is more appropriate for fitting a medium sized sample of objects. It assumes that the gravitational energy released in the disc at each radius is emitted as a blackbody only down to a given radius, R_{corona}. Below this radius, it further assumes that the energy can no longer be completely thermalised, and is distributed between the soft excess component and the high energy tail. Thus the model includes all three components which are known to contribute to AGN SED in a self consistent way. As such it represents an improvement on the fits in VF07 in several respects, by including the soft excess and by requiring energy conservation, and it improves on Done & Kubota (2006) by including the power law tail. Figure 2.1a shows a cartoon of the above physical scenario of the model, along with the resultant spectrum. This model is available from `Xspec` v12 as *optxagn* (Done et al. 2011).

However, the assumption of completely thremalised emission may not be true in some cases because AGN discs can also be dominated by electron scattering rather

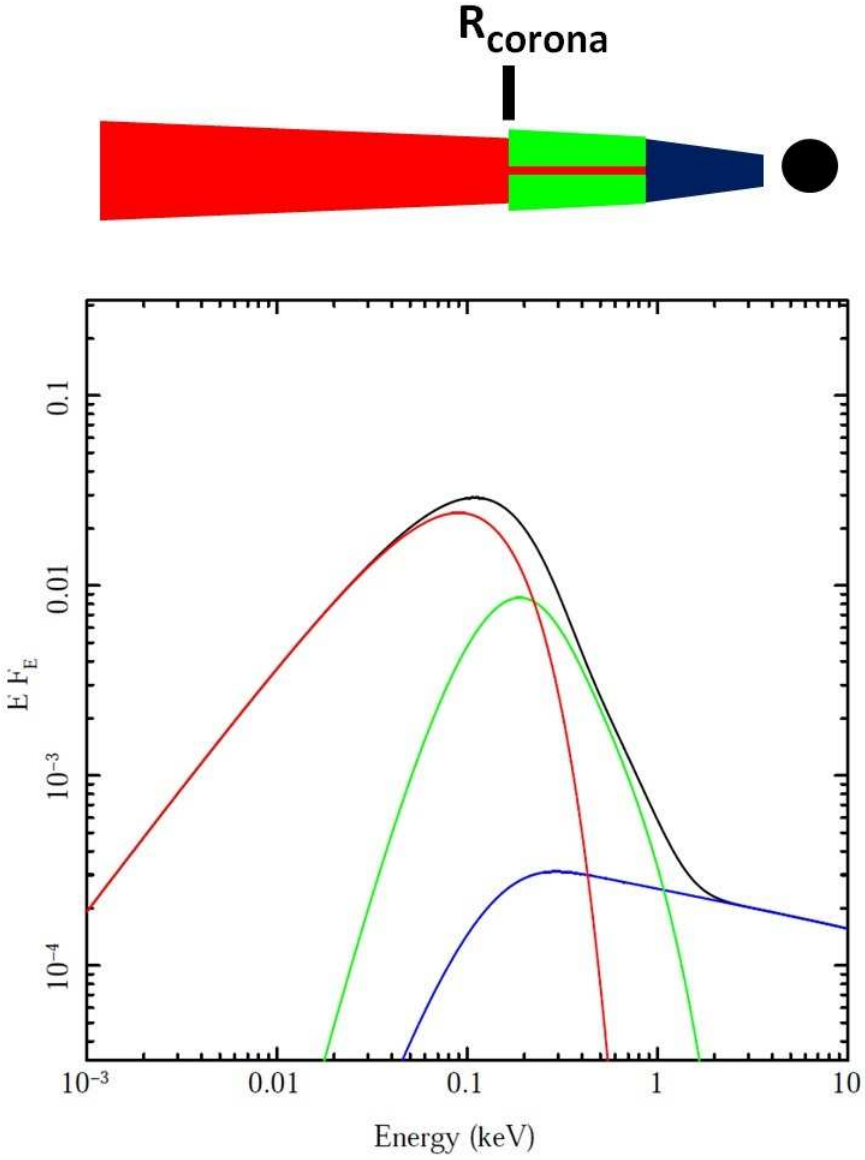

Figure 2.1: A schematic of the model geometry and resultant spectra, with outer disc (red) which emitts as a blackbody, and an inner disc (green) where the emission is Compton upscattered by a low temperature, optically thick electron population. Some fraction of the energy is also Compton upscattered by a high temperature, optically thin electron population in a corona (blue) to produce the hard X-ray power law tail. Figure is adopted from Done et al. (2011).

than absorption if the temperature in some disc regions is well above the Hydrogen ionization energy of 13.6 eV or 10^5 K (e.g. Ross, Fabian & Mineshige 1992). This is because the absorption opacity depends on physical conditions such as temperature, density and photon energy, while electron scattering opacity is constant. Typically, $\kappa_{abs} \propto nT^{-\beta}$ where n is the density and T is the temperature. $\beta \approx 3.5$ for both free-free and bound-free absorptions. As $n \propto M^{-1}$ and $T \propto M^{-1/4}$, we have $\kappa_{abs} \propto M^{-1/8}$. Thus for an AGN and a BHB of the same Eddington ratio, electron scattering is more important in AGN discs. However, electron scattering is only important in disc regions where $T > 3{\times}10^4$ K so that enough Hydrogen atoms are ionized. The maximum effective temperature of the accretion disc is $kT \sim 10(\dot{m}/M_8)^{1/4}$ eV (where $\dot{m} = L_{bol}/L_{Edd}$, $M_8 = M/10^8$ $M_\odot$), thus electron scattering opacity can only dominate in AGNs with both low mass and high mass accretion rate such as NLS1s (e.g. Boller, Brandt & Fink 1996). A typical colour temperature correction of 2.6 is expected for an AGN of $M_{BH}{=}10^6 M_\odot$, $\lambda_{Edd}{=}1.0$ (Davis et al. 2006), which when combined with the already hot disc due to the low mass, results in a disc spectrum that extends significantly into the soft X-ray region.

It is not realistic to directly use results from full disc radiative transfer models to conduct spectral fitting for a big sample of AGNs. Therefore, an approximation can be made by introducing a colour temperature correction f_{col} to the standard accretion disc spectrum. Davis et al. (2006) derives:

$$f_{col} \sim (72/T_{keV})^{1/9} \tag{2.1}$$

where T_{keV} is the maximum effective disc temperature. This equation was derived for BHBs but can also be applied to AGNs (Done et al. 2011). Figure 2.2 shows a standard disc spectrum for a black hole of $M = 10^6$ $M_\odot$ and $L/L_{Edd} = 1$ (black dashed line) corrected by $f_{col} = 2.6$ (blue solid line) and is compared to the disc spectrum calculated from the full radiative transfer (red solid line). This colour temperature corrected disc spectrum is a good approximation to the spectrum derived from full disc radiative transfer models and can be used for spectral fitting. This model is available from `Xspec` v12 as either *optxagn* where users can define their own f_{col}, or *optxagnf* where the colour temperature correction is calculated for

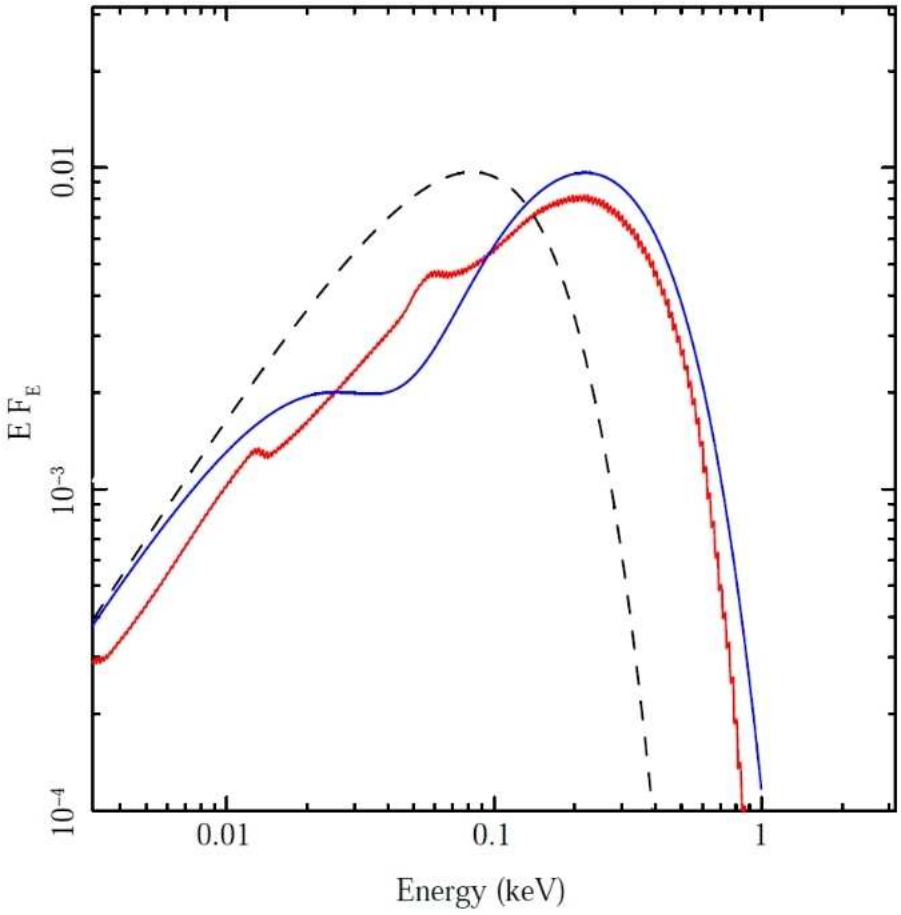

Figure 2.2: a standard disc spectrum for a black hole of $M = 10^6\ M_\odot$ and $L/L_{Edd} = 1$ (black dashed line) corrected by $f_{col} = 2.6$ for all radii with $T > T_{scatt} = 10^5$ K (blue solid line) and is compared to the disc spectrum calculated from the full radiative transfer (red solid line). Figure is adopted from Done et al. (2011).

each temperature from the approximations given in Done et al (2011).

Such colour temperature corrected SED models have never been used in AGN broadband SED fittings. Therefore, in the following sections I will always use *optxagn* without colour temperature correction first so that the results are more comparable with previous works, then *optxagnf* will be used to study the differences introduced by colour temperature correction.

2.3 Source Selection

We searched the *XMM-Newton Master Log & Public Archive* for pointed observations with exposure times in the PN instrument of $\geq$ 50000 s in "subject_category" "AGN, QSOs, BL-Lacs and XRB". This resulted in 115 observations available at the time of our study (November 2008). We further refined this criteria to include only those objects with PN count rates of $\gtrsim$ 1.0 counts/s, to include only bright sources for which the variability can be well determined.

We also searched the *XMM-Newton Serendipitous Source Catalogue (2XMMi Version)* for serendipious bright AGN detected in similarly long exposures, by setting pn_8_flux $\geqslant 10^{-12}$ erg cm^{-2} s^{-1} and pn_ontime$\geqslant$50000 s. This yielded 29 observations.

We then combined these two samples to give a total of 68 individual sources. For each dataset we calculated the fractional variability amplitude using `lcstats` in `xronos 5.21`. This is defined as the root mean square of the intrinsic (corrected for error bars) variance about the lightcurve mean, σ^2, normalised to this mean, I. Only sources which are strongly and significantly variable can provide constraints on the energy dependence of the variability, so we select only sources for which the *rms* is $\geq$ 0.1 at more than 3 sigma significance (determined from the uncertainty on the *rms*, which relates to the χ^2 distribution as the variance is a sum of squares, see e.g Done et al. (1990)). This filtering leaves 19 AGNs.

We then excluded 2 known BL Lac objects (PKS2155-304 and 0716+714) since their X-ray variablity is thought to be due to jet related processes. For the two observations of NGC 4051, one (0157560101) only has an exposure time of 49917

s, while the other (0109141401) does not have the pn_time value in the catalog, so they were formerly excluded by the filtering. However, since NGC 4051 is a well known, bright, NLS1 and our study is not a statistical study, we still included these two observations. This inclusion should not affect our general conclusions. We also included the famous Seyfert 2 AGN, MCG-5-23-16 (0302850201), although its *rms* variability is only 0.073. This gives us a total of 19 AGNs for subsequent study, with one or more selected observations for each of them.

For each of these datasets we calculated the fractional variaibility amplitude as a function of energy using the method of Gierliński & Done (2006). This showed the standard range of *rms* spectral shapes. Only RX J0136.9-3510 (0303340101) displayed the very different type of *rms* spectrum associated with the QPO AGN, RE J1034+396, in which the fractional amplitude rises as a function of energy, then remains high. Having identified this unusual AGN, we investigate its properties and compare it with RE J1034+396 in more detail below.

2.4 RX J0136-3510: lightcurve and *RMS* Spectrum

The lightcurve and *rms* spectrum are extracted from the X-ray data (0.3-10 keV), using `SAS7.1.0` and `xronos5.21`. We use regions with radius of 70″, 40″ and 40″ for pn, MOS1 and MOS2, respectively. No significant pile-up is seen from the `SAS` command `epatplot` so no central region was excluded. There are high background flares during the first 10000 s, so we exclude these data, resulting in ∼40000 s (with background count rate$<$ 0.4 counts/s) for the *rms* spectrum generation. Figure 2.3 shows the resultant total lightcurve (PN, MOS1 and MOS2), binned on 200 s. The source shows strong variability (also seen by Ghosh et al. 2009, in preparation), with the *rms* fractional variation being 0.13. However, there is no obvious QPO, and a power spectral analysis shows no peaks above even 1σ significance using the method of Vaughan (2005).

We rebin the lightcurve on 2000 s in order to provide enough count statistics

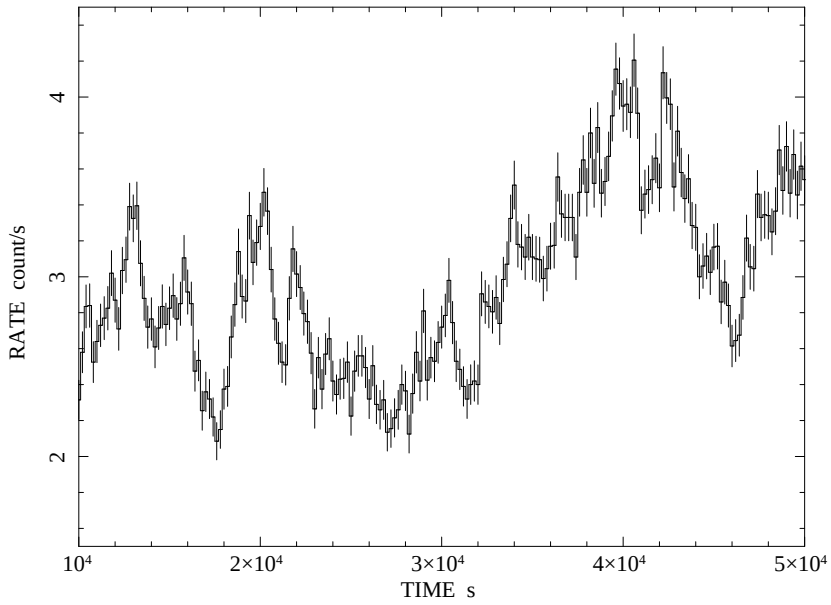

Figure 2.3: Background subtracted lightcurve of RX J0136.9-3510 binned on 200 s. The exposure start time (UTC) is 2005-12-14 20:45:30, but the first 10 ks was excluded due to the high background contamination.

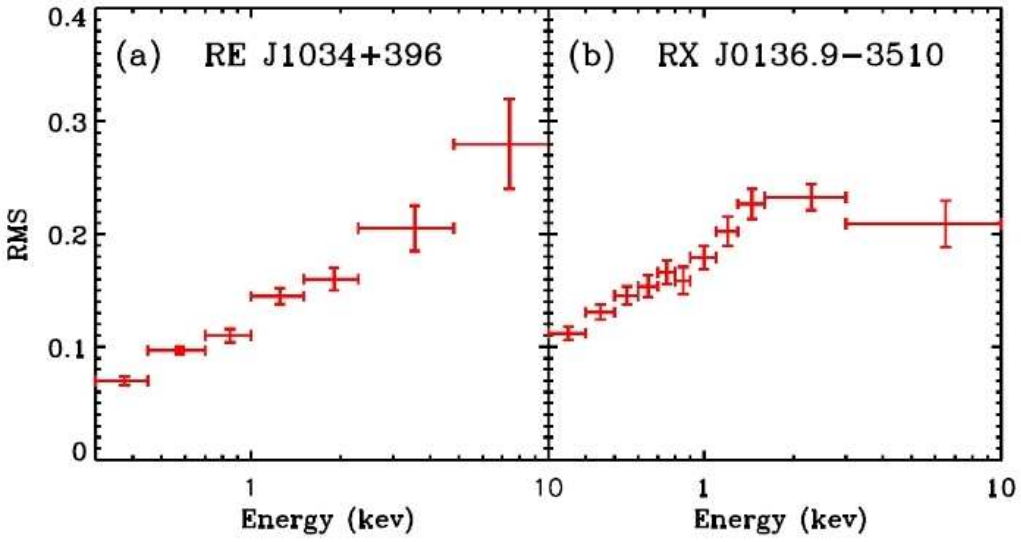

Figure 2.4: Similar *rms* spectra between RE J1034+396 (panel a, 100s binning time) and RX J0136.9-3510 (panel b, 2000s binning time).

to calculate the fractional variability as a function of energy. Figure 2.4b shows that this *rms* rises steeply from 0.3 keV to ∼2 keV, then flattens off. The weak decrease from 2-10 keV is not significant as the low count rate means their are large uncertainties on the last point. We also calculated the *rms* spectra from 200 s binning, but this is not significantly different. This rms spectra is very similar as the rms spectra for RE J1034+396 binned at 100s. (Figure 2.4b). The mass of RX J0136.9-3510 is 10-50× higher than RE J1034+396 (see next section below), thus similar variabilities in RX J0136.9-3510 and RE J1034+396 must have different timescales scaling with the black hole mass.

2.5 Black Hole Mass Estimation

The optical spectrum has an $FeII/H\beta$ flux ratio of $\sim$ 8.3 Grupe et al. 1999), compared to the $\sim$ 1 average for NLS1s (Véron-Cetty, Véron & Goncalves 2001), making RX J0136.9-3510 an unusual NLS1 (Ghosh et al. 2004). We use the optical spectrum shown in Fig 2.5 (D. Grupe, private communication) to estimate the black hole mass. The Hβ line width is used as a proxy for this (see Woo & Urry 2002 and references therein) from

$$M_{BH} = 4.817\times[\frac{\lambda L_{\lambda}(5100\mathring{A})}{10^{44} ergs^{-1}}]^{0.7} FWHM^2 \tag{2.2}$$

Comparing this method for a sample of AGN with reverberation mapping, the rms difference is about 0.5 dex (Woo & Urry 2002). The flux at $\lambda = 5100\mathring{A}$ from the optical spectrum is $\sim$1.5×10^{-16}erg cm^{-2}s^{-1}. The luminosity distance is D_L = 1455.2 Mpc for $z = 0.289$ assuming $H_0 = 72$ km Mpc^{-1}, $\Omega_M = 0.27$, and $\Omega_{vac} = 0.73$.

Estimating the FWHM of the line is not straightforward as the Hβ line profile is complex. There is clearly also a component from the extended narrow line region (NLR). This should be similar to the profile of the [OIII] emission line. So Grupe et al. (1999) use a template constructed from the [OIII]λ5007 line to represent the narrow component, together with a broader Gaussian component, with FWHM=1320 km/s, to reconstruct the $H\beta$ line. This gives a black hole mass estimate of 1.3×10$^7 M_{\odot}$.

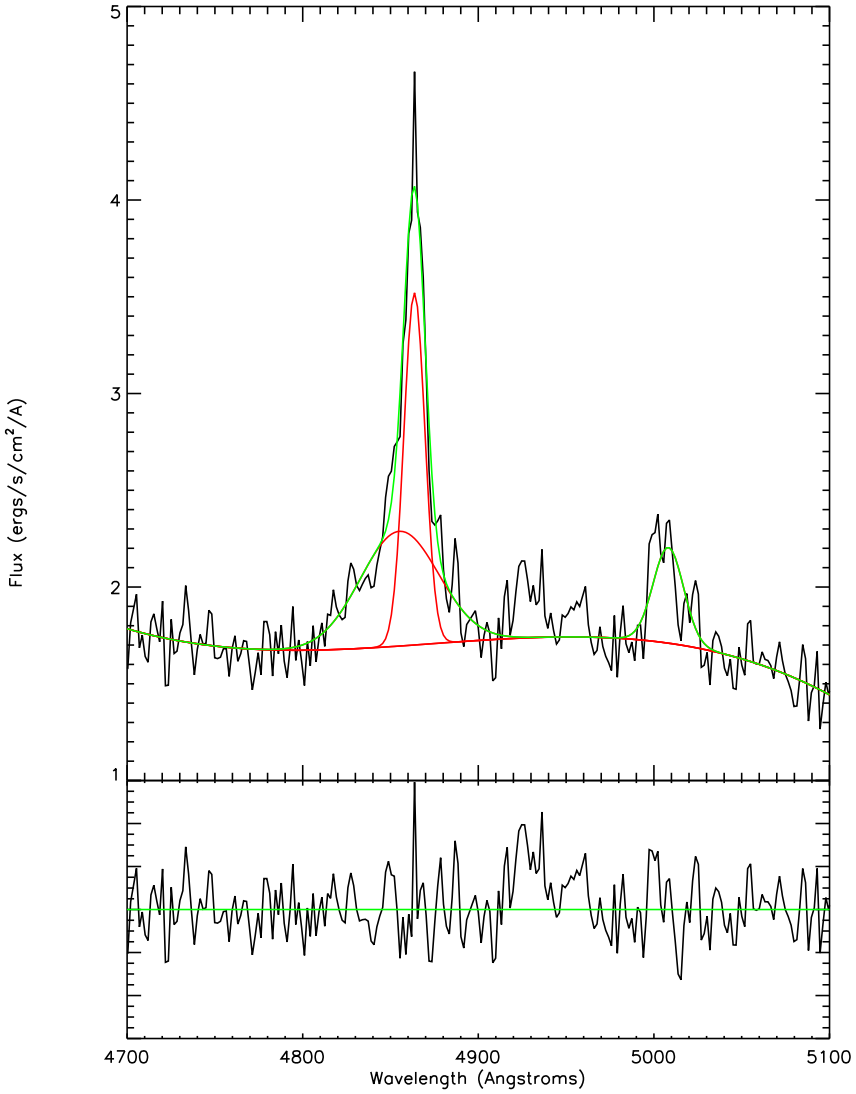

Figure 2.5: The optical spectrum of RX J0136.9-3510, including the Hβ emission line fitting. The data is from Grupe D. and we show this figure with his permission.

However, the optical spectrum plainly has limited signal-to-noise, and the [OIII] 5007 line is probably contaminated by FeII emission as it should be in 3:1 ratio with the (unobserved) [OIII] line at 4959Å. Hence we perform our own best fit of the Hβ line profile with a gaussian of width 870 km/s for the narrow line component, see Figure 2.5. This gives a FWHM for the broad component of 3200±2600 km s^{-1}, with a (not significant) blueshift of -370±1100 km s^{-1}. Using our new value for the FWHM, the resultant black hole mass is $7.85\times10^7 M_\odot$.

Even with the lower black hole mass estimate, this AGN is still probably $\sim 10\times$ more massive than the QPO AGN, RE J1034+396, (with the later mass estimate being $\sim 50\times$ larger). Thus any similar QPO in RX J0136.9-3510 would be on timescales 10-50$\times$ larger, requiring a much longer X-ray observation in order to detect it.

2.6 Broad band SED Analysis and Eddington Ratio

We use the standard products to obtain the XMM-Newton X-ray (PN) spectra and optical/UV (OM) photometry. We then combine these with selected continuum points from the (non-simultaneous) optical spectum (D. Grupe, private communication) using `FLX2XSP` to incorporate these into the same format as the XMM-Newton data. We likewise include the J,H and K near infrared flux points from 2MASS, and perform all spectral fitting using `xspec11.3.2`.

2.6.1 SED Fitting in `Xspec` Using *diskpn+compTT+bknpl*

We follow the approach of Vasudevan & Fabian (2009) in modelling the broadband SED, using *diskpn* to model an accretion disc extending down to the last stable orbit around a non-spinning black hole. However, our source is at $z = 0.289$ so we modify the *diskpn* code to incorporate the redshift dependance. The normalisation of the *diskpn* model is $(M^2 \cos i)/(D_{kpc}^2 \beta^4)$ where M is the mass in solar units, D_{kpc} is the distance in kpc, and the cosine of the inclination and colour temperature correc-

Table 2.1: The best-fit parameters for the model in Figure 2.6.

constant 2	T_{disk} (eV)	kT_e (keV)	τ	N_{comp}	Γ_{pow}	N_{pow}	χ^2_ν/d.o.f
$0.92^{+0.10}_{-0.10}$	$7.93^{+0.28}_{-0.31}$	$0.28^{+0.03}_{-0.02}$	$12.17^{+0.72}_{-0.75}$	$10.64^{+2.37}_{-1.73}$	$2.28^{+0.07}_{-0.08}$	$1.12^{+0.55}_{-0.37}$	475/493

tion ($\cos i$ and β, respectively) are both set to unity following Vasudevan & Fabian (2009). We start at the highest estimated black hole mass in Section 2.5, which gives a *diskpn* normalization of 2910, and fix this in the spectral fitting. Compton scattering of these disc photons can be approximated by a broken power law (*bknpower*), with index of $\Gamma = 0.33$ below a break at $3kT_{disk}$. We then added a low temperature Comptonisation component to model the soft excess, using *comptt*, with seed photons set to the disc temperature. We assume that these intrinsic components are absorbed by both gas and dust in our Galaxy, and so fix this parameter to the the Galactic HI column[1] (*wabs*) value of $N_H = 0.0208\times10^{22}$ cm^{-2}. The reddening (*redden*) is linked to this assuming a E(B-V)=$1.74\times10^{-22}N_H$ (Spitzer 1978). Since the optical data were not simultaneous with the UV and X-ray data, we allow for long time-scale variation as a constant offset in normalisation between the XMM-Newton data and the optical spectrum. We exclude the infrared data points from our spectral fitting, since the model we use describes the intrinsic emission from the accretion flow whereas the infrared emission is likely due to reprocessing of the UV emission by dust in the host galaxy, plus a possible contribution from intrinsic starlight. The resultant best-fit parameters are given in Table 2.1.

Figure 2.6 shows the rebinned data (black), with the optical flux corrected for their best fit normalisation of $\sim 0.92\times$ that of the XMM-Newton UV and X-ray spectra, and all datapoints are corrected for absorption/reddening. This model is a good description of the overall shape of the optical/UV/X-ray spectrum and gives a bolometric (0.001-100 keV) flux of 1.1×10^{-10}erg cm^{-2}s^{-1}, corresponding to a bolometric luminosity of 2.7×10^{46}erg s^{-1}.

Using our own fitting value for the FWHM, from which the resultant black hole mass is $7.85\times10^7 M_\odot$, the Eddington ratio for RX J0136.9-3510 is as high as ~ 2.7! Moreover, if we adopt the lower estimated black hole mass which is $1.3\times10^7 M_\odot$, then

[1]http://heasarc.gsfc.nasa.gov/cgi-bin/Tools/w3nh/w3nh.pl

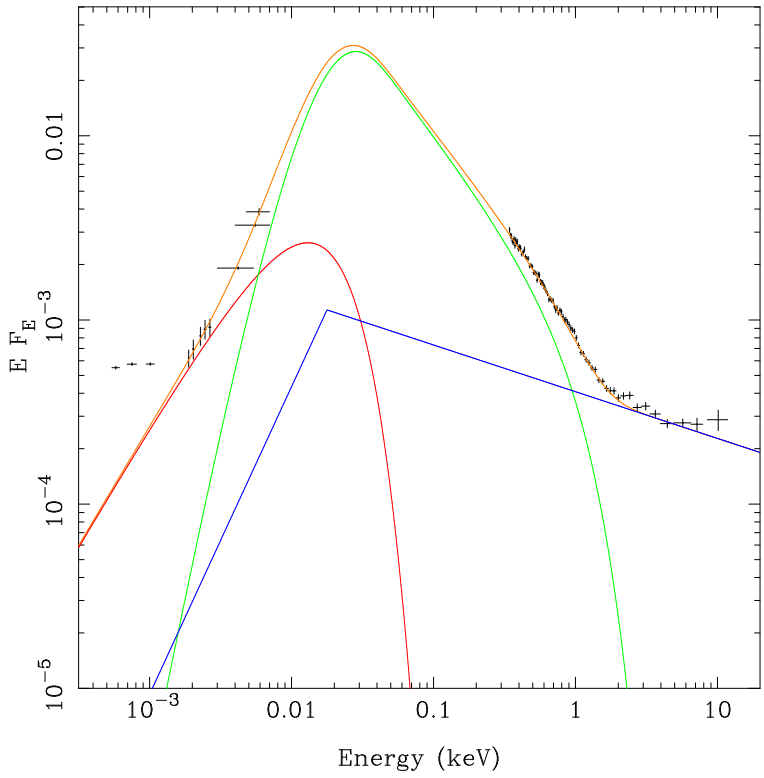

Figure 2.6: RX J0136.9-3510 unfolded spectrum. All data points from different wave bands are included in this figure, though the infrared points are not included in the model fitting. The model spectrum without galactic extinction and dust reddening is also generated and superposed on the source spectrum, with red representing redshifted disk component, green representing *compTT* and blue representing *bknpower*. The orange line shows the total model spectrum.

	Model	N_H (10^{20} cm^{-2})	M_{BH} ($10^6 M_\odot$)	L/L_{Edd}	r_{cor} (R_g)	kT_e (keV)	τ	Γ	f_{pl}	χ^2/ν
RE J1034	A	1.7	1.2	5.0	31	0.23	11	2.2	0.05	1.12
	B	4.9	5.8	1.1	14	0.18	15	2.2	0.12	1.66
RX J0136	A	0.0	14	24	13	0.31	11	2.2	0.22	1.28
	B	0.0	48	3.9	16	0.30	11	2.2	0.24	1.80

Table 2.2: Broadband SED Fitting Parameters of RE J1034+396 and RX J0136.9-3510 for Model-A (*optxagn*, assume $f_{cor} = 1$) and Model-B (*optxagnf*) (see Figure 2.7). N_H: the intrinsic N_H column density; r_{cor}: corona radius; kT_e and τ: electron temperature and optical depth of the low energy Comptonisation component; f_{pl}: the fraction of coronal emission powers the high energy Comptonisation component; Γ: photon index of the high energy Comptonisation component.

the normalization of *diskpn* is 80, and the resultant disk temperature rises to 31 eV. The UV region is then dominated by disk emission, though the Comptonisation still is required to model the soft X-ray excess. This gives a bolometric flux of 8.8×10^{-11} ergs s^{-1} cm^{-2}, giving an even higher Eddington ratio of 13.2! This is the highest known Eddington ratio for an AGN (Vasudevan & Fabian 2009; Shen et al. 2008). Thus modelling the spectral energy distribution with the two extreme mass estimates gives a range for the Eddington ratio of RX J0136.9-3510 of 2.7-13.2. Even without models, simply integrating the observed spectrum using a straight line to connect the UV and soft X-ray data gives an Eddington ratio of ~ 1 for the highest black hole mass, making this a robustly super-Eddington source.

2.6.2 SED Fitting in `Xspec` Using *Optxagn(f)*

In this section, we apply the *optxagn(f)* model in `Xspec` v12 to both RE J1034+396 and RX J0136.9-3510 to show their broadband SED similarity. The spectral data of RE J1034+396 is from the `EPIC` and `OM` monitor of `XMM-Newton` and the Sloan Digital Sky Survey (SDSS) (see Chapter 3).

First we use *optxagn* by assuming $f_{cor} = 1$ (Model-A). A value for the black hole mass is derived from Equation 2.2 but is allowed to change during the spectral fitting. We also included two sets of corrections for attenuation (*reddening*-*wabs*),

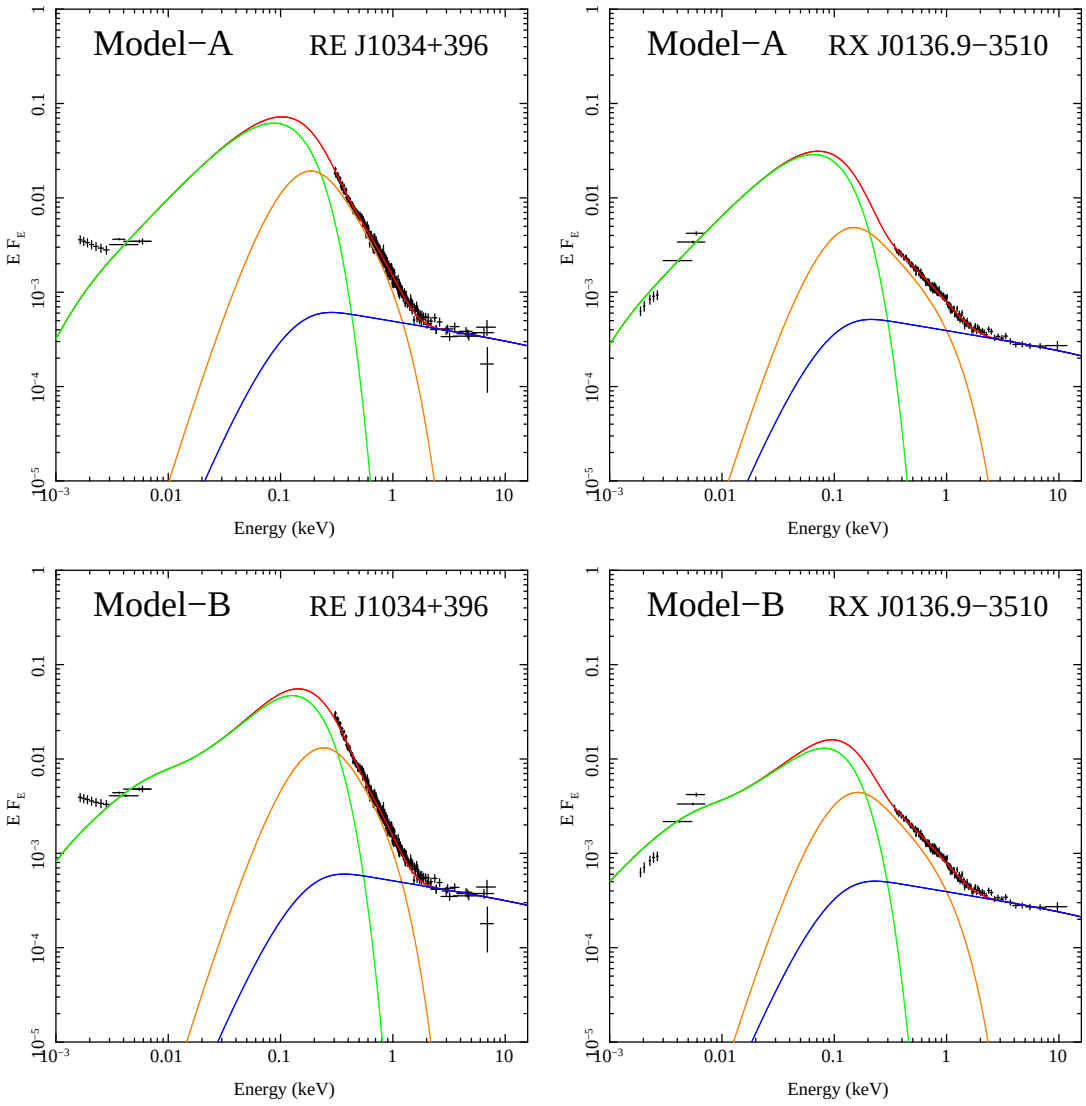

Figure 2.7: Broadband SED fitting of RE J1034+396 and RX J0136.9-3510 using Model-A (*optxagn* with $f_{col} = 1$) and Model-B (*optxagnf*). The SED consists of accretion disc (solid green), low temperature Comptonisation (solid orange) and high temperature Comptonisation (solid blue), under the physical scenario presented in Figure 2.1.

to account for the line of sight Galactic absorption and for the absorption intrinsic to each source, the latter is redshifted (*zred* and *zwabs* in XSPEC). The Galactic HI column density is fixed at the value taken from Kalberla et al. (2005), but the intrinsic HI column density is left as a free parameter. The standard dust to gas conversion formula of E(B-V)=$1.7\times10^{-22}N_H$ (Bessell 1991) is used for both Galactic and intrinsic reddening. We set the initial value of the power law photon index to be that of the photon index in the 2-10 keV energy band, but it can vary during the fitting process. However, we set an upper limit of 2.2 for the power law photon index, not only because the photon index is < 2.2 for the majority of Type 1 AGNs (Middleton, Done & Gierliński 2007) but also because otherwise the much higher signal-to-noise in the soft excess in some observed spectra can artificially steepen the hard X-ray power law and result in non-physical best-fit models. Then *optxagnf* is used to include the effect of colour temperature correction (Model-B). Similarly, absorptions are included in the model.

Figure 2.7 presents the SED fitting results. Best-fit parameters are listed in Table 2.6.2. It is obvious that the broadband SEDs of RE J1034+396 and RX J0136.9-3510 are quite similar to each other, the SED parameters are also similar. Compared with the SED decomposition in Figure 2.6, the additional constraint of energy conservation in *optxagn(f)* results in an accretion disc dominated SED decomposition for RX J0136.9-3510. The mass accretion rate in both of these two sources is quite high, so colour temperature correction is significant and causes the black hole mass from Model-B to be higher than from Model-A. The Eddington ratio obtained from Model-B is also lower. However, both models result in super-Eddington mass accretion rate, confirming the robust existence of super-Eddington accretion flows in both of these two sources.

2.7 Summary and Conclusion

In this chapter we present new broadband SED models which combine a standard accretion disc, a low temperature Comptonisation and a high temperature Comptonisation by introducing a corona radius. Electron scattering is also considered in

these models which results in colour temperature correction for high temperature disc spectra.

We also report that RX J0136.9-3510 is the only well observed, X-ray bright, variable AGN which has a similar energy dependence to its X-ray variability as the so far unique QPO AGN, RE J1034+396. After applying various SED models to their optical, UV and X-ray data, we find that both sources have similar Eddington ratios of around 3, although the larger mass of RX J0136.9-3510 means any QPO is undetectable in its data. The broad band SED of RX J0136.9-3510 is also remarkably similar to that of RE J1034+396, being well decomposed into a truncated multi-colour disc component, a low temperature, optically thick Comptonisation component, plus a high temperature, optically thin Comptonisation component. Spectra such as this have also been fit by "slim" disc models (Abramowicz, Kato & Matsumoto 1989), where the accretion rate is so high that radiation cannot easily escape vertically before it is carried radially (advected) along with the flow (Puchnarewicz et al. 2001; Wang & Netzer 2003). However, simple slim disc models do not fit the curvature of the soft X-ray spectra as well as Comptonisation (Middleton et al. 2009), although more complex models of slim discs do include such scattering in the disc atmosphere (e.g. Kawaguchi 2003).

Low temperature, optically thick Comptonisation is also occasionally seen in the stellar mass black hole binary systems, for example in the most extreme mass accretion rate spectra of GRS 1915+105 (Middleton et al. 2006; Middleton et al. 2009). Recent studies of spectra of the Ultra-Luminous X-ray sources also indicates that these are well modelled by such material (Gladstone, Roberts & Done 2009). This evidence suggests that there is indeed a distinct spectral state which can only be attained by super Eddington flows (Gladstone, Roberts & Done 2009). Future long duration X-ray observations of AGN should reveal additional examples, and objects with low black hole masses are potential QPO candiates.

Chapter 3

Type 1 AGN Study - I. Optical and Broadband SED Modeling

3.1 Introduction

The observed spectral differences between various types of AGN are not only due to selective absorption and orientation effects, as implied by the simplest version of AGN unification model (Antonucci 1993), but also result from a wide range in basic physical parameters, such as black hole mass and accretion rate (e.g. Boroson & Green 1992; Boller, Brandt & Fink 1996; Done & Gierliński 2005; Zhou et al. 2006). To better understand the accretion processes occurring close to the super massive black hole (SMBH), we construct broadband SEDs. Galactic dust reddening, together with the intrinsic reddening of the AGN itself, attenuates the optical/UV band emission. Furthermore, Photoelectric absorption from gas modifies the lower energy X-ray continuum. But these factors can be quantified and corrected. The uncertainty of these corrections must be small if we only focus on the unobscured sources. Thereby we can recover the intrinsic SED, except for the unobservable far-UV region. If we have reliable data on both sides of the energy gap between the UV and soft X-ray, we can apply a multi-component model which spans across it.

In this chapter we define an X-ray/optically selected sample of 51 AGN, all of which have low reddening (so excluding Seyfert 2s and 1.9/1.8s), to construct SEDs ranging from about 0.9 microns to 10 keV. We also apply corrections for the permitted iron features, the Balmer continuum and stellar contribution, in order to

model the non-stellar continuum free from emission line effects. Included in this sample are a number of NLS1s, a subclass of AGN whose permitted line widths are comparable to those of forbidden lines. Their [OIII]λ5007/Hβ ratio is also lower than the typical value of broad line Seyfert 1s (BLS1s) (Shuder & Osterbrock 1981; Osterbrock & Pogge 1985). For consistency with previous work, we classify AGNs in our sample as NLS1s if they have ratios of [OIII]λ5007/H$\beta < 3$ and FWHM$_{H\beta} <$ 2000 km/s (Goodrich 1989). We identify 10-12 NLS1s in our sample[1].

All objects in our sample have high quality optical spectra taken from the Sloan Digital Sky Survey (SDSS) DR7, X-ray spectra from the XMM-Newton EPIC cameras, and in some cases simultaneous optical/UV photometric data points from the XMM-Newton OM. Combining these data reduces the impact of intrinsic variability and provides a good estimate of the spectral shape in the optical, near UV and X-ray regions. In addition, by analyzing the SDSS spectra, we can derive the parameters of the principal optical emission lines and underlying continuum. An important result from reverberation mapping study is the correlation between black hole mass, monochromatic luminosity at 5100 Å and Hβ FWHM (e.g. Kaspi et al. 2000; Woo & Urry 2002; Peterson et al. 2004). We measure these quantities from the SDSS spectra, and then estimate black hole masses using this correlation.

Compared with previous studies mentioned in Chapter 1.5, a significant improvement of our work is that we employ a new broadband SED model which combines disc emission, low temperature Comptonisation and a high temperature Comptonisation component in the context of an energetically self-consistent model for the accretion disc emission (i.e. the *optxagn(f)* models presented in Chapter 2). To be more consistent and comparable with previous works, we do not consider the effect of colour temperature correction in this chapter, and just use *optxagn* with $f_{col} = 1$ to perform broadband SED fitting. Spectral fitting results from the colour temperature corrected model *optxagnf* will be discussed separately in Chapter 5 and

[1]Although 2XMM J112328.0+052823 and 1E 1346+26.7 have Hβ FWHMs of 2000 $km\ s^{-1}$, 2050 $km\ s^{-1}$ respectively, they both have Hα FWHM of 1700 $km\ s^{-1}$, and also share other NLS1's spectral characteristics. Thus they could both potentially be classified as NLS1s, making a total of 12.

compared with the results in this chapter.

By fitting *optxagn* ($f_{col} = 1$) to our data, we can reproduce the whole broadband SED from the optical to X-ray. From this detailed SED fitting, we derive a number of interesting AGN properties such as: the bolometric luminosity, Eddington ratio, hard X-ray slope, and the hard X-ray bolometric correction. Combining all the broadband SED parameters with the optical parameters, we can provide further evidence for many previously suggested correlations, including all the correlations between optical and X-ray claimed in previous work, plus many others such as the Hβ FWHM versus X-ray slope, black hole mass versus Eddington ratio, [OIII]λ5007 emission line and the high excitation lines (e.g. [FeVII]λ6087, [FeX]λ6374) versus their ionizing flux (e.g. Boroson & Green 1992; Boller, Brandt & Fink 1996; Grupe et al. 1998; Grupe et al. 1999; Sulentic et al. 2000; Mullaney et al. 2009).

This chapter is organized as follows. Section 2 describes the sample selection and data analysis procedures. The detailed spectral fitting methods and results including Balmer line fitting, optical spectral fitting and broadband SED fitting are each discussed in sections 3, 4 and 5, separately. We present the statistical properties of our sample in section 6. The summary and conclusions are given in section 7. A flat universe model with Hubble constant of $H_0 = 72$ km s^{-1} Mpc^{-1}, $\Omega_M = 0.27$ and $\Omega_\Lambda = 0.73$ is adopted. In the next chapter, we will present our analysis of correlations between selected optical/UV emission features and the SED components, and discuss their physical implications. All the results in this chapter are contained in the already published paper Jin et al. (2011).

3.2 Sample Selection and Data Assembly

To identify a sample of Type 1 AGNs having both high quality X-ray and optical spectra, we performed a cross-correlation between `2XMMi` catalog and `SDSS DR7` catalog. We filtered the resulting large sample as described below. Our final sample consists of 51 Type 1 AGNs including 12 NLS1s, all with high quality optical and X-ray spectra and low reddening/absorption, and with Hβ line widths ranging from 600 $km\ s^{-1}$ up to 13000 $km\ s^{-1}$. All the sources are listed in Table 3.1.

3.2.1 The Cross-correlation of 2XMMi & SDSS DR7

The first step was to cross-correlate between `2XMMi` and `SDSS DR7` catalogs. The `2XMMi` catalog contains 4117 XMM-Newton EPIC camera observations obtained between 03-02-2000 and 28-03-2008, and covering a sky area of ~ 420 deg^2. The `SDSS DR7` is the seventh data release of the Sloan sky survey. The SDSS spectroscopic data has sky coverage of ~ 8200 deg^2, with spectra from 3800 Å to 9200 Å, and spectral resolution between 1800 and 2200.

Our cross-correlation consisted of three steps:

1. We first searched for all XMM/SDSS position pairs that lay within $20''$ of each other, resulting in 5341 such cases.

2. For these 5341 unique X-ray sources, we imposed two further selection criteria: that source positions be separated by less than $3''$, or that sources be separated by no more than $3 \times$ the XMM-Newton position uncertainty and no more than $7''$. This filtering resulted in 3491 unique X-ray sources. The $3''$ separation is chosen because we want to include all possible XMM/SDSS pairs during these early filtering steps. From the 2XMMi and SDSS DR7 cross-correlation, there are 114 XMM/SDSS pairs whose separations are less than $3''$, but are still nevertheless greater than $3 \times$ the XMM position uncertainty. We included all of these pairs. The $7''$ separation upper limit mitigates spurious matches, especially for fainter objects and/or those located far off-axis.

3. We selected only objects classified as extragalactic, giving a total of 3342 for further analysis.

3.2.2 Selection of Seyfert 1 with High Quality Spectra

Within these 3342 unique X-ray sources which satisfied all the above criteria, we applied further filtering to select only Type 1 AGNs having both high quality optical and X-ray spectra. The five steps in the filtering were as follows:

1. In order to obtain black hole mass estimates, we require $H\beta$ and $H\alpha$ emission lines to be measurable. So we only selected sources with $H\beta$ in emission (as indicated by the SDSS $H\beta$ line models with at least 3σ significance and $EW > 0$) and redshift

Table 3.1: The Seyfert 1 Galaxy Sample Set

ID	Common Name[a]	Redshift	2XMMi Catalog IAU Name (2XMM[b])	XMM-Newton Obs Date	SDSS DR7 MJD-Plate-Fibre	SDSS Obs Date	EPIC Counts[c]
1	UM 269	0.308	J004319.7+005115	2002-01-04	51794-0393-407	2000-09-07	19126
2	MRK 1018	0.043	J020615.9-001730	2005-01-15	51812-0404-141	2000-09-25	2056
3	NVSS J030639	0.107	J030639.5+000343	2003-02-11	52205-0709-637	2001-10-23	35651
4	2XMMi/DR7	0.145	J074601.2+280732	2001-04-26	52618-1059-399	2002-12-10	9679
5	2XMMi/DR7	0.358	J080608.0+244421	2001-10-26	52705-1265-410	2003-03-07	2912
6	HS 0810+5157	0.377	J081422.1+514839	2003-04-27	53297-1781-220	2004-10-19	4189
7	RBS 0769	0.160	J092246.9+512037	2005-10-08	52247-0766-614	2001-12-04	32731
8	RBS 0770	0.033	J092342.9+225433*	2006-04-18	53727-2290-578	2005-12-23	104028
9	MRK 0110	0.035	J092512.8+521711	2004-11-15	52252-0767-418	2001-12-09	515453
10	PG 0947+396	0.206	J095048.3+392650	2001-11-03	52765-1277-332	2003-05-06	58555
11	2XMMi/DR7	0.373	J100025.2+015852	2003-12-10	52235-0501-277	2001-11-22	7187
12	2XMMi/DR7	0.206	J100523.9+410746	2004-04-20	52672-1217-010	2003-02-02	5437
13	PG 1004+130	0.241	J100726.0+124856	2003-05-04	53055-1744-630	2004-02-20	3781
14	RBS 0875	0.178	J103059.0+310255	2000-12-06	53440-1959-066	2005-03-11	69434
15	KUG 1031+398	0.043	J103438.6+393828	2002-05-01	53002-1430-485	2003-12-29	63891
16	PG 1048+342	0.160	J105143.8+335927	2002-05-13	53431-2025-637	2005-03-02	47858
17	1RXS J111007	0.262	J111006.8+612522*	2006-11-25	52286-0774-600	2002-01-12	6147
18	PG 1115+407	0.155	J111830.2+402554	2002-05-17	53084-1440-204	2004-03-20	64601
19	2XMMi/DR7	0.101	J112328.0+052823	2001-12-15	52376-0836-453	2002-04-12	10098
20	RX J1140.1+0307	0.081	J114008.7+030710	2005-12-03	51994-0514-331	2001-03-26	35616
21	PG 1202+281	0.165	J120442.1+275412	2002-05-30	53819-2226-585	2006-03-25	66550
22	1AXG J121359+1404	0.154	J121356.1+140431	2001-06-15	53466-1765-058	2005-04-06	12975
23	2E 1216+0700	0.080	J121930.9+064334	2002-12-18	53140-1625-134	2004-04-26	8028
24	1RXS J122019	0.286	J122018.4+064120	2002-07-05	53472-1626-292	2005-04-12	8338
25	LBQS 1228+1116	0.236	J123054.1+110011	2005-12-17	52731-1232-417	2003-04-02	165823
26	2XMMi/DR7	0.304	J123126.4+105111	2005-12-17	52731-1232-452	2003-04-02	8816
27	MRK 0771	0.064	J123203.6+200929	2005-07-09	54481-2613-342	2008-01-15	40705
28	RX J1233.9+0747	0.371	J123356.1+074755	2004-06-05	53474-1628-394	2005-04-14	6041
29	RX J1236.0+2641	0.209	J123604.0+264135*	2006-06-24	53729-2236-255	2005-12-25	17744
30	PG 1244+026	0.048	J124635.3+022209	2001-06-17	52024-0522-173	2001-04-25	8509
31	2XMMi/DR7	0.316	J125553.0+272405	2000-06-21	53823-2240-195	2006-03-26	7591
32	RBS 1201	0.091	J130022.1+282402	2004-06-06	53499-2011-114	2005-05-09	209458
33	2XMMi/DR7	0.334	J132101.4+340658	2001-01-09	53851-2023-044	2006-04-26	4425
34	1RXS J132447	0.306	J132447.6+032431	2004-01-25	52342-0527-329	2002-03-09	6305
35	UM 602	0.237	J134113.9-005314	2005-06-28	51671-0299-133	2000-05-07	18007
36	1E 1346+26.7	0.059	J134834.9+263109	2000-06-26	53848-2114-247	2006-04-23	71985
37	PG 1352+183	0.151	J135435.6+180518	2002-07-20	54508-2756-228	2008-02-12	36171
38	MRK 0464	0.050	J135553.4+383428	2002-12-10	53460-2014-616	2005-03-31	13974
39	1RXS J135724	0.106	J135724.5+652506	2005-04-04	51989-0497-014	2001-03-21	12081
40	PG 1415+451	0.114	J141700.7+445606	2002-12-08	52728-1287-296	2003-03-30	55786
41	PG 1427+480	0.221	J142943.0+474726	2002-05-31	53462-1673-108	2005-04-01	70995
42	NGC 5683	0.037	J143452.4+483943	2002-12-09	52733-1047-300	2003-04-04	18885
43	RBS 1423	0.208	J144414.6+063306	2005-02-11	53494-1829-464	2005-05-04	37568
44	PG 1448+273	0.065	J145108.7+270926	2003-02-08	54208-2142-637	2007-04-18	134532
45	PG 1512+370	0.371	J151443.0+365050	2002-08-25	53083-1353-580	2004-03-14	40432
46	Q 1529+050	0.218	J153228.8+045358	2001-08-21	54563-1835-054	2008-04-07	10952
47	1E 1556+27.4	0.090	J155829.4+271715	2002-09-10	52817-1391-093	2003-06-27	6995
48	MRK 0493	0.031	J155909.6+350147	2003-01-16	53141-1417-078	2004-05-14	124115
49	II Zw 177	0.081	J221918.5+120753	2001-06-07	52221-0736-049	2001-11-08	36056
50	PG 2233+134	0.326	J223607.6+134355	2003-05-28	52520-0739-388	2002-09-03	7853
51	MRK 0926	0.047	J230443.3-084111	2000-12-01	52258-0725-510	2001-12-15	59513

[a] for some targets without well-known names, we simply use '2XMMi/DR7';

[b] the full name is '2XMM J...'; for targets with * symbol, the full names is '2XMMi J...';

[c] the total counts in all three EPIC monitors, namely pn, MOS1 and MOS2, and there are at least 2000 counts in at least one of these three monitors;

$z < 0.4$. This selection resulted in 802 unique X-ray sources, and 888 XMM/SDSS pairs (since some X-ray objects were matched with more than one SDSS spectrum).
2. Then we searched for the Type 1 AGNs (including subtypes 1.0, 1.5, 1.8 and 1.9) which have a minimum of 2000 counts in at least one of the three EPIC cameras. Our search retrieved 96 such broad line AGNs. We then inspected each of these XMM/SDSS pairs, to confirm that all the matches were indeed genuine.
3. From inspection of the SDSS spectra, we excluded 22 sources whose blueward part of the $H\beta$ line showed strong reddening or low S/N, which would distort the $H\beta$ line profile. We also excluded one object, RBS 0992, because its SDSS spectrum did not show an $H\beta$ line, due to a bad data gap. We ensured that the remaining 73 objects all had good $H\beta$ line profiles.
4. As a simple method to assess the spectral quality of the X-ray data, we used *wabs*power-law* model in `xspec11.3.2` to fit the rest-frame 2-10 keV X-ray spectra of all 73 objects. The *error* command was used to estimate the 90% confidence region for the *photon index* parameter. Based on the results, 16 objects with *photon index* uncertainties greater than 0.5 were thereby excluded, leaving 57 Type 1 AGNs with relatively well constrained 2-10 keV spectra.
5. By examining the 0.2-10 keV X-ray spectra, we excluded another 6 objects (i.e. IRAS F09159+2129, IRAS F12397+3333, PG 1114+445, PG 1307+085, PG 1309+355 and PG 1425+267) whose spectral shapes all showed clear evidence of an absorption edge at $\sim$0.7 keV (possibly originating from combined Fe I L-Shell and O VII K-Shell absorptions (Lee et al. 2001; Turner et al. 2004)). This is a typical spectral signature of a warm absorber (e.g. Nandra & Pounds 1994; Crenshaw, Kraemer & George 2003). By removing such objects with complex X-ray spectra, our broadband SED fitting is simplified. Our final sample contains 51 Type 1 AGNs.

3.2.3 Characteristics of the Sample

The sample selection procedure described above ensures that every source in our AGN sample has both high quality optical and X-ray spectra. In addition, a large fraction of the sample have simultaneous optical/UV photometric points from the

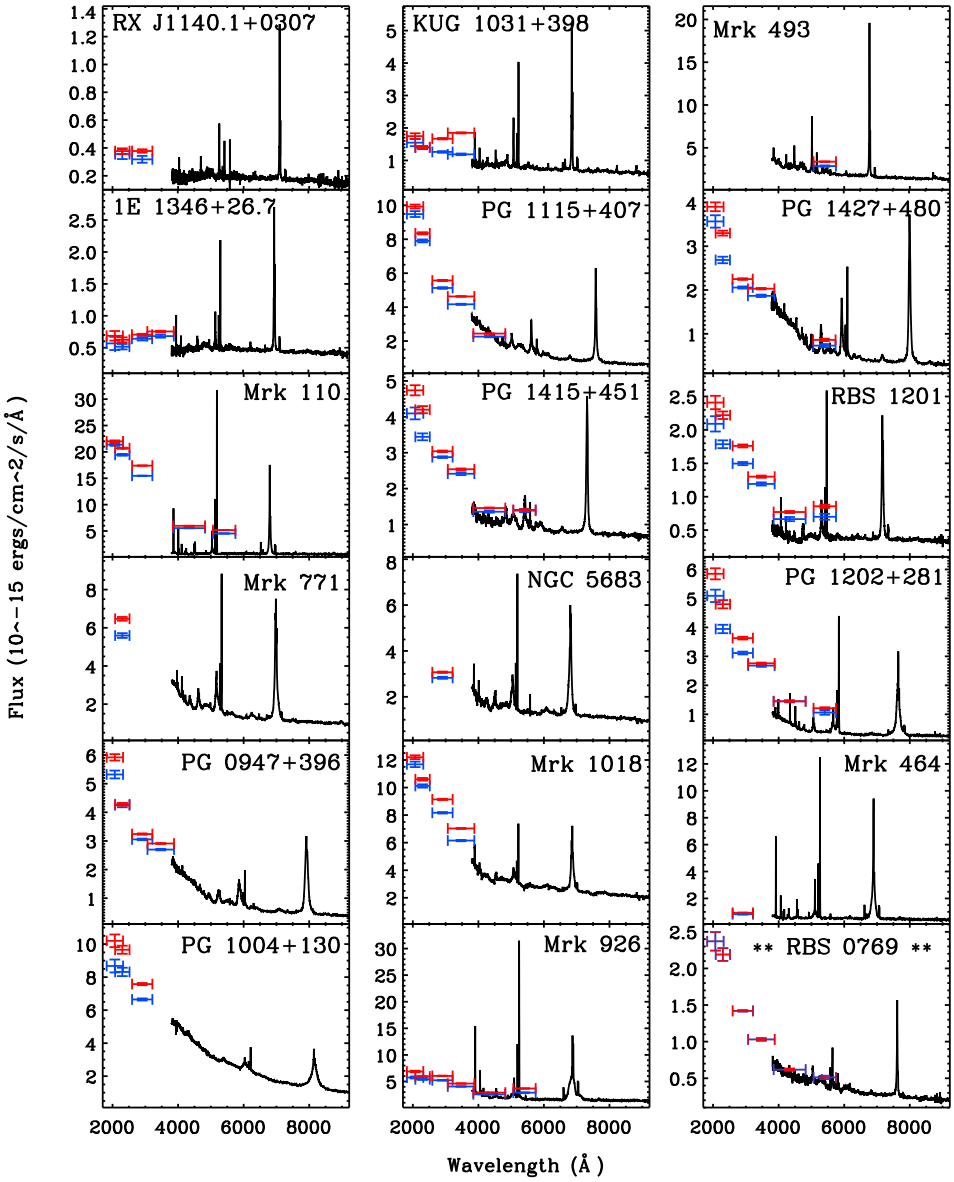

Figure 3.1: The aperture effect correction results for 17 extended sources in the sample. The point like source RBS 0769 (the last figure marked by **) is also shown for comparison. We over-plot OM data points on to the SDSS spectrum. Red OM points are data obtained directly from the OM PPS files. Blue OM points are the corresponding data after applying a smaller 6″ aperture to all OM filters, and applying appropriate OM corrections to the flux eg. deadtime correction, coincidence loss correction and OM time sensitivity degradation correction.

OM. Such high quality data enables accurate spectral fitting. In the optical band our sample is selected to have low reddening, since if present this would significantly modify the intrinsic continuum as well as the optical emission lines. This requirement reduces the complexity and uncertainty in our modeling of the intrinsic continuum, and also increases the overall quality of Hβ and Hα line profiles useful for estimating the black hole masses. Furthermore, low reddening is essential in the UV band. The inclusion of OM-UV photometric data observed simultaneously with the X-ray spectra provides a reliable link between these bands. This helps to reduce fitting uncertainty of the SED resulting from optical and X-ray variability. Besides, all sources are well constrained in the 2-10 keV band, which is directly associated with the compact emitting region of the AGN. Our exclusion of objects with evidence of a warm absorber means that the 2-10 keV spectral index is likely to be intrinsic rather than hardened by absorption in the soft X-ray region.

In summary, compared with previous AGN samples used for broadband SED modelling, the spectrally 'cleaner' nature of our sample should make the reconstructed broadband SEDs more reliable. Consequently, the parameters derived from the broadband spectral fitting should be more accurate. This may reveal new and potentially important broadband correlations, which we will discuss in detail in the next chapter.

3.2.4 Additional Data

The 51 Type 1 AGNs all have SDSS survey-quality spectra (flagged as "sciencePrimary" in SDSS catalog), including 3 objects that have multiple SDSS spectra (i.e. NVSS J030639, 1RXS J111007 and Mrk1018). In such cases we adopt the SDSS spectrum which connects most smoothly with the OM data.

For each object, we used all available EPIC X-ray spectra (i.e. pn, MOS1 and MOS2) for the broadband SED modeling, unless the spectrum had few counts and low S/N. We also searched through the `XMM-OM SUSS` catalog for all data in the OM bands (i.e. V, B, U, UVW2, UVM2 and UVW1), which are observed simultaneously with the corresponding EPIC spectrum. Of our 51 sources, we have 14 sources

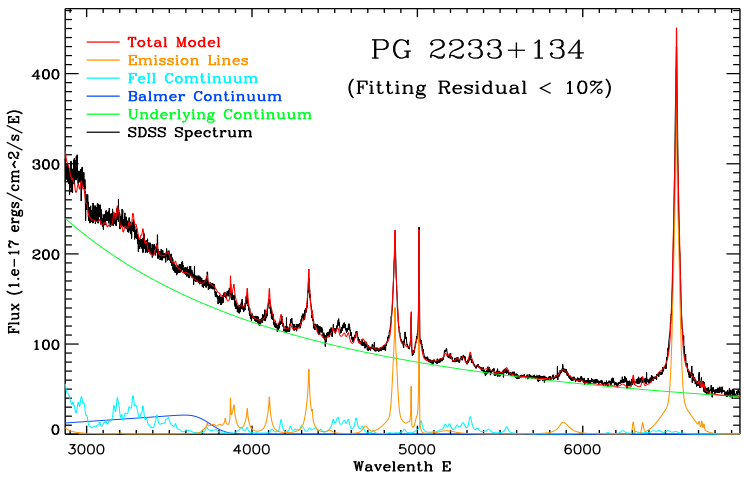

Fig-2a: An Example of SDSS Spectrum Fitting

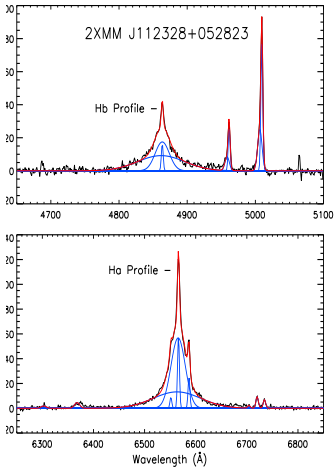

Fig-2b: Balmer Line Fitting

Figure 3.2: An example of results from SDSS spectrum fitting. The left panel shows a good fit for PG 2233+234. The black line is the observed spectrum, the red line is the total model spectrum. The green line represents the observed underlying continuum. The Balmer continuum (blue), FeII emission (light blue) and other strong emission lines (orange) are shown underneath. The right panel shows an example of detailed line profile fitting to the FeII subtracted region around the Hβ (upper) and Hα lines (lower) including Hα, Hβ, [OIII] λ5007/4959 doublets, [NII] λ6585/6548 doublets, Li λ6708, [SII] λ6717/6733 doublets, [OI] λ6300/6363 doublets. In our profile fitting, three Gaussian components are used for Hβ and Hα, two components for [OIII] λ5007, and one Gaussian for all other lines. The various Gaussian profiles are shown in blue, the total model is shown in red.

with SDSS optical spectra and XMM EPIC X-ray spectra, and 37 sources which in addition to this also have XMM-OM photometry.

3.2.5 OM Data Corrections and Aperture Effects

In the procedure of combining the SDSS spectra and OM data points, we identified that in some objects there is a clear discrepancy between these two data sets. The OM points often appear higher on the spectral plots (brigher) than is consis-

tent from a smooth extrapolation of the SDSS spectral shape. In fewer cases this discrepancy appears in the opposite sense, with the OM points apparently too low (fainter), see Figure 3.1 for some examples). This discrepancy may arise for several reasons, including a simple aperture effect. Compared to 3″ diameter for the SDSS spectroscopy fibres, the OM monitor has a much larger aperture, i.e. 12″ and 35″ diameter for the OM optical and OM UV filters respectively (Antonio Talavera.OMCal Team 2009). If the host galaxy is sufficiently extended, e.g. in the case of RE J1034+396, the larger aperture of the OM would include more host galaxy emission than that in the SDSS spectrum (see also section 3.5.3 for other possible reasons to account for this discrepancy). To investigate the aperture issue in more detail, we performed the following tests:

(1) We examined the combined SDSS and OM data plots, searching for those objects with excess OM flux compared with that expected from the extrapolated SDSS spectrum. We identified 27 such cases out of the 51 sources;

(2) Within this sample of 27 sources, we checked the catalog flag for an extended source in each OM filter. We noted those flagged as an extended source in at least one OM filter. This yielded 13 sources out of the 27.

(3) We also extracted the SDSS CCD images for all 51 objects and visually checked whether they appeared extended. As a result, we included another 4 objects for which their SDSS CCD images show that their host galaxy is extended beyond the 3″ diameter of the SDSS aperture. Either they were not flagged as extended sources in any OM filter, or they did not have any OM optical data. For these 17 objects, an aperture effect could at least be partially responsible for an excess flux in the OM data.

(4) For these 17 objects we downloaded all available OM image files. In each OM image, we applied a 6″ diameter aperture from which to extract the flux. We used the same sized aperture placed on a blank region of sky close to the object, to estimate the background. The quoted PSF FWHM of the OM for the different filters are: V(1.35″), B(1.39″) , U(1.55″), UVW1(2.0″), UVM2(1.8″), UVW2(1.98″). Thus in all cases 6″ is at least 3×PSF FWHM. So this aperture includes effectively all optical flux for a point source, and more than 90% that from a UV point source

detected by the OM.

Before subtracting the background flux from the source+background flux, we performed three count rate calibrations, according the method described in the OM instrument document.[2] The first is the deadtime correction, required because for a small fraction of the exposure time the CCD is in readout mode, and so cannot record events. The second calibration is for coincidence losses, which occur when more than one photon arrives on the CCD at the same location and within the same frametime, so results in under counting. The third calibration is for the OM time sensitivity degradation correction. We performed these calibrations, according to the algorithms set out in the OM instrument document, separately for the background and source+background count rates. We then subtracted the background count rate from the source+background count rate to obtain the corrected source count rate.

Figure 3.1 shows the OM data points before and after correction for aperture effects for the 17 objects. The reduced OM aperture does improve the alignment between the OM points and SDSS spectrum. This correction not only lowers the OM flux, but also changes the continuum shape defined by the OM points. Although choice of an aperture smaller than $6''$ will lower the OM fluxes by a larger factor, it will also introduce uncertainties and systematics caused by the PSF. Therefore we compromise by adopting a $6''$ diameter aperture. In our subsequent SED modeling we use the aperture corrected OM data.

3.3 Optical Spectral Modeling: The Emission Lines

Our optical spectral modeling employs linked $H\alpha$ and $H\beta$ profile fitting and the complete optical spectral fitting. We wrote the code in IDL (Interactive Data Language) v6.2, to perform all the optical spectral fitting. The 'MPFITEXPR' program from the Markwardt IDL Library is incorporated within our code to perform the Levenberg-Marquardt least-squares algorithm used to obtain the best-fit parameters.

[2]URL: http://xmm2.esac.esa.int/docs/documents/CAL-TN-0019.ps.gz; Also see the XMM-Newton User Handbook: http://xmm.esac.esa.int/external/xmm_user_support/documentation/uhb/index.html.

The SDSS spectra (stored in SDSS *spSpec* files) were extracted directly from the SDSS DR7 data archive and analyzed in IDL using our code. A detailed description of our spectral modeling procedures is presented in the following subsections.

3.3.1 Profile Fitting of the Hα, Hβ and [OIII]λ5007 Emission Lines

Based on current AGN emission line models, there are thought to be stratified regions emitting different lines. These regions are divided somewhat arbitrarily into a narrow line region (NLR), a broad line region (BLR) and possibly an intermediate line region (ILR, e.g. Grupe et al. 1999; Hu et al. 2008; Mei, Yuan & Dong 2009; Zhu, Zhang & Tang 2009). Following previous studies, we use several separate Gaussian profiles representing each of these emitting regions to model the Balmer line profiles.

The Hα and Hβ line profiles each pose distinct difficulties for the spectral analysis. In the case of the $H\beta$ line, the permitted FeII emission features (which are often strong in NLS1s) and broad HeII 4686 line blended with the $H\beta$ line, which can affect the determination of the underlying continuum and hence the $H\beta$ line profile. For the $H\alpha$ line, there is the problem of blending with the [NII] λ6584,6548 doublet, improper subtraction of which may distort $H\alpha$'s intrinsic profile. Our approach, therefore, is to fit $H\alpha$ and $H\beta$ simultaneously using the same multi Gaussian components. The assumed similarity between the intrinsic profiles of these two Balmer lines assists in deblending from other nearby emission lines, and should yield a more robust deconvolution for the separate components of their profile.

3.3.2 The FeII Problem

We use the theoretical FeII model templates of Verner et al. (2009). These include 830 energy levels and 344,035 transitions between 2000Å and 12000 Å, totaling 1059 emission lines. The predicted FeII emission depends on physical conditions such as microturbulence velocity and hardness of the radiation field, but we use the template which best matches the observed spectrum of I ZW 1 (Boroson & Green

1992; Véron-Cetty et al. 2004) i.e. the one with $n_H = 10^{11}\ cm^{-3}$, $v_{turb} = 30\ kms^{-1}$, $F_{ionizing} = 20.5\ cm^{-2}s^{-1}$. Detailed modelling of high signal-to-noise spectra shows that the FeII emission is often complex, with four major line systems in the case of 1 Zw 1, (one broad line system, two narrow high-excitation systems and one low-excitation system: Véron-Cetty et al. 2004; Zhou et al. 2006; Mei, Yuan & Dong 2009). However, for simplicity we will assume only one velocity structure and convolve this template with a single Lorentzian profile.

We fit this to the actual FeII emission line features between 5100 Å and 5600 Å (no other strong emission lines lie in this wavelength range) of the de-redshifted SDSS spectra, leaving the FWHM of the Lorentzian and the normalization of the FeII as free parameters. The resulting best-fit FeII model to this restricted wavelength range, was then extrapolated and subtracted from the entire SDSS spectrum. A major benefit from subtracting the FeII features is that the profiles of the [OIII] λ5007 lines no longer have apparent red-wings. This is particularly important for the NLS1s, where the FeII emission is often strong. After subtracting FeII, we used either 2 or 3 Gaussian components (depending on the profile complexity) to fit the [OIII] λ5007 line.

3.3.3 Deconvolution of the Balmer Lines

After fitting the [OIII] λ5007 line, we start to fit the Hα and Hβ line profiles simultaneously. Following previous studies we consider a simplified picture in which the Balmer lines have three principal components, namely a narrow component (from the NLR), an intermediate component (from a transition region ILR between the NLR and BLR or from the inner edge of dusty torus (Zhu, Zhang & Tang 2009)), and a broad component (from the BLR). The intermediate and broad components are both represented by a Gaussian profile, whereas the narrow component is assumed to be similar to that of [OIII] λ5007. Since we do not know whether or not the Balmer decrements are the same in these different emitting zones, the relative strengths of different line components were not fixed, but their FWHM and relative velocity were both kept the same. The [OIII] λ4959 line was set at 1/3 that

of [OIII] λ5007 from atomic physics. The [NII] λ6584,6548 line doublet were also fixed to the [OIII] λ5007 line profile. For simplicity, the [SII] λ6733,6717 doublet, [OI] λ6300,6363 doublet and Li 6708 were all fitted with a single Gaussian profile separately, because they are all relatively weak lines and do not severely blend with Balmer lines.

In order to separate the narrow component of the Balmer lines from the other components as accurately as possible, particularly for NLS1s and some broad line objects which lack clear narrow line profiles, we applied the following four different fitting methods:

1. The profile of the narrow component is held the same as the entire [OIII] λ5007 profile; and the normalization of each component in the $H\alpha$ and $H\beta$ lines are left as free parameters;

2. Only the central narrow component of the [OIII] λ5007 profile is used to define the profile of the Balmer narrow component, and of the [NII] λ6585,6550 doublet; the normalization of each component in the $H\alpha$ and $H\beta$ lines are free parameters;

3. The shape of the narrow component is held the same as the entire [OIII] λ5007 profile, and also the normalization of the $H\beta$ line narrow component is set to be 10% of [OIII] λ5007, this ratio being an average for the NLR in typical Seyfert 1s (Osterbrock & Pogge 1985; Leighly 1999); all other components have their normalizations as free parameters;

4. All conditions are the same as in method 3, except that the Balmer line narrow component and the [NII] λ6584,6548 doublet adopt the central narrow Gaussian component of the [OIII] λ5007 line.

We applied each of the above fitting methods to every object in our sample, and then compared the results. For those objects with clear narrow components to their Balmer lines, we used the best fitting result from method 1 and 2. For the other objects whose narrow components were not clearly defined or even visible, we adopted method 3 and method 4, unless method 1 or 2 gave much better fitting results. Figure 3.2 right panel shows an example of our fitting. Results for the whole sample are shown in Figure A.1.

After obtaining the best-fit parameters, we used the intermediate and broad

components to reconstruct the narrow-line subtracted $H\beta$ line profile, and then measured the FWHM from this model. The rationale for using this method, instead of directly measuring the FWHM of the $H\beta$ line from the data, is because for low signal/noise line profiles direct measurement of FWHM can lead to large uncertainties, whereas our profile models are not prone to localized noise in the data. The Hβ FWHM measurements for each of the 51 sources, after de-convolving using the instrumental resolution of 69 kms^{-1}, are listed in Table 3.3.

3.4 Optical Spectral Modeling

In order to obtain the underlying continuum, we must model the entire SDSS spectrum so that we can remove all the emission lines as well as the Balmer continuum and host galaxy contribution. As we are now concerned with the broad continuum shape, we choose to refit the FeII spectrum across the entire SDSS range, rather than restricting the fit to the Hα and Hβ line regions as discussed in the previous section.

Figure 3.2 shows an illustrative example of our optical spectral fitting, and the results for each of the 51 sources are presented in Figure A.1. In the following subsections we give further details of the components that make up these modeled spectra.

3.4.1 Emission Lines Including FeII

We use the models for [OIII], $H\alpha$ and $H\beta$ as derived above. We add to this a series of higher order Balmer lines: from 5→2 ($H\gamma$) to 15→2. We fix the line profile of these to that of $H\beta$ up to 9→2, then simply use a single Lorentzian profile for the rest weak higher order Balmer lines. We fix the line ratios for each Balmer line using the values in Osterbrock (1989), Table 4.2, with T_e between 10,000 K and 20,000 K. We similarly use a single Lorentzian to model the series of Helium lines (HeI 3187, HeI 3889, HeI 4471, HeI 5876, HeII 3204, HeII 4686) and some other emission lines (MgII 2798, [NeIII] λ3346,4326, [OII] λ3727,3730, [OI] λ6302,6366, [NII] λ6548,6584, Li 6708, [SII] λ6717,6733).

We use the same model for the FeII emission as described in Section 3.3.1. However we now fit this to the entire SDSS wavelength range, rather than restricting the fit to 5100–5600 Å.

3.4.2 The Balmer Continuum

Another potentially significant contribution at shorter wavelengths is from the Balmer continuum. Canfield & Puetter (1981) and Kwan & Krolik (1981) predicted the optical depth at the Balmer continuum edge to be less than 1, we use Equation 3.1 to model the Balmer continuum under the assumptions of the optically thin case and a single-temperature electron population (also see Grandi 1982; Wills, Netzer & Wills 1985).

$$F_v^{BC} = F_v^{BE} e^{-h(v-v_{BE})/(kT_e)} \quad (v \geqslant v_{BE}) \tag{3.1}$$

where F_v^{BE} is the flux at Balmer edge, v_{BE} corresponds to the Balmer edge frequency at 3646Å. T_e is the electron temperature. h is the Planck's constant, k is the Boltzmann's constant. This Balmer continuum equation is then convolved with a Gaussian profile to represent the real Balmer bump in SDSS spectra.

There are several parameters that may slightly modify or significantly change the shape of the Balmer continuum. It is already seen that the electron temperature T_e appearing in Equation 3.1 and the optical depth can both change the Balmer continuum shape, but there are additional important factors. Any intrinsic velocity dispersion will Doppler broaden all the Hydrogen emission features. Therefore a better description of the Balmer continuum can be obtained by convolving Equation 3.1 with a Gaussian profile, whose FWHM is determined by the line width of $H\beta$ (or other broad lines), as shown by Equation 3.2, where G(x) represents a Gaussian profile with a specific FWHM.

$$F_\lambda^{BC} = F_\lambda^{BE} e^{hc/(\lambda_{BE} kT_e)} \int_0^{+\infty} e^{-hc/(\lambda kT_e)} G(\lambda_1 - \lambda) d\lambda_1 \tag{3.2}$$

Figure 3.3 shows how the Balmer continuum's shape depends on the electron temperature and velocity broadening in Equation 3.2. The electron temperature modifies the decrease in the Balmer continuum towards shorter wavelengths, but

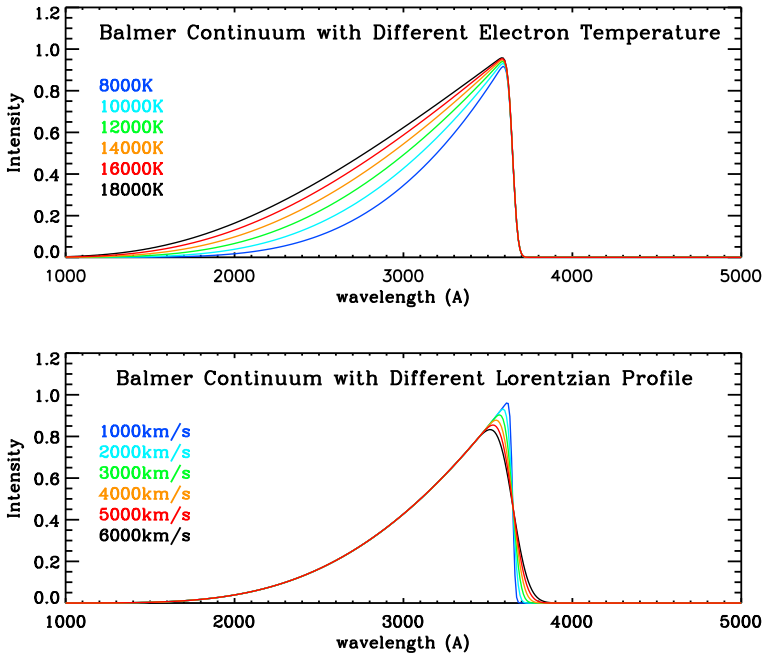

Figure 3.3: The Balmer continuum models of Grandi (1982). The upper panel shows the dependence of the model on the electron temperature. The lower panel shows the dependence of the model on the FWHM of the convolved Lorentzian profile.

has little effect on the broadening of (Balmer Photo-recombination) BPR edge. On the contrary, velocity broadening mainly affects the shape of the BPR edge, but the emission longward of 3646Å is still very weak compared to the emission blueward of the BPR edge, i.e. the BPR edge is still sharp.

We initially applied Equation 3.2 to fit the Balmer continuum bump below 4000Å in the SDSS spectra. We assumed the velocity profile for the convolution was a Gaussian with its FWHM determined from the $H\beta$ line profile, and the wavelength of the position of the BPR edge was taken as the laboratory wavelength of 3646Å. However, this model did not provide an acceptable fit, for example see the model shown by the blue line in Figure 3.4. It appears that the observed spectrum requires a model with either a more extended wing redward of the BPR edge, or a BPR edge that shifts to longer wavelength than 3646Å. However, additional velocity broadening should affect both the Balmer continuum and Balmer emission lines equally, as they are produced from the same material, although the multiple components

present in the line make this difficult to constrain.

One way the wavelength of the edge may be shifted without affecting the lines is via density (collisional, or Stark) broadening (e.g. Pigarov et al. 1998). Multiple collisions disturb the outer energy levels, leading to an effective n_{max} for the highest bound level $\ll \infty$, i.e. lowering the effective ionization potential. We set the edge position and the FWHM as free parameters, and let the observed spectral shape determine their best fit values. The red line shown in Figure 3.4 represents a good fit, obtained with FWHM of 6000 kms^{-1} and the BPR edge wavelength of 3746 Å, which implies $n_{max} \sim 12$. The theoretical n_{max} can be determined by the plasma density N_e and temperature T_e as $n_{max} = 2 \times 10^4 (T_e/N_e)^{1/4}$ (Mihalas 1978), so for a typical temperature of $10^4 - 10^5$ K, the required density is 7×10^{16}-7×10^{17} cm^{-3}. Such high density is not generally associated with the BLR clouds, and may give support to models where the low ionization BLR is from the illuminated accretion disc (e.g. Collin-Souffrin & Dumont 1990). However, any reliable estimation of the density would require more accurate subtraction of other optical components such as the FeII line blends and many other non-hydrogen emission lines, which is not the focus of this thesis. Nonetheless, this remains an interesting problem which is worthy of further study.

Yet another issue in modeling the Balmer continuum is how to quantify the the total intensity of this continuum component, especially when there is limited spectral coverage below 4000Å, which makes it difficult to define the overall shape. The theoretical flux ratio between the Balmer continuum and the $H\beta$ line under case B conditions can be expressed by Equation 3.3 (Wills, Netzer & Wills 1985),

$$I(Bac)/I(H\beta) = 3.95\ T_4^{0.4} \tag{3.3}$$

but other theoretical calculations of photonionization models show that by varying the Balmer optical depth, electron temperature and electron number density, this can result in very different values of I(Bac)/I(Hβ). For example, Canfield & Puetter (1981)s calculation resulted in a I(Bac)/Hα range of 0.05∼10, Kwan & Krolik (1981) suggested I(Bac)/I(Hβ)=1.6∼15, and other theoretical work also confirmed a large range in flux ratios (Puetter & Levan 1982; Kwan 1984; Hubbard & Puetter 1985).

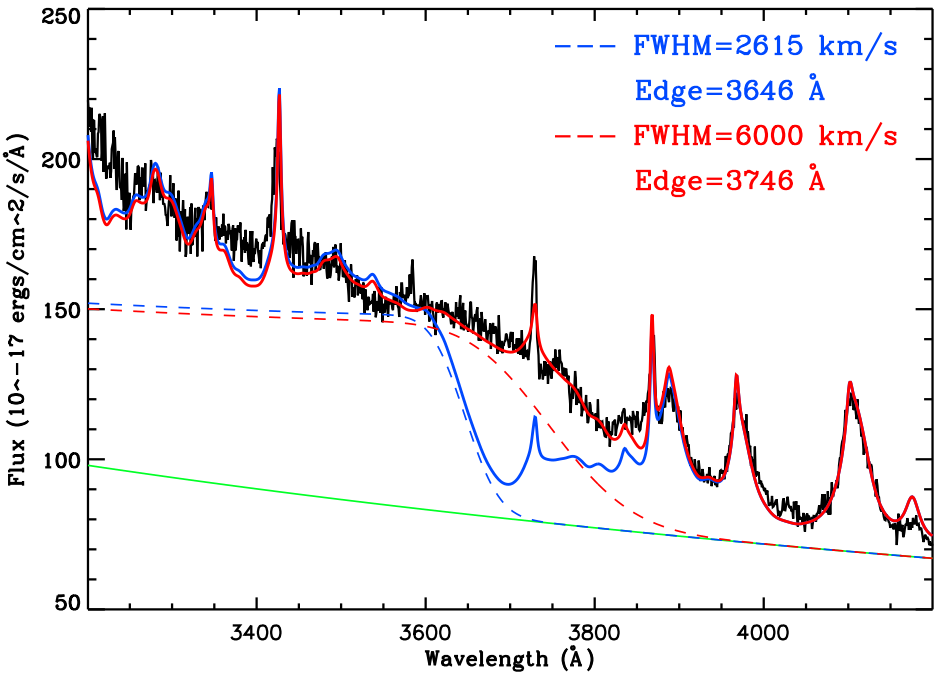

Figure 3.4: An expanded view of the region around the BPR edge in PG 1427+480. The blue and dashed lines represent the Balmer continuum model superposed on the underlying disc continuum (green solid line) using standard parameters (blue dash), and also a set of best fit parameters (red dash line). The red and blue solid lines are models of the total optical spectrum, including the corresponding Balmer continuum components and plus other components described in the text. The observed spectrum is shown in black.

The observed ranges in I(Bac)/I(Hβ) are also large. Canfield & Puetter (1981) showed an observed range of $\sim$0.5$-$3 for I(Bac)/I(Hα). Wills, Netzer & Wills (1985) observed 9 intermediate redshift QSOs whose I(Bac)/I(Hβ) ranges from 4.65 to 9.5. Thus we were unable to constrain the intensity of the whole Balmer continuum by using a standard flux ratio fixed to the other Balmer emission lines. As a result, we must rely on the shape of the observed Balmer bump, and then adopt the model's best fit parameters.

However, this limitation in defining the Balmer bump introduces uncertainties in modeling the underlying continuum, because over-subtraction of the Balmer bump will depress the slope of the remaining underlying continuum, and vice-versa. In the course of the broadband SED fitting described in section 3.5, we found that the temperature of the accretion disc (determined by black hole mass) is sensitive to the slope of optical continuum, unless the continuum slope is in the opposite sense to that of the accretion disc model and thus can not be fitted, or there are OM points providing stronger constraints. We also found that a flatter optical continuum may lead to a lower best-fit black hole mass, although this also depends on other factors. Therefore, the subtraction of the Balmer continuum can have an impact on the modeling of broadband SED and the best-fit black hole mass. The influence of this depends on the relative importance of other SED restrictions. This is the reason why the Balmer continuum must be carefully modeled and subtracted.

3.4.3 The Intrinsic Underlying Continuum

Our basic assumption is that the residual optical spectrum, after subtraction of the Balmer continuum, FeII emission and other emission lines mentioned previously, arises mainly from the accretion disc emission. As a reasonable approximation over a limited wavelength range we use a power-law of the following form to fit the underlying continuum,

$$F(\lambda) = C_1 \cdot (\lambda/5100\mathring{A})^{-C_2} \tag{3.4}$$

The power-law approximation for the optical underlying disc continuum is also widely adopted in previous and recent AGN optical spectral studies. (e.g. Grandi

1982; Tsuzuki et al. 2006; Zhou et al. 2006; Landt et al. 2011).

We model the dust reddening using the Seaton (1979)'s 1100Å to 10000Å reddening curve, and we apply this to the overall model, i.e. emission lines, Balmer continuum and the disc continuum. There are also other reddening curves available such as Fitzpatrick (1986) for the Large Magellanic Cloud, Prévot et al. (1984) and Bouchet et al. (1985) for the Small Magellanic Cloud and Calzetti et al. (2000) for starburst galaxies, but over the wavelength range of 2500Å to 10000Å, the difference between these reddening curves is small, except for Calzetti et al. (2000)'s curve which is appropriate for starburst galaxies, and is thus not applicable for our AGN sample.

3.4.4 The Host Galaxy Contribution

Many previous studies on AGN's optical/infrared spectra have adopted a power law as a reasonable approximation for the accretion disc continuum blueward of 1μm (e.g. Mei, Yuan & Dong 2009; Bian & Huang 2010), but these studies also needed to include additional contributions from the host galaxy and emission from the dusty torus to account for the extra continuum emission at long wavelengths of the optical spectrum (e.g. Kinney et al. 1996; Mannucci et al. 2001; Landt et al. 2011). In our work we have also identified an inconsistency between the 3000Å−8000Å spectral shape and a single power law shape (i.e. the flat optical spectrum problem discussed in Section 3.5.3). The blue end of the optical spectrum, presumed to arise from a standard accretion disc, often shows a steeper spectral slope than the red end.

However, in our sample we found evidence suggesting only a weak if any, contribution from the host galaxy. For example, the optical spectra of our sample do not show the strong curvature characteristic of the presence of a stellar component in a host galaxy. Furthermore, the good quality optical spectra do not exhibit stellar absorption features (see Section 3.5.3 and Figure 3.5). In fact the 3″ diameter fibre used to obtain the SDSS spectra also helps to reduce the contribution of stellar emission from a host galaxy, particularly for nearby sources in our sample such as KUG 1031+398. This evidence argues against the possibility that the red optical

continuum is primarily dominated by host galaxy emission. In fact, it is possible that the observed additional component arises due to emission from the outer regions of a standard accretion disc (e.g. Soria & Puchnarewicz 2002; Collin & Kawaguchi 2004; Hao et al. 2010). The existence of such an additional red optical continuum component reduces the consistency of a power law fit to the optical spectra.

3.4.5 The Optical Spectrum Fitting

Our optical spectral fitting is performed only for data blueward of 7000Å. The choice to truncate the model at 7000Å is made for several reasons. We wish to include Hα line in the spectral fitting range, and the broad wing of Hα profile sometimes extend to ∼7000Å (e.g. PG 1352+183, RBS 1423, Mrk 926). There are some objects whose SDSS spectra extend only to ∼6700Å (e.g. 2XMM J080608.0+244421, HS 0810+5157, 2XMM J100025.2+015852). The choice of 7000Å, rather than a longer wavelength, is to maintain consistency of optical spectral fitting for the whole sample. The final reason concerns an aspect of the power law fitting. We found that in some objects (e.g. PG 1115+407, LBQS 1228+1116, PG1352+183), a flat slope power-law under predicts the observed emission at ∼7000Å. Therefore, if we include longer wavelengths than 7000Å, our power law fitting for the standard accretion disc continuum towards the blue optical spectra would be biased by other continuum emission at these longer wavelengths, and so affect the broadband SED fitting. Consequently, we chose to truncate our optical spectral fitting at 7000Å.

However, we still cannot be sure that the underlying continuum is totally free from other non-disc continuum components. So after completing the fitting procedure, we then checked the spectral fitting status within two narrow wavebands, i.e. 4400Å - 4800Å and 5100Å - 5600Å. Emission features if present in these two wavebands are mainly from FeII emission, and the underlying continua of these two wavebands should be totally dominated by the accretion disc emission. Assuming that the FeII emission lines within these two wavebands have similar relative intensity ratios as in the FeII template described in Section 3.3.2, the best-fit underlying power-law plus FeII emission model should have good fitting status in both of these

two wavebands. In general, the best-fit model derived from the full optical spectrum fit also gives reasonably good fitting status in both of these two narrow wavebands. However, in some cases the model over-predicted the flux in 5100Å - 5600Å but under-predicted the flux in 4400Å - 4800Å, so that we should slightly increase the slope of power-law to produce better spectral fitting in these two wavebands. We adopted these parameter values in preference to those directly from the full spectrum fit, as they should be more immune to problems such as host galaxy or hot dust contamination.

3.5 The Broadband SED Modeling

3.5.1 Data Preparation

For each object we extracted the original data files (ODFs) and the pipeline products (PPS) from XMM-Newton Science Archive (XSA) [3]. In the following data reduction process, tasks from XMM-Newton Science Analysis System (SAS) v7.1.0 were used. First, `EPCHAIN/EMCHAIN` tasks were used to extract events unless the events files had already been extracted for each exposure by PPS. Then `ESPFILT` task was used to define background Good Time Intervals (GTIs) that are free from flares. In each available EPIC image, a 45″ radius circle was used to extract the source region, and an annulus centered on the source with inner and outer radii of 60″ and 120″ was used to define the background region. For other sources listed in the region files of PPS that are included in these regions, these were subtracted using the default radii generated by PPS, which scaled with the source brightness. Then the GIT filter, source and background region filters were applied to the corresponding events files to produce a set of source and background events files. We only accepted photons with quality flag =0 and pattern 0−4. The `EPATPLOT` task was then used to check for pile-up effects. When pile-up was detected, an annulus with inner and outer radii of 12″ and 45″ was used instead of the previous 45″ radius circle to define the source region. Then source events files were reproduced using the new source region

[3] http://xmm.esac.esa.int/external/xmm_data_acc/xsa/index.shtml

Table 3.2: Broadband SED Fitting Parameters, and Model Outputs (L_{bol}, f_d, f_c, f_p). ID: object number, the same as Table 3.1; $N_{H,gal}$ and $N_{H,int}$: the fixed Galactic and free intrinsic neutral hydrogen column densities in 10^{20} cm^{-2}; Γ_{pow}: the power-law component's slope in the SED fitting, (*) denotes the objects whose power-law slopes hit the uplimit of 2.2 and were fixed there; Fpl: the fraction of power-law component in the total reprocessed disc emission; R_{cor}: corona (truncation) radius in unit of Gravitational radii (r_g) within which all disc emission is reprocessed into the Comptonisation and power-law components; T_e: temperature of the Compton up-scattering electron population; Tau: optical depth of the Comptonisation component; log(M_{BH}): the best-fit black hole mass; log($\dot{M}$): total mass accretion rate; L_{bol}: bolometric luminosity integrated from 0.001 keV to 100 keV; f_d, f_c, f_p: luminosity fractions of disc emission, soft Comptonisation and hard X-ray Compotonisation components in the bolometric luminosity; χ^2: the reduced χ^2 of the broadband SED fitting.

ID	$N_{H,gal}$ $\times 10^{20}$	$N_{H,int}$ $\times 10^{20}$	Γ_{pow}	Fpl	R_{cor} r_g	T_e keV	Tau	$log(M_{BH})$ $M_\odot$	$log(\dot{M})$ $g\ s^{-1}$	L_{bol} 10^{44}	f_d	f_c	f_p	χ^2 $redu$
1	1.79	0.00	1.71	0.69	100.	0.262	17.2	8.61	26.06	58.9	0.19	0.25	0.56	1.00
2	2.43	1.06	1.77	0.39	100.	0.226	15.7	7.85	25.21	8.28	0.19	0.49	0.32	0.97
3	6.31	9.88	1.91	0.25	11.9	0.108	20.0	7.41	25.92	42.9	0.87	0.10	0.03	1.57
4	3.49	2.81	1.66	0.50	100.	0.312	15.4	8.78	25.41	13.3	0.19	0.41	0.40	1.15
5	3.53	4.03	2.12	0.36	54.9	0.205	14.9	7.87	26.28	98.4	0.32	0.44	0.24	1.10
6	4.24	0.00	1.93	0.46	23.9	0.347	12.6	8.50	26.33	111	0.59	0.22	0.19	1.02
7	1.33	3.74	2.20*	0.29	8.37	0.137	40.3	7.00	26.53	175	0.26	0.53	0.21	1.20
8	3.12	7.35	1.82	0.15	24.1	1.380	3.44	7.09	25.85	36.6	0.58	0.35	0.06	1.39
9	1.30	1.36	1.71	0.71	12.9	0.360	11.1	6.96	25.94	45.0	0.84	0.05	0.11	17.2
10	1.74	0.00	1.91	0.32	100.	0.295	13.8	8.47	26.20	81.5	0.19	0.55	0.26	1.72
11	1.72	2.00	1.71	0.49	20.2	0.449	9.23	7.80	26.02	53.8	0.65	0.18	0.17	1.01
12	1.20	1.08	1.68	0.48	20.6	0.402	11.4	7.79	25.27	9.46	0.65	0.18	0.17	1.20
13	3.56	0.00	1.37	0.87	10.9	0.146	17.9	9.20	26.52	170	0.90	0.01	0.09	3.12
14	1.76	0.00	1.72	0.71	100.	0.294	16.0	8.24	25.82	33.6	0.19	0.23	0.58	1.07
15	1.31	2.43	2.20*	0.09	14.2	0.214	12.3	6.23	25.31	10.4	0.80	0.18	0.02	2.27
16	1.70	0.65	1.72	0.31	100.	0.327	13.0	8.33	25.85	36.2	0.19	0.56	0.25	1.44
17	0.65	0.85	1.74	0.14	48.7	0.326	11.4	7.97	25.85	36.5	0.35	0.56	0.09	1.08
18	1.45	0.19	2.20*	0.24	29.5	0.254	13.6	8.17	26.18	76.9	0.51	0.37	0.12	1.37
19	3.70	1.41	1.98	0.19	45.8	0.142	21.5	7.71	24.85	3.61	0.37	0.52	0.12	1.10
20	1.91	4.77	2.20*	0.36	9.63	0.210	16.8	6.46	25.36	11.9	0.94	0.04	0.02	1.39
21	1.77	0.00	1.79	0.75	22.7	0.206	19.6	7.98	26.09	63.4	0.61	0.10	0.29	3.59
22	2.75	8.84	1.86	0.21	50.5	0.108	25.1	7.84	25.42	13.5	0.34	0.52	0.14	1.09
23	1.59	0.00	1.41	0.45	86.9	0.626	9.59	7.99	25.02	5.40	0.22	0.43	0.35	0.99
24	1.63	0.00	1.82	0.94	32.2	0.182	32.2	8.26	25.96	46.5	0.48	0.03	0.49	2.13
25	2.34	0.00	1.79	0.40	25.7	0.351	12.9	8.49	26.26	94.2	0.56	0.27	0.17	1.83
26	2.31	7.25	2.10	0.03	33.8	0.310	9.69	7.37	26.23	87.7	0.46	0.52	0.02	1.14
27	2.75	0.00	1.85	0.22	37.6	0.554	8.29	7.50	25.44	14.2	0.43	0.45	0.12	1.12
28	1.45	0.00	1.69	0.60	71.3	0.353	13.7	8.24	25.81	33.0	0.26	0.30	0.45	1.26
29	1.18	1.36	2.00	0.12	30.9	0.389	8.85	7.76	26.03	55.1	0.49	0.45	0.06	1.24
30	1.87	2.64	2.20*	0.36	9.67	0.234	16.9	6.79	25.77	30.3	0.94	0.04	0.02	1.03

Table 3.2: continued...

ID	$N_{H,gal}$ $\times 10^{20}$	$N_{H,int}$ $\times 10^{20}$	Γ_{pow}	Fpl	R_{cor} r_g	T_e keV	Tau	$log(M_{BH})$ $M_\odot$	$log(\dot{M})$ $g\ s^{-1}$	L_{bol} 10^{44}	f_d	f_c	f_p	χ^2 redu
31	0.84	0.00	1.68	0.54	100.	0.404	12.9	8.70	25.84	35.9	0.19	0.37	0.43	0.99
32	0.90	0.14	1.80	0.44	100.	0.388	12.2	7.69	25.15	7.30	0.19	0.46	0.35	1.66
33	1.07	0.82	2.18	0.57	15.0	0.226	15.6	7.78	25.96	47.3	0.78	0.10	0.13	1.15
34	1.83	0.93	1.90	0.33	100.	0.252	14.8	8.71	26.03	55.1	0.19	0.54	0.26	1.11
35	1.76	0.90	1.80	0.83	100.	0.202	20.4	7.67	26.13	69.8	0.19	0.14	0.67	1.05
36	1.18	3.94	2.18	0.22	16.2	2.000	2.71	6.52	25.13	6.90	0.75	0.20	0.05	1.81
37	1.82	0.00	2.04	0.38	100.	0.219	17.2	8.23	25.88	39.3	0.19	0.50	0.31	1.33
38	1.42	0.37	1.58	0.97	100.	0.251	25.0	7.69	24.54	1.80	0.19	0.02	0.79	1.28
39	1.36	4.77	2.10	0.11	40.6	0.281	11.4	7.01	25.17	7.57	0.40	0.53	0.07	1.90
40	0.77	5.21	2.05	0.06	24.0	0.930	4.28	7.41	26.26	93.6	0.59	0.39	0.02	2.27
41	1.81	0.00	1.90	0.39	28.9	0.298	14.0	8.39	26.10	65.2	0.52	0.30	0.19	1.63
42	2.86	3.29	1.84	0.41	100.	0.083	31.3	7.74	24.68	2.45	0.19	0.47	0.33	1.01
43	2.69	0.00	1.71	0.58	55.8	0.406	11.9	8.07	26.10	64.7	0.31	0.29	0.40	1.29
44	2.78	5.90	2.17	0.04	27.6	0.501	6.71	7.26	26.13	68.6	0.53	0.45	0.02	2.33
45	1.46	0.00	1.82	0.49	41.0	0.286	14.1	8.62	26.75	290	0.40	0.30	0.30	2.42
46	4.02	0.55	1.81	0.81	100.	0.207	20.3	8.56	25.58	19.4	0.19	0.15	0.66	1.12
47	3.78	16.69	1.82	0.25	100.	0.115	29.8	7.96	25.62	21.5	0.19	0.61	0.20	0.99
48	2.11	0.87	1.85	0.19	18.1	0.525	8.61	7.19	25.16	7.40	0.70	0.24	0.06	1.19
49	4.90	0.36	2.20*	0.33	72.5	0.211	19.6	7.73	25.15	7.33	0.25	0.50	0.25	1.15
50	4.51	0.00	2.20*	0.80	7.88	0.131	48.5	7.86	27.42	1350	0.98	0.00	0.01	1.39
51	2.91	1.53	1.79	0.95	100.	0.112	45.2	7.65	25.32	10.8	0.19	0.04	0.77	1.38

filter. Source and background spectra were extracted from these events files for each available EPIC exposure. Tasks `RMFGEN/ARFGEN` were used to produce response matrices and auxiliary files for the source spectra. These final spectra were grouped with a minimum of 25 counts per bin using the `GRPPHA v3.0.1` tool for spectral fitting in XSPEC v11.3.2. To prepare the OM data, the *om_filter_default.pi* file and all response files for the V,B,U, UVW1, UVM2, UVW2 filters were downloaded from the OM response file directory in HEASARC Archive[4]. We then checked the OM source list file for each object to see if there were any available OM count rates. Each count rate and its associated error were entered into the *om_filter_default.pi* file and then combined with the response file of the corresponding OM filter, again by using the `GRPPHA` tool to produce OM data that could be used in XSPEC.

Finally, the XMM-Newton EPIC spectra are combined with the aperture corrected OM photometric points, and the optical continuum points produced from the optical underlying continuum (obtained from the full optical spectrum fitting) using `FLX2XSP` tool. From these data we constructed a broadband nuclear SED of each AGN. There is a ubiquitous data gap in the far UV region which is due to photoelectric absorption by Galactic gas. Unfortunately, in most cases of low-redshift

[4]http://heasarc.gsfc.nasa.gov/FTP/xmm/data/responses/om/

Table 3.3: Broadband SED Key Parameters. ID: object number, the same as Table 3.1; $\Gamma_{2-10keV}$: the slope of the single power-law fitted to 2-10 keV spectrum. $L_{2-10keV}$: 2-10 keV luminosity (in 10^{44} erg s^{-1}); $\kappa_{2-10keV}$: the 2-10keV bolometric correction coefficient; $\lambda L_{2500\mathring{A}}$: the monochromatic luminosity at 2500Å (in 10^{43} erg s^{-1}); νL_{2keV}: the monochromatic luminosity at 2keV (in 10^{43} erg s^{-1}); α_{ox}: the optical X-ray spectral index; λL_{5100}: the monochromatic luminosity at 5100Å (in 10^{44} erg s^{-1}); κ_{5100}: the 5100Å bolometric correction coefficient; $FWHM_{H\beta}$: the narrow component subtracted Hβ FWHM; L_{bol}/L_{Edd}: the Eddington Ratio.

ID	$\Gamma_{2-10keV}$	$L_{2-10keV}$ $\times 10^{44}$	$\kappa_{2-10keV}$	$\lambda L_{2500\mathring{A}}$ $\times 10^{43}$	νL_{2keV} $\times 10^{43}$	α_{ox}	λL_{5100} $\times 10^{44}$	κ_{5100}	$FWHM_{H\beta}$ $km\ s^{-1}$	L_{bol}/L_{Edd}
1	1.69±0.06	4.941	11.9	81.3	25.6	1.19	8.15	7.24	13000	0.11
2	1.67±0.10	0.469	17.7	18.4	2.47	1.33	0.791	10.5	6220	0.089
3	1.77±0.07	0.289	149	41.0	1.91	1.51	1.35	31.7	2310	1.3
4	1.80±0.11	0.567	23.6	12.8	3.15	1.23	1.91	6.98	10800	0.017
5	2.10±0.22	2.284	43.2	134	12.9	1.39	5.48	18.0	2720	1.0
6	1.93±0.18	4.855	22.9	290	27.6	1.39	14.8	7.52	5430	0.27
7	2.39±0.22	0.267	657	61.3	2.43	1.54	1.95	89.6	1980	13
8	1.84±0.04	0.418	87.7	23.5	2.89	1.35	0.539	68.1	2840	2.3
9	1.76±0.01	0.839	53.8	22.7	5.35	1.24	0.113	399	3030	3.8
10	1.92±0.05	3.532	23.1	205	23.1	1.36	7.59	10.8	4810	0.21
11	1.71±0.11	1.811	29.8	78.9	9.03	1.36	3.75	14.4	5640	0.66
12	1.68±0.23	0.502	18.9	21.2	1.57	1.43	1.04	9.12	4390	0.12
13	1.37±0.12	0.751	227	790	2.99	1.93	42.6	4.00	10800	0.082
14	1.69±0.04	3.189	10.6	50.2	17.0	1.18	3.91	8.60	7060	0.15
15	2.35±0.12	0.042	251	2.89	0.353	1.35	0.204	51.1	988	4.7
16	1.78±0.07	1.502	24.2	90.8	8.24	1.40	4.26	8.53	3560	0.13
17	1.80±0.20	0.779	46.9	71.7	3.62	1.50	3.31	11.1	2250	0.30
18	2.23±0.08	1.254	61.5	157	9.67	1.46	6.11	12.6	2310	0.40
19	1.98±0.18	0.084	43.1	8.59	0.497	1.47	0.443	8.19	2000	0.054
20	2.34±0.12	0.053	224	4.44	0.476	1.37	0.215	55.4	774	3.1
21	1.70±0.04	3.856	16.5	109	20.5	1.28	2.22	28.6	6090	0.51
22	1.70±0.09	0.396	34.1	27.3	2.17	1.42	0.983	13.8	7050	0.15
23	1.80±0.19	0.145	37.5	11.5	0.907	1.42	0.708	7.66	1980	0.043
24	1.83±0.18	4.735	9.84	106	25.1	1.24	6.64	7.01	13900	0.20
25	1.88±0.03	3.054	30.9	249	20.0	1.42	8.44	11.2	4980	0.24
26	2.09±0.25	0.362	243	63.3	2.60	1.53	2.04	43.2	1720	2.9
27	1.94±0.04	0.277	51.5	20.3	2.51	1.35	0.988	14.4	4310	0.34
28	1.71±0.14	2.951	11.2	63.6	13.2	1.26	4.80	6.91	4240	0.15
29	2.00±0.12	0.726	76.0	76.3	4.75	1.46	3.25	17.0	3560	0.73
30	2.46±0.09	0.146	207	13.4	1.28	1.39	0.452	67.2	954	3.8
31	1.69±0.14	2.420	14.9	53.6	11.9	1.25	6.49	5.54	6810	0.055
32	1.88±0.03	0.464	15.8	13.7	2.97	1.26	0.512	14.3	3100	0.12
33	2.14±0.21	1.157	41.0	69.7	7.55	1.37	4.03	11.8	5690	0.60
34	1.90±0.14	2.489	22.2	140	13.5	1.39	10.8	5.13	3310	0.082
35	1.76±0.07	3.918	17.9	67.5	51.5	1.04	3.59	19.5	2790	1.2
36	2.20±0.08	0.091	76.3	3.31	0.651	1.27	0.244	28.4	1890	1.6
37	1.95±0.08	1.768	22.3	88.8	12.3	1.33	5.39	7.30	3960	0.18
38	1.55±0.09	0.175	10.3	1.89	0.768	1.15	0.197	9.16	6630	0.028
39	2.17±0.20	0.079	96.5	6.89	0.737	1.37	0.233	32.6	991	0.56

Table 3.3: continued...

ID	$\Gamma_{2-10keV}$	$L_{2-10keV}$ $\times 10^{44}$	$\kappa_{2-10keV}$	$\lambda L_{2500\AA}$ $\times 10^{43}$	νL_{2keV} $\times 10^{43}$	α_{ox}	λL_{5100} $\times 10^{44}$	κ_{5100}	$FWHM_{H\beta}$ $km\ s^{-1}$	L_{bol}/L_{Edd}
40	2.02±0.06	0.468	200	70.0	3.54	1.50	2.05	45.7	2790	2.8
41	1.94±0.05	2.444	26.7	167	15.8	1.39	6.26	10.4	2610	0.20
42	1.76±0.11	0.158	15.5	4.92	0.804	1.30	0.265	9.28	4920	0.034
43	1.74±0.07	4.524	14.3	109	25.7	1.24	4.36	14.9	4550	0.43
44	2.25±0.05	0.236	292	45.5	2.13	1.51	2.36	29.2	1070	2.9
45	1.82±0.06	17.502	16.6	645	98.4	1.31	30.4	9.58	10900	0.53
46	1.81±0.12	2.175	8.93	19.0	10.4	1.10	2.97	6.55	9930	0.041
47	1.45±0.25	0.868	24.9	36.6	4.39	1.35	0.931	23.2	4100	0.18
48	2.03±0.11	0.101	73.2	8.71	0.734	1.41	0.278	26.7	1190	0.37
49	2.40±0.22	0.200	36.8	14.5	1.69	1.36	0.719	10.2	1340	0.11
50	2.41±0.18	3.299	411	860	27.3	1.57	29.5	46.0	2200	14
51	1.67±0.03	1.659	6.50	12.5	8.30	1.07	0.624	17.3	11100	0.19

AGN, their intrinsic SED also peaks in this very UV region, and so this unobservable energy band often conceals a large portion of the bolometric luminosity. In order to account for this, and to estimate the bolometric luminosity, we fit the X-ray and UV/optical continua all together using a new broadband SED model (Done et al. 2011, XSPEC model: *optxagn*). We then calculate the bolometric luminosity by summing up the integrated emission using the best-fit parameters obtained for each continuum component.

3.5.2 The Broadband SED Model

We use *optxagn* (with $f_{col} = 1$) in `Xspec` v12 to perform the broadband SED fitting. The two key free parameters are the black hole mass and mass accretion rate in terms of Eddington. The optical/UV data constrains the mass accretion rate through the outer disc, provided we have an estimate of the black hole mass. We constrain this by our analysis of the $H\beta$ emission line profile. The main difference from previous studies based on non-reverberation samples is that we do not directly use the FWHM of the Hβ profile to derive the black hole mass. Rather, we use the FWHM of the intermediate and broad line component determined from the emission line fitting results presented in Section 3.3.1. These are then used in Equation 3.5 (Woo & Urry 2002 and references therein) to derive the black hole mass limits required for the SED fitting:

$$M_{BH} = 4.817\times[\frac{\lambda L_{\lambda}(5100\AA)}{10^{44} ergs^{-1}}]^{0.7} FWHM^2 \quad (3.5)$$

where $L_\lambda(5100\text{Å})$ is measured directly from the SDSS spectra. The rms difference between the black hole masses from this equation and from the reverberation mapping study is $\sim$0.5 dex. Thus we also adopted any best-fit values that fell below the original lower limit (which was set by FWHM of the intermediate component) by less than 0.5 dex. With this method, the best-fit black hole mass found by SED fitting is always consistent with the prediction from the Hβ profile. Section 3.6.5 discusses the differences between the best-fit black hole masses and those estimated using other methods.

Once the black hole mass is constrained, the optical data then sets the mass accretion rate $\dot{M}$, and hence the total energy available is determined by the accretion efficiency. We assume a stress-free (Novikov-Thorne) emissivity for a Schwarzschild black hole, i.e. an overall efficiency of 0.057 for $R_{in} = 6R_g$. Thus the total luminosity of the soft excess and power law is $0.057\dot{M}c^2(1 - R_{in}/R_{corona})$. This constrains the model in the unobservable EUV region, with the input free parameter R_{corona} setting the model output of the luminosity ratio between the standard disc emission and Comptonisation components. The upper limit of R_{corona} is set to be 100 R_g, which corresponds to 81% released accretion disc energy. This upper limit is based on the requirement that the seed photons should be up-scattered (Done et al. 2011). We assume that both the Comptonisation components scatter seed photons from the accretion disc with temperature corresponding to R_{corona}. The other model input parameters are; the temperature (kT_e) and optical depth (τ) of the soft Comptonisation component which are determined by the shape of the soft X-ray excess, the spectral index (Γ) of the hard X-ray Comptonisation that produces the 2-10 keV power law, with electron temperature fixed at 100 keV. The model output f_{pl} represents the fraction of the non-thermalised accretion energy (i.e. given by the luminosity originating from the region of R_{corona} to R_{in}), which is emitted in the hard X-ray Comptonisation.

The same constrains are set as in Chapter 2.6.2 on the Galactic and intrinsic absorptions and the hard X-ray power law photon index. All free parameters used in the broadband SED fitting are listed in Table 3.4.5. For completeness, we also explicitly calculate the fraction of the total luminosity carried by each component

of the model (i.e. disc: f_d; soft Comptonization: f_c; hard X-ray Comptonization: f_p) from the model fit parameters R_{cor} and F_{pl} (see Table 3.4.5) [5]. Table 3.3 lists the important characteristic parameters. The main uncertainty in these parameters, especially the black hole mass, is dominated by other systematic uncertainties introduced by the observational data, model assumptions (e.g. the assumption of a non-spinning black hole and the inclination dependence of the disc emission) and the analysis methods involved. Therefore the parameter fitting uncertainties which are often less than 10%, are not significant in comparison, and thus are not listed. The statistical properties of these parameters are discussed in Section 3.6.

3.5.3 Problems in The SED Fitting

We further discuss two problems we encountered during the fitting procedure in the following subsections. The first problem is the discrepancy between the OM and SDSS continuum points (mentioned in Section 3.2.5). The second problem is that of the observed flat optical continuum, whose shape cannot be accounted for in our SED model (mentioned in Section 3.4.4).

The discrepancy between the OM photometry and the SDSS continuum

There remains a significant discrepancy between many of the OM and SDSS continuum points, even after applying the aperture correction discussed in Section 3.2.2 (see Figure A.1). The OM points often appear above (brighter) the extrapolation of the SDSS continuum to the OM wavelengths. We identify three possible reasons for this discrepancy:

(1) Remaining aperture effects: There is an aperture difference between the SDSS fibres (3″diameter) and the OM apertures we used (6″diameter). Clearly the OM points will still include more host galaxy starlight than the SDSS points, and so will appear above the SDSS spectrum.

(2) Contamination from emission lines: The wavelength ranges for each OM

[5] a full description of the model parameters can be found on the XSPEC web page: http://heasarc.nasa.gov/xanadu/xspec/models/optxagn.html

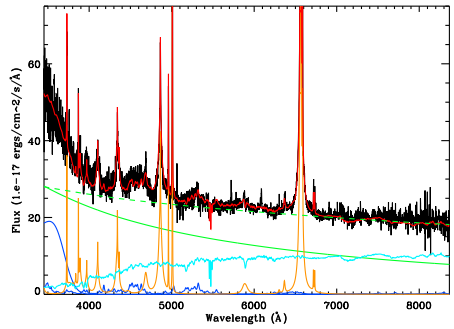

Fig-a1: 2XMM J112328.0+052823 Optical Spectrum

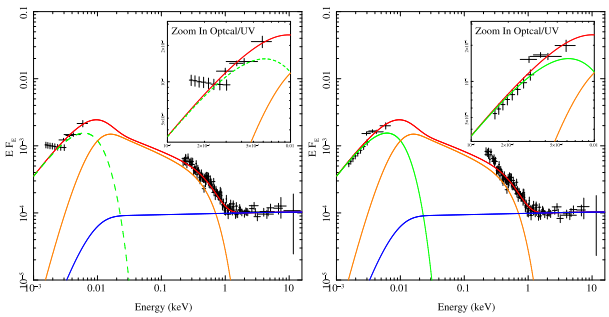

Fig-a2: SED Fitting Before and After Host Galaxy Subtraction

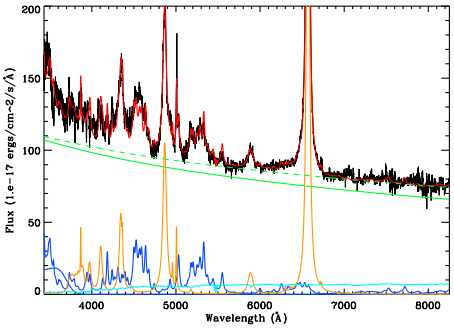

Fig-b1: PG1415+451 Optical Spectrum

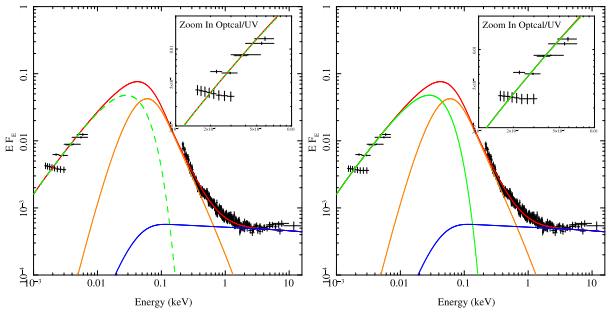

Fig-b2: SED Fitting Before and After Host Galaxy Subtraction

Figure 3.5: A comparison between the results of two subtractions of host galaxy contribution. 2XMM J112328+052823 (Fig-a1 and Fig-a2) shows an underlying continuum that more closely resembles a disc continuum (solid green line in Fig-a1) after modelling and subtracting the host galaxy contribution (light blue spectrum in Fig-a1). The left panel of Fig-a2 shows the original broadband SED fitting without subtracting the host galaxy contribution. The dashed green line shows the modelled accretion disc emission in the best-fit SED. The inserted panel shows a magnification of the fit in the optical/UV region, where a big discrepancy exists between the SDSS data and best-fit SED model. The right panel of Fig-a2 is the new SED fit using the new underlying disc continuum (shown as solid green line in Fig-a1) after subtracting the host galaxy contribution. The new fit is improved in the optical region compared with the previous results in the left panel of Fig-a2. In contrast to the above example, PG 1415+451 (Fig-b1 and Fig-b2) has little host galaxy contribution in the SDSS optical spectrum (see the light blue component in Fig-b1), and its broadband SED fitting in the optical region remains poor regardless of the amount of host galaxy subtraction applied (see the two panels in Fig-b2). The spectral template for Elliptical galaxies in Kinney et al. (1996) was used in both cases since their host galaxies both have elliptical morphologies in SDSS image.

filter (over which the effective transmission is greater than 10% of the peak effective transmission) are as follows: UVW2 1805-2454Å, UVM2 1970-2675Å, UVW1 2410-3565Å, U 3030-3890Å, B 3815-4910Å, V 5020-5870Å. We exclude the contribution from strong optical emission lines within the OM U, B, V bandpass (and also the Balmer continuum contribution in U band) by using the best-fit optical underlying continuum which excludes such features from the SDSS spectral fitting. In fact, this was an important initial motivation of the study, i.e. to obtain more accurate estimates of the true underlying continuum rather than simply to use the SDSS 'ugriz' photometric data. Inclusion of strong emission lines within these photometric data would result in over-estimation of the optical continuum, and so compromise our aim to study the shape of the optical underlying continuum. This is an important spectral characteristic used to constrain the accretion disc component in the SED fitting (see also the discussion in section 5.1.2). There are some strong emission lines within the UV bandpasses such as Lyα, CIV 1549, CIII 1909 and MgII 2798, whose fluxes are not available from SDSS spectrum. Accurate subtraction of these line fluxes for each object would require new UV spectroscopy. We conclude that inclusion of emission line flux within the OM photometric points may account for some of the observed discrepancy.

(3) Intrinsic source variability: AGN are well known to be variable across their SEDs. In general there is a significant time difference between acquistion of the SDSS and OM-UV data, so intrinsic variation may contribute to any observed discrepancy. Mrk 110 is the most extreme example of this phenomena in our sample, as its SDSS spectrum has a very large discrepancy compared with the OM data. The recent paper by Landt et al. (2011) gives another set of optical spectra for Mrk 110, which is more consistent with our best-fit model. It shows that the inclusion of OM data is useful to help identify cases such as this. As an additional test for variability, we assembled all available GALEX data for our sample. We find that 43 objects in our sample have GALEX data. Using a GALEX aperture of 12″, which is limited by the PSF and which is also similar to the UV OM apertures, we compare these values with the SED model. The ratio of the GALEX data and our SED model within the same bandpass differ by less than a factor of 2 for the majority of our sample, and

significantly the flux ratio distribution is almost symmetric and is centered close to unity. This suggests that the non-simultaneous OM and SDSS data is not likely to be a major impediment to our modeling.

In effect, these three factors will merge together to produce the observed discrepancy between the SDSS and OM data. Since the combined effects of Point (1) and (2) which will add flux and generally be greater than that caused by optical/UV variability as shown by previous long term reverberation mapping studies (Giveon et al. 1999; Kaspi et al. 2000), we should treat the OM points included in our SED modeling as upper limits when interpreting the results of our modeling. Indeed, the 90% confidence uncertainties in the BH masses derived directly from the XSPEC fitting are almost certainly small compared with the systematic errors introduced by the above uncertainties.

The observed flat optical continuum

A related problem in our fitting is about the SDSS continuum shape. For some AGNs, their SDSS continuum data points exhibit a very different spectral slope from that of the SED model. This cannot be reconciled by adjusting the parameters of the accretion disc model, and thus implies the presence of an additional component at longer optical wavelengths, which flattens compared with that predicted by the accretion disc models. One obvious explanation for this flux excess is the contribution from the host galaxy. In late type host galaxies such as elliptical and S0 galaxies, emission from their old stellar populations peaks at near infrared wavelengths. Kinney et al. (1996) combined spectra of quiescent galaxies and constructed an average spectral template for each morphological type, including bulge, elliptical, S0, Sa, Sb, Sc and starburst galaxies. For some objects in our sample with high S/N SDSS spectra which show at least marginal stellar absorption features, we have added the corresponding type of host galaxy spectral template taken from Kinney et al. (1996), into the overall SDSS spectral fitting. This revised the underlying continuum in the optical, and was then used in the broadband SED fitting. We are then able to compare it with the original fit, to see how the subtraction of a stellar population template effects the overall SED fitting.

Figure 3.5 shows two examples. The first is 2XMM J112328.0+052823, in which after subtracting the host galaxy component, the observed optical continuum is closer to the slope of the SED model. However, the results for PG1415+451 in Figure 3.5 lower panel imply that its host galaxy cannot be the origin of the flat optical spectrum. The reason is that its optical spectrum does not show any strong stellar absorption features. This means that the maximum amount of host galaxy contribution is small, and so and there remains a substantial inconsistency in the slope versus the SED model. In addition to 2XMM J112328.0+052823 above, only Mrk1018 and 2XMM J125553.0+272405 show clear stellar absorption features. Also the 3″ diameter fibre excludes much of the host galaxy component at these redshifts. Therefore, on these general grounds we conclude that host galaxy contamination is small for most sources in our sample, and consequently cannot fully account for the observed flat optical continuum. Additional support for this view comes from good correlations between the X-ray components and the red optical continuum, suggesting that this extra optical flux is likely related to the intrinsic activity (e.g. Soria & Puchnarewicz 2002; Collin & Kawaguchi 2004; Hao et al. 2010; Landt et al. 2011).

3.6 Statistical Properties of The Sample

Histograms of data on our sample are shown in Figure 3.6, Figure 3.8 and Figure 3.9, including redshift, HI column density, optical and X-ray modeling parameters etc. The red region in the histograms show the distributions for the 12 NLS1s in our sample. It is clear that NLS1s are distinct among the whole sample in several respects.

3.6.1 General Properties

Figure 3.6 shows some basic properties of our sample which are not model dependent: (1). Redshift: the sample's redshift ranges from 0.031 (Mrk 493) to 0.377 (HS 0810+5157). The NLS1s are found mainly at lower redshifts, with $< z >_n = 0.12$ compared to the $< z >_n = 0.19$ for the BLS1s. For comparison we see that the

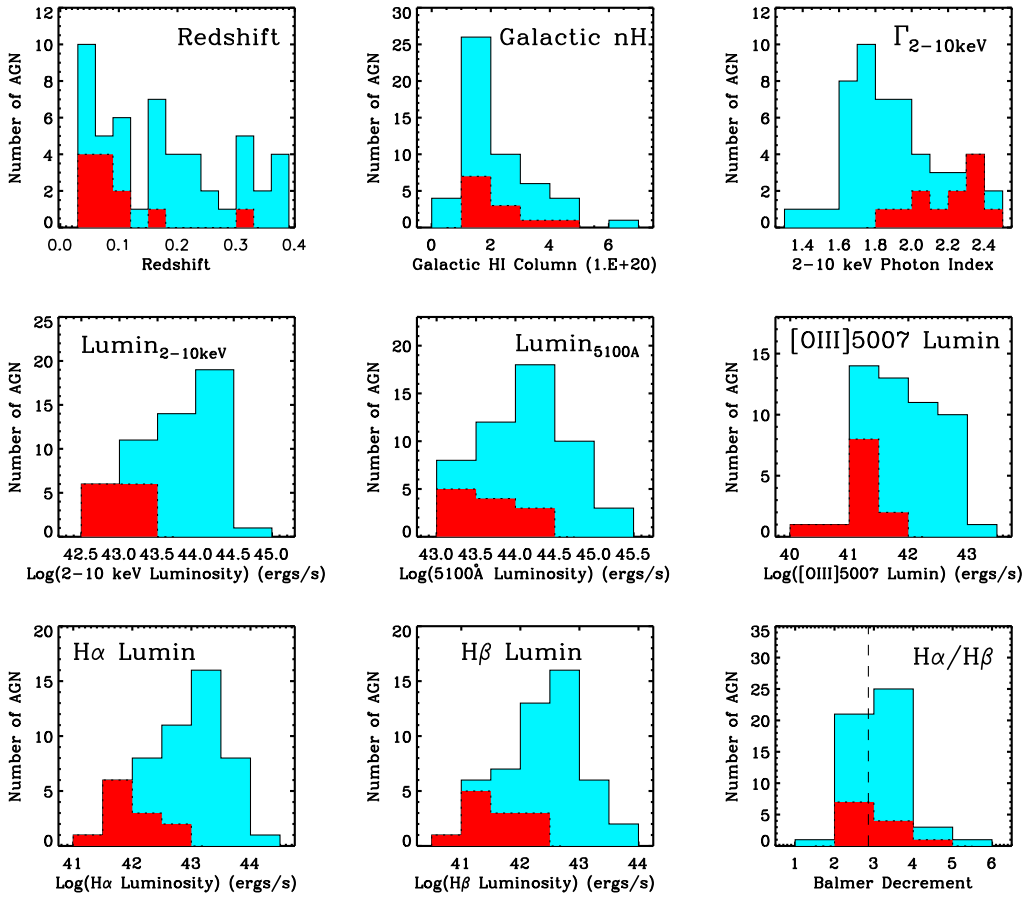

Figure 3.6: Distributions of our sample for different properties. In each panel the blue areas show the distribution for the whole sample, while the red areas show the distribution for the 12 NLS1s in our sample. We note that the Hα, Hβ and [OIII] λ5007 luminosities are based on results of line profile fitting, after subtracting the blends from other nearby emission lines (see Section 3.3.1). For comparison we also indicate the Balmer decrement value of 2.86, found under case B recombination, as shown by dashed line in the same panel.

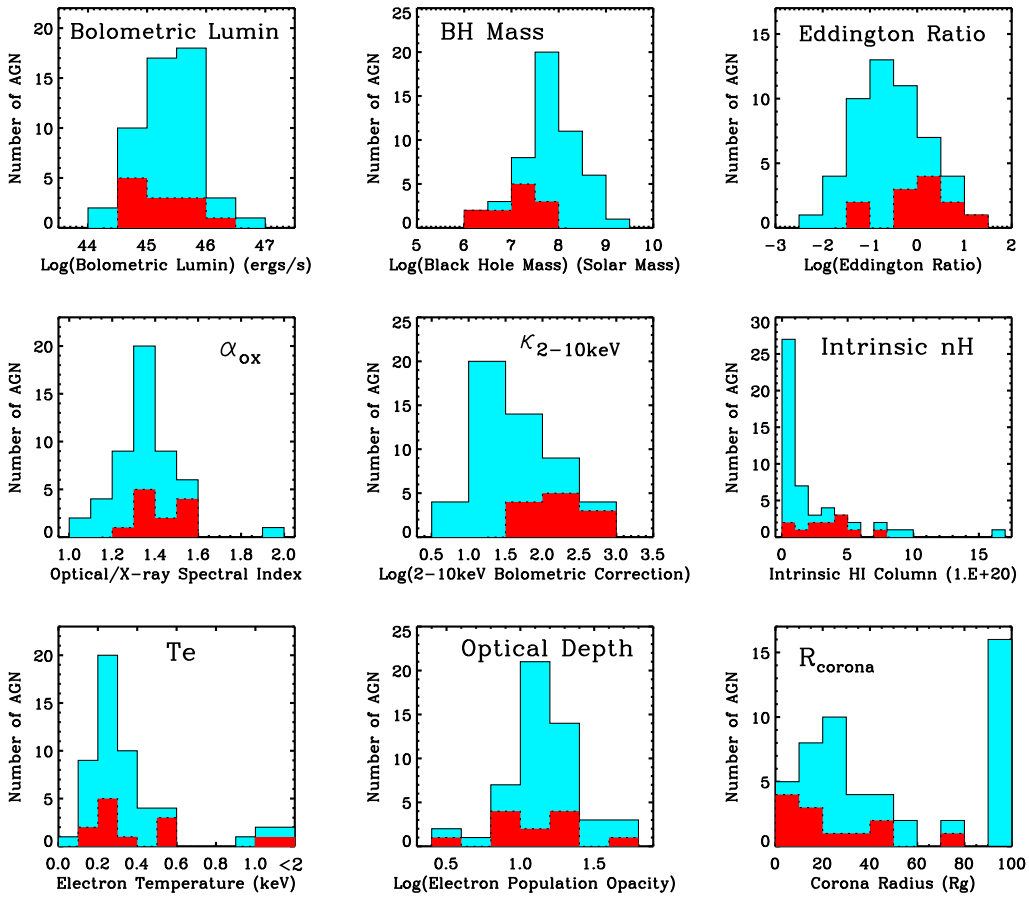

Figure 3.7: The distribution of model dependent parameters using the same colour coding as in Figure 3.6. Comments on each distribution are given in Section 3.6.2.

sample of VF07 has a similar redshift range, but it has a lower average redshift of 0.10.

(2). The Galactic nH: the average Galactic nH is 2.25×10^{20}.

(3). The photon indexes obtained from simple power law fits to the restricted energy range of 2-10 keV. The NLS1s cluster on the higher photon index side, with an average of 2.21±0.20, which differs from the sample average of 1.92±0.25 and the BLS1s' average of 1.83±0.18. This means that NLS1s tend to have softer X-ray spectra, which is further confirmed in the following section on the mean SEDs.

(4). The X-ray continuum and 2-10 keV luminosity: this distribution shows that NLS1s have lower 2-10 keV luminosities in spite of their steeper slopes. We note that the VF07 sample has a similar distribution, except for their inclusion of three extremely low X-ray luminosity AGN (i.e. NGC4395, NGC3227 and NGC6814), these objects were not included in our sample due to our selection criteria and/or a lack of SDSS spectra.

(5). The optical continuum luminosity at 5100 Å. On average the NLS1 have lower optical luminosities than BLS1.

(6-8). The [OIII] λ5007, Hα and Hβ emission line luminosities. Again the NLS1s have on average lower luminosities than BLS1s.

(9). The Balmer decrement. The average value for the whole sample is 3.14±0.62, and for NLS1s is 3.05±0.38. This difference is not statistically significant, but we return to the issue in the next chapter, where we consider the separate components as well as the overall profile.

3.6.2 Results from The Broadband SED Modeling

Figure 3.7 shows properties derived from the SED fits:

(1). The bolometric luminosity: the distribution range is between $1.8\times10^{44} ergs\ s^{-1}$ (Mrk 464) and $1.4\times10^{47} ergs\ s^{-1}$ (PG 2233+134). There is no clear difference in the distribution of the complete sample and the sub-set of NLS1s. The average luminosity is Log(L_{bol})=45.49±0.55, which is consistent with the value of 45.19±1.01 found in VF07 sample, except for the three extremely nearby and low luminosity

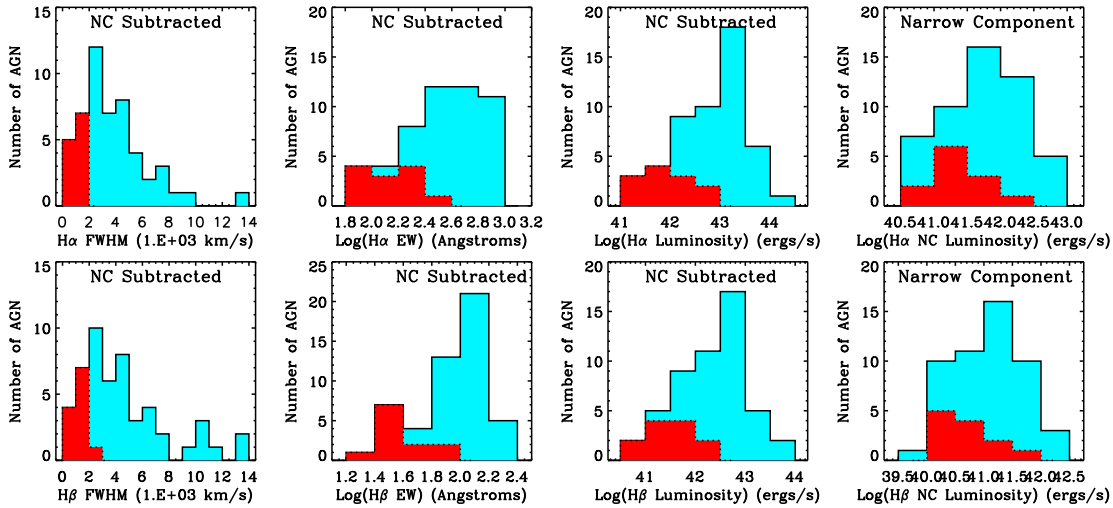

Figure 3.8: The Balmer line parameter distributions. The first row is for Hα and the second is for Hβ. We combine the intermediate and broad components in each Balmer line profile to form the total broad line properties, giving values of the FWHM, EW and luminosity. The final panel shows the luminosity distribution of the narrow component for comparison. The distributions for the 12 NLS1s are indicated by the red regions, as in Figure 3.6.

AGNs in VF07.

(2). The black hole mass: using the best-fit black hole masses, the whole sample peaks between $10^7 M_\odot$ and $10^8 M_\odot$. Equation 3.5 suggests that the black hole mass should depend on both Hβ FWHM and L_{5100}, and the results from our SED fitting suggest that NLS1s with smaller Balmer line FWHM do indeed harbour lower mass black holes. KUG 1034+396 has the lowest black hole mass in our sample. The value of $1.7\times10^6 M_\odot$ is consistent with the estimate based on the first firmly detected AGN QPO (quasi periodic oscillation) found in this source (Gierliński et al. 2008). Again we can compare our results with those of VF07 sample. We find that their average black hole mass is 7.89±0.82, calculated using the M(L_{5100}, $FWHM_{H\beta}$) relation. Adopting this same method for our sample, we find a very similar average of 7.99±0.93. Our best-fit masses have a slightly lower average value of 7.83±0.64 (also see Section 3.6.5 for a comparison of different estimates of black hole masses).

(3). The Eddington ratio: the average values are 3.21±3.07 for NLS1 which display

a wide dispersion, and 0.57±0.50 for BLS1 and 0.93±0.85 for the whole sample. Of the eight objects whose Eddington ratios are above 1, six are NLS1 galaxies, and the highest value is 14.2 (PG 2233+134). Clearly, NLS1s tend to have larger Eddington ratios. Our Eddington ratio distribution is also similar to that found in the sample of VF07 whose average value is 0.47±0.44, except that their distribution has a more pronounced peak at ∼0.1.

(4). The α_{ox} index, is defined between restframe continuum points at 2500 Å and 2 keV (see Lusso et al. 2010 and references therein). The distribution for NLS1 is peaked at marginally higher values than for BLS1.

(5). The κ_{2-10} bolometric correction, is defined as L_{bol}/L_{2-10} (see VF07 and references therein). We find that NLS1s have a significantly higher fraction of their bolometric luminosity emitted as hard X-rays than the BLS1s. Compared with the VF07 sample, both distributions peak at κ_{2-10}=10∼30, but our sample shows a smoother distribution decreasing as κ_{2-10} increases after ∼30, and so results in a slightly higher average value of κ_{2-10}.

(6). The intrinsic nH: This distribution shows that the intrinsic equivalent neutral hydrogen column densities are low for our sample, which is a natural consequence of our initial sample selection criteria. The NLS1s have slightly higher intrinsic absorption than BLS1s, which may imply a slightly higher dust reddening. However the distribution of Balmer decrements shows no significant difference between these two types of AGNs.

(7). The temperature of the Comptonisation component used to describe the soft X-ray excess. This is close to 0.2 keV in all objects, confirming the trend seen in previous studies for this component to exhibit a narrow range of peak energy (Czerny et al. 2003; Gierliński & Done 2004). The distribution peak at this energy is more marked for the BLS1 than for NLS1, although the small number statistics means that this difference cannot be considered as definitive for our sample.

(8). The optical depth of the soft excess Comptonised component. It is clear that this component is always optically thick, with most objects having $\tau \sim 10-30$. There is no significant difference in temperature or optical depth between the broad and narrow line objects.

(9). There is a difference in the corona radii distribution between the BLS1s and NLS1s. Corona radius controls the relative amount of power emerging from the accretion disc and the soft X-ray excess/hard tail. There are two peaks in the distribution for the broad line objects, one between 10 and 20 R_g (where $R_g = GM/c^2$), and the other at 100 R_g (which is set as the upper limit of this parameter in our broadband SED model). By contrast these radii in NLS1 are consistent with just the first peak. At first sight this is surprising, since NLS1 are expected to be those with the strongest soft X-ray excess. However, their similar soft excess temperatures around 0.2 keV suggests that atomic processes may be significant (reflection and/or absorption from partially ionized material), and this may influence our fits. The average corona radii are 32±26 R_g for NLS1, 59±37 R_g for BLS1 and 53±36 R_g for the whole sample. This supports the conclusion of VF07 that high Eddington ratio AGN have lower coronal fractions compared to those with low Eddington ratios.

3.6.3 Balmer Line Parameter Distribution

Figure 3.8 shows further details of the modeled profiles of $H\alpha$ (first row), and $H\beta$ (second row).

(1). The FWHM of the broad emission profile. This is calculated from co-adding the two best fit Gaussian profiles for the broad and intermediate line components, and then using the resultant profile to determine the FWHM. This is equivalent to subtracting the narrow line core from the observed profile and measuring the resultant FWHM.

Note, the NLS1s by definition have Hα < 2000 km s^{-1}.

(2-3). The equivalent widths and line luminosities are again measured using the total broad emission line profile as above. The NLS1s have both lower equivalent widths and line luminosities.

(4). By contrast, there is no pronounced difference between NLS1s and BLS1s in their Balmer narrow line component. This suggests that the narrow line region is less influenced by whatever difference in properties is responsible for the defining difference between NLS1s and BLS1s in the broad line region.

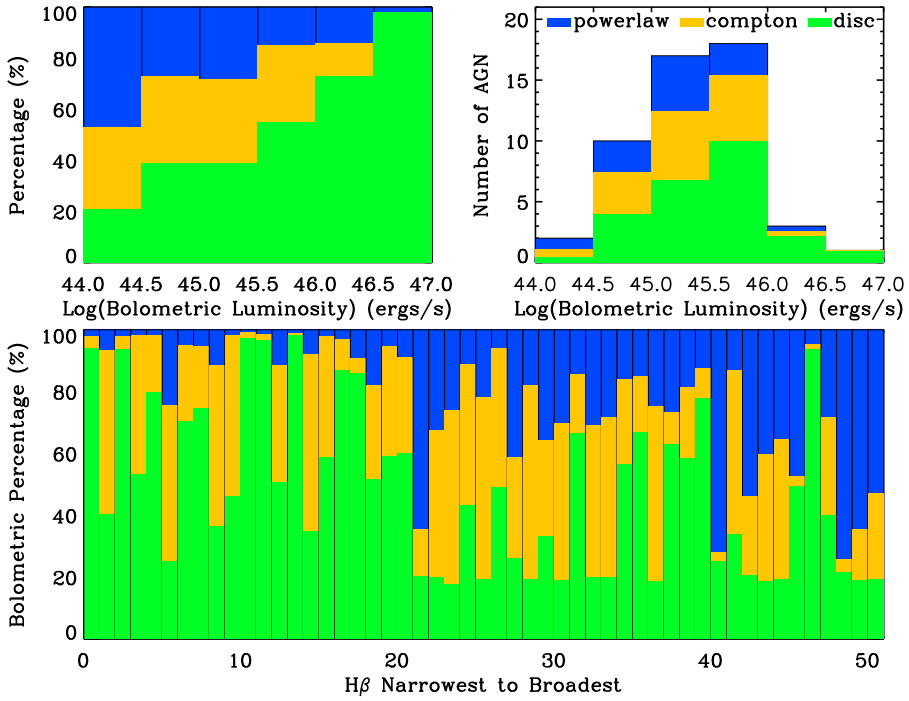

Figure 3.9: The bolometric luminosity distribution for the different continuum components of the SED, i.e. accretion disc (green), Comptonisation (orange) and hard X-ray Comptonisation (blue). The upper left panel shows the percentage within each luminosity bin for each of these three SED components. The Upper right panel shows the luminosity distribution of the whole sample, with each bin divided into three regions according to the fractional contribution from the different components in that luminosity bin. The lower panel shows how the contribution from each component changes as a function of rank order in Hβ FWHM, after the narrow line component has been removed.

3.6.4 The Bolometric Luminosities

The fraction of the total luminosity contained in each component of the SED model is shown in Figure 3.9. The upper left panels show these fractions as a function of the bolometric luminosity. It seems that as the bolometric luminosity increases, the disc component slightly increases in importance. However, the total numbers of objects at high luminosities is small, as seen in the upper right panels, where the fraction is multiplied by the number of objects in the bin, so we should be cautious

Table 3.4: The average black hole masses, as shown in Figure 3.10.

	NLS1	BLS1	ALL
$<M_{BH,IC}>$	6.58±0.49	8.09±0.56	7.73±0.84
$<M_{BH,BC}>$	7.72±0.49	9.05±0.55	8.74±0.78
$<M_{BH,IC+BC}>$	6.75±0.49	8.37±0.65	7.99±0.93
$<M_{BH,\sigma}>$	6.57±0.46	7.89±0.47	7.58±0.73
$<M_{BH,FIT}>$	7.11±0.54	8.05±0.48	7.83±0.64
$<M_{BH,RP}>$	7.42±0.39	8.44±0.53	8.20±0.66

about this finding.

The lower panel shows this fraction for each of the objects ranking from the smallest to biggest $H\beta$ FWHM. Thus low rank objects have the narrowest $H\beta$ (and hence are by definition NLS1s). These also have the lowest black hole masses and highest Eddington ratios. They are more likely to have a smaller fraction of their total luminosity emitted in the soft X-ray excess component, than the BLS1s. This relates to the issue of the corona radii, see Point (9) of Section 3.6.2. There are also some BLS1s which have an apparently high fraction of power in their soft X-ray excesses, but they may also have alternative spectral fits including reflection and/or absorption.

We note that in all these plots the lower limit to the disc fraction of 0.19 results from setting an upper limit of 100 R_g for the corona radius parameter, as mentioned in Section 3.5.2

3.6.5 The Black Hole Mass

The black hole mass is one of the key parameters used in our SED fitting, and it largely determines the continuum shape in the optical/UV region. The masses derived from reverberation mapping are considered to be the most accurate, but the total number of objects which have been studied using this technique is still relatively small (e.g. Peterson et al. 2004; Denney et al. 2010; Bentz et al. 2010). In the absence of reverberation mapping, the empirical relation between M_{BH} and

Hβ linewidth and L_{5100} is often used as a proxy to estimate the black hole mass (Peterson et al. 2004). A serious limitation of this method is that it is still not clear which specific measure of the Hβ profile provides the closest association with the velocity dispersion of the gas in the broad line region.

There are various alternative measures of the velocity width used for determining the black hole mass, including the FWHMs of the intermediate component (IC) and the broad component (BC) (e.g. Zhu, Zhang & Tang 2009). One could also use the model independent second momentum (e.g. Peterson et al. 2004; Bian et al. 2008), or more simply the FWHM of the Hβ line after subtracting the narrow component (NC) (e.g. Peterson et al. 2004). The NC subtracted FWHM and the second momentum estimates often lie within the range of values covered by the IC and BC FWHMs, except for some peculiar objects such as those with broad double-peaked profiles, for example UM 269. Given all these uncertainties we decided to adopt the the best-fit black hole mass obtained from the SED model, rather than simply fixing it at a value determined from a specific linewidth measurement. Moreover, it is now suggested that radiation pressure may be important in modifying the black hole mass derived using the relation between M_{BH} and L_{5100} and Hβ FWHM, especially for objects with high Eddington ratios such as most NLS1s (e.g. Marconi et al. 2008).

In order to compare our results with those from other studies, we have made various estimates of black hole masses for every source in our sample as follows:
(1) $M_{BH,IC}$, $M_{BH,BC}$ and $M_{BH,IC+BC}$ are derived using Equation 3.5 with different Hβ FWHMs obtained from our Balmer line fitting procedure.
(2) $M_{BH,\sigma}$ is the black hole mass calculated from the second momentum of the total Hβ line profile (see Peterson et al. (2004) for details of the definition of 'second momentum'), by using $R_{BLR} \propto L_{5100}^{0.518}$ and a geometry factor of $f = 3.85$. These assumptions are considered to be appropriate when using second momentum as a measure of the velocity dispersion in BLR (Bentz et al. 2006; Collin et al. 2006; Bian et al. 2008).
(3) $M_{BH,RP}$ is the black hole mass corrected for radiation pressure, using equation (9) in Marconi et al. (2008) with $f = 3.1$, $log(g) = 7.6$.

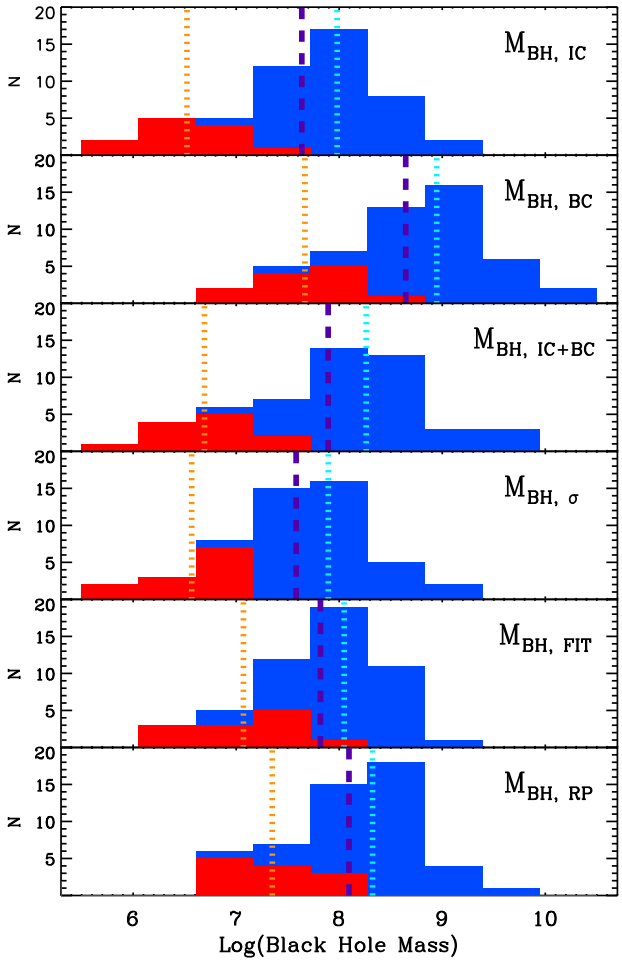

Figure 3.10: A comparison of various methods used to derive black hole mass. The total distributions are shown with the 12 NLS1s show by the red regions. The purple dashed line indicate the average black hole mass for the whole sample. The orange and cyan dotted lines indicate the average masses of NLS1s and BLS1s, respectively. The average values are listed in Table 3.4. Values for individual objects are listed in Table B.2.

We compare the black hole mass distributions obtained from these different methods in Figure 3.10. The mean values are listed in Table 3.4.

The $M_{BH,IC}$ and $M_{BH,BC}$ represent the two extreme estimates of black hole masses. The $M_{BH,IC}$ could still be influenced by contamination from a NLR component, especially for NLS1s where deconvolution of the narrow and broad components is very difficult. If there is a residual narrow line component, it will introduce a bias that underestimates black hole masses. Conversely, using $M_{BH,BC}$ is more likely to bias towards higher black hole masses, due to the presence of low contrast very broad wings often seen in Hβ profiles. We found $FWHM_{IC+BC}/\sigma_{H\beta}$=1.30±0.39 for our sample, which is consistent with 1.33±0.36 found by Bian et al. (2008). This leads to slightly lower values of $M_{BH,\sigma}$ than $M_{BH,IC+BC}$, but these two methods both give black hole masses between $M_{BH,IC}$ and $M_{BH,BC}$, with $M_{BH,IC+BC}$ spanning a broader mass range.

Our best-fit SED black hole masses ($M_{BH,FIT}$) are also distributed between $M_{BH,IC}$ and $M_{BH,BC}$, with similar average masses as $M_{BH,IC+BC}$ (a comparison is shown in Figure 3.11 Panel-A). Note that $M_{BH,FIT}$ is a free parameter in the SED fitting unless it hits the lower or upper limits set by $M_{BH,IC}$ and $M_{BH,BC}$, which occasionally happened (see Table B.2). It is clearly shown in Figure 3.11 that the black hole masses from the SED fitting are not consistent with estimates based on either extremely narrow or extremely broad lines. So for NLS1s, the mean $M_{BH,FIT}$ is 0.36 dex higher than $M_{BH,IC+BC}$; while for BLS1s, the mean $M_{BH,FIT}$ is 0.22 dex lower than $M_{BH,IC+BC}$. Interestingly, this also implies that the $M_{BH,FIT}$ of NLS1s may have less deviation from the established M-σ_* relation than that using the M(L_{5100}, $FWHM_{H\beta}$) relation as shown in several previous studies (e.g. Wang & Lu 2001; Bian & Zhao 2004; Zhou et al. 2006).

The situation may be further complicated as Marconi et al. (2008) showed that NLS1s could be consistent with the M-σ_* relation if a correction for radiation pressure is applied to black hole masses derived from M(L_{5100}, $FWHM_{H\beta}$). In our sample, correction for radiation pressure adds to the average $M_{BH,IC+BC}$ by 0.67 dex for NLS1, 0.07 dex for BLS1 and 0.21 dex for the whole sample. We also found a very similar mass distribution between $M_{BH,RP}$ and $M_{BH,FIT}$, except for an average

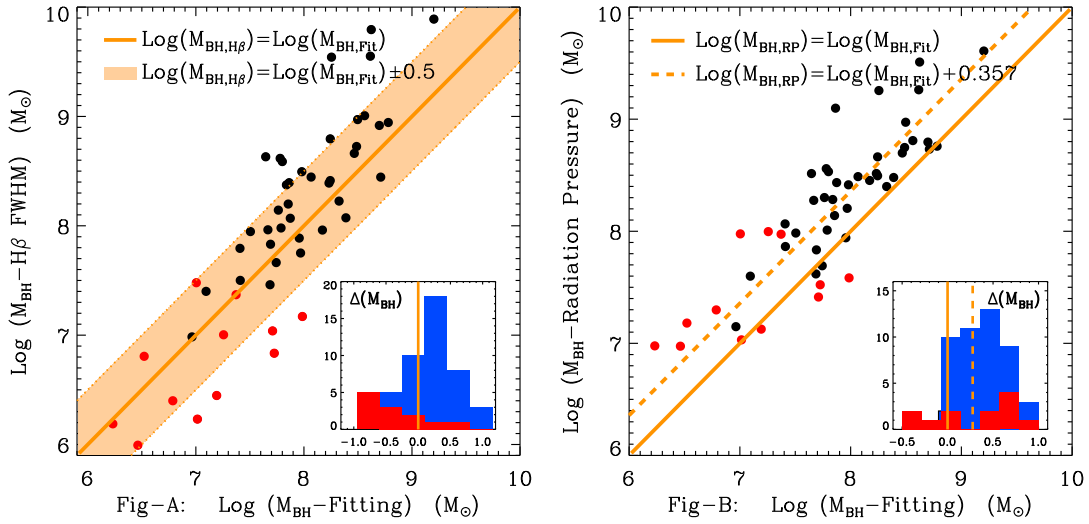

Figure 3.11: Correlations of best-fit black hole mass ('M_{BH}-Fitting' or '$M_{BH,FIT}$') vs. Hβ FWHM determined black hole mass ('M_{BH}-Hβ FWHM' or '$M_{BH,IC+BC}$') and vs. radiation pressure corrected black hole mass ('M_{BH}-Radiation Pressure' or '$M_{BH,RP}$'). Red points represent the 12 NLS1s. The inserted panel in panel-A shows the distribution of the mass difference between $M_{BH,IC+BC}$ and $M_{BH,FIT}$, while the inserted panel in panel-B shows the distribution of the mass difference between $M_{BH,RP}$ and $M_{BH,FIT}$. Red regions highlight the distribution of NLS1s.

of 0.36 dex higher in $M_{BH,RP}$. The differences between the average mass of NLS1s and BLS1s are 0.78 dex and 0.72 dex in $M_{BH,RP}$ and $M_{BH,FIT}$, respectively (see Figure 3.11 Panel-B). Therefore, if $M_{BH,RP}$ can provide a good match to the M-Sigma relation even down to low mass NLS1s as proposed by Marconi et al. (2008), then our SED determined $M_{BH,FIT}$ may also give similar results. This implies that the suggested deviation from the M-σ_* relation for NLS1s may not be an intrinsic property, but rather a consequence of using black hole estimates based on M(L_{5100}, $FWHM_{H\beta}$) relation, which may not be appropriate for NLS1s (e.g. Grupe & Mathur 2004; Komossa 2008).

3.6.6 The Average SEDs

Elvis et al. (1994) constructed SED templates for both radio-loud and radio-quiet AGN, based on a sample of 47 quasars between redshift 0.025 and 0.94. VF07 modeled optical-to-X-ray SED for a sample of 54 AGNs with redshifts between 0.001 and 0.371, and showed that the SED was related to Eddington ratio. They also suggested that $\kappa_{2-10keV}$ is well correlated with Eddington ratio. In a later study (Vasudevan & Fabian 2009) based on SED modeling of 29 local AGNs from Peterson et al. (2004), the SED dependence on Eddington ratio was reinforced. Recently, Lusso et al. (2010) studied 545 X-ray selected type 1 AGN over the redshift range of 0.04 to 4.25. They computed SEDs at different redshifts, and investigated α_{ox} correlations with other parameters such as redshift, $\kappa_{2-10keV}$, λ_{Edd} etc.

We present a mean SED for our sample which is sub-divided according to their $H\beta$ FWHM. This gave three sub-samples, those with the narrowest lines, those with moderately broad lines, and those with very broad lines. All objects were de-redshifted to their local frame. First, each of the best-fit SEDs was divided into 450 energy bins between 1 eV and 100 keV. For each energy bin we calculated the monochromatic luminosity for the sub-sample with 12 NLS1s, using their individual SED models. Then an average value and standard deviation in each energy bin were calculated in logarithm space. Thus a mean SED for the 12 NLS1s was constructed. Using the same method for the 12 moderate and 12 broadest line objects, their mean SEDs were produced. The total SED energy range is 1 eV to 100 keV, but we note that only spectral ranges from 1.5-6 eV and 0.3-10 keV are actually covered by the observational data, and all other ranges are based on model extrapolations.

Obviously, limitations of our mean SEDs include the relatively small sample sizes comprising the SEDs, and the redshift restriction $z < 0.4$. On the other hand, we have assembled high quality data sets of optical, UV and X-ray observations. The exclusion of objects with high intrinsic absorption in the optical/UV helps to simplify the modeling assumptions. Our exclusion of warm-absorber objects may have introduced unknown selection effects, but again this simplified the SED modeling. Our model of the accretion flow also includes more detailed physical assumptions

on the optical-to-X-ray spectrum than in previous broadband SED studies. These advantages make our broadband SED fitting more physically plausible. Thus our mean SEDs too should be more reliable, especially in the unobservable far UV region, where often the peak of the energy is emitted.

Figure 3.12 shows the mean SEDs for the three subsets of our sample. We caution that there is still substantial spectral diversity within each subsample, and echo Elvis et al. (1994)'s warning that if AGN SEDs are simply averaged without considering their detailed intrinsic properties, then the dispersion in the resultant mean SED will be large, so the mean SED may lose some useful information about AGN properties. Nevertheless, there appears to be a clear SED connection with Hβ FWHM. As the line width increases, so the big blue bump (BBB) in the UV region becomes weaker relative to the hard X-rays, and its peak shifts towards lower energy. Also the spectral slope at high energies becomes harder.

This evolution in spectral shape is similar to that found by VF07 and Vasudevan & Fabian (2009), in which two mean SEDs of different mean Eddington ratio were compared. This relation might be expected since the FWHM and Eddington ratio are also strongly (anti)correlated in our sample. VF07 interpreted the spectral diversity as a scaled up version of the different accretion states of Galactic black hole binaries. The low Eddington ratio AGN could be analogous to the low/hard state in black hole binaries in having a weak disc giving a strong high energy tail, and the high Eddington ratio sources are analogous to the high/soft state, in which the disc emission dominates. Our SED templates do not extend down to such low Eddington ratios as in VF07, but we still see a similar behaviour.

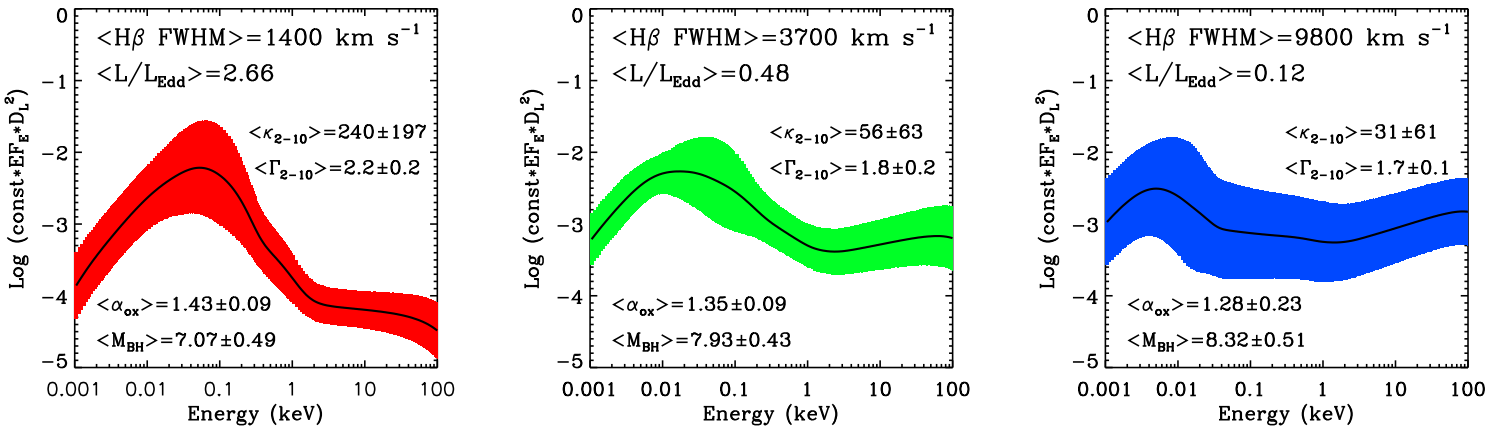

Figure 3.12: The average SED of our sample. The panel on the left shows the averaged SED for the 12 NLS1s (including two marginal NLS1s, 2XMM 112328.0+052823 and 1E 1346+26.7). The average Hβ FWHM is 1400 $\pm$ 500 km s^{-1}. The red area indicates a one standard deviation region on either side of the average spectrum. The central panel is for 12 objects with moderate line width. The average FWHM is 3700 $\pm$ 600 km s^{-1}. The green region indicates one standard deviation. The panel on the right is the mean SED for the 12 broadest line objects in our sample, including the one double-peak source. The average FWHM is 9800 $\pm$ 2900 km s^{-1}. We also show the average value of the 2-10 keV power-law photon index, the 2-10 keV bolometric correction, and the α_{ox} value with a one sigma error. D_L on the Y-axis title is the luminosity distance. The unit of Y-axis is 'keV (ergs s^{-1} keV^{-1})' in logarithm. The same arbitrary constant of 1.31×10^{-46} is used for rescaling each plot.

3.7 Summary and Conclusions

In this chapter we presented a spectral study of 51 unobscured Type 1 AGNs, including 12 NLS1s. We assembled X-ray data from the EPIC monitor on board the XMM-Newton satellite, and optical data from the SDSS DR7. In addition we added optical/UV data from the XMM-Newton OM monitor when available. Our results confirm some previously known correlations. For example, NLS1s often have softer power-law fits from 2-10 keV, and have lower 2-10 keV luminosities. Their Hα, Hβ and [OIII]λ5007 lines are also less luminous on average than found in BLS1s.

• We use detailed models to fit the $H\alpha$ and $H\beta$ line profiles, with multi-components to deblend the narrow, intermediate and broad components by means of simultaneous modeling of the FeII continuum and other blended lines. We then use results from the $H\beta$ line fitting to constrain the black hole mass. The FWHM of the intermediate and broad components give a lower and upper limit for the mass, respectively. This supports previous studies which find that NLS1s tend to have lower black hole masses and higher Eddington ratios, although their bolometric luminosities are not significantly different from those of BLS1s.

• We include the Balmer continuum and permitted iron emission, and extend the modeling across the entire SDSS spectrum in order to isolate the intrinsic optical underlying continuum. However, this pure optical continuum is often (in 32/51 objects) flatter than is predicted by the standard accretion disc model. This could indicate some contamination from the host galaxy, but the lack of stellar absorption features in most of the SDSS spectra suggests that this cannot be a general explanation. Instead it seems more likely that there is an additional component in the optical region related to the AGN, which is as yet not well understood.

• We also show that the Balmer continuum is not well modeled if the edge wavelength is fixed at its laboratory value of 3646Å. It is shifted redwards, and smoothed by more than predicted by the FWHM of the Balmer emission lines. These effects could both be produced by density broadening. Potentially more detailed models of the optical emission could employ this as a new diagnostic tool for studying the physical conditions e.g. electron density and temperature, in the

innermost Balmer emitting regions.

• The optical, UV and X-ray data were fitted using a new broadband SED model (*optxagn* in `Xspec` v12), which assumes that the gravitational potential energy is emitted as optically thick blackbody emission at each radius down to some specific corona radius. Below this radius the remaining energy down to the last stable orbit is divided between a soft X-ray excess component and a hard X-ray tail. This energetically constrains the model fits in the unobservable EUV region. We construct the resulting SEDs for each of the sources.

• A multi-component decomposition of the broadband SED shows that relative contributions to the bolometric luminosity from the accretion disc, Compotonisation and power law components vary among sources with different luminosity and Hβ linewidth. We find a slight increase in contribution from the accretion disc as the luminosity increases, but a larger sample with more sources at both low and high luminosities is needed to confirm this.

• Our study also supports the distinctiveness of the NLS1s among the whole sample. We find that NLS1s tend to have a softer 2-10 keV spectrum, lower 2-10 keV luminosity, lower black hole mass, higher Eddington ratio and higher α_{ox} index. However NLS1s do not stand out from the whole sample in terms of their bolometric luminosity distribution. We estimate the corona radii for every AGN in our sample from the SED fitting. This shows that on average NLS1s have smaller corona radii, and correspondingly a smaller coronal component contribution.

• We compare the best-fit black hole masses with those corrected for radiation pressure, and other estimates of black hole mass based on the R_{BLR}-L_{5100} relation, including numerous options for measuring the velocity width of the Hβ emission line. These results show that the black holes masses derived from SED fitting have a similar distribution to that derived from profiles corrected for radiation pressure effects, except for an offset of 0.3 dex lower in both the NLS1 and BLS1 subsamples. The black hole mass difference between NLS1s and BLS1s from these two methods (i.e. SED fitting and radiation pressure corrected profiles) are both smaller than inferred from other mass measurements. This implies that compared with black hole mass estimates based only on the Hβ FWHM, NLS1s may lie closer to the

established M-σ_* relation at the low mass end, when their black hole masses are corrected for radiation pressure, and when we use masses derived from our SED fitting.

• Finally, we form three broadband SED templates by co-adding SEDs in three subsamples (consist of 12 objects in each) to examine how the broadband SED depends on $H\beta$ FWHM velocity width, and by extending the Eddington ratio. The results show that there is a change in the SED shape as the FWHM increases, with NLS1s having the largest big blue bump in the extreme-UV region. Other important parameters such as $\Gamma_{2-10keV}$, $\kappa_{2-10keV}$ and α_{ox}, also change as the Hβ FWHM increases. The implications of correlations among these parameters will be discussed in Chapter 5.

Chapter 4

Type 1 AGN Study - II. X-ray and Optical Spectral Relation

4.1 Introduction

In Chapter 3, we presented modelling results for a sample of 51 unobscured nearby Type 1 AGNs. From the spectral fitting we derived numerous spectral parameters that were not contaminated by X-ray or optical obscuration. In this chapter, we aim to investigate the link between the central ionization flux characterized by the unobscured hard X-ray, and the properties of the various optical emission lines and the continuum. We conduct this investigation by studying the profile of various emission lines, and the luminosity correlations between hard X-ray and various optical emission features, making use of the spectral fitting results in Chapter 3.

Narrow Line Seyfert 1s (NLS1s) are often considered as a special type of AGN whose permitted line width is comparable to other forbidden lines, and their [OIII] λ5007/Hβ flux ratio is lower than is typical of normal Seyfert 1s (Shuder & Osterbrock 1981; Osterbrock & Pogge 1985). We have shown in Chapter 3 that NLS1s were often found to have low black hole masses (e.g. Wang & Lu 2001; Bian & Zhao 2004; Zhou et al. 2006; Komossa & Xu 2007; Zhu, Zhang & Tang 2009, hereafter: Zhu09). These may be systematically lower than predicted by the M-σ_* relation which holds well for BLS1s (Grupe & Mathur 2004; Mathur & Grupe 2005). The NLS1s also have high Eddington ratios (Boroson 2002; Komossa 2008). It is thus proposed that NLS1's central black hole may still be growing (e.g. Mathur,

Kuraszkiewicz, & Czerny 2001; Komossa & Mathur 2001; Komossa 2008). In addition, NLS1s have softer 2-10 keV spectra, lower 2-10 keV luminosities, higher α_{ox} values and more energetic BBB (see Chapter 3 and references therein). In this chapter, we continue to pay special attention to the NLS1 subset in our sample and show how they behave differently from other sources in the cross-correlation study.

This chapter is organized as follows. We first review some most important characteristics of the sample in Section 2, in order to emphasize that our study conducted in the following sections should be related to the most intrinsic properties of AGN's bare core. Section 3 will present the 'Optical to X-ray Correlation Spectrum (OXCS)' based on our new 'Correlation Spectrum Technique (CST)', from which various correlation features related to the hard X-ray luminosity are found in the optical spectrum. Section 4 will study the cross-correlation between different Balmer line components and broadband SED components. Section 5 will focus on correlations related to the Balmer line equivalent width (EW). Section 6 will study the physical properties of different Balmer emission line regions. [OIII] λ5007 line's property and its correlation with different SED components are put in Section 7. Summary and conclusion will be made in Section 8. Following Chapter 3, flat universe model is adopted with the Hubble constant $H_0 = 72$ km s^{-1} Mpc^{-1}, $\Omega_M = 0.27$ and $\Omega_\Lambda = 0.73$. All the results presented in this chapter has been submitted to MNRAS as Jin et al. (2012a).

4.2 The Sample and The Spectral Modelling

4.2.1 Sample Selection

The sample used in this chapter is a nearby unobscured Type 1 AGN sample derived from the cross-correlation of 2XMMi & SDSS DR7 catalogs. The main selection steps are listed below for completeness. A full source list and more detailed explanation of the sample selection can be found in Chapter 3.

(1) We searched 2XMMi and SDSS DR7 catalogs and identified 3342 extragalactic sources with both X-ray and optical spectra.

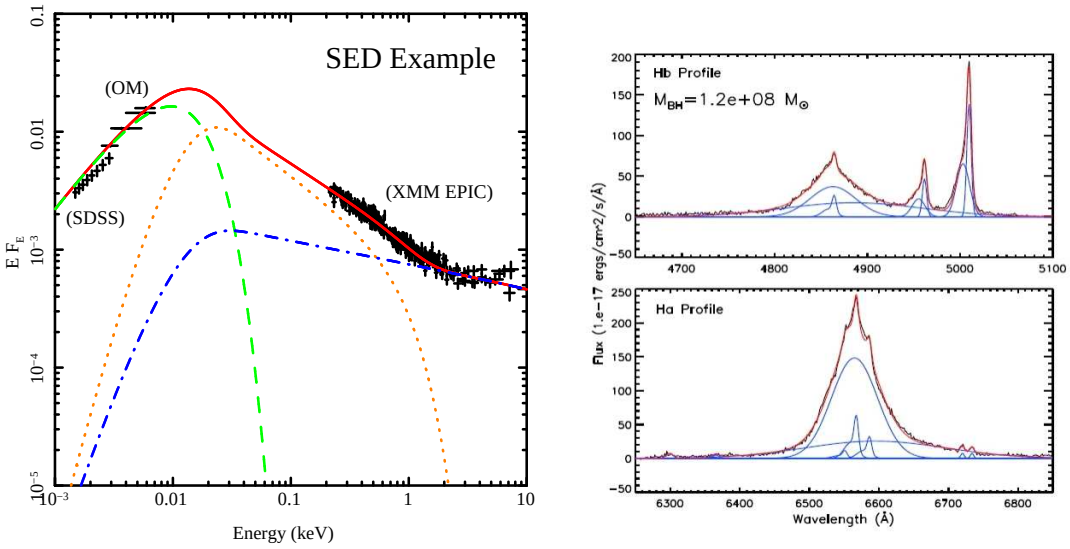

Figure 4.1: Examples of spectral fitting in Chapter 3. Left panel shows the broad-band SED fitting of PG 1115+407 which consists of a modified accretion disc (green dashed line), a soft X-ray Comptonisation (orange dotted line) for the soft X-ray excess and a hard X-ray Comptonisation (blue dash-dotted line) for the hard X-ray power law tail. Right panel shows the emission line fittings of RBS 1423 around Hα and Hβ. Blue solid lines represent different line components.

(2) Within these sources, we selected those with $H\beta$ in emission and redshift $z < 0.4$, so that both the Hα and Hβ emission lines are covered by the SDSS spectra. This assists on the modelling of the Balmer lines (see Chapter 3). This selection resulted in 802 unique X-ray sources.

(3) Within this sample set, we identified 96 Type 1 AGNs with a minimum of 2000 counts in at least one of the three XMM-Newton EPIC cameras, to ensure high X-ray spectral quality.

(4) We then excluded 23 sources whose $H\beta$ line was distorted due to strong reddening, low S/N or bad data gap in the SDSS spectra, so the remaining sample contains 73 AGNs.

(5) For each of the 73 sources, a power law model was fitted to the rest-frame 2-10 keV X-ray spectra. 16 objects with photon index uncertainties greater than 0.5 were thereby excluded, leaving 57 Type 1 AGNs with relatively well constrained 2-10 keV spectra.

(6) Another 6 objects were excluded due to the obvious signature of warm absorption at ∼0.7 keV.

The final sample contains 51 AGNs with 12 AGNs being classified as NLS1 using the conventional definition (Goodrich 1989), while the others are all BLS1s. Most objects in this sample are radio quiet, except for 3 sources that were reported as radio loud, i.e. PG 1004+130, RBS 0875 and PG 1512+370. High quality XMM-Newton EPIC X-ray spectra and SDSS optical spectra are available for every source in this sample. In addition, simultaneous optical/UV photometric data from the XMM-Newton OM monitor are available for 37 sources.

We exclude PG 1004+130 from all correlations as it is a BAL quasar, so its X-ray flux is likely to be heavily obscured even though it does not show clear evidence for absorption edges (Miller et al. 2006). We also exclude Mrk 110 from the optical correlations (Sections 3, 4 and 5) as this shows strong optical variability (Kollatschny et al. 2001; Kollatschny 2003) and the SDSS spectrum is very different from the (non-simultaneous) XMM-Newton OM data (see Chapter 3). However, the [OIII] line luminosity does not change with the optical continuum, so we include this object in the [OIII] versus broad band SED correlations in Section 7.

4.2.2 Selection Bias

Our sample distributes evenly within $0.031 < z < 0.377$ with a mean redshift $< z >= 0.137^{+0.158}_{-0.073}$. Its selection is mainly based on both high quality optical and X-ray spectra, thus any AGN that was not detected or only marginal detected by SDSS or XMM-Newton would not be included in the sample, i.e. sources with low mass accretion rate or strong obscuration were excluded. Further selection criteria are more related to specific spectral characteristics, such as excluding objects with heavy optical reddening, Type 2 objects and X-ray warm absorber objects. Therefore it will be hard to directly estimate the bias due to these selection effects. However, we could compare our sample's general properties with previous samples. We found that our sample had very similar redshift, 2-10 keV luminosity and bolometric luminosity distributions as Vasudevan & Fabian (2007)'s sample (hereafter: VF07), except

that VF07's sample also includes some extremely nearby and low X-ray luminosity sources such as NGC 4395, NGC 3227 and NGC 6814, which did not fall into our sample. The redshift distribution of our sample is also similar as Grupe et al. (2010), except that their sample has a bigger fraction of lower redshift sources ($< z >= 0.112 \pm 0.077$). The selection effect regarding the broadband SED shape should be weak, which is because the broadband SEDs of our sample have shown a very strong shape diversity, with the intrinsic optical to X-ray spectral index α_{ox} ranges 1∼2. It is true that any objects with extraordinary optical to X-ray luminosity ratios would not be included in our sample. But such odd broadband SEDs are more likely due to optical or X-ray obscuration, rather than being intrinsic to AGN, thus they are no longer the type of unobscured sources we need in this sample.

4.2.3 Major Sample Properties

The most important characteristic of this particular sample is the high quality of both their optical and X-ray spectra. In the optical, none of these sources suffer strong dust reddening, thus all sources have very clear optical underlying continuum superposed by a series of clear broad and narrow emission lines. In the X-ray our selection criteria have excluded sources whose spectra from XMM-Newton have low signal to noise or contain strong warm absorber features (i.e. the absorption edge at ∼0.7 keV, from combined absorption features from partially ionized Oxygen and Iron, see e.g. Lee et al. 2001; Turner et al. 2004). The rest of the sources all have high quality X-ray spectra which represent the emission from the AGN's core emission.

4.2.4 The Spectral Modelling

Another important characteristic is the availability of all important spectral parameters from optical to X-ray for the whole sample, which results from our thorough modelling of the multi-component Balmer lines, optical spectrum and broadband SED.

In the emission line fitting (e.g. Figure 4.1 right panel), two Gaussian components were used to fit the [OIII] λ5007 line, i.e. a central component and a blue component. Then the whole profile of [OIII] λ5007, i.e. including both central and blue components, was used in the fitting of the narrow component of Balmer lines. Two additional Gaussian profiles were included in fitting each of the Hα and Hβ lines, so that each line contains a narrow component (NC), an intermediate component (IC) and a broad component (BC). All other strong nearby emission lines, e.g. [NII] $\lambda\lambda$6585/6548 doublets, Li λ6708, [SII] $\lambda\lambda$6717/6734, are included by adding more Gaussian profiles into the whole model. Various constrains were set for these Gaussian components which are all described in Chapter 3.

In the broadband SED fitting (e.g. Figure 4.1 left panel), we made use of a new SED model (*optxagn* model in `Xspec` v12: Done et al. 2011), which modifies the accretion disc emission (the green dashed line) by assuming a corona radius within which all accretion disc emission is transferred to a soft X-ray Comptonisation component (the orange dotted line) to account for the observed soft X-ray excess, plus a hard X-ray Comptonisation component (the blue dash-dotted line) to model the hard X-ray power law tail. We rebuilt the broadband SED from the optical to hard X-ray by extrapolating the best-fit model over the unobservable UV/soft X-ray region, and then derived all the SED parameters. Detailed descriptions of these spectral fitting can be found in Chapter 3.

4.3 The Optical to X-ray Correlation Spectrum (OXCS)

4.3.1 The Motivation of OXCS

The hard X-ray emission from AGN rises from Compton up-scattering of disc photons by a high temperature (100s of keV) electron population which forms a corona region located above the accretion disc. Although this hard X-ray emission may only contribute a small fraction of the total central ionizing flux (depending on the corona radius, see Chapter 3), it is capable of penetrating deeply into the most dense

gas regions near AGN's core, which emits some specific line species. Provided that the intrinsic hard X-ray emission is not heavily absorbed and the optical spectrum is not heavily reddened, we can identify those optical emission features closely linked with the high energy core emission by testing their correlation with the hard X-ray. As noted above, our sample was selected based on the unobscured nature of both the optical and X-ray spectra, so the hard X-ray luminosity can be used as a reliable diagnostic to investigate its relation to the optical spectral properties. Here we propose and test a new type of spectrum, the 'Optical to X-ray Correlation Spectrum (OXCS)' (see Figure 4.2). This is a direct extension of previous monochromatic luminosity correlation studies between X-ray and optical e.g. L_{2keV} vs. $L_{2500\mathring{A}}$ (e.g. Green et al. 2009; Lusso et al. 2010).

4.3.2 Construction of OXCS

The principle behind the OXCS is to cross-correlate the hard X-ray luminosity (here we choose the luminosity of 2-10 keV: $L_{2-10keV}$) with the monochromatic luminosities at each wavelength of the optical spectrum for the whole sample of objects. Then we plot the correlation coefficient against the wavelength, to see how the correlation changes with wavelength. For each source in the sample, we corrected the SDSS spectra for Galactic reddening and de-redshifted them to their rest frame. We define a standard optical spectral region that is covered by the SDSS spectrum of every source (around 3700-6700Å), and calculate the monochromatic luminosity at 1000 wavelengths distributed evenly across this spectral range. The Spearman's rank test was used to cross-correlate these monochromatic luminosities with $L_{2-10keV}$, and so the Spearman's ρ coefficient was derived at each of the 1000 wavelengths. Figure 4.2 plots the Spearman's ρ coefficient against the wavelength for the 12 NLS1 (red line) and 37 BLS1 (blue line). The wavelengths of some of the most prominent optical emission and absorption features in a typical AGN spectrum are indicated in the plot. Note that the spectral coverage is not exactly the same for different OXCS subsets, because these subsets have slightly different redshift ranges.

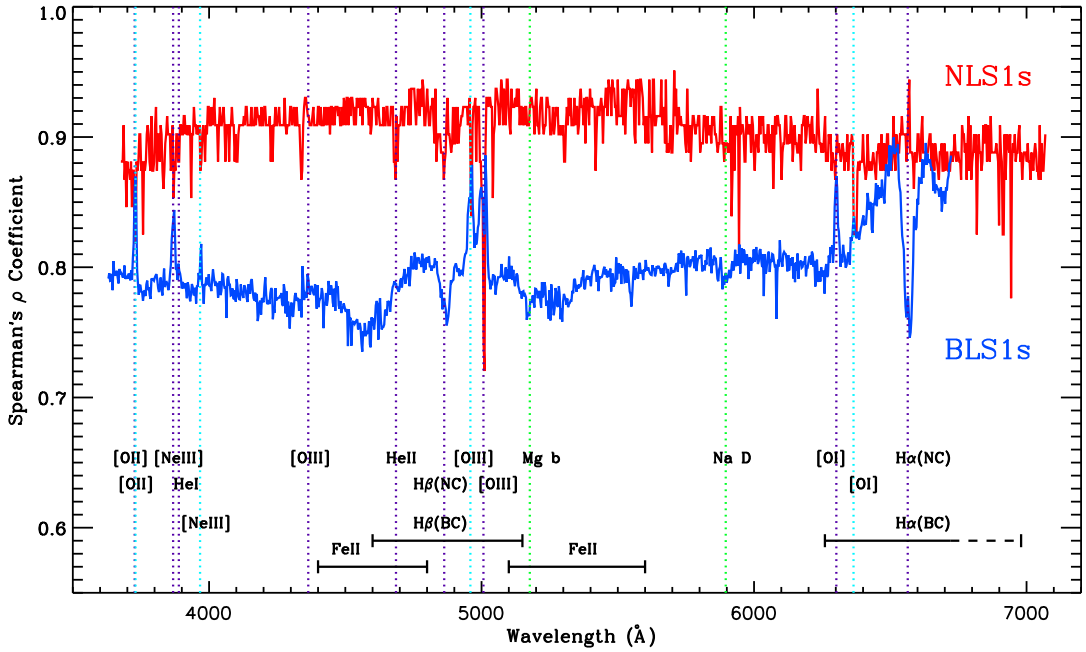

Figure 4.2: The OXCSs for our sample, the method of constructing them is described in Section 4.3.2. The red line is the OXCS for the 12 NLS1s in our sample. The blue line is the OXCS for the 37 BLS1s in our sample. Purple and cyan dotted lines indicate the wavelengths of some most prominent optical emission lines for a typical AGN, with cyan lines indicating the weaker line of any doublets. Green dotted lines indicates the wavelengths of Mg b and Na D stellar absorption features. '(NC)' is the narrow component, while '(BC)' is the broad component. The dashed region of Hα(BC) means that this region is not covered by the BLS1 OXCS.

4.3.3 Correlation Features

Within the limited wavelength range of OXCS, the underlying continuum correlation would not be expected to change significantly, and so it forms a basic correlation level that is relatively flat in OXCS. Superposed on this basic correlation continuum there are various emission and absorption-line-like features, which shows that those lines have stronger or weaker correlation with $L_{2-10keV}$ than the underlying continuum. We identify some of the most noticeable characteristics in the OXCSs as below:

(1) $L_{2-10keV}$ emission correlates well with the entire optical underlying continuum. The underlying correlation is ∼0.8 in the BLS1 OXCS, and ∼0.9 in the NLS1 OXCS. A noticeable phenomena is that the underlying correlation does not decrease significantly towards either the blue or red end of the optical spectral range. This confirms that our sample suffers little intrinsic reddening, and that the optical continua redward of 5000Å are dominated by AGN emission, i.e. the host galaxy contamination is small in most cases. There is also suggestions about the existence of an extra component contributing optical emission at redward of 5000Å, which is probably originated from the self-gravity dominated region of accretion disc (Vanden Berk et al. 2001; Collin & Huré 2001; Puchnarewicz et al. 2001; Soria & Puchnarewicz 2002; Pierens, Huré & Kawagushi 2003; Collin & Kawaguchi 2004; Hao et al. 2010; but see Landt et al. 2011). But we find it difficult to investigate this component merely using SDSS spectra due to the difficulties in accurately subtracting the host galaxy emission.

(2) In the BLS1 OXCS, the broad wings of Hα and Hβ correlate better with $L_{2-10keV}$ than the optical continuum, and so result in the apparent broad-wing-like features around 4860Å and 6565Å. However, the core region of Balmer lines has a much weaker correlation with $L_{2-10keV}$ as shown by the two narrow correlation dips centred at 4862.68Å and 6564.61Å in the OXCSs. This directly shows that the Balmer lines in BLS1s consist of (at least) two components, from the NLR and BLR of different physical conditions. We will investigate this issue further in later sections. The [OIII] $\lambda\lambda$4959/5007 doublets in BLS1s show a very strong correlation with $L_{2-10keV}$,

in spite that the [OIII] $\lambda\lambda$4959/5007 originates in the NLR far from AGN's core. We will investigate this in more detail in Section 4.7. The Balmer line profile in NLS1s is not strongly broadened, so the NLS1 OXCS does not exhibit similar correlation bumps around Balmer lines as in the BLS1 OXCS. In contrast to the BLS1s, the [OIII] $\lambda\lambda$4959/5007 in NLS1s also have much weaker correlation with $L_{2-10keV}$ than their local optical continuum.

(3) The BLS1 OXCS also exhibit emission-line-like features at the wavelengths of some other emission lines in a typical BLS1 optical spectrum, such as [NeIII] $\lambda\lambda$3869/3967, [OI] $\lambda\lambda$6300/6364 and [OII] $\lambda\lambda$3726/3729. This suggests that these emission lines all correlate strongly with the hard X-rays. However, [OI] λ6300 is a relatively weak line, and its prominence in the OXCS may support the existence of dense gas clouds near AGN's core inside which gas stays neutral or at low ionization. Only hard X-rays can penetrate into these clouds and produce such low ionization lines. The fact that [OII] $\lambda\lambda$3726/3729 correlates quite well with $L_{2-10keV}$ suggests that reddening is indeed quite low for our sample, since otherwise the presence of dust would tend to diminish any correlation. It is apparent that in terms of the OXCS around emission lines, the NLS1s are different from BLS1s. This may be a result of geometrical effects, or that the line emitting regions in NLS1s are not as closely associated with hard X-ray emission as in the BLS1s.

(4) On the contrary, it is seen that the stellar absorption lines Mg b and Na D do not correlate well with $L_{2-10keV}$, producing absorption-like features in the OXCSs. Neither does FeII emission in the ranges 4400-4800 Å and 5100-5600 Å correlate with $L_{2-10keV}$, especially for BLS1s.

4.3.4 The Correlation Spectrum Technique (CST)

More generally, the OXCS provides a new tool for spectral studies based on medium to large samples of objects. We will name this the 'Correlation Spectrum Technique (CST)'. As shown above, an example of the CST is the OXCS, which has proved to

be useful for investigating hard X-ray related correlations in the optical spectrum for different AGN populations.

Using hard X-ray as a diagnostic, we can also apply the CST to spectra of longer wavelengths such as near and far infrared, provided that an AGN sample with good spectral data is available. We can also use luminosities other than hard X-ray as the diagnostic in CST. For example, in Section 4.7.2 we constructed the 'SED to [OIII] λ5007 Correlation Spectrum (SOCS)', in which case the CST uses the luminosity of [OIII] λ5007 to produce the correlation spectrum from optical to hard X-ray for different sample subsets.

4.4 Balmer Line Luminosity

For Type 1 AGN, each Balmer line profile consists of two to three distinct components, i.e. narrow component (NC) from the narrow line region (NLR) which extends a few hundred parsecs from the central black hole (e.g. Bennert et al. 2006; Heckman et al. 2005), broad component (BC) from the broad line region (BLR) which is tens of light-days from the black hole (e.g. Kaspi et al. 2005; Bentz et al. 2006). Sometimes another intermediate component (IC) is present, with moderate linewidth which is probably originated from the intermediate line region (ILR) which may extend up to the region of the inner radius of the dusty torus (e.g. Zhu09). Therefore the distance of these line emitting regions from the compact AGN goes as NLR, ILR, BLR from the farthest to the closest. Among these emission line regions we may also expect a density gradient and a correlation trend with the central ionizing flux. The correlation between the Balmer line luminosity and X-ray luminosity has been known long ago (e.g. Ward et al. 1988), but the hard X-ray correlations for different Balmer line components have never been studied. Now our sample with both high quality optical and X-ray spectra provides an opportunity for this study.

4.4.1 Balmer Line Component Luminosity vs. $L_{2-10keV}$

We have shown in the previous section that different components in the Hα and Hβ lines may have different correlation status with $L_{2-10keV}$. In this section we

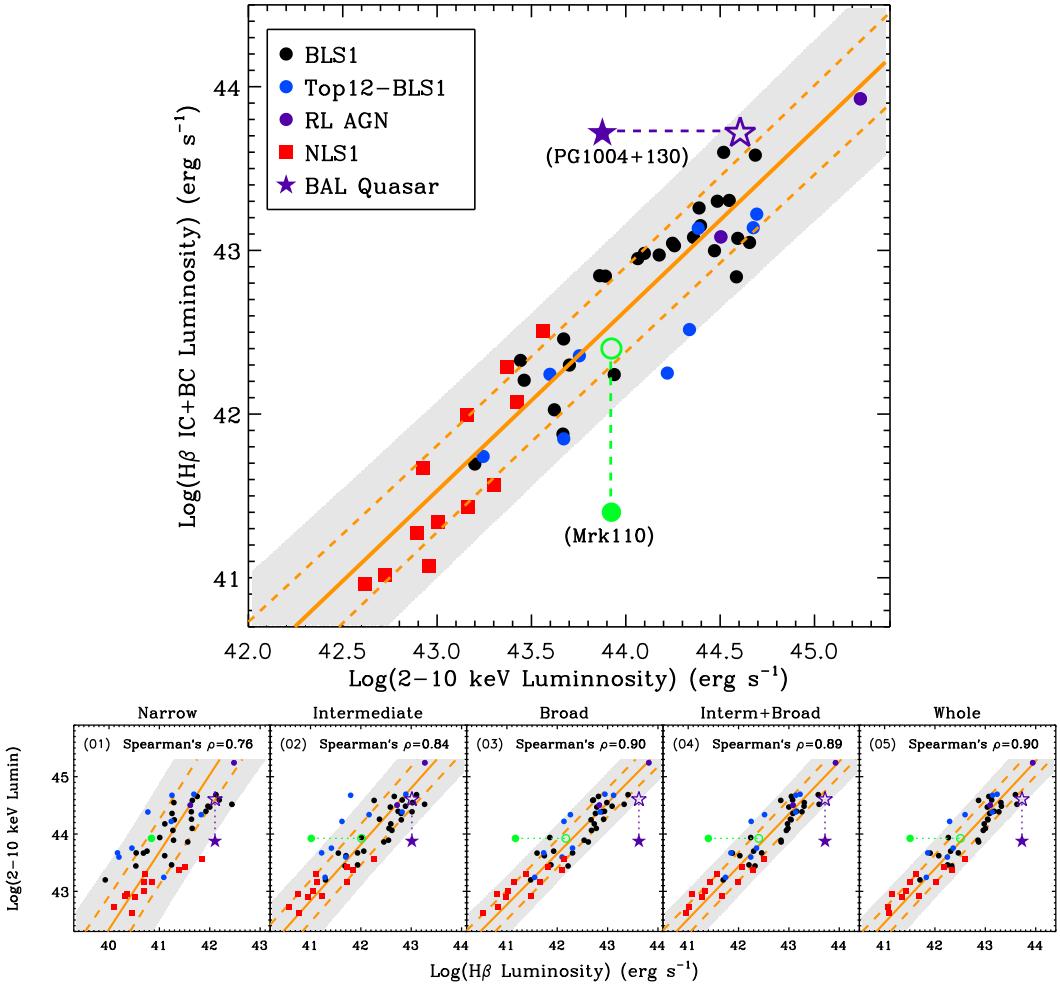

Figure 4.3: The luminosity correlation between Balmer line components and 2-10 keV. The upper figure shows Hβ luminosity (NC subtracted) vs. $L_{2-10keV}$. The connected filled and empty purple stars indicate the position of PG 1004+130 before and after being corrected for the 0.73 dex (Miller et al. 2006). The connected filled and empty green circles indicate different optical positions of Mrk 110 as calculated from the SDSS spectrum and the FAST spectrum (Landt et al. 2011). The solid orange line shows the linear regression line treating $L_{2-10keV}$ as the independent variable, with the two dashed orange lines indicating the $\pm1\sigma$ region for new observations, and the shaded region showing the $\pm2\sigma$ region. The lower panels present the same type of correlations for different Hβ components, i.e. Hβ NC, IC, BC, IC+BC (or NC-sub) and the whole line. In each plot, Spearman's rank coefficients were calculated after excluding PG 1004+130 and Mrk 110. The regression coefficients are listed in Table C.2.

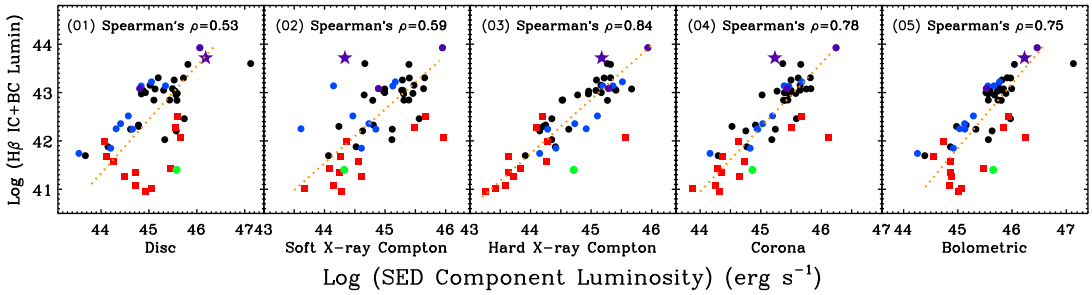

Figure 4.4: The luminosity correlations between Hβ IC+BC and broadband SED components. 'Corona' means the coronal luminosity, which is the sum of the luminosities of the soft and hard X-ray Comptonisation components. Different symbols represent different type of sources as explained in Figure 4.3. In each panel the Spearman's rank coefficient is given, along with the orange dotted line indicating the bisector regression line.

investigate the correlation of $L_{2-10keV}$ with the individual components (Narrow, Intermediate and Broad) derived from our Balmer line decompositions for each source in Chapter 3. The best correlation is for $L_{2-10keV}$ vs. Hβ IC+BC (i.e. the combination of NC and BC, equivalent to NC subtracted Hβ) luminosity, shown in the upper panel in Figure 4.3. NLS1 (red squares) and BLS1 (blue circles) clearly lie on the same strong correlation. Spearman's rank test gives a correlation coefficient of $\rho_s = 0.9$ and probability of random distribution of $d_s = 8.1 \times 10^{-19}$.

We also plot the uncorrected data from our two excluded sources (PG 1004+130: purple star and Mrk 110: green circle) on the correlation. These strongly deviate from the best-fit line (orange solid line), the $\pm1\sigma$ lines (orange dash lines) and the $\pm2\sigma$ region (light gray region). However, PG 1004+130 is the only BAL quasar in our sample, whose X-ray was reported as being 0.73 dex weaker than normal PG RLQs after correcting for intrinsic absorption and normalizing to similar optical/UV luminosities (Miller et al. 2006). Mrk 110's optical continuum is highly variable (Kollatschny et al. 2001; Kollatschny 2003). The SDSS spectrum of Mrk 110 is $\sim$1 order of magnitude less luminous than the FAST optical spectrum (Landt et al. 2011), which is just the required amount of correction we need to pull Mrk 110 back onto the best-fit correlation line. Therefore, we conclude that this tight correlation

between Hβ IC+BC luminosity and 2-10 keV luminosity is an intrinsic property. We propose that if an AGN is found to strongly deviate from this correlation, then it is likely that its X-ray or optical emission is obscured.

We calculated three types of regression lines as described in Isobe et al. (1990). Since Hα also gives similar results (see Table 4.1), we give bisector regression equations for both Hβ and Hα:

(i) $L_{2-10keV}$ expressed by the Balmer line Luminosities:

$$LogL_{2-10} = (0.83\pm0.03)LogL_{H\alpha(NCsub)} + (8.35\pm1.43) \quad (4.1)$$

$$LogL_{2-10} = (0.83\pm0.04)LogL_{H\beta(NCsub)} + (8.56\pm1.52) \quad (4.2)$$

(ii) Balmer line Luminosities expressed by $L_{2-10keV}$:

$$LogL_{H\alpha(NCsub)} = (1.20\pm0.05)LogL_{2-10} - (9.50\pm2.09) \quad (4.3)$$

$$LogL_{H\beta(NCsub)} = (1.18\pm0.04)LogL_{2-10} - (9.17\pm2.04) \quad (4.4)$$

Using the above equations we estimate that PG 1004+130's X-ray luminosity is weaker than normal Type 1 AGNs by 1.0±0.3 dex, which is slightly higher than Miller et al. (2006)'s estimation of 0.73 dex weaker than normal PG radio-loud quasars with similar optical/UV luminosities based on their X-ray spectral analysis.

The lower panels in Figure 4.3 show the (weaker but still very significant) correlations for the different line components. It is clear that the BC has the best correlation with hard X-ray emission as found previously; IC+BC and the whole Hβ line also show good correlations; the NC related correlations are not as good as others. This confirms that the BLR has the closest link with the AGN's central X-ray continuum.

We note that the well-known Malmquist bias (Gonzalez & Faber 1997, and references therein) will be partly responsible for these correlations, but it should affect all of the correlations equally. Hence the change in correlation strengths among the different Balmer line components should be real. We also examined these correlations using flux instead of luminosity, and a very similar trend of strength of correlation was found for NC, IC and BC. Note that the components in Hα show similar correlation status as in Hβ (see Table 4.1).

Table 4.1: The luminosity correlations between Balmer line components and 2-10 keV. The Bisector regression coefficients in the equation: $\mathrm{Log}(L_{BalmerLine})=\beta_0\mathrm{Log}(L_{2-10keV})+\xi_0$ are listed, along with the Spearman's rank correlation coefficients ($\rho_s,\ d_s$) as defined in Table C.2.

Line Comp.	Bisector Regress Coef.		Rank Cor.	
Hα	β_0	ξ_0	ρ_s	d_s
NC vs. $L_{2-10keV}$	1.00±0.06	-2.01±3.28	0.76	-10
IC vs. $L_{2-10keV}$	1.18±0.05	-9.00±2.26	0.92	-20
BC vs. $L_{2-10keV}$	1.23±0.05	-11.51±2.19	0.93	-22
IC+BC vs. $L_{2-10keV}$ (i.e. NC-sub)	1.20±0.05	-9.50±2.09	0.94	-22
Whole vs. $L_{2-10keV}$	1.15±0.04	-7.66±1.95	0.93	-22
Hβ	β_0	ξ_0	ρ_s	d_s
NC vs. $L_{2-10keV}$	1.02±0.07	-3.49±3.35	0.76	-10
IC vs. $L_{2-10keV}$	1.17±0.05	-9.41±2.54	0.86	-15
BC vs. $L_{2-10keV}$	1.21±0.05	-10.67±2.09	0.93	-21
IC+BC vs. $L_{2-10keV}$ (i.e. NC-sub)	1.18±0.04	-9.17±2.04	0.92	-20
Whole vs. $L_{2-10keV}$	1.15±0.04	-7.91±1.97	0.93	-21

4.4.2 Cross-correlation between Balmer Line Components and Broadband SED Components

In Chapter 3 we decomposed the Balmer lines into broad, intermediate and narrow components. We also decomposed the broadband SED into three components, namely the disk, soft X-ray Comptonisation and hard X-ray Comptonisation. Thus it is possible for us to correlate each line component with each SED component. The results are presented in Table C.2 and Figure C.1. Note that for every source we subtracted the FeII emission from the nearby region of Hβ line before conducting the line decomposition, thus the dispersion in these correlations is not related to the FeII contamination. We find that among the three SED components, the hard X-ray Comptonisation produces the best correlations, while the accretion disc emission and soft X-ray Comptonisation show weaker correlations. Among the different Balmer line components, the correlation strengthens from NC, IC to BC. Figure 4.4 shows the correlation status for Hβ IC+BC vs. broadband SED components. It is clear that the best correlation is found in the hard X-ray component though the correlation is also good for adding both soft and hard X-ray Comptonisation together as total corona luminosity.

Figure 4.4 also shows that for BLS1s the Hβ IC+BC correlate well with the accretion disc luminosity and bolometric luminosity. However, NLS1s are much more dispersed in these correlation plots, and thus dilute the correlation strength of the whole sample. We need a larger sample to confirm the different behaviors of NLS1s and BLS1s in these correlations.

4.5 Balmer Line Equivalent Width (EW)

4.5.1 Balmer Line Component EW vs. $L_{2-10keV}$

In the previous section we reported the strong correlation between Hβ luminosity and $L_{2-10keV}$ as $L_{H\beta} \propto L_{2-10kV}^{1.15\pm0.04}$ for the whole Hβ line, and $L_{H\beta(IC+BC)} \propto L_{2-10kV}^{1.18\pm0.04}$ for the IC plus BC in Hβ. The index 1.18±0.04 is bigger than unity which indicates that the luminosity of broader components of Hβ increase faster than linearly with

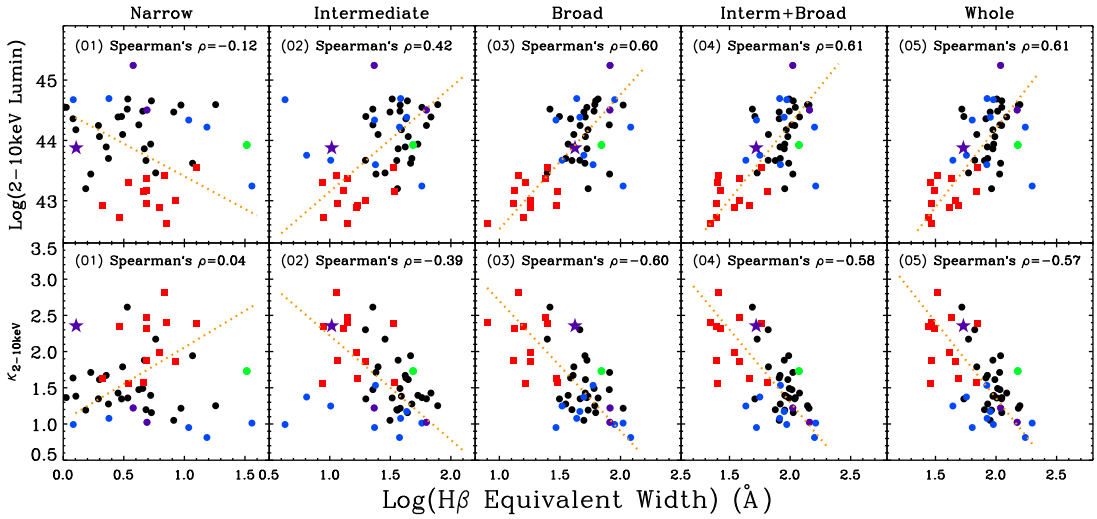

Figure 4.5: The correlations of Hβ component EW vs. $L_{2-10keV}$ (first row), $\kappa_{2-10keV}$ (second row). Different symbols represent the same type of sources as in Figure 4.3. Spearman's rank coefficients are calculated for the whole sample. The orange dotted line indicates the bisector regression line.

L_{2-10kV} (also see Table 4.1). The situation is the same for Hα. In order to investigate this issue further, we study the properties of Balmer line EW. We perform the cross-correlation between $L_{2-10keV}$ and Hβ component EW. Figure 4.5 shows the results. There is no correlation between $L_{2-10keV}$ and Hβ NC EW, but the correlations between $L_{2-10keV}$ and Hβ IC, BC EWs are significant as confirmed by Spearman's rank test (see Table C.2). A bisector regression analysis shows that Hβ IC+BC EW $\propto L_{2-10kV}^{0.45\pm0.03}$.

We also find clear anti-correlations between the 2-10 keV bolometric correction (i.e. $\kappa_{2-10keV}$=$L_{bol}/L_{2-10keV}$) and Hβ EWs, as shown in the second row of Figure 4.5. $\kappa_{2-10keV}^{-1}$ is the fraction of 2-10 keV emission in the Bolometric luminosity, thus these correlations suggest that as the fraction of 2-10 keV emission increases, the EWs of Hβ IC and BC also increase. This is not surprising since there is no correlation between Hβ EWs and the bolometric luminosity, as shown in Table C.2 the Spearman's rank correlation coefficients (ρ_s) are only -0.08, 0.13, 0.21, 0.22 and 0.22 for L_{bol} vs. the EW of Hβ NC, IC, BC, IC+BC and the whole line, respectively. The sources with large $\kappa_{2-10keV}$ are mostly NLS1s which tend to have high mass accretion

rates in terms of Eddington, L_{bol}/L_{Edd} (Vasudevan & Fabian 2007, 2009; Paper-I; Jin et al. in prep., hereafter: Paper-III). However, when we directly cross-correlated Eddington ratio with the various Hβ EWs, no significant correlations were found (Figure C.2). Similar results were found when using Hα line instead of Hβ.

4.5.2 Does A Balmer Line Baldwin Effect Exist?

The existence of the Hβ Baldwin effect is controversial. It was reported by Zhu09 that the Hβ IC EW anti-correlates with the monochromatic luminosity at 5100Å (hereafter: L_{5100}), with Pearson rank correlation coefficient being -0.48 and at 99% level of smaller than 0, while the BC EW and the whole NC subtracted Hβ EW does not correlate with L_{5100}. They suggest this should be due to the flat geometry of ILR and spherical geometry of BLR, but they did not mention whether such anti-correlation could also be found in their Hα IC or not. To compare with Zhu09's results, we use our Balmer line fitting results to perform similar correlation test.

We first investigate the correlation between $L_{2-10keV}$ and L_{5100} which can be seen directly from the OXCSs in Figure 4.2. The $L_{2-10keV}$ vs. L_{5100} correlation is plotted in Figure 4.6 with Spearman's $\rho_s = 0.88$ and $d_s = 1.1 \times 10^{-16}$. The bisector regression lines are found to be:
(i) L_{5100} expressed by $L_{2-10keV}$:

$$Log(L_{5100}) \;=\; (0.92 \pm 0.05) Log(L_{2-10keV}) \;+\; (3.76 \pm 2.24) \qquad (4.5)$$

(ii) $L_{2-10keV}$ expressed by L_{5100}:

$$Log(L_{2-10keV}) \;=\; (1.08 \pm 0.06) Log(L_{5100}) \;-\; (4.07 \pm 2.66) \qquad (4.6)$$

Considering the strong correlations reported in previous paragraphs between Hβ IC, BC EWs and $L_{2-10keV}$, the correlations between Hβ IC, BC EW and L_{5100} were expected. However, we do not confirm any strong positive or negative correlations between Hβ IC, BC EWs and L_{5100}, though there is a large scatter in these cross-correlation plots, as shown in Figure C.2 and Table C.2. There is a weak anti-correlation between NC EW and L_{5100}. We therefore conclude that no evidence of

Baldwin effect is found in our study for Balmer IC and BC, but there may be such an effect for NC.

In fact, there are some important uncertainties in Balmer line decomposition and L_{5100}, which need to be considered before studying the Baldwin Effect of Balmer line components:

(1) The spectral quality of the Balmer line profile is crucial since currently decomposition of Balmer line totally depends on the line profile. This is more of a problem for Hβ since strong reddening can significantly reduce its S/N and distort its profile, so the Hβ decomposition for such reddened sources will be unreliable. But this is not a problem for our low reddening sample.

(2) Even with high quality Balmer line profiles, the line decomposition still has uncertainties. It is highly probable that the Balmer lines in Type 1 AGN must contain at least a NC and a BC. Assuming a Gaussian or Lorentzian profile for the BC, an additional IC is required during the line fitting procedure by the χ^2 statistics. However, the assumption of Gaussian or Lorentzian profile is not secure. In some cases, Balmer lines also exhibit a double-peak profile (Eracleous & Halpern 2003; Strateva et al. 2006; Bian et al. 2007) or an extended flat red wing (e.g. Mrk 0926, see Chapter 3), which causes problem for the three-component decomposition.

(3) The L_{5100} may not have just one contributor. In addition to the standard accretion disc emission in the optical, L_{5100} may also contain stellar emission from host galaxy. It was reported that an additional component, probably from the outer region of accretion disc where self-gravity dominates, might also contribute a significant fraction of L_{5100} (see Section 4.3.3).

Therefore, it is difficult to find the intrinsic correlations between Balmer line component EWs and L_{5100} due to the above uncertainties, and so the existence of Baldwin effect in any Balmer line component is still unclear.

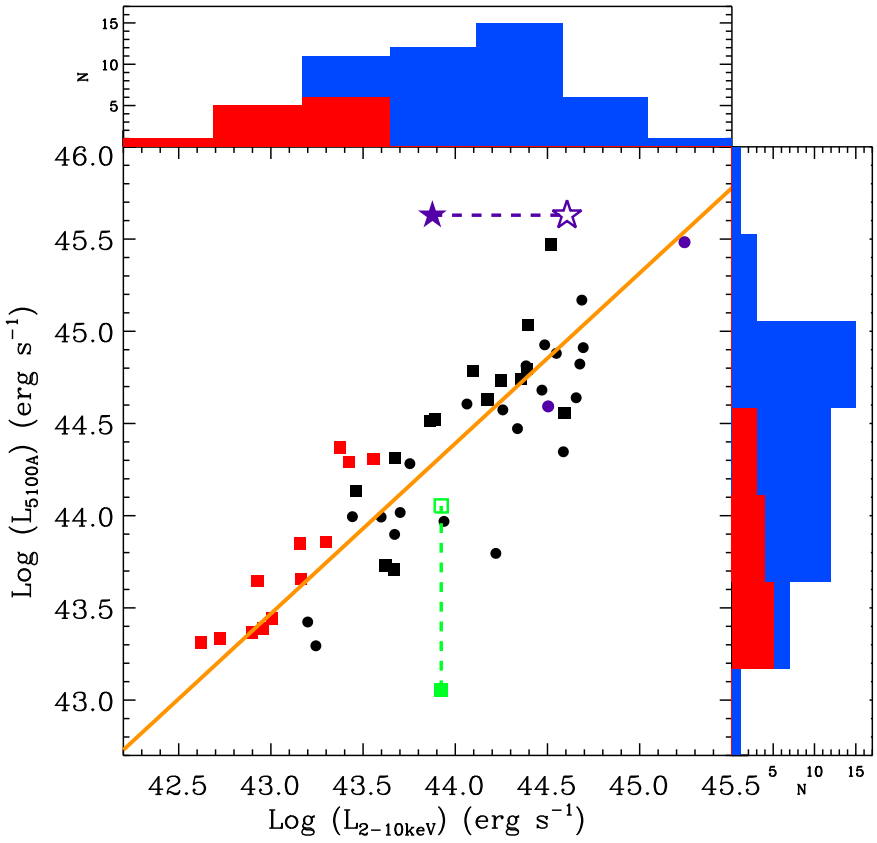

Figure 4.6: $L_{2-10keV}$ vs L_{5100}. Different symbols represent the same type of sources as in Figure 4.3. Solid orange line is the bisector regression line assuming $L_{2-10keV}$ is the independent variable. In each histogram, the red region highlights the distribution of the 12 NLS1s in our sample.

4.5.3 Balmer Line Component EW vs. FWHM and BH Mass

Another result we found for Balmer line EW is its correlation with Balmer line width and black hole mass. We cross-correlate the Hβ component EWs with the Hβ FWHM$_{IC+BC}$ and the 'best-fit' black hole mass (see the description of 'best-fit' black hole mass in Chapter 3). Figure 4.7 shows our results. It is clear that there are significant correlations between FWHM, black hole mass and the EWs of IC and BC. The best correlation is again found in BC. The results suggest that as the black hole mass increases (so does the Balmer line width), the emission from the ILR and BLR becomes more luminous relative to the continuum luminosity. We also note from Figure 4.7 that if you only consider BLS1s (circular points in Figure 4.7), then these is almost no correlation either between Hβ FWHM and component EWs or between black hole mass and Hβ component EWs. The broadest 12 BLS1s (blue circular symbols) exhibit larger scatter than the rest of the sources. However, the correlation between Hβ BC EW and black hole mass is very strong for NLS1s (red square symbols). There also seems to be a weak anti-correlation between black hole mass and Hβ NC EW. Similar results can be found replacing Hβ with Hα.

4.5.4 The Nonlinear Dependence of Balmer IC and BC Luminosities on L$_{2-10keV}$ and L$_{5100}$

As shown in previous sections that the relations between L$_{H\beta(IC+BC)}$, L$_{2-10keV}$ and L$_{5100}$ can be expressed as:

$$L_{H\beta(IC+BC)} \propto L_{2-10keV}^{1.18\pm0.04} \propto L_{5100}^{1.28\pm0.05} \tag{4.7}$$

Similar results can be found for Hα. Such non-linear dependences imply that if the continuum luminosity is the first-order factor, then there must be a second-order factor causing the EW of Balmer line IC and BC to depend on L$_{2-10keV}$. This second-order factor could be the covering factor of the ILR and BLR seen from the central ionizing continuum. AGNs with higher L$_{2-10keV}$ and L$_{5100}$ may also have larger ILR and BLR covering factors, making their Balmer IC and BC EWs larger

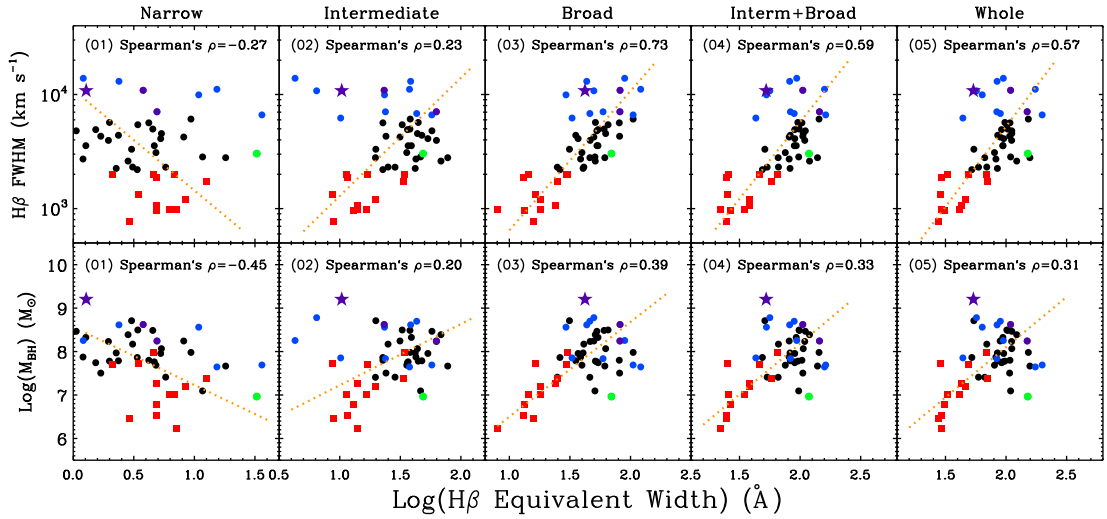

Figure 4.7: The correlations of Hβ component EW vs. Hβ IC+BC FWHM (first row) and best-fit black hole mass (second row). Different symbols represent the same type of sources as in Figure 4.3. Spearman's rank coefficients were calculated for the whole sample. The orange dotted line indicates the bisector regression line.

than in the AGNs of low $L_{2-10keV}$ and L_{5100}.

4.6 The Properties of ILR And BLR

4.6.1 Balmer Decrement

In addition to the luminosity and EW of Balmer line IC and BC, we can also investigate the intrinsic properties of ILR and BLR by studying the profiles of Hα and Hβ. The Balmer decrement is one of the main parameters to investigate. It was reported that the change in Balmer decrement may arise from changes in the physical conditions of the partially ionized line emitting regions (Kwan & Krolik 1979; Kwan & Krolik 1981; Mathews, Blumenthal & Grandi 1980 and Canfield & Puetter 1981). For example, a decrease of Balmer decrement may be due to an increase of electron density N_{e^-}, or an increase of ionization parameter Ξ (i.e. the ratio of the photon density to the gas density), or an increase of Lyα optical depth $\tau_{Ly\alpha}$ (Krolik & McKee 1978; Davidson & Netzer 1979; Shuder82). A high Balmer decrement can also be explained by a high dust abundance. This argument was used

Table 4.2: The mean Balmer Decrements of different line components for NLS1 population, BLS1 population and the whole sample.

Line Comp.	NLS1	BLS1	Whole Sample
NC	4.31±1.09	5.02±1.96	4.85±1.81
IC	3.50±0.61	5.24±2.33	4.83±2.18
BC	2.19±0.52	2.11±0.91	2.13±0.84
IC+BC (i.e. NC-sub)	2.73±0.30	3.12±0.79	3.03±0.73
Whole Line	2.94±0.30	3.16±0.72	3.11±0.65

as evidence in Zhu et al. (2009) to support the link between ILR and dusty torus. Therefore, Balmer decrements can be used as a clue to infer the physical conditions of the emission line region, and so it is important to obtain an accurate measurement of the decrement value. We calculated the Balmer decrement between Hα and Hβ for each line component. Figure 4.8 shows our results. The five histograms from top to bottom show Balmer decrement (Hα/Hβ) distributions of NC, IC, BC, IC+BC and the whole line. The mean Balmer decrements with 1 standard deviation are also listed in Table 4.2.

The results show that although the Balmer decrements of the whole Balmer line distribute around 3, the situation for different line components is quite different. The NLR has a big range of Balmer decrement values, with most probable value lying between 3.5-4.5, and a mean value of 4.85±1.81. Therefore, it may imply the presence of some dust in the NLR. The IC from ILR also has a big mean decrement of 4.83±2.18, while The BC from BLR has a small mean decrement of 2.13±0.84. However, the Balmer decrement of the IC+BC distributes around 3, which seems that the low decrement in BC and high decrement in IC are artificially due to our multi-Gaussian decomposition. To investigate this issue, we conduct the following study.

First, we think that the Balmer decrement we found for NLR is correct, based on the fact that this component has a narrow width, and is matched to the observed [OIII] profile. For BLS1s, the profile of the NC is easy to define as a small spike

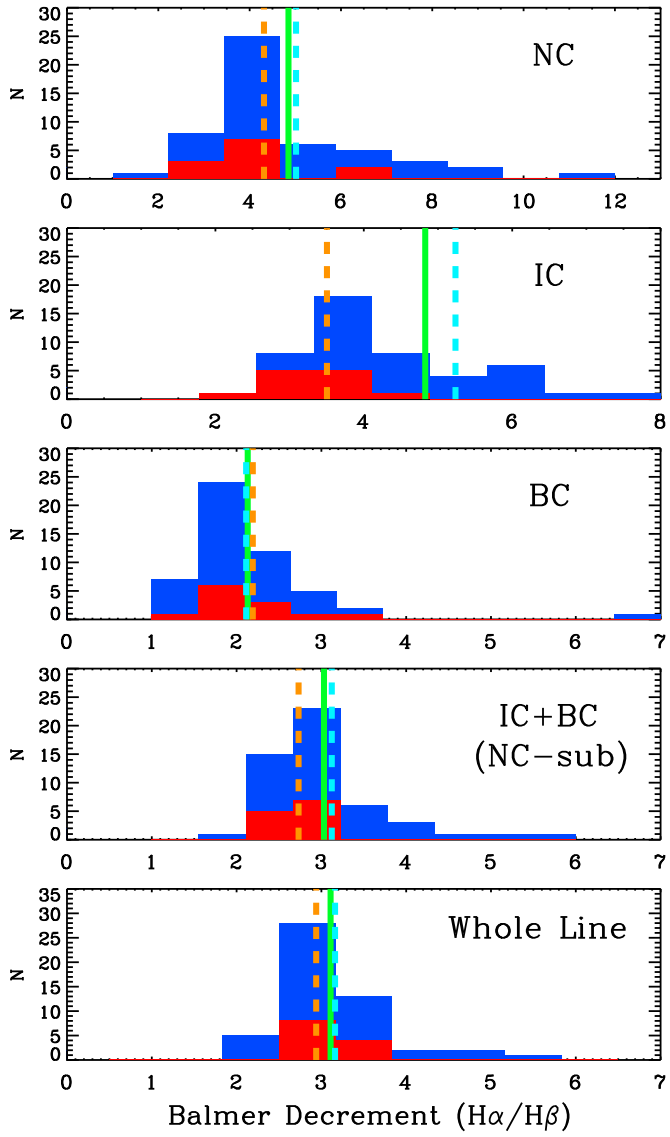

Figure 4.8: Balmer decrement distributions of different Balmer line components. In each panel the entire histogram shows the distribution of the whole sample, with green solid line indicating the mean decrement value. Red region highlights the distribution of the 12 NLS1s and the orange dashed line indicates their mean decrement value. The cyan dashed line shows the mean decrement value of the BLS1s. The mean decrements are also listed in Table 4.2.

superposed on the much broader line wings (see the Balmer line profiles in Chapter 3); while for NLS1s, untangling of the NC may introduce bigger uncertainties. However, since the NLR is far from AGN's centre and thus much less sensitive to the AGN's central properties, we should not expect big difference in NLR's properties between BLS1s and NLS1s, such as Balmer decrement. This is consistent with what we see in Figure 4.8, that the mean decrement values are similar between NLS1 and BLS1. This supports our assertion that the NC decomposition is reliable, and the derived high Balmer decrement in NLR is real for the majority of sample sources.

Second, we have reason to conclude that our decrement distributions for the IC and BC are also intrinsic to Balmer line regions. To prove this, we must first note that our combined Hβ and Hα line fitting has ensured very similar line decompositions for the two Balmer lines. To be specific, the IC and BC have the same central velocity shifts and FWHM in both Hβ and Hα, but the IC and BC can have very different relative fluxes (for more detailed description see Chapter 3). The observed decrement distribution differences between IC and BC reveal real changes in the decrement values across the emission line profile.

To see this directly, we divided each of the two Balmer lines into 10 segments in the velocity space from -5000 km s^{-1} to 5000 km s^{-1}, and calculated the decrement value in each segment. We performed this spectral analysis for each object in our sample. Then the average decrement value in each segment was calculated for sources with a reliable decrement measurement in that segment. This method is model-independent except for the subtraction of the local underlying continuum and removal of the [NII] λ6584,6550 doublets which uses the line fitting results from Chapter 3. The mean values for NLS1 subset and BLS1 subset in each segment are plotted in Figure 4.9. We see that the decrement peaks at the line centre and then decreases towards both sides. This suggests a low decrement in the broad wings, which is mainly modelled by the BC, and so supports the low decrement value found for the BC. For BLS1 subset, the decrement in the red side (indicating a positive velocity) is lower than in the blue side (negative velocity). It also appears in Figure 4.9 that NLS1s tend to have lower Balmer decrements than BLS1s in each segment. However, Figure 4.8 shows that the BC decrement distributions for

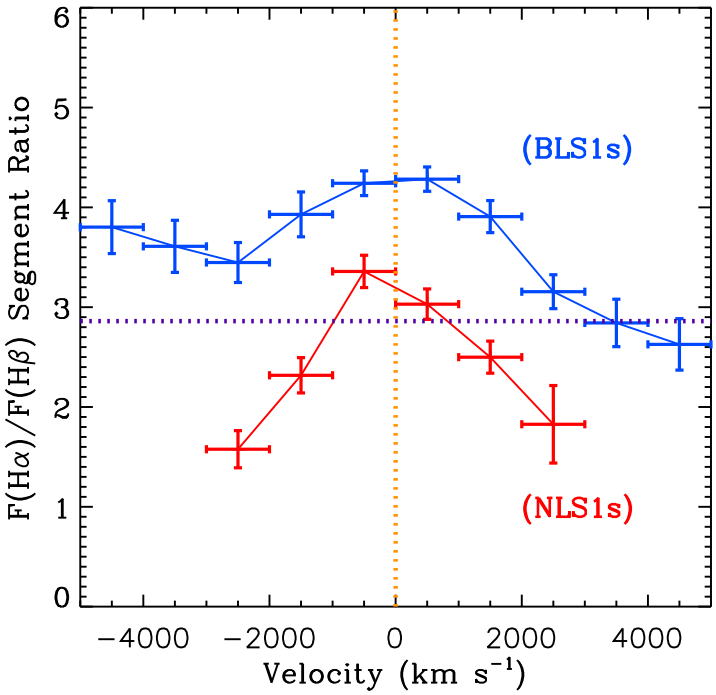

Figure 4.9: Balmer decrement changing across the Balmer line profile from $+\ 5000\ km\ s^{-1}$ to $-\ 5000\ km\ s^{-1}$. Each data point represents the average decrement value in that segment with the vertical bar showing the ± 1 standard error. Blue points show the results for the BLS1s; red points show the results for NLS1s. But due to the small line width of NLS1, the flux outside +/− 3000 km s^{-1} for NLS1s is of low S/N, thus only the mean decrement values in the central +/− 3000 km s^{-1} region were calculated and shown. The horizontal purple dotted line is a reference line at $F(\alpha)/F(\beta) = 3$.

the NLS1s and BLS1s are similar, although they are sometimes of low contrast to the continuum. Thus it suggests that the observed lower Balmer decrement of NLS1s is mainly due to the lower decrement value of the IC in NLS1s, which is also consistent with the IC decrement distributions in Figure 4.8. Therefore, we conclude that the observed differences in Balmer decrement distributions between different line components are mainly due to the complex decrement status across the Balmer line profile, with the broad wings having a lower decrement value and contributing mainly to the BC.

There is also support for our findings from previous work by Shuder (1982) (hereafter: Shuder82), who showed ratios of the Hα and Hβ lines for 18 Seyfert 1 AGNs. They reported that the average Hα/Hβ ratio ranged from 4.8 in the core to 2.2 in the wings, which is very similar to what we have found. They explained this as approaching the inner region of AGN, the velocity dispersion would increase, and so do the N_{e^-} and Ξ. This is also consistent with the systematic inflow velocity we found for the BC as we will discuss later. Zhu09 also reported that the Balmer decrement in the IC was 4.78 and in BC it was 2.54, although their line decomposition for Hα and Hβ were not linked as in our study. However, they explained this high decrement in IC as due to the higher dust reddening in the ILR, and so could support the link between ILR and dusty torus. Therefore, the Balmer decrement change can be explained by either dust abundance or line optical depth processes. Since it is likely that BLR is closer to the core region than the ILR, timing analysis such as detailed reverberation mapping of Balmer lines can be used to distinguish the radii between ILR and BLR. If the ILR is connected with BLR, then the changes of physical parameters such N_{e^-}, Ξ and $\tau_{Ly\alpha}$ may be the explanation of the higher Balmer decrement in ILR than in BLR. Alternatively, if the ILR is confirmed to be a distinct region from BLR and is close to the dusty torus, then dust reddening may be a more plausible answer. Finally, we find no correlation between the Balmer decrement and the bolometric luminosity, as was suspected by Shuder82.

4.6.2 Balmer Line Component Fraction

Zhu09 proposed an evolutionary scenario for the emission line region, which claimed that as the black hole mass and luminosity increased, ILR and BLR would become closer to each other and finally merge. In our sample 49 of the 51 sources require including two broad Gaussian components to fit their Balmer lines, as suggested by the Bayesian Information Criteria (BIC). The fraction of each Gaussian component is calculated for both Hα and Hβ, and cross-correlated against the black hole mass, bolometric luminosity and the component line width. The results are listed in Table 4.3. The dominant component in Hβ is IC, but in Hα it is BC. The NC

Table 4.3: The fraction of each Balmer line component and its correlations with black hole mass (M_{BH}), bolometric luminosity (L_{bol}) and the Hβ IC+BC FWHM. ρ_s and d_s are Spearman's rank coefficients as explained in Table C.2.

	frac	vs. M_{BH}		vs. L_{bol}		vs. FWHM	
Hα		ρ_s	d_s	ρ_s	d_s	ρ_s	d_s
NC	10±8	-0.6	-6	-0.2	-1	-0.7	-7
IC	53±11	0.1	-0	-0.1	-0	0.1	-0
BC	37±11	0.4	-2	0.3	-2	0.4	-2
IC+BC	90±8	0.6	-6	0.2	-1	0.7	-7
Hβ	%	ρ_s	d_s	ρ_s	d_s	ρ_s	d_s
NC	7±6	-0.6	-5	-0.2	-1	-0.5	-4
IC	38±12	-0.0	-0	0.0	-0	-0.4	-2
BC	55±14	0.4	-2	0.1	-0	0.5	-5
IC+BC	93±6	0.6	-5	0.2	-1	0.5	-4

fraction is ∼10% in both lines.

We confirm a weak anti-correlation between the IC fraction and IC FWHM of Hβ (Spearman's $\rho_s = -0.4$, $d_s = -2$), similar to that found by Zhu09. But no such anti-correlation was found in Hα. So we conclude that it is still not clear whether the anti-correlation between the IC fraction and IC FWHM is an intrinsic property of the ILR. We did not find any correlation in the IC or BC fractions vs. black hole mass or bolometric luminosity. Therefore, the scenario proposed by Zhu09 regarding the geometry of ILR and BLR can not be confirmed by the results of our study. Instead, our results suggest that the ILR may simply be an intermediate region between BLR and NLR regardless of the black hole mass and bolometric luminosity. As the black hole mass increases, the luminosities of NC, IC and BC in both Hα and Hβ all increase, but the luminosity of IC and BC increase more significantly than the NC, resulting in the significant anti-correlation between the black hole mass and NC fraction.

4.6.3 Balmer Line Shape

Dependences on Eddington ratio

The complex Balmer line profile can often be well modelled using contributions from the NLR, ILR and BLR, but it is also likely that local turbulence in the BLR may further broaden the Balmer line profile and be responsible for the presence of a very broad wing. Collin et al. (2006) (hereafter: Collin06) divided the reverberation-mapped sample into two populations: sources in the first population have narrower Hβ lines with more extended wings, along with higher Eddington ratios; while sources in the second population have broader but flat-topped Hβ lines, together with lower Eddington ratios. They found a weak anti-correlation between FWHM/σ_{line} and Eddington ratio where σ_{line} is the second moment of Hβ line (see the definition given in Peterson et al. 2004). This can be explained in terms of higher turbulence in the core region of high Eddington ratio AGNs. We can explore this result for our sample.

The second moment was measured from the NC subtracted Hβ line profile. It is clear from the definition that the flux farther from the line centre would have more contribution to the total second moment, thus σ_{line}/FWHM$_{IC+BC}$ can be a representative of the broad wing strength compared to the whole line profile, i.e. a higher value of σ_{line}/FWHM$_{IC+BC}$ corresponds to stronger broad wings. In our Balmer line profile fitting, the broad wing is mainly modelled by the BC, thus the FWHM ratio between BC and IC should have similar physical meaning as σ_{line}/FWHM$_{IC+BC}$. We correlate both σ_{line}/FWHM$_{IC+BC}$ and FWHM$_{BC}$/FWHM$_{IC}$ with Eddington ratio (L$_{bol}$/L$_{Edd}$).

Figure 4.10 shows our results. Orange points are the binned values over X-axis (Eddington ratio) with one standard error in the Y-axis (line width ratio). Note that the errors of Eddington ratio and line width ratio for each data points are dominated by systematical uncertainties in the spectral fitting which is difficult to quantify (see Chapter 3), thus the individual point error-bars are not provided. Such uncertainties are likely to increase the dispersion of the sample in this correlation plot. However, positive correlations have been confirmed in both panels with Spearman's rank test

being ρ_s=0.47, $d_s = 10^{-3}$ (upper panel) and ρ_s=0.35, $d_s = 10^{-2}$ (lower panel). Our results confirm the correlation between Hβ line profile and L_{bol}/L_{Edd}. Interestingly, we also find similar correlations when replacing L_{bol}/L_{Edd} with $\kappa_{2-10keV}$ and α_{ox}. For σ_{line}/FWHM$_{IC+BC}$, the Spearman's test has ρ_s=0.46 ($d_s = 10^{-3}$) for $\kappa_{2-10keV}$ and ρ_s=0.51 ($d_s = 10^{-4}$) for α_{ox}. For FWHM$_{BC}$/FWHM$_{IC}$, the Spearman's test has ρ_s=0.54 ($d_s = 10^{-4}$) for $\kappa_{2-10keV}$ and ρ_s=0.54 ($d_s = 10^{-4}$) for α_{ox}. But since the Eddington ratio is an intrinsic AGN parameter, and it also correlates with both $\kappa_{2-10keV}$ and α_{ox} (Vasudevan & Fabian 2007; Vasudevan & Fabian 2009; Lusso et al. 2010; Grupe et al. 2010), it may be the driving parameter that regulates the Balmer line shape, as was also suggested by Collin06. Therefore, the FWHM of the BC may depend primarily on black hole mass, but it may also be regulated by L_{bol}/L_{Edd}. This also explains the stronger correlation between black hole mass and the IC FWHM than between black hole mass and the BC FWHM.

Inflow Implied by the Balmer Line Profile

Another effect that may change the width of the whole Balmer line is the systematic velocity structure of the BLR as evinced by the general redshift of the BC and IC. It was found previously that both the IC and BC may be associated with inflows (e.g. Sulentic et al. 2000; Hu et al. 2008). Our analysis also shows that for the whole sample both IC and BC have a wide range of velocity shifts relative to the central component of [OIII] λ5007, but on average we find a statistically significant shifts of 100 km s^{-1} for the IC and 550 km s^{-1} for the BC. The inflow velocity we find for the BC is also consistent with the $\sim$400 km s^{-1} typical inflow velocity of the FeII emission features found by Hu et al. (2008), supporting their conclusion that FeII emitting region may trace some portions of the BLR exhibiting inflow. It seems probable that there is a velocity gradient within the BLR clouds, with the inner region of the BLR having a higher inflow speed, which gives rise to the extended red wing. However, the multi-Gaussian Balmer line decomposition method used in this study cannot resolve the detailed changes in the kinematics and physical conditions within BLR. Therefore, a much more detailed broad line spectral and timing study is required. The relative velocity shifts between the IC and BC determines the asymmetry of

the Balmer lines, but we did not find any significant correlation between the relative velocity shift and Eddington ratio. So the relative velocity shift cannot explain the correlation between $\sigma_{line}/FWHM_{IC+BC}$ and L_{bol}/L_{Edd}.

4.6.4 Summary of results for the ILR and BLR

To summarize the previous subsections, we propose the following characteristics of the ILR and BLR. First, these two regions are likely to be closely related, with the ILR being an extension of the BLR. We found no evidence to support the ILR being a distinct region from the BLR. The inner region of the BLR may produce the red wing of the Balmer profile, indicating an systematic inflow velocity. The physical parameters change continuously from the ILR into the BLR, probably with increasing electron density, ionization parameter and Lyα optical depth. The inflow velocity of the ILR gas is smaller than the BLR. The possibility that the ILR is associated with the dusty torus cannot be ruled out, and indeed its Balmer Decrement is higher than found for the BLR. Unfortunately we are unable to draw any firm conclusions about the geometry of the ILR or BLR. A second-order factor such as the covering factor of the ILR and BLR may cause the faster than linear dependence of the Balmer IC and BC luminosities on the continuum luminosity. Considering the tight correlations between the IC FWHM, BC FWHM and black hole mass, both the ILR and BLR should be gravitational bound and Virialized. For the BC from BLR, its FWHM may further be affected by the Eddington ratio through the process of local turbulence. Different inflow velocities of the ILR and BLR may also modify the shape of the Balmer lines.

4.7 Properties of Emission Line [OIII] λ5007

The NLR may extend hundreds of parsecs from the AGN's compact core. It is ionized by the central continuum in a bi-conical geometry with an axis defined by the plane of the dusty torus. Since the NLR extends far from the dusty torus, the intrinsic dust reddening is expected to be low. Therefore in both Type 1 and Type 2 AGNs, the luminosity of narrow optical emission lines from NLR can provide an

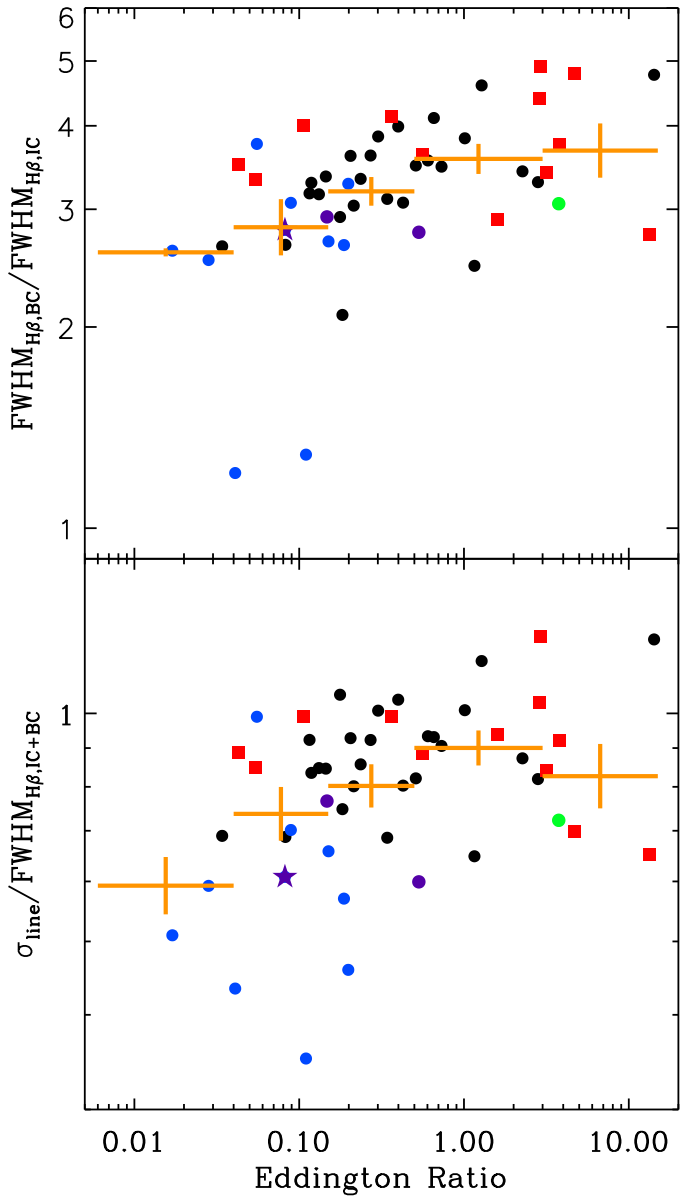

Figure 4.10: The Hβ line shape correlation with Eddington ratio. The upper panel uses FWHM$_{BC}$/FWHM$_{IC}$ to represent Hβ shape, while the lower panel uses σ_{line}/FWHM$_{IC+BC}$ instead. In each panel the various symbols represent the same type of sources as in Figure 4.3. The orange data points are the binned data for different Eddington ratio bins with 1 standard error on the Y-axis.

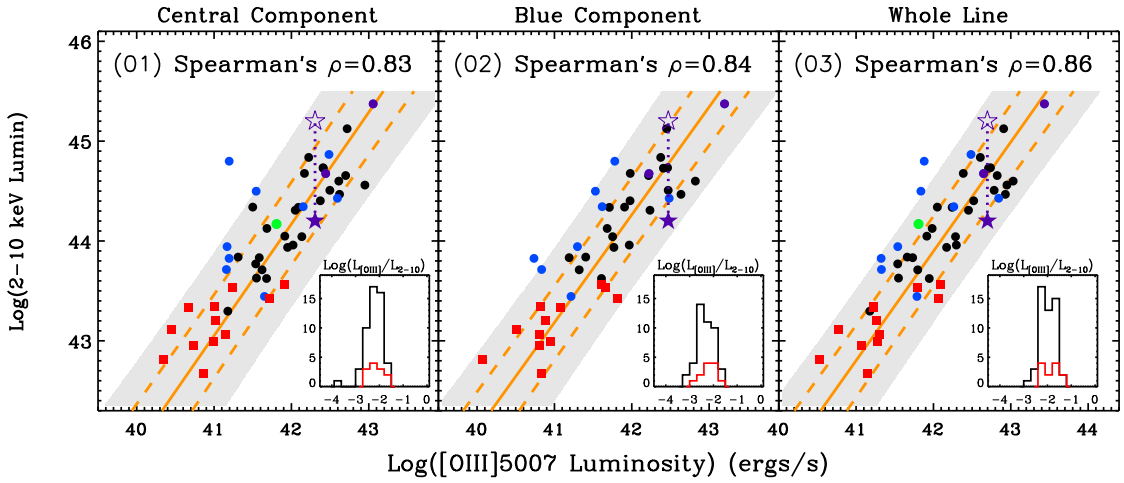

Figure 4.11: The luminosity correlations between components of [OIII] λ5007 and $L_{2-10keV}$. All symbols and lines have the same meanings as in Figure 4.3. In each panel, a histogram is shown for the $Log(L_{[OIII]\lambda5007}/L_{2-10keV})$ values of our sample, with the red histogram highlighting the NLS1s.

orientation-independent estimate of the central ionizing radiation (e.g. Mulchaey et al. 1994; Heckman 1995).

4.7.1 [OIII] λ5007 Component Luminosity vs. $L_{2-10keV}$

As one of the strongest narrow forbidden lines, [OIII] λ5007 is often employed as a proxy to estimate the intrinsic luminosity of type 2 AGN (e.g. Heckman et al. 2004; Brinchmann et al. 2004). This is not only because of its large EW, but also because it is free from serious contamination of other spectral features. Heckman et al. (2005) (hereafter: Heckman05) used [OIII] λ5007 as an optical selection criteria to study the difference between optical and X-ray selected AGN samples. They showed a tight correlation between [OIII] λ5007 luminosity and hard X-ray luminosity for Type 1 AGNs in both optical and X-ray selected samples. But the correlation is much weaker for an optically selected Type 2 AGN sample, which is mainly due to their X-ray weakness resulting from intrinsic photoelectric absorption. Since our Type 1 AGN sample has been carefully selected based on the high quality optical and X-ray spectra and the absence of severe absorption, our [OIII] λ5007 vs. rest frame 2-10 keV luminosity correlation should be indicative of intrinsic connections.

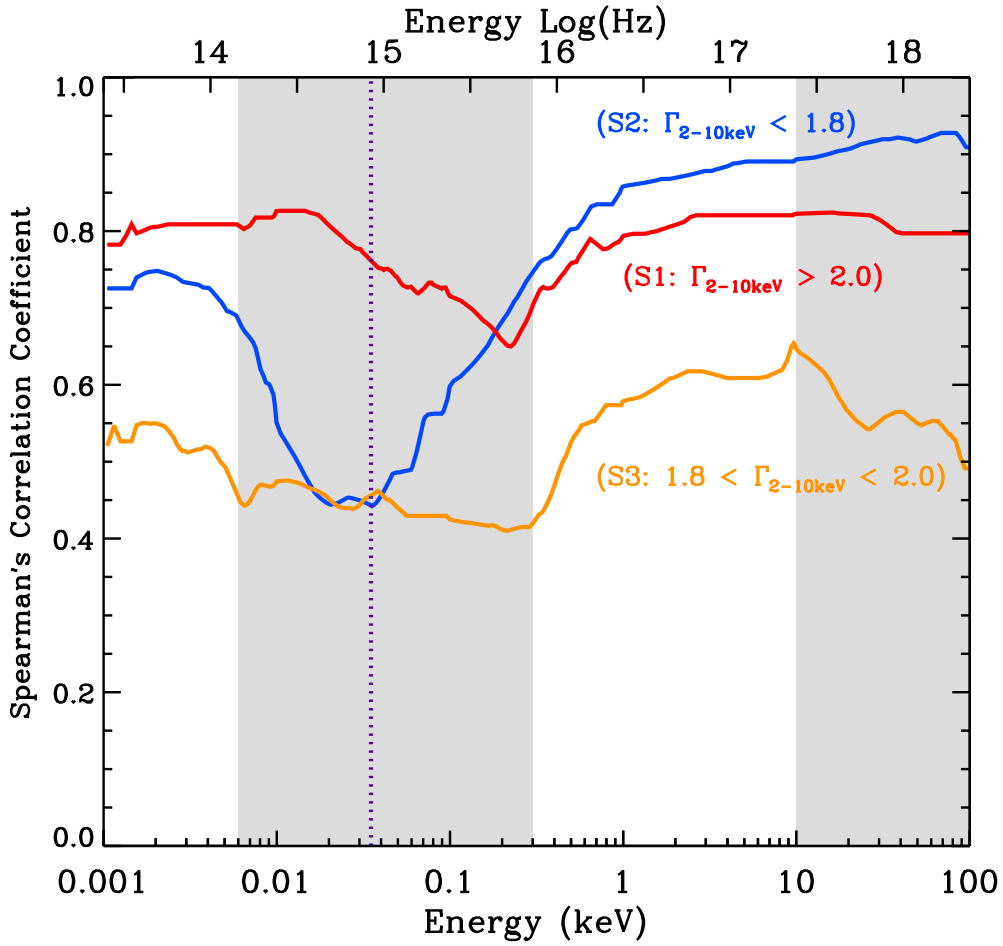

Figure 4.12: The 'SED to [OIII] λ5007 Correlation Spectra (SOCS)'. This is produced by calculating the Spearman's rank coefficient between the [OIII] λ5007 luminosity and the luminosity contained in each energy bin of broadband SED, thus the bigger coefficient indicates the better correlation in that energy bin. Lines of different color show the SOCS of different subsets as been labelled in the plot. The $\Gamma_{2-10keV} \geq 2.0$ subset (S1: red line) contains 16 AGNs; the $\Gamma_{2-10keV} \leq 1.8$ subset contains (S2: blue line) 18 AGNs; the $1.8 < \Gamma_{2-10keV} < 2.0$ subset (S3: orange line) contains 16 AGNs. Only spectral ranges below 0.006 keV and above 0.3 keV have observational data. The ionizing flux responsible for [OIII] λ5007 emission is above 0.035 keV as shown by the purple dotted line. The two shaded regions are where model extrapolation was used.

We also find that the line profile of [OIII] λ5007 consists of two components, a dominant central component and a blue-shifted component. Thus we analyze these two components separately.

Figure 4.11 shows our results. We find that both components in [OIII] λ5007 have very strong correlations with $L_{2-10keV}$, as confirmed by the Spearman rank test. The total [OIII] λ5007 line correlates slightly better with $L_{2-10keV}$ than the two separate components, suggesting that the central ionizing radiation ionizes both the outflowing [OIII] λ5007 region (which produces the blue component), and the spatially more extended [OIII] λ5007 region (which produces the central component). The solid orange line is the regression line assuming $L_{2-10keV}$ to be the independent variable. The two dashed orange line indicate the $\pm1\sigma$ region for new observation. The shaded region denotes the $\pm2\sigma$ region.

Again, we put our two excluded objects on the correlation. Mrk 110 (green circle) sits on the best fit line as neither its X-ray nor its [OIII] line luminosity are affected by the optical continuum variability. The X-ray weakness of PG 1004+130 (purple star) does not cause strong deviation in these correlation plots considering the dispersion. The other outlier is 1RXS J122019 (the blue circle point farthest from the shaded region) whose SDSS spectrum shows that this is one of the 'broadest' BLS1s, but its narrow lines (including [OIII] λ5007,4959 doublets) are much weaker relative to the broad lines than any other sources in our sample. It is possible that compared with other sources, 1RXS J122019 has a smaller NLR covering factor.

We also calculated $\mathrm{Log}(L_{[OIII]\lambda5007}/L_{2-10keV})$ using the luminosity of the whole [OIII] λ5007 line. We derived a mean value of -1.88±0.31 for the whole sample, and -1.78±0.30 for the 12 NLS1s. This is consistent with but slightly lower than -1.59±0.48 reported by Heckman05 based on their sample of 20 Seyfert 1s, which is likely due to the fact that their sample includes sources with strong X-ray absorption, e.g. they included Type 1 AGNs such as NGC 3227 and Mrk 766 whose X-ray spectra are absorbed by a warm absorber. Trouille & Barger (2010) (hereafter: TB10) reported -1.85±0.5 for their 19 BLAGN sources with $z < 0.5$ and -1.76±0.5 for their ∼100 BLAGNs with $z < 0.85$. Georgantopoulos & Akylas (2010) (hereafter: GA10) reported -1.98±0.39 for their 34 Seyfert 1s. These values are all consistent with

ours within 1σ. Our mean $\mathrm{Log}(\mathrm{L}_{[OIII]\lambda5007}/\mathrm{L}_{3-20keV})$ value is -2.00±0.33, which is consistent with -1.96∼2.14 reported by Heckman05. Note that compared with previous works, our sample is spectrally 'cleaner', i.e. more carefully selected for low reddening and absorption sources. Thus our mean $\mathrm{Log}(\mathrm{L}_{[OIII]\lambda5007}/\mathrm{L}_{2-10keV})$ and $\mathrm{Log}(\mathrm{L}_{[OIII]\lambda5007}/\mathrm{L}_{3-20keV})$ are better constrained as having smaller dispersions.

The correlations between [OIII] λ5007 and $\mathrm{L}_{2-10keV}$ can be used to estimate the intrinsic hard X-ray luminosity especially for nearby Type 2 AGNs and calculate the X-ray luminosity function (e.g. Sazonov & Revnitsev 2004; Shinozaki et al. 2006; Yencho et al. 2009; GA10). We present our OLS bisector regression lines below:
(i) $\mathrm{L}_{[OIII]\lambda5007}$) expressed by $L_{2-10keV}$ and $L_{3-20keV}$:

$$LogL_{[OIII]5007} = (1.06\pm0.05)LogL_{2-10} - (4.44\pm2.64) \tag{4.8}$$

$$LogL_{[OIII]5007} = (1.02\pm0.05)LogL_{3-20} - (2.93\pm2.65) \tag{4.9}$$

(ii) $L_{2-10keV}$ and $L_{3-20keV}$ expressed by $\mathrm{L}_{[OIII]\lambda5007}$):

$$LogL_{2-10} = (0.94\pm0.05)LogL_{[OIII]5007} + (4.20\pm2.26) \tag{4.10}$$

$$LogL_{3-20} = (0.98\pm0.05)LogL_{[OIII]5007} + (2.87\pm2.43) \tag{4.11}$$

Note that since the luminosity measurements of both [OIII] λ5007 and $\mathrm{L}_{2-10keV}$ may contain uncertainties from the intrinsic absorptions and variability, the OLS bisector regression method is more appropriate than the standard OLS method used in previous works. Combining previous results from Heckman05, TB10 and GA10 with ours, we can conclude that such tight luminosity correlations between hard X-ray and [OIII] appear valid for at least $z < 0.85$, $\mathrm{Log}(\mathrm{L}[OIII]\lambda5007)$=38−44 and $\mathrm{Log}(\mathrm{L}_{2-10keV})$=40−46.

4.7.2 The SED to [OIII] λ5007 Correlation Spectra (SOCS)

The ionizing energy for [OIII] λ5007 is 0.035 keV, thus all photons above this energy can in principle produce [OIII] λ5007 emission. As another application of CST, we cross-correlate [OIII] λ5007 luminosity with the luminosity contained in the continuum SED in each energy bin from optical to X-ray, and produce the 'SED to

[OIII] λ5007 correlation spectrum (SOCS)'. Our broadband SED model consists of three components: the disc, soft X-ray Comptonisation and hard X-ray Comptonisation. The soft and hard Comptonisation components can both contain a significant amount of energy above 0.035 keV, the disc emission may also extend above this energy when the black hole mass is small and mass accretion rate is high (Done et al. 2011). We divided our sample into three subsets: $\Gamma_{2-10keV} \geq 2.0$ (S1: 16 AGNs), $\Gamma_{2-10keV} \leq 1.8$ (S2: 18 AGNs) and $1.8 < \Gamma_{2-10keV} < 2.0$ (S3: 16 AGNs). PG 1004+130 is excluded due to its unique SED shape but Mrk 110 is now included since the previous section shows that its [OIII] and hard X-ray luminosity are not distorted by the optical continuum variability. S1 includes all 12 NLS1s, while S3 contains the broadest BLS1s. A SOCS was calculated for each of the three subsets.

Figure 4.12 shows the resultant SOCSs. Note: in this study only spectral ranges below 0.006 keV and above 0.3 keV have observational data. Overall, [OIII] λ5007 correlates best with hard X-rays above 2 keV. It is also well-correlated with the optical emission. However, the correlation in the UV/X-ray region is poor, which may be caused by the spectral modification due to Galactic and intrinsic extinction. This indicates that the hard X-ray ionizing flux also has a strong link with the optical flux which is presumably dominated by accretion disc emission.

Regarding the SOCS of different subsets, we find that S1 has the strongest correlations in the optical/UV band, which implies that our broadband SED fitting may be more reliable for sources in S1 whose soft X-ray excess is more likely to be a real extra component (Middleton et al. 2009; Jin et al. 2009; Middleton, Uttley & Done). The S2 group shows highly significant correlations in the hard X-ray band, which may imply that the hard X-ray power law tail of $\Gamma_{2-10keV} \leq 1.8$ is an intrinsic separate component rather than being an artifact caused by absorption or reflection (Done et al. 2011). Therefore, the S1 and S2 groups may indeed represent two distinct types of AGNs (e.g. NLS1s and BLS1s). We also find that the correlation for S3 in optical and X-ray bandpasses is much less significant than for either S1 or S2. This may indicate that other spectral factors such as absorption and reflection, may be more important for the sources in S3, in which case our three-component SED model is too simple to recover their intrinsic SEDs.

4.7.3 Outflow of NLR Implied by [OIII] λ5007 Profile

The two components in the profile of [OIII] λ5007 have been reported previously. Bian, Yuan & Zhao (2005) indicated that these two components are related to two physically distinct regions. Komossa et al. (2008) also reported blue outliers in [OIII] λ5007 whose blue-shift velocity is up to 500$\sim$1000 km s^{-1}, favoring a decelerating wind NLR scenario. These results are all confirmed by our study. We find that for our sample, the velocity shift of the blue component in [OIII] λ5007 relative to the central component ranges from -610 to -0 km s^{-1}, and the mean velocity is -130^{+80}_{-230} $km\ s^{-1}$. We also find a strong correlation between the FWHM and velocity shift of the blue component, as Spearman rank test gives: ρ_s=0.52 and $d_s = 10^{-4}$. The larger FWHM of the blue component implies a smaller distance from AGN's core region, so this correlation suggests that the outflow velocity of inner NLR emitting [OIII] λ5007 is higher than that in the outer NLR. An outflow speed decreasing as it flows away from the centre is a signature of decelerating wind.

4.8 Summary and Conclusions

In this chapter, we made use of the detailed spectral fitting of an AGN sample reported in Chapter 3, to study their optical spectral properties using their hard X-ray luminosity as a diagnostic. Our study focused on the Hβ, Hα and [OIII] λ5007 emission lines and the underlying continuum. The main results are summarized below.

• The OXCSs have been constructed for different subsets of AGNs using our new spectral analyzing technique called CST. The OXCSs reveal many correlation features with $L_{2-10keV}$ across the entire optical spectrum. Some were known previously, others are new. For example, the entire optical underlying continuum strongly correlates with $L_{2-10keV}$. [NeIII] $\lambda\lambda$3869/3967, [OI] $\lambda\lambda$6300/6364, [OII] $\lambda\lambda$3726/3729, [OIII] $\lambda\lambda$4959/5007 and the IC and BC in Balmer lines all well correlate with $L_{2-10keV}$ especially for BLS1s. However, stellar absorption lines, FeII and the NC in the Balmer lines have much weaker or no correlation with $L_{2-10keV}$. We

find some evidence for differences in the OXCSs between NLS1s and BLS1s.

• A cross-correlation between luminosities of Hβ and Hα line components and the broadband SED components was performed. The results suggest that among the three SED components, the hard X-ray power law component correlates the best with Balmer line luminosity, and the correlations strengthen from the NC, IC to BC of Balmer lines. This supports the view that the BC has the closest link with AGN's central UV/X-ray continuum emission.

• Significant correlations were found between the Hβ component EWs and $L_{2-10keV}$, $\kappa^{-1}_{2-10keV}$, Hβ FWHM and black hole mass, although these correlations become weaker for the BLS1 subset alone. By cross-correlating Balmer line component EWs with L_{5100}, no evidence for the 'Baldwin Effect' was found for the IC and BC, but such effect is weakly detected for the NC.

• Our results suggest a faster than linear dependence of Balmer line IC and BC luminosities on the underlying continuum (e.g. $L_{2-10keV}$ and L_{5100}; Equation 4.7), implying the presence of a second-order factor. We propose that this second-order effect could be the covering factor of the BLR and ILR seen by the central UV/X-ray continuum, so that higher $L_{2-10keV}$ and L_{5100} sources may also have larger ILR and BLR covering factors.

• We carried out detailed Balmer line shape studies in order to reveal the nature of ILR and BLR. We found that the Balmer Decrement value, defined by Hα/Hβ, peaks at the line centre and decreases towards both sides, with the red wing having a lower decrement than the blue wing for BLS1 subset. This was also consistent with IC's average decrement value of 4.83±2.18 compared to the BC's 2.13±0.84. These results, along with the systematic inflow speed we found in the BC (mean velocity: 550 km s^{-1}), support the scenario that the inner region of BLR forms the red wing while the outer edge links with the ILR. Compared to the ILR, the BLR may have higher inflow speed, higher electron density, larger ionization parameter or higher Lyα optical depth, A weak correlation between the shape of Balmer line profile and Eddington ratio was confirmed. A higher Eddington ratio corresponds to a more extended wing relative to the overall Balmer line structure. This implies that the velocity width of the Balmer line is not simply determined by the black hole mass,

but also affected by local turbulence whose strength depends on the Eddington ratio. The higher Balmer decrement in ILR than in BLR could also be explained of the ILR has a higher dust abundance, but we found no other evidence to support ILR's link with the dusty torus. A weak anti-correlation between the EW of Balmer line NC and black hole mass was found.

• In our study of [OIII] λ5007, we confirmed its tight correlation with $L_{2-10keV}$ and $L_{3-20keV}$. We found that the blue and central components of [OIII] λ5007 should be added together to provide the best correlation with hard X-rays. Using our best-fit broadband SEDs from Chapter 3, we produced the SOCSs for different sample subsets. The SOCSs show strong correlations between [OIII] λ5007 luminosity and the continuum luminosities in either optical or hard X-ray bandpass. Subset S1 and S2 both have highly significant correlations in the hard X-ray band, which implies that the shape of hard X-ray power law tail in these two subsets are intrinsic in spite of their totally different photon indices. But the SED of moderate $\Gamma_{2-10keV}$ sources in S3 may be more complex.

• The mean outflow velocity of the blue component in [OIII] λ5007 is $-130^{+80}_{-230}\ km\ s^{-1}$. The strong correlation between the FWHM and velocity shift of the blue component in [OIII] λ5007 suggests that the outflow speed of [OIII] λ5007 clouds decreases from the central region outwards, suggesting a decelerating wind.

• In this chapter, we present well constrained equations which can be used to convert between the luminosity of Balmer line broad component and the intrinsic $L_{2-10keV}$ (Equation 4.1∼4.4), between the intrinsic L_{5100} and $L_{2-10keV}$ (Equation 4.5∼4.6), and between the [OIII] λ5007 luminosity and the intrinsic $L_{2-10keV}$ and $L_{3-20keV}$ (Equation 4.8∼4.11). We suggest that these equations be used for inferring the intrinsic optical and X-ray luminosities of obscured sources such as BAL quasars or Type 2 AGNs, and for calculating the X-ray luminosity function. Considering the limited redshift range of and size of our sample, similar studies should be carried out on larger samples to test the robustness and evolution of these equations at high redshift, which requires high quality infrared spectra. In the next chapter, we are going to discuss the broadband SED properties of the same sample.

Chapter 5

Type 1 AGN Study - III. Broadband SED Properties

5.1 Introduction

The number of AGN with both high quality optical/UV and X-ray spectra is relatively small, thus much effort in the literature is devoted to searching for correlations among key SED parameters, especially those parameters capable of influencing the properties of broadband SED, such as black hole mass (M_{BH}), Eddington ratio (λ_{Edd}), bolometric luminosity (L_{bol}), 2-10 keV luminosity ($L_{2-10keV}$), 2-10 keV photon index ($\Gamma_{2-10keV}$), Hβ FWHM, the optical-to-X-ray spectral index (α_{ox}, defined as Equation 5.1, e.g. Lusso et al. 2010, hereafter: Lusso10), 2-10 keV bolometric correction ($\kappa_{2-10keV}$, defined as $L_{bol}/L_{2-10keV}$, e.g. Vasudevan & Fabian 2007, 2009 hereafter: VF07, VF09) and 5100Å luminosity scaling factor (κ_{5100}, defined as L_{bol}/L_{5100} where L_{5100} is the monochromatic luminosity at 5100Å, Kaspi et al. 2000).

Then for those many AGNs lacking sufficient spectral information, these correlations can be used to predict the SEDs that cannot be defined from direct observation. Indeed, many such parameter correlations have been proposed. For example, VF07 reported a strong correlation between $\kappa_{2-10keV}$ and λ_{Edd} (VF07; VF09; Lusso10). Correlations were also found between Hβ FWHM vs. $\Gamma_{2-10keV}$ (e.g. Leighly 1999; Reeves & Turner 2000; Shemmer et al. 2006, hereafter: Shemmer06; Shemmer et al. 2008, hereafter: Shemmer08; Zhou & Zhang 2010, hereafter: Zhou10a), λ_{Edd}

vs. $\Gamma_{2-10keV}$ (e.g. Lu & Yu 1999; Porquet et al. 2004; Wang, Watarai & Mineshige 2004; Bian 2005; Shemmer06; Shemmer08) and Hβ FWHM vs. λ_{Edd} (e.g. Grupe10; Chapter 3). The correlation between L_{2500} and L_{2keV} is another important result, which led to further correlation studies related to α_{ox}, L_{2500}, L_{2keV} and redshift (e.g. Green et al. 2009, see references given in Table 5.2). In table D.1, we list some of the principal parameters, and list the relevant papers discussing the correlations. Later in this chapter we will discuss some other additional correlations between e.g. M_{BH} vs. $\Gamma_{2-10keV}$ and M_{BH} vs. $\kappa_{2-10keV}$, in the context that changes in these parameters are caused by changes in the fundamental physical processes.

However, due to the difficulty in obtaining and analyzing both optical/UV and X-ray spectra for a large sample, these parameter correlations are reported separately and based on different samples, rather than being studied systematically for a single well-defined sample. Furthermore, most of the previous samples were not selected based on their spectral properties, so effects such as reddening will introduce biases into the cross-correlations. The lack of a self-consistent physically motivated broadband model, has also been a problem when performing a more detailed SED study.

In Chapter 3 we defined a sample of 51 Type 1 AGNs with both optical/UV and X-ray spectra which are of high quality, and without evidence of complex spectral absorption features e.g. a warm absorber. Based on this bright and unobscured Type 1 AGN sample, we applied our latest optical and broadband SED model to perform the spectral fitting, and so matched the optical spectrum and produced a broadband SED for each AGN in the sample. This is so far the most detailed spectral analysis for a medium sized sample of AGNs, with such well defined high quality spectra. In Chapter 4 we studied the profile of various emission lines, and the luminosity correlations between hard X-ray and various optical emission features, based on the same sample and the spectral fitting results in Chapter 3. This chapter is also based on Chapter 3, but focuses on the properties of the broadband SED and all the SED parameters mentioned above. We will study this issue by first investigating the numerous correlations previously reported among these SED parameters. Then a set of mean SEDs based on these parameters are constructed and studied in detail.

Table 5.1: The mean parameter values with one standard deviation for our sample, together with some recently published samples. Lusso10: Lusso et al. (2010); Grupe10: Grupe et al. (2010); Zhou10a: Zhou & Zhang (2010); VF07,09: Vasudevan & Fabian (2007, 2009). m: the Eddington ratios were calculated using the luminosity dependent 2-10 keV bolometric correction in Marconi et al. (2004); r: the black hole masses are from the reverberation mapping study in Peterson et al. (2004).

Sample	Redshift	$\Gamma_{2-10keV}$	$\kappa_{2-10keV}$	κ_{5100}	λ_{Edd}	FWHM$_{H\beta}$ $km\ s^{-1}$	M$_{BH}$ $log(M_\odot)$	α_{ox}	L$_{bol}$ $log(erg\ s^{-1})$
This Work	$0.137^{+0.158}_{-0.073}$	1.91±0.26	38^{+58}_{-23}	15^{+14}_{-7}	$0.27^{+0.61}_{-0.19}$	3560^{+3880}_{-1860}	7.93±0.52	1.35±0.14	45.47±0.57
Lusso10	$1.440^{+1.020}_{-0.597}$	—	27^{+28}_{-14}	—	—	—	—	1.40±0.16	45.54±0.57
Grupe10	0.112±0.077	—	—	—	1.87±3.26	—	—	1.42±0.17	—
Zhou10a	$0.050^{+0.103}_{-0.034}$	1.97±0.29	—	—	$^{m}0.24^{+0.76}_{-0.18}$	2600^{+2500}_{-1280}	—	—	—
VF09	$0.033^{+0.074}_{-0.023}$	1.85±0.32	28^{+74}_{-20}	—	0.18±0.16	—	^{r}7.93±0.66	1.39±0.24	44.89±1.00
VF07	$0.064^{+0.147}_{-0.044}$	—	26^{+39}_{-16}	—	$0.15^{+0.76}_{-0.13}$	—	7.89±0.82	—	45.20±1.01

In the broader context of accretion processes there are three accretion states in Galactic black hole binary (BHB) systems, namely the 'hard' state (low/hard state), 'thermal state' (high/soft state) and 'very high' state (SPL-steep power law state), with quasi periodic oscillation (QPO) being most common in the 'very high' state (Remillard & McClintock 2006). In this scenario the Eddington ratio is the primary indicator of these accretion states, and the change from high to low Eddington ratio corresponds to transitions through the 'very high', 'high/soft' and 'low/hard' state. It has been proposed that the accretion processes in AGNs are scaled up counterparts those in BHBs (Done & Gierliński 2005; McHardy et al. 2006; Gierliński et al. 2008; Middleton et al. 2009; Jin et al. 2009). Therefore the Eddington ratio may also be a good indicator an AGN's accretion state, and so determine the shape of its SED. However, a BHB system undergoes an outburst over tens of days, and exhibits clear spectral state changes (Remillard & McClintock 2006; Done, Gierliński & Kubota 2007). However, a similar change in the accretion state of an AGN will take very much longer. So we observe a snapshot SED for an AGN in a particular accretion state, by constructing a set of mean SEDs, based on sources with similar values of key parameters. In this chapter we suggest that these may represent similar accretion states to those often seen in a BHB, and explain why there are many strong correlations among the various SED parameters.

This chapter is organized as follows. Section 2 gives a brief description of the main characteristics of the sample, and the method used for fitting the broadband SED. Further details of this are presented in Chapter 3. In Section 3 we examine the parameter correlations across five parameter groups. Some significant new correlations are proposed. In Section 4 we perform a systematic study of all correlations among the 9 selected key SED parameters, and build a cross-correlation matrix. A principal component analysis technique is used on this correlation matrix in order to derive the eigenvectors. In Section 5 various mean SEDs are constructed, based on the mean value ranges of the 9 parameters. In Section 6 we investigate further the reliability of these correlations, including the effect of correction for radiation pressure correction. In Section 7 we summarize our results, and propose topics for further study. Following previous chapters, a flat universe model with a Hubble con-

stant of $H_0 = 72$ km s^{-1} Mpc^{-1}, $\Omega_M = 0.27$ and $\Omega_\Lambda = 0.73$ is adopted. The results presented in this chapter has been submitted to MNRAS as Jin et al. (2012b). The content related to the mean SEDs at different Eddington ratios has been published separately in Done et al. (2011).

5.2 Properties of the Sample and Broadband SED Modeling

The AGN sample used in this chapter is from the cross-correlation of SDSS DR7 and XMM-Newton catalogs. The detailed sample selection criteria and sample properties can be found in Chapter 3. The main properties of the sample include the following: (i) the AGN are nearby Type 1s with redshift <0.4. This limit is imposed so as to include the Hα emission line. The redshift distribution is very similar to the sample of VF07 (see Chapter 4). (ii) both high quality SDSS and XMM-Newton spectra are available for every source. (iii) all sources are unobscured. No significant optical reddening, X-ray absorption or evidence of a warm absorber is seen in the spectra, except for PG 1004+130 whose weak and featureless X-ray emission is still under debate (Miller et al. 2006). This criterion means that the observed spectra are very likely directly related to emission from the bare central core. This reduces dispersions caused by non-intrinsic effects in the correlations. (iv) three sources in our sample are radio-loud i.e. PG 1004+130, RBS 0875 and PG 1512+370, and so the vast majority of the sample are radio-quiet. (v) the Hβ FWHM of the sample ranges from 600 km s^{-1} to 13000 km s^{-1}, including 12 NLS1s.

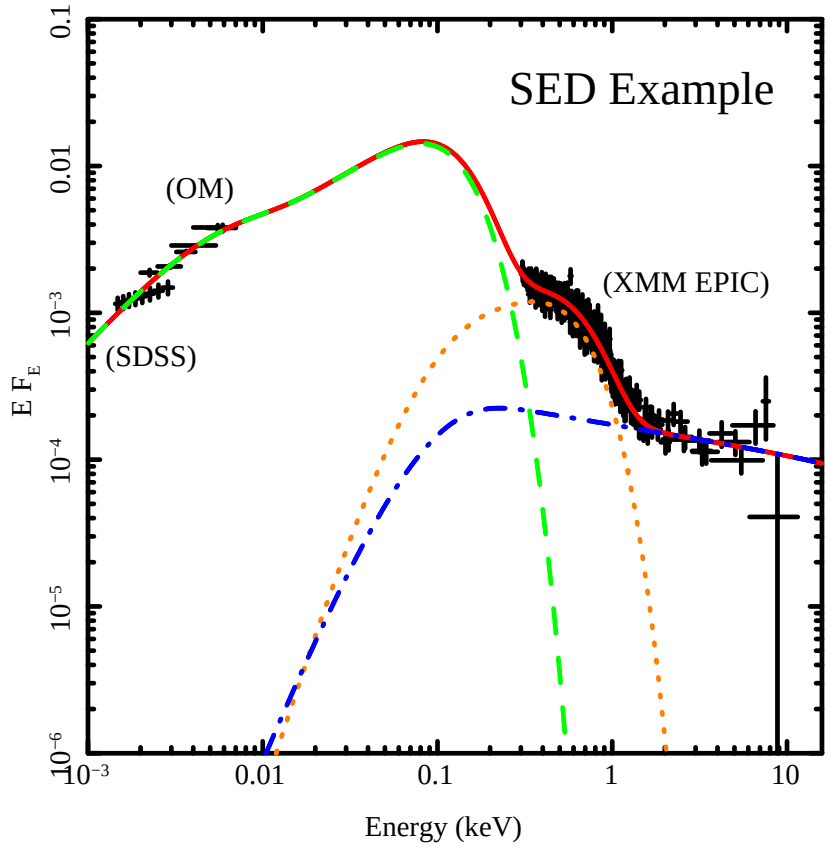

Figure 5.1: An example of the broadband SED fitting using *optxagnf* model in `Xspec` v12 which includes the effect of a colour correction. The data is taken from SDSS and XMM-Newton observations of RBS 769. The solid red line shows the total model; the dashed green line shows the colour corrected and truncated accretion disc emission; the dotted orange line shows the low temperature optically thick Comptonisation; the dot-dash blue line shows the high temperature optically thin Comptonisation. The reduced χ^2 is 1.16 for this spectral fitting.

Table 5.2: Comparison of regression line coefficients for L_{2keV}, L_{2500}, α_{ox} and redshift Correlations. Lusso10: Lusso et al. (2010); Grupe10: Grupe et al. (2010); Green09: Green et al. (2009); Just07: Just et al. (2007); Steffen06: Steffen et al. (2006); Strateva05: Strateva et al. (2005); Hasinger05: Hasinger (2005). *opt*: optically selected sample. *xray*: X-ray selected sample. [1]linear regression results using L_{2keV} and L_{2500} from the reconstructed broadband SED corrected for both intrinsic and Galactic reddening/extinction. [2]linear regression when L_{2keV} and L_{2500} were not corrected for the best-fit intrinsic reddening/extinction, but corrected for the Galactic value. [a]for the SDSS main sample + high-z sample + Sy 1 Sample (see Strateva05). [z]only for the zBox subsample described in Green09. [*]measured directly from the regression line in Fig.5(b) of Hasinger05.

	L_{2keV} vs. L_{2500}		α_{ox} vs. L_{2500}		α_{ox} vs. L_{2keV}		α_{ox} vs. Redshift	
Sample	β_1^{bi}	ξ_1^{bi}	β_2^{em}	ξ_2^{em}	β_3^{em}	ξ_3^{em}	β_4^{em}	ξ_4^{em}
[1]This Work	0.95±0.06	-2.04±1.77	0.07±0.02	-0.61±0.60	-0.03±0.03	2.17±0.76	0.16±0.13	1.31±0.03
[2]This Work-R_{int}	0.91±0.05	-0.69±1.68	0.08±0.02	-0.92±0.57	-0.01±0.03	1.55±0.76	0.23±0.13	1.26±0.03
Lusso10^{xray}	0.76±0.02	3.51±0.64	0.15±0.01	-3.18±0.22	0.02±0.01	0.86±0.34	0.06±0.01	1.26±0.02
Grupe10^{opt}	—	—	0.11±0.01	-1.18±0.31	—	—	—	—
Green09^{opt}	1.12±0.02	-7.59±0.64	0.06±0.01	-0.32±0.26	0.10±0.01	1.38±0.21	-0.001±0.14^{z}	—
Just07^{opt}	0.71±0.01	4.88±0.63	0.14±0.01	-2.71±0.21	0.09±0.01	-0.90±0.36	—	—
Steffen06^{opt}	0.72±0.01	4.53±0.69	0.14±0.01	-2.64±0.24	0.08±0.02	-4.1±0.39	0.08±0.01	1.40±0.01
Strateva05^{opt}	0.65±0.02^{a}	6.73±0.64^{a}	0.14±0.01^{a}	-2.62±0.25^{a}	—	—	non-linear	non-linear
Hasinger05^{xray}	1.0*	-3.7*	—	—	—	—	—	—

Based on the high quality spectra, Chapter 3 conducted detailed spectral analysis for each source in the sample. In the optical spectral fitting, a complete model with multiple components were used, including the underlying continuum approximated by a power law, the Balmer continuum, the FeII 'false' continuum and all strong emission lines. The Hα and Hβ lines were fitted using three Gaussian components, i.e. a narrow component, an intermediate component and a broad component. The broadband SED model used in Chapter 3 (hereafter Model-A) consists of the following three continuum components: 1. emission from a modified standard accretion disc, whose energy within the corona radius is completely reprocessed into the other two high energy Comptonisation components; 2. emission from the low temperature, optically thick Comptonisation, which mainly accounts for the soft X-ray excess; 3. emission from the high temperature, optically thin Comptonisation which gives the power law shape of the hard X-ray spectrum above 2 keV. Both Galactic extinction and the small amount of intrinsic reddening/extinction are included in the model.

However, in Chapter 3 we did not consider the effect of a colour temperature correction in the accretion disc model (e.g. Ross, Fabian & Mineshige 1992; Davis & Hubeny 2006). This effect is due to the fact that higher temperature photons emerge from regions deeper in the accretion disc. The absorption opacity decreases significantly as the black hole mass increases ($\kappa_{abs} \propto M^{-1/8}$, Done et al. 2011), and so electron scattering opacity is much more important in AGNs than in BHBs. However, the electron scattering is only important in regions of the disc where $T > 3\times10^4$ K, so that sufficient hydrogen atoms are ionized. The maximum effective temperature of the accretion disc is $kT \sim 10(\dot{m}/M_8)^{1/4}$ eV (where $\dot{m} = L_{bol}/L_{Edd}$, $M_8 = M/10^8$ M$_\odot$), so the electron scattering opacity can only dominate in AGNs with both a low mass black hole and a high mass accretion rate, such as the NLS1s (e.g. Boller, Brandt & Fink 1996). A typical colour temperature correction of 2.6 is predicted for an AGN with M$_{BH}$=10^{6}M$_\odot$, λ_{Edd}=1.0 (Davis et al. 2006). This effect combines with an already hot disc due to the low black hole mass, resulting in a disc spectrum that extends significantly into the soft X-ray range.

In this chapter, we re-fit all the broadband SEDs in our sample using the (*optxagnf* in `Xspec` v12) model which applies a colour temperature correction for the

Comptonised accretion disc model (hereafter Model-B). Figure 5.1 shows an example of the broadband SED fitting to the multi-waveband spectra of RBS 769. A detailed description of Model-B in comparison with the earlier Model-A (i.e. *optxagn*), can be found in Chapter 3. The set of fitting parameters for each source, based on Model-B, is given in Table D.2. Section 5.7.3 discusses the statistical differences resulting from using Model-B and Model-A for our sample.

All the principal SED parameters such as λ_{Edd}, $\kappa_{2-10keV}$ and α_{ox} are calculated from the new model fitting (Table D.3). A cross-correlation study of the various parameters is then conducted. In Table 5.1 we compare the mean values of some SED parameters our sample with those for samples used in previous work. The result of correlations established in these previous studies will be compared with ours in the following sections.

There are two sources that we treated as being anomalous in our study. The first is PG 1004+130, a broad absorption line (BAL) quasar, whose X-ray was reported as being extraordinarily weak. Although its X-ray spectrum does not show clear absorption edges, it is nevertheless likely to be heavily absorbed, or has a different origin of X-rays, such as a sub-parsec-scale jet. It has been suggested that the X-ray emission from PG 1004+130 could be 0.73 dex weaker than normal PG radio loud quasars (PG RLQs), even after correcting for its intrinsic absorption (Miller et al. 2006). Due to its distinct X-ray spectrum (and correspondingly different X-ray parameters), we did not include this source in our regression analysis. In Chapter 4, we proposed that an order of magnitude increase in the hard X-ray flux of PG 1004+130 is required to make its properties consistent with other sources. The other anomalous source is Mrk 110, whose SDSS spectrum is not consistent with its OM data (see Chapter 3). However, the optical spectrum obtained using FAST shown in Landt et al. (2011), is consistent with the OM data, and is also an order of magnitude brighter than the SDSS spectrum. Therefore the SDSS spectrum of Mrk 110 is not consistent with its broadband SED parameters, and so we exclude Mrk 110 from the cross-correlation analysis.

5.3 Investigating the Correlations for Various SED Parameter Groups

In this section we divide the SED parameters into several sub-groups, based on correlations reported in the literature (see Section 5.1), and then conduct a cross-correlation analysis within each group.

5.3.1 Group 1: L_{2500}, L_{2keV} and α_{ox}

The α_{ox} index has been used as the indicator of the SED shape for more than thirty years. It is often used as an indication of the AGN's broadband SED, to convert between the AGNs' optical luminosity function (OLF) and X-ray luminosity function (XLF) (e.g. Hopkins, Richards & Hernquist 2007, hereafter: Hopkins07 ; Tang, Zhang & Hopkins 2007, hereafter: Tang07). It is defined as Equation 5.1 (Tananbaum et al. 1979):

$$\alpha_{ox} = -\frac{Log(F(2keV)/F(2500\mathring{A}))}{2.605} \tag{5.1}$$

Note that the negative sign in Equation 5.1 is not included in some previous work (e.g. Steffen et al. 2006; Just et al. 2007; VF07), thus their α_{ox} is negative. But in this chapter we follow the definition in Lusso10 and Grupe10 to ensure a positive α_{ox}. Many studies have been carried out on the evolution of α_{ox} with both luminosity and redshift (e.g. Avni & Tananbaum 1982; Wilkes et al. 1994; Strateva et al. 2005; Steffen et al. 2006; Just et al. 2007; Green et al. 2009, hereafter: Green09; Lusso10; Grupe10), which may provide clues on the emission mechanism. The value of α_{ox} has been found in the range 1.2∼1.8, with a mean value of ∼1.5. Correlations have also been found between L_{2keV}, L_{2500}, α_{ox} and redshift, with the primary correlation being $L_{2keV} \propto L_{2500}^{\beta}$. The slope index β was often found to deviate from unity for both optically selected (e.g. Strateva et al. 2005; Steffen et al. 2006; Just et al. 2007) and X-ray selected AGN samples (e.g. Lusso10). However, La Franca, Franceschini & Cristiani (1995) re-analyzed Wilkes et al. (1994)'s sample by considering both variables and intrinsic scattering, and found that β was consistent with unity. Green09 collected a large, well-defined

sample of 2308 SDSS/ChaMP QSOs in the redshift range 0.2∼5.4, and concluded that β is not less than unity.

The reality of a non-linear correlation in L_{2keV} vs. L_{2500} remains an open question, but one possible explanation could be a selection effect in a flux limited sample for which dispersions in the optical and X-ray luminosity are not equal, or which change with cosmic time (Yuan, Siebert & Brinkmann 1998, hereafter: Yuan98; Tang07). However, the possibility of a truely intrinsic non-linear correlation cannot be ruled out. A non-linear L_{2keV} vs. L_{2500} correlation implies that there is a dependence of α_{ox} on L_{2keV} and L_{2500} (e.g. Vignali, Brandt & Schneider 2003; Just et al. 2007; Lusso10), but this is still a matter of debate (Yuan98; Tang07).

To further test the basis of these correlations, we also calculated the values of L_{2keV}, L_{2500} and α_{ox} from our best-fit model of the SEDs, and then preformed the same cross-correlation analysis. The limitation of our results arises from the lack of actual spectral coverage at 2500Å for the 16 sources without OM UVW1 and UVM2 data. The luminosity and redshift range of our sample is also relatively small. But on the merit side we have included two inputs of reddening/absorption to model both the Galactic and the AGN's intrinsic extinction during the broadband SED fitting, so our values of L_{2keV}, L_{2500} and α_{ox} should be closer to those of the intrinsic source. The unobscured nature of our sample and the exclusion of warm absorber sources also helps reduce uncertainties in the corrections caused by reddening/absorption.

The L_{2keV} vs. L_{2500} Correlation

Figure 5.2 shows our L_{2keV} vs. L_{2500} correlation. The statistical methods used are the same as in Lusso10, i.e. we use the full parametric estimate and maximized regression (EM) algorithm. We use this to derive two regression lines assuming, first L_{2keV}, then L_{2500} to be the independent variable. Then the bisector of the two regression lines is calculated using the equations in Isobe et al. (1990). This method is more appropriate in cases where the cross-correlations are dominated by intrinsic scatter. The correlations found are as follows:

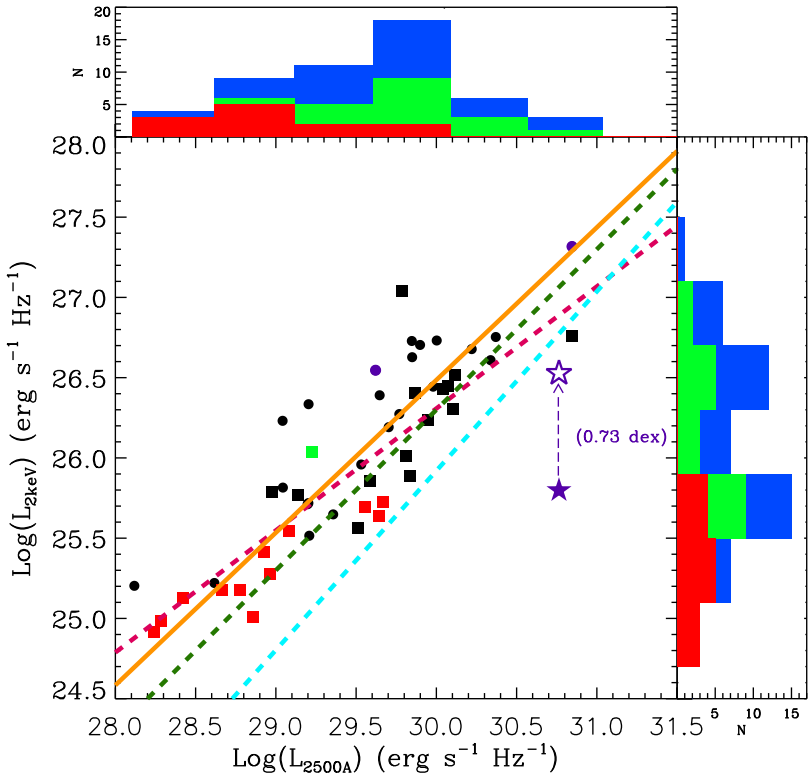

Figure 5.2: The cross-correlatin between L_{2500} and L_{2keV}. The solid orange line is the bisector regression line for our sample, while regression lines of other studies are plotted as dashed lines in different colours. The red symbols represent NLS1s; purple symbols show the radio loud AGN; the green symbol is Mrk 110. The filled purple star is the BAL-quasar PG 1004+130, and the open purple star is the position if its intrinsic X-ray flux was 0.73 dex higher (Miller et al. 2006). The square symbols show all Population A sources whose Hβ FWHM is less than 4000 km s^{-1}. In the two histograms the green and red regions are for the Population A sources, and the red region indicates the 12 NLS1s. The dashed green line is based on Hasinger05; the dashed cyan line is based on Green09; the dashed pink line is based on Lusso10.

(i) the EM regression line, when L_{2500} is assumed to be the independent variable:

$$Log(L_{2keV}) = (0.83\pm0.05)Log(L_{2500}) + (1.59\pm1.55) \quad (5.2)$$

(ii) the EM regression line, when L_{2keV} is assumed to be the independent variable:

$$Log(L_{2keV}) = (1.09\pm0.09)Log(L_{2500}) - (6.17\pm2.66) \quad (5.3)$$

(iii) the bisector of the above two regression lines (the solid orange line in Figure 5.2)

$$Log(L_{2keV}) = (0.95\pm0.06)Log(L_{2500}) - (2.04\pm1.77) \quad (5.4)$$

The Spearman's rank test gives a rank coefficient of $\rho_s = 0.87$, and the probability of deviation from a random distribution is $d_s = 1.2\times10^{-16}$, confirming a very high level of significance. We superimpose PG 1004+130 (filled purple star) on Figure 5.2, showing that it lies far from the correlation due to its unusual X-ray weakness. It matches much better to the regression line if corrected in L_{2keV} by 0.73 dex (Miller et al. 2006, the empty purple star in Figure 5.2).

Our correlation between L_{2keV} vs. L_{2500} is close to linear, but previous studies have found a wide range of values as listed in Table 5.2. Figure 5.2 plots these results for comparison. The correlation found by Hasinger05 (green dashed line) which is based on an X-ray selected sample, is the most consistent with our sample, whereas the slope found by Lusso10 (pink dashed line) is significantly flatter. Our slope is also consistent with Green09 (cyan dashed line) in which a large sample of optically selected quasars is analyzed. We note that our sample only covers the low luminosity region of the sample in Green09. The NLS1s are the least luminous sources. The different value of the Y-axis intercept in Green09 may be due to their larger sample and larger luminosity dispersion.

There can be several reasons for the difference between our results and Lusso10. Firstly there may be a selection effect of a flux limited sample if there are different amounts of dispersion in optical and X-ray luminosities (Yuan98; Tang07). More importantly, our sample is corrected for both Galactic and intrinsic reddening/absorption in the host Galaxy through the spectral fitting whereas that of Lusso10 is only corrected for Galactic absorption. We remove the intrinsic reddening correction and re-compute the EM regression, with results given in Table 5.2

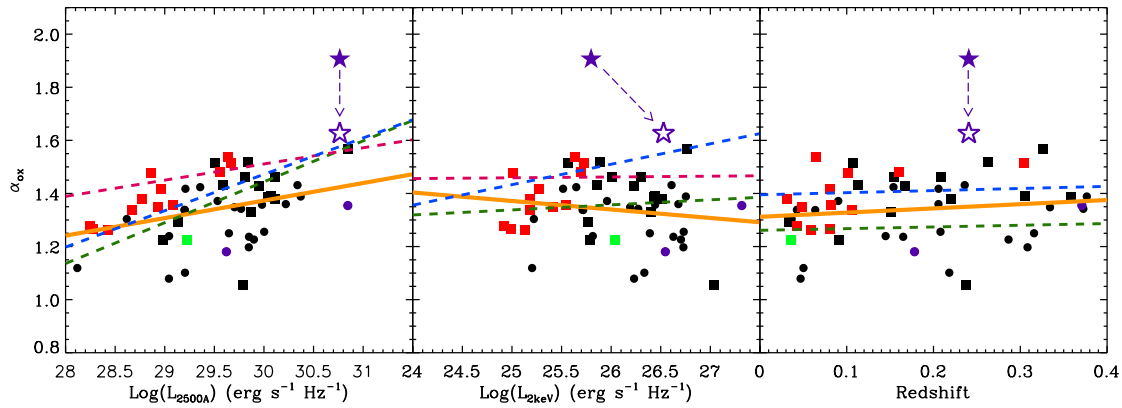

Figure 5.3: α_{ox} vs. L_{2500}, L_{2keV} and redshift. Each symbol represents the same type of source as in Figure 5.2. In each panel the solid orange line is the OLS regression line for our sample, assuming the X-axis variable to be the independent variable. The dashed blue line is based on Steffen06; the dashed pink line on Green09; and the dashed green line on Lusso10.

under the row 'This Work-R_{int}' The dust reddening and gas absorption column are related by, E(B-V)=1.7×($N_H/10^{22}$)cm^{-2} (Bessell 1991), which means that L_{2500} is suppressed much more severely than L_{2keV}. Hence the removal of intrinsic reddening correction decreases our correlation slope from 0.95 (±0.06) to 0.91 (±0.05). Thus the intrinsic reddening can flatten the correlation, but it does not seem to be enough on its own to explain the difference with Lusso10, unless their sample is strongly reddened in the optical.

The α_{ox} vs. L_{2keV}, L_{2500} and Redshift Correlations

To further investigate the correlation between the optical/UV and X-ray continua, we adopt the same approach as in previous work to produce α_{ox} vs. L_{2500}, α_{ox} vs. L_{2keV} and α_{ox} vs. redshift correlations. If we assume $L_{2keV} \propto L_{2500}^{\beta}$, then $\alpha_{ox} \propto L_{2500}^{1-\beta}$ and $\alpha_{ox} \propto L_{2keV}^{\beta(1-\beta)}$ are expected by definition. However, the Spearman's rank test does not imply very strong correlations: $\rho_s = 0.31, d_s = 0.03$ for α_{ox} vs. L_{2500}; $\rho_s = -0.13, d_s = 0.35$, for α_{ox} vs. L_{2keV}; $\rho_s = 0.19, d_s = 0.18$, for α_{ox} vs. redshift. The regression lines were derived have a large uncertainty. The results are presented in Figure 5.3 and listed in Table 5.2. The solid orange line in each panel of Figure 5.3

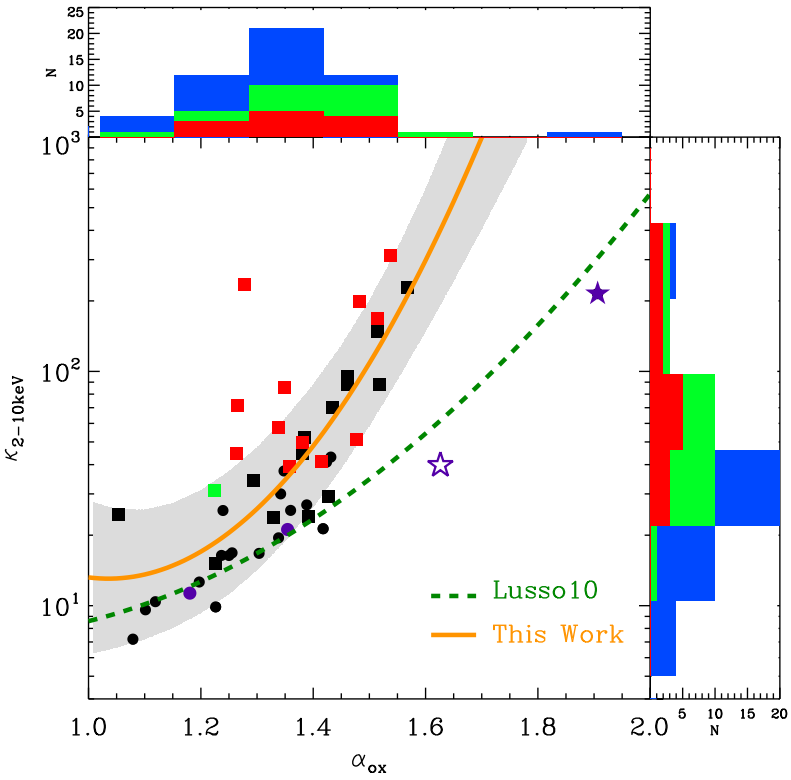

Figure 5.4: $\kappa_{2-10keV}$ vs. α_{ox}. Each symbol represents the same type of source as in Figure 5.2. The solid orange line is the best fit line found using a second order polynomial, and the shaded area is the $\pm 1\sigma$ zone.

is our EM regression line, compared with some previous work shown by dashed lines. Note that our results are limited to redshift $z < 0.4$, $L_{2500} < 10^{+31}$ erg s^{-1} Hz^{-1} and $L_{2keV} < 10^{+27.5}$ erg s^{-1} Hz^{-1}. Our results also suggest that the cross-correlations in α_{ox} vs. L_{2500} and L_{2keV} are dominated by the AGN's intrinsic dispersion.

5.3.2 Group 2: α_{ox}, $\kappa_{2-10keV}$ and λ_{Edd}

As mentioned in the previous section α_{ox} is often used as a proxy for the broadband SED shape. Since L_{bol} is often dominated by the big blue bump (BBB) peaking in the unobservable EUV region (Walter & Fink 1993). $\kappa_{2-10keV}$, defined as $L_{bol}/L_{2-10keV}$, is also an indicator of the SED shape. λ_{Edd} is an important parameter which relates directly to the accretion processes close to the central SMBH. Therefore, correlations are to be expected between λ_{Edd}, $\kappa_{2-10keV}$ and α_{ox}.

The α_{ox} vs. $\kappa_{2-10keV}$ Correlation

Lusso10 reported a tight second-order polynomial correlation for $\kappa_{2-10keV}$ vs. α_{ox}. We find a similar correlation for our sample. Spearman's rank test shows $\rho_s = 0.73$ and $d_s = 2\times10^{-9}$. We also fitted a second-order polynomial to the correlation and obtained the following equation:

$$Log(\kappa_{2-10keV}) = (5.7\pm3.4) - (8.8\pm5.2)\alpha_{ox} + (4.3\pm2.0)\alpha_{ox}^2 \quad (5.5)$$

Figure 5.4 shows our best-fit polynomial (solid orange line) with $\pm1\sigma$ dispersion region (the shaded region). Note that our fit excludes BAL quasar PG 1004+130 (purple star in Figure 5.4). The best-fit polynomial from Lusso10 is plotted as the dashed green line, which is not as steep as ours. The reason is that our value of $\kappa_{2-10keV}$ (and L_{bol}) is higher than found by Lusso10, especially for the narrow line objects (the average $\kappa_{2-10keV}$ for our 12 NLS1s is 86^{+96}_{-45}). Lusso10 constructed their broadband SEDs by first assuming a power law extending from the optical to 500Å, then connecting the continuum at 500Å linearly to that at 1 keV, and finally by extrapolating from 1 keV towards higher energies, using an exponentially cut-off power law. This model substantially underestimates L_{bol} for narrow line objects because such objects often have strong soft-X-ray excesses which contain a large fraction of the L_{bol} (Middleton et al. 2009; Jin et al. 2009; Chapter 3). Our detailed broadband SED fitting has modeled this soft-excess feature by including a low temperature optically thick Comptonization component. We claim that this results in a more accurate estimate of L_{bol} (Chapter 3). So certainly for the nearby Type 1 AGNs (redshift < 0.4), the $\kappa_{2-10keV}$ vs. α_{ox} correlation we find should be more reliable. How the correlation behaves at high redshift requires further study, but Lusso10 has shown that such a second-order polynomial correlation still holds for Type 1 AGNs up to redshifts $z = 4$.

The α_{ox} vs. λ_{Edd} Correlation

The existence of a correlation of α_{ox} vs. λ_{Edd} remains unclear. VF07 found no correlation between these quantities, and so they proposed that α_{ox} did not provide useful information on the broadband SED shape. S08 confirmed VF07's result

for their sample of 35 moderate to high luminosity radio-quiet AGN. On the contrary, Lusso10 did find a correlation between α_{ox} and λ_{Edd}, although with a large dispersion. This was confirmed by Grupe10 for their sample containing 92 soft X-ray selected AGNs, but their correlation was both flatter and stronger than that of Lusso10. We use our sample to investigate this situation, and our results are shown in Figure 5.5. The Spearman's rank test gives $\rho_s = 0.35$ and $d_s = 1\times10^{-2}$, suggesting that a correlation does exist. We then applied the ordinary least squares (OLS) regression, assuming λ_{Edd} to be the independent variable, and found the following relation:

$$\alpha_{ox} = (0.079\pm0.038)Log(\lambda_{Edd}) + (1.384\pm0.029) \tag{5.6}$$

Figure 5.5 shows our results. Our correlation has less dispersion than found by VF07 and Lusso10, but more dispersion than that from Grupe10. The exclusion of a correlation is at the $\sim2\sigma$ significance level, which is less significant than in Lusso10 and Grupe10. Our regression line slope is consistent with but slightly flatter than that in Lusso10 ($\beta = 0.133\pm0.023$) and Grupe10 ($\beta = 0.11\pm0.02$). This is partly because our estimation of L_{bol} is higher than for previous work, due to the inclusion of a soft X-ray excess in our model. Therefore our value of λ_{Edd} is also higher for the NLS1s and other relatively narrow line objects. Another reason could be a selection effect due to our low redshift criterion ($z < 0.4$), while Lusso10's sample covers a larger range in redshift ($0.04 < z < 4.25$). The positive correlation of α_{ox} vs. redshift reported by Lusso10 implies that sources at higher redshift have statistically steeper α_{ox}. Indeed their sample contains many objects with $\alpha_{ox} > 1.5$ and $z > 0.4$, which populate the empty region above $\alpha_{ox} = 1.5$ in Figure 5.5 and create a higher dispersion. This can also explain the difference between Lusso10 and Grupe10, since Grupe10's sample is also a nearby AGN sample with redshift $z < 0.3$. These results suggest that α_{ox} cannot be used to infer the mass accretion rate in terms of Eddington (λ_{Edd}).

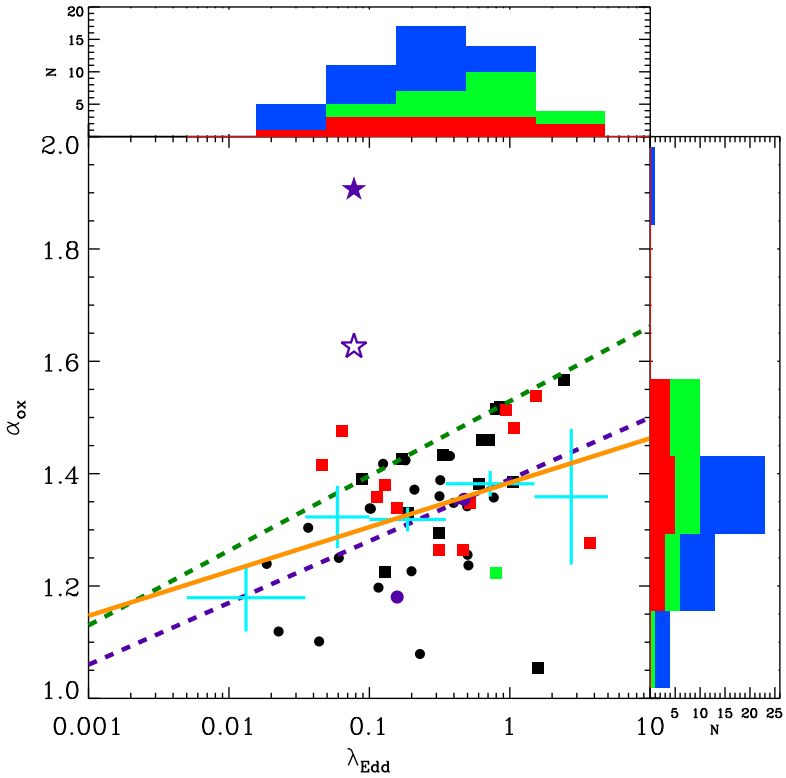

Figure 5.5: λ_{Edd} vs. α_{ox}. Each symbol represents the same type of source as in Figure 5.2. The solid orange line is the bisector regression line determined by our sample. The cyan crosses are the binned data points of our sample. The dashed green line is from Lusso10; the dashed purple line is from Grupe10.

The $\kappa_{2-10keV}$ vs. λ_{Edd} Correlation

Wang, Watarai & Mineshige (2004) reported the correlation between $\kappa_{2-10keV}$ and λ_{Edd}, which was later confirmed by VF07,09. Most recently, Lusso10 also found this correlation for the 545 X-ray selected type 1 AGNs from the XMM-COSMOS survey. They suggested that the observed step change in this correlation does not result from the L_{bol} dependence on both $\kappa_{2-10keV}$ and λ_{Edd}. In our study we also find that λ_{Edd} is correlated with $\kappa_{2-10keV}$. A Spearman's rank test resulted in $\rho_s = 0.60$, $d_s = 5\times10^{-6}$ for the whole sample, and $\rho_s = 0.60$, $d_s = 5\times10^{-6}$ for the 12 NLS1s. Figure 5.6 shows our results, together with the results from VF07,09 and Lusso10. We performed an EM regression analysis and derived the following equations:
(i) An EM regression with λ_{Edd} being the independent variable

$$Log(\kappa_{2-10}) = (0.482\pm0.088)Log(\lambda_{Edd}) + (1.840\pm0.071) \quad (5.7)$$

(ii) An EM regression with $\kappa_{2-10keV}$ being the independent

$$Log(\kappa_{2-10}) = (1.179\pm0.166)Log(\lambda_{Edd}) + (2.232\pm0.090) \quad (5.8)$$

(iii) bisector of the above two lines (solid orange line in Figure 5.6):

$$Log(\kappa_{2-10}) = (0.773\pm0.069)Log(\lambda_{Edd}) + (2.004\pm0.049) \quad (5.9)$$

Our regression lines are highly consistent with the binned points from VF07,09 and also the regression line reported by Lusso10. The two lowest data bins from VF07,09 seem to have a relatively high deviation from the correlation lines, which may imply a change in slope of the correlation for sources with $\lambda_{Edd} < 0.01$. But we cannot test this possibility from our data due to the exclusion of sources with low λ_{Edd} resulting from our sample selection (Chapter 3).

The results show that the $\kappa_{2-10keV}$ vs. λ_{Edd} correlation extends up to high $\kappa_{2-10keV}$ ($\sim$100) and super Eddington accretion rates ($\sim$10); such objects are mainly NLS1s (red square symbols in Figure 5.6) and some other relatively narrow line sources (black square symbols). We also note that the dispersion in our regression line is smaller than that in VF07,09 and Lusso10, in spite of the different methods used in deriving L_{bol} and the different redshift ranges. This suggests that the

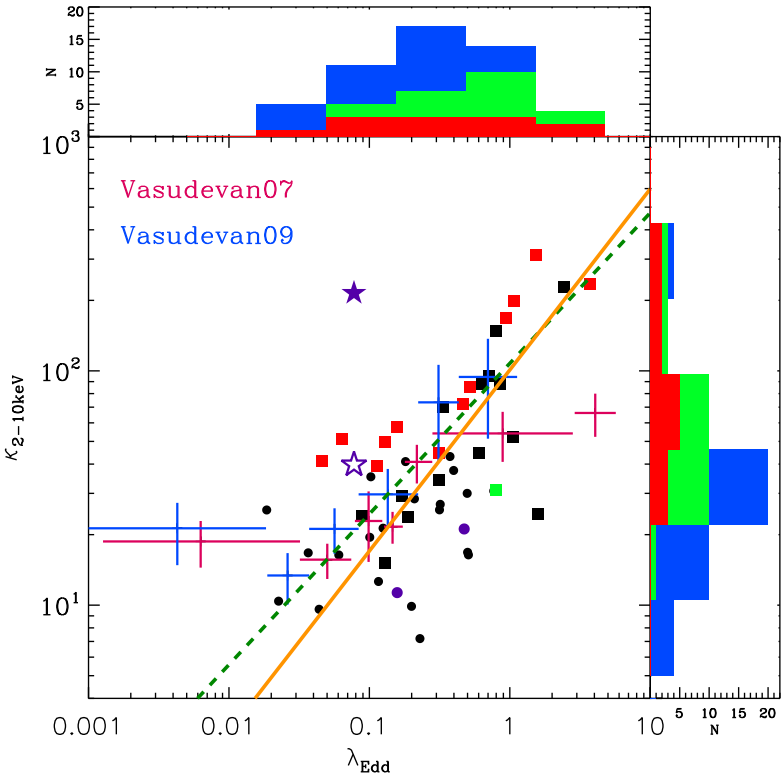

Figure 5.6: λ_{Edd} vs. $\kappa_{2-10keV}$. Each symbol represents the same type of source as in Figure 5.2. The solid orange line is the bisector regression line determined for our sample. The binned data points are from VF07 (pink) and VF09 (blue). The dashed green line is from Lusso10.

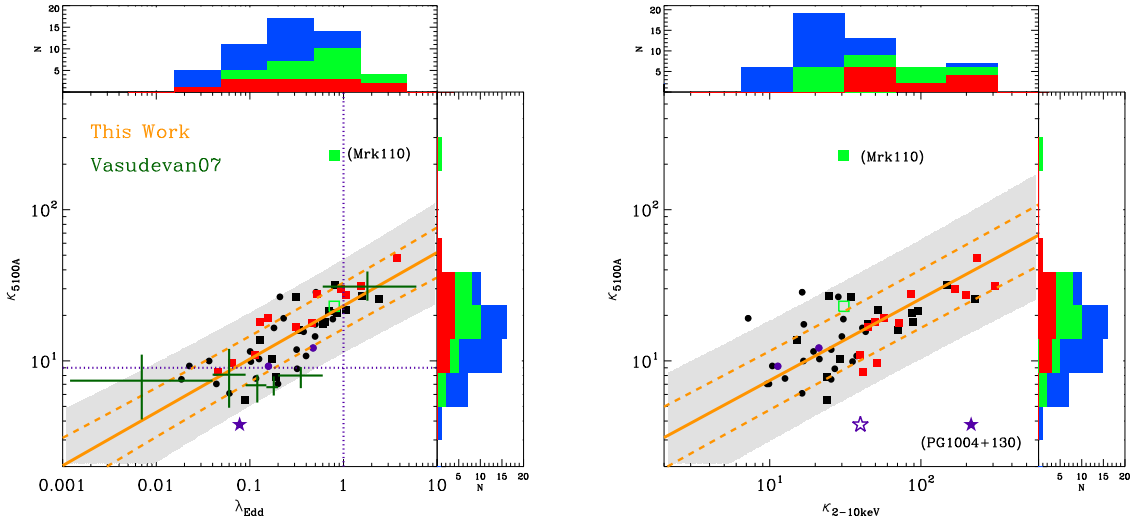

Figure 5.7: κ_{5100} vs. λ_{Eddr} and $\kappa_{2-10keV}$. Each symbol represent the same type of source as in Figure 5.2. In the left panel, the solid orange line is the OLS line assuming λ_{Eddr} to be the independent variable. The two dashed orange lines show the $\pm1\sigma$ region, and the shaded region is the $\pm2\sigma$ region. The green open square symbol is Mrk 110 reported by Landt et al. (2011). The vertical and horizontal purple lines are for κ_{5100}=9 and λ_{Eddr}=1. The symbols and lines in the right panel have the same meaning as those in the left panel.

dispersion observed in the correlation is intrinsic. In Figure 5.6, we see that PG 1004+130 (filled purple star) deviates far from the regression line (also more than 3σ from VF07,09's binned data points), confirming its anomalously weak $L_{2-10keV}$. Increasing its $L_{2-10keV}$ by 0.73 dex (open purple star) moves it much closer to the correlation line.

5.3.3 Group 3: κ_{5100}, λ_{Eddr} and $\kappa_{2-10keV}$

The 5100Å monochromatic continuum luminosity (L_{5100}) is often used to estimate L_{bol}, particularly for very large samples of AGN, when broadband SED modeling for every source is not practical. The conventional method is to use a constant scaling factor $\kappa_{5100} = 9$ (Kaspi et al. 2000; Richards et al. 2006: 10.3±2.1), or κ_{5100} value that is anti-corrected with L_{bol} (Marconi et al. 2004, hereafter: Marconi04). VF07 showed that for high λ_{Edd} sources such as many of the NLS1s, there is a

clear deviation from constant $\kappa_{5100} = 9$. In addition, potential contamination from the host galaxy will introduce dispersion into the κ_{5100} vs. λ_{Edd} correlation for low luminosity sources. However, this should not be a severe problem for our sample since in our sample host galaxy is not dominating (Chapter 3). In our study a much stronger correlation was found in κ_{5100} vs. λ_{Edd} as the Spearman's rank test gives ρ_s=0.81 (d_s=4×10^{-13}). Motivated by the strong correlations between λ_{Eddr} and $\kappa_{2-10keV}$, we also found a strong correlation between κ_{5100} and $\kappa_{2-10keV}$, with a Spearman's rank test of ρ_s=0.64 (d_s=9×10^{-7}).

The left panel of Figure 5.7 shows the correlation between κ_{5100} and λ_{Edd}. The solid orange line is the OLS regression line, the two dashed orange lines show the $\pm1\sigma$ region, and the shaded region is the $\pm2\sigma$ region. For a specific λ_{Edd} value, the 1σ dispersion of κ_{5100} is $\sim$ 0.17 dex. The binned data points from VF07 are also shown in the plot for comparison. VF07's results are consistent with ours within $\pm2\sigma$, but our correlation is much stronger. This may be attributed to the high spectral quality of our sample and the carefully derived κ_{5100} and λ_{Edd}, based on our detailed broadband SED fitting. It also shows that the distribution of κ_{5100} peaks at 10$\sim$20, with a 1σ dispersion of 0.29 dex. For the NLS1s, the mean κ_{5100} increases to 20 (1σ = 0.23 dex). This means that using a $\kappa_{5100} = 9$ (the horizontal purple line in the left panel Figure 5.7) would significantly underestimate the intrinsic L_{bol} and λ_{Edd}, especially for samples containing sources with high λ_{Edd} e.g. the NLS1s. The OLS regression line that assumes λ_{Edd} to be the independent variable can be expressed by the following equation:

$$Log(\kappa_{5100}) = (0.467 \pm 0.045) Log(\lambda_{Edd}) + (1.430 \pm 0.027) \tag{5.10}$$

We superimpose the SDSS and FAST (Landt et al. 2011) data from Mrk 110 (filled and open green square, respectively) on Figure 5.7. This shows the large optical variability in the spectrum. The FAST data is much more consistent with the XMM-Newton OM and also matches very well with the regression line. This supports the reliability of the correlation.

The strong correlation between κ_{5100} and $\kappa_{2-10keV}$ (shown in the right panel of Figure 5.7) is an expected result, given that both κ_{5100} and $\kappa_{2-10keV}$ strongly

correlate with λ_{Edd}. Such a correlation is also reasonable considering the strong correlation between $L_{2-10keV}$ and L_{5100} (Chapter 3I). The 1σ dispersion of $\kappa_{2-10keV}$ is 0.40 dex, which is larger than that 0.29 dex for κ_{5100}. The $\pm1\sigma$, $\pm2\sigma$ zones are also shown in the Figure. The bisector regression line can be expressed by the following equation:

$$Log(\kappa_{5100}) = (0.593 \pm 0.053)Log(\kappa_{210}) + (0.239 \pm 0.086) \quad (5.11)$$

Mrk 110 and PG 1004+130 are superimposed on the plot, and their corrected positions are much more consistent with the regression lines.

Marconi04 proposed that κ_{5100} anti-correlated with L_{bol}, but our study does not support such an anti-correlation, although our sample only occupies the L_{bol} region above $10^{10.7}$ $L_{\odot}$ in Fig. 3 left panel of Marconi04. A Spearman's rank test for our sample gives ρ_s=0.12 (d_s=0.39), suggesting no correlation. The sources lying between 10^{11} $\sim10^{12.5}$ $L_{\odot}$ have a mean κ_{5100}= 16, with a 1σ dispersion of 0.29 dex. So we find that our κ_{5100} values for these objects are much higher than reported in Elvis et al. (1994) and Marconi04.

5.3.4 Group 4: $\Gamma_{2-10keV}$, λ_{Edd} and $\kappa_{2-10keV}$

The strong correlation between 2-10 keV photon index ($\Gamma_{2-10keV}$) and λ_{Edd} has been studied in detail for the past ten years (e.g. Lu & Yu 1999; Wang, Watarai & Mineshige 2004; S06,08; Zhou10a). It is proposed that increasing the mass accretion rate leads to enhanced emission from the accretion disc, resulting in more seed photons from the disc, which then increases the Compton cooling of the corona, and softens the Comptonized hard X-ray spectrum, i.e. the slope of $\Gamma_{2-10keV}$ increases. It was also reported that both $\Gamma_{2-10keV}$ and λ_{Edd} strongly correlate with the FWHM of Hβ (e.g. Brandt, Mathur & Elvis 1997; S06,08; Grupe10), therefore these three parameters all strongly correlate with each other. However, S06,08 found that the correlation of $\Gamma_{2-10keV}$ vs. $FWHM_{H\beta}$ is weakened by the inclusion of highly luminous sources, but that the correlation of $\Gamma_{2-10keV}$ vs. λ_{Edd} still exists. This implies that the correlation of $\Gamma_{2-10keV}$ vs. λ_{Edd} is more fundamental. We also mentioned in Section 5.3.2 that the strong correlation between λ_{Edd} and $\kappa_{2-10keV}$ is confirmed,

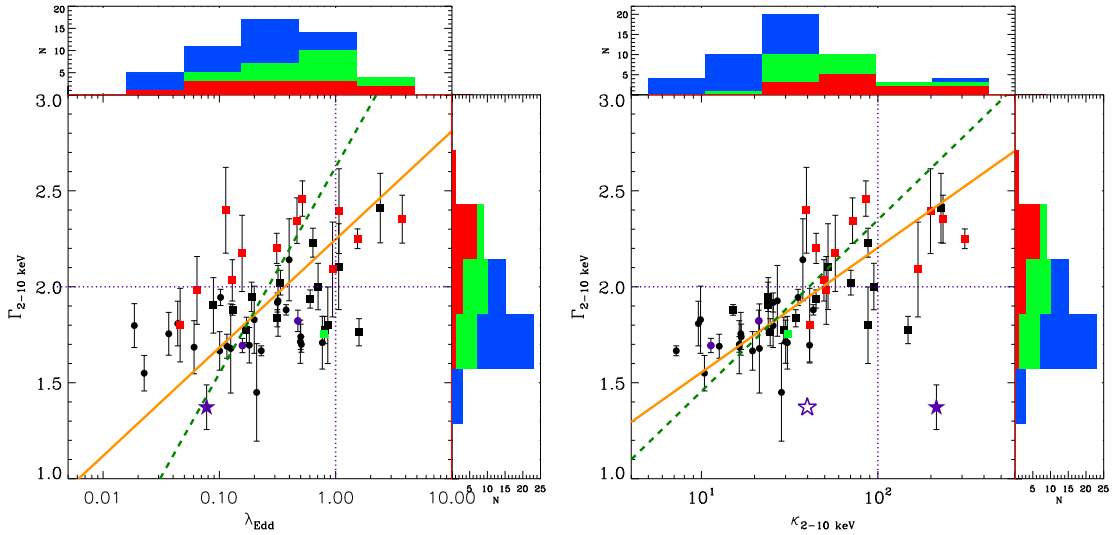

Figure 5.8: $\Gamma_{2-10keV}$ vs. λ_{Eddr} and $\kappa_{2-10keV}$. Each symbol represents the same type of source as in Figure 5.2. In the left panel, the solid orange line is the bisector regression line. The dashed green line is that reported by Zhou10b. The vertical and horizontal purple lines are for $\Gamma_{2-10keV}$=2 and λ_{Eddr}=1. The symbols and lines in the right panel have the same meaning as those in the left panel. The vertical purple line is for $\kappa_{2-10keV}$=100. PG 1004+130 was excluded when performing the regression, but assuming its intrinsic X-ray flux to be 1 dex higher and a $\Gamma_{2-10keV}$ ∼1.8 would make it consistent with the other sources. It is shown as the open purple star in both panels.

thus a strong correlation between $\Gamma_{2-10keV}$ and $\kappa_{2-10keV}$ is expected. Indeed, such a correlation has been reported recently by Zhou & Zhao (2010), hereafter: Zhou10b. In this section we carry out a similar cross-correlation study, to test the robustness of previous claims.

The Correlations and Regression Lines

The two panels in Figure 5.8 show our correlations between $\Gamma_{2-10keV}$, λ_{Edd} and $\kappa_{2-10keV}$. Table 5.3 summarizes the numerical results. Significant correlations are confirmed based on the Spearman's rank test: ρ_s=0.40 (d_s=4×10^{-3}) for $\Gamma_{2-10keV}$ vs. λ_{Edd}, and ρ_s=0.73 (d_s=4×10^{-9}) for $\Gamma_{2-10keV}$ vs. $\kappa_{2-10keV}$.

Following S08's approach, we applied the χ^2 minimization method for $\Gamma_{2-10keV}$ vs. λ_{Edd} correlation, assuming $\Gamma_{2-10keV} = \beta Log(\lambda_{Edd}) + \xi$. A typical error of 10% was assumed for λ_{Edd}. The small error in $\Gamma_{2-10keV}$ for Mrk 110 (square green symbol) caused the slope β to be 0.018±0.019, which is clearly not the best-fit line for the whole sample. We therefore excluded Mrk 110 and so found a more reasonable slope of 0.189±0.026, but this is still ∼5σ away from 0.31±0.01 reported by S08 using the same method. It implies that the χ^2 minimization technique may not be an appropriate method for quantifying this correlation, because it can be strongly biased by sources with small error in the $\Gamma_{2-10keV}$ measurement (if the 2-10 keV spectrum has high S/N). The $\chi^2/\nu = 6.5$ in our fitting means that this correlation contains a big intrinsic dispersion along with the observational dispersion, thus the method of assuming χ^2/ν ∼1 by taking intrinsic dispersion into account is more appropriate. This method gives slopes of 0.202±0.061 and 0.226±0.026 before and after excluding Mrk 110, so the results are less sensitive to individual sources of much smaller error bars. The intrinsic dispersion is 0.18, which is 86% of the total dispersion, and is also consistent with $\Delta\Gamma_{2-10keV}$ ∼0.1×$\Gamma_{2-10keV}$ reported in S08. The bisector regression line is derived. The result is plotted as a solid orange line in the left panel of Figure 5.8, and it can be expressed by the following equation:

$$Log(\lambda_{Edd}) = (1.773 \pm 0.238)\Gamma_{2-10keV} - (3.983 \pm 0.469) \quad (5.12)$$

The slope is ∼2σ steeper than the bisector slope of 0.9±0.3 reported by S08 (dashed

Table 5.3: The line coefficients found using different regression methods for the correlations of $\Gamma_{2-10keV}$ vs. λ_{Eddr} and $\kappa_{2-10keV}$.

		$Log(\lambda_{Edd})=\beta\Gamma+\xi$	$Log(\kappa_{210})=\beta\Gamma+\xi$
OLS(Y|X)	β	0.918±0.269	1.115±0.172
	ξ	-2.325±0.527	-0.573±0.329
OLS(X|Y)	β	4.730±1.217	2.209±0.283
	ξ	-9.650±2.304	-2.675±0.525
Bisector	β	1.753±0.239	1.533±0.153
	ξ	-3.931±0.471	-1.376±0.288
χ^2 min	β	4.416±0.510	2.620±0.184
	ξ	-8.761±0.946	-3.447±0.343
$\chi^2/\nu \sim 1$	β	1.274±0.283	1.529±0.183
	ξ	-3.003±0.544	-1.372±0.350

green line in the left panel of Figure 5.8). This discrepancy may be due to the different methods used to estimate the bolometric luminosity. We will discuss this point in Section 5.3.4.

Similar analytical methods were applied to the relation of $\Gamma_{2-10keV}$ vs. $\kappa_{2-10keV}$. Zhou10b reported a slope of 2.52±0.08, using standard χ^2 minimization and assuming $\kappa_{2-10keV} = \beta Log(\Gamma_{2-10keV}) + \xi$. This is consistent with our value of $\beta = 2.620\pm0.184$ with a $\chi^2/\nu = 2.78$. Considering the intrinsic scatter, Zhou10b reported a slope of 1.12±0.30 by adding 0.32 dex of intrinsic dispersion to reduce χ^2/ν to unity (the dashed green line in the right panel of Figure 5.8). Applying the same method to our sample resulted in a slope of 1.529±0.183, which is steeper than found by Zhou10b. The intrinsic dispersion found by us is 80% of the total dispersion. The bisector regression method gives a slope of 1.533±0.153 (the solid orange line in the right panel of Figure 5.8) and can be expressed by the following equation:

$$Log(\kappa_{2-10keV}) = (1.533 \pm 0.153)\Gamma - (1.376 \pm 0.288) \tag{5.13}$$

This is also consistent with the results found by assuming $\chi^2/\nu \sim 1$.

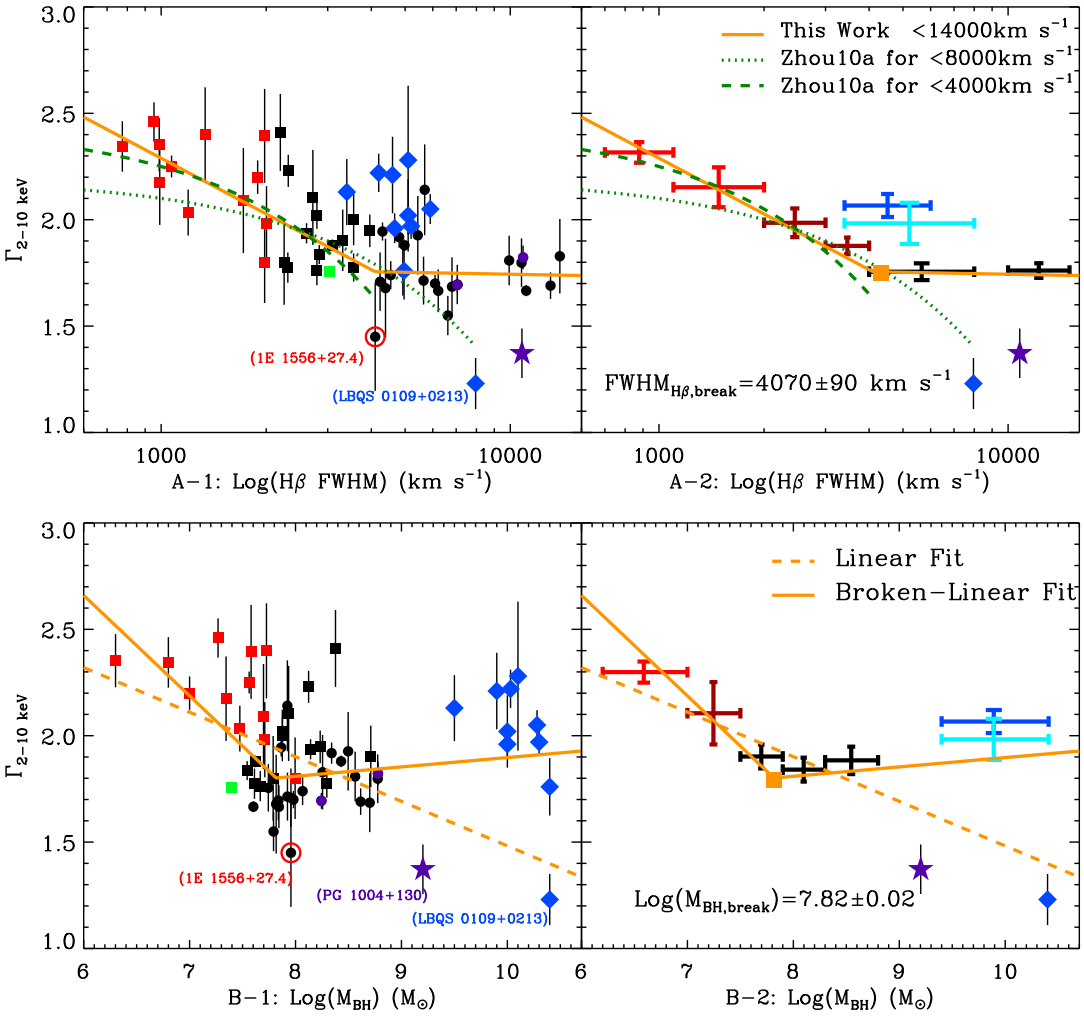

Figure 5.9: $\Gamma_{2-10keV}$ vs. FWHM of Hβ and M_{BH}. In the upper left panel, a broken line is fitted to the sample using the minimum χ^2 method. S06,08 proposed the linear correlation between $\Gamma_{2-10keV}$ and Log(Hβ FWHM) was not followed by their 10 extremely high luminosity sources, so we plot their sample as blue diamond symbols for comparison. In the right panel binned points are plotted with 1 standard error of $\Gamma_{2-10keV}$ in order to show the break points more clearly. The two red points only include the NLS1s, the two dark points are the broadest BLS1s. The cyan point is the binned point for the whole sample of S06,08. The blue point is the binned point for S06,08's sample but excluding LBQS 0109+0213 whose $\Gamma_{2-10keV}$ is anomalously low. The square orange point is the break point. 1E 1556+27.4 shown by the red circle is another source with $\Gamma_{2-10keV}$ <1.5. In the second row, the symbols all have the sample meaning as in the first row. We plot the linear regression line as the dashed orange line.

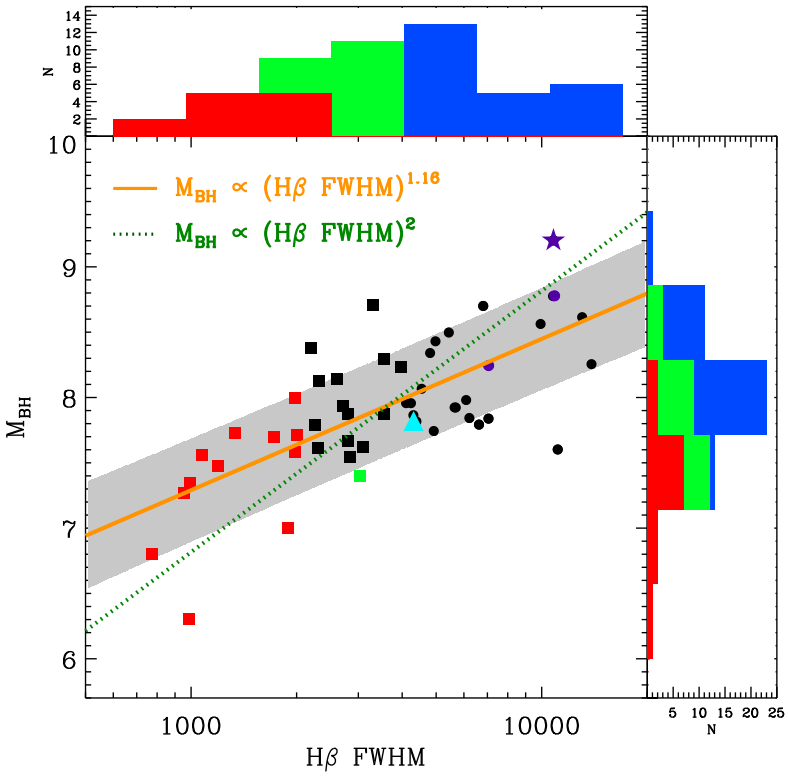

Figure 5.10: M_{BH} vs. Hβ FWHM. The symbols used represent the different types of source as in Figure 5.2. The solid orange line is the OLS regression line, assuming Hβ FWHM to be the independent variable. The shaded region is the $\pm 1\sigma$ region of the regression line. The cyan triangle shows the position of (FWHM$_{H\beta,break}$, Log(M$_{BH,break}$)) in Figure 5.9.

Advances from Our Correlation Analysis

Compared with the results found by S08 and Zhou10b, our study of $\Gamma_{2-10keV}$ vs. λ_{Edd} and $\kappa_{2-10keV}$ provides the following advances.

(1) We have confirmed these correlations based on sample of twice the size of those in S08 and Zhou10b, including more sources with high values of λ_{Edd}, $\Gamma_{2-10keV}$ and $\kappa_{2-10keV}$, which significantly extend the previous correlations (see Figure 5.8). The regression line fits are better constrained and cover wider parameter space. The difference between our regression lines and those of previous studies may be partially due to the fact that we have more sources of most extreme λ_{Edd}.

(2) Our sample has been carefully screened to exclude sources with a strong warm absorber. These sources may have $\Gamma_{2-10keV}$ and higher $\kappa_{2-10keV}$ artificially lower than the intrinsic values. Our sample quality is essential to reduce the dispersion and so reveal intrinsic correlations.

(3) Our estimates of L_{bol} were derived from the broadband SED fitting, which was based on high quality spectra and a new multi-component model. We claim this to be more reliable than the procedure used in previous studies. A conventional method is to apply a multiplication factor to L_{5100} to estimate L_{bol}. However, we showed in Section 5.3.3 that κ_{5100} is well correlated with λ_{Edd}, rather than being constant or dependent on L_{bol}, consequently the conventional scaling from L_{5100} to L_{bol} is likely to result in poor accuracy in some cases. The L_{bol} used in Zhou10b does come from VF09's broadband SED model for the reverberation mapped sample, but it does not take account of the 'soft X-ray excess' component or where the disc peaks in the EUV. Therefore the L_{bol} we calculate will be larger than previous works, especially for those sources with a strong 'soft excess', Our λ_{Edd} and $\kappa_{2-10keV}$ will also be higher, which could account for the differences in slope between our regression lines and those reported in previous work.

5.3.5 Group 5: $\Gamma_{2-10keV}$, Hβ FWHM and M_{BH}

The $\Gamma_{2-10keV}$ vs. Hβ FWHM Correlation

The correlations between the soft/hard X-ray slopes and the Balmer line velocity width have been the subject of much work. Laor et al. (1994) studied 23 ROSAT selected bright quasars, and found an anti-correlation between the 0.2-2 keV slope (α_X) and the Hβ line width. Later Boller, Brandt & Fink (1996) showed that NLS1s tend to have softer X-ray spectra. Brandt, Mathur & Elvis (1997) extended this anti-correlation to include the 2-10 keV slope, by showing that NLS1s also have steeper hard X-ray continua than BLS1s, a result which was confirmed and extended by other studies (e.g. Grupe et al. 1999; Leighly 1999; Piconcelli et al. 2005; Brocksopp et al. 2006; S08; Zhou10a). However, there is large scatter within this correlation, and the trend seems to invert below $\sim$1000 km s^{-1} for NLS1s (Zhou et al. 2006). The observed large scatter is to be expected since we know that it is not a single variable that determines the spectral slope in either the soft or the hard X-ray region. In the soft X-ray region, the extinction, a soft-excess component and a warm absorber will all influence the spectral shape, which would require very detailed modeling. The situation for the 2-10 keV region is somewhat less complicated since often a single power law dominates (e.g. Middleton, Done & Gierliński 2007), but a warm absorber and reflection may still modify the hard X-ray spectral shape. In summary, the true correlation can only be found when the intrinsic X-ray continuum is used.

Our sample selection has ensured that every object in the sample has high quality 2-10 keV spectra, without significant cold gas absorption or a warm absorber (Chapter 3). We confirm that there is an anti-correlation between $\Gamma_{2-10keV}$ and Hβ FWHM, see Figure 5.9. The Spearman's rank test gives ρ_s=-0.72 (d_s=4.9$\times$10^{-9}). The best-fit lines from Zhou10a are also plotted in Figure 5.9 as the cyan lines. Compared with their linear correlation in using FWHM$_{H\beta}$, we find that the linear correlation using Log(FWHM$_{H\beta}$) is better. Previous work also noted that the correlation may change form at $\sim$4000 km s^{-1} (Sulentic et al. 2008). Therefore we fit a broken power law to the $\Gamma_{2-10keV}$ vs. Log(FWHM$_{H\beta}$) data, and find the following

best-fit parameters:

(i) when Log(FWHM$_{H\beta}$) $\leqslant$ 3.61,

$$\Gamma = (-0.87 \pm 0.02) Log(FWHM_{H\beta}) + (4.90 \pm 0.09) \quad (5.14)$$

(ii) when Log(FWHM$_{H\beta}$) $>$ 3.61,

$$\Gamma = (-0.03 \pm 0.02) Log(FWHM_{H\beta}) + (1.86 \pm 0.09) \quad (5.15)$$

The best-fit break FWHM$_{H\beta}$ is 4070±90 km s^{-1} (Log(FWHM$_{H\beta}$) = 3.61±0.01), which is consistent with that found by Sulentic et al. (2008).

The only source included in the correlation whose $\Gamma_{2-10keV} < 1.5$, is 1E 1556+27.4, (the data for PG 1004+130 is superimposed but not used for the regression). A closer examination of the spectrum of this AGN shows that it probably has a strong reflection component modifying its intrinsic hard X-ray power law slope (Chapter 3). All other objects have values consistent with $\Gamma_{2-10keV} > 1.5$. The differences in the results of Zhou10a and our work are not only because we performed our correlation fitting using Log(FWHM$_{H\beta}$), but also because their sample did not exclude BAL quasars and warm absorbers, whose low values of $\Gamma_{2-10keV}$ are probably not intrinsic. This will bias the correlation and increase the scatter.

Our sample includes six objects with FWHM$_{H\beta}$ >10000 km s^{-1}. These are the sources have average $<\Gamma_{2-10keV}>$= 1.76±0.14 independent of the FWHM$_{H\beta}$. This is slightly lower but still consistent with the $\Gamma_{2-10keV} = 1.97 \pm 0.31$ index found by S06,08, who included more high redshift, high luminosity sources, with FWHM$_{H\beta}$ > 10000 km s^{-1}.

The $\Gamma_{2-10keV}$ vs. M$_{BH}$ Correlation

The Hβ FWHM is frequently used to estimate the M$_{BH}$, using the relation M$_{BH} \propto$ FWHM$^2_{H\beta}$ (Wandel, Peterson & Malkan 1999; Woo & Urry 2002). The correlation of $\Gamma_{2-10keV}$ vs. FWHM$_{H\beta}$ implies a similar correlation in $\Gamma_{2-10keV}$ vs. M$_{BH}$. This is confirmed in our study as shown in the second row of Figure 5.9. The Spearman's rank test gives ρ_s=-0.3 (d_s=3×10^{-2}). The correlation shows a change in slope at Log(M$_{BH}$) = 7.82±0.02, which can be expressed as follows:

(i) when Log(M_{BH}) $\leqslant$ 7.82,

$$\Gamma_{2-10keV} = (-0.472 \pm 0.013) Log(M_{BH}) + (5.494 \pm 0.116) \quad (5.16)$$

(ii) when Log(M_{BH}) $>$ 7.82,

$$\Gamma_{2-10keV} = (0.044 \pm 0.011) Log(M_{BH}) + (1.458 \pm 0.091) \quad (5.17)$$

We show a plot of FWHM$_{H\beta}$ vs. M_{BH} in Figure 5.10. This is an independent plot as our M_{BH} are derived from the SED continuum fits rather than being directly measured from FWHM$_{H\beta}$. The OLS regression gives $M_{BH} \propto$ FWHM$_{H\beta}^{1.16}$, with a $1\sigma = 0.4$ dex. The cyan triangle symbol in the figure shows the position of the break in FWHM$_{H\beta}$ vs M_{BH}. We note that this point lies within $\pm 1\sigma$ of the regression line, suggesting that the similar correlations found between $\Gamma_{2-10keV}$ vs. Log(FWHM$_{H\beta}$) and $\Gamma_{2-10keV}$ vs. Log(M_{BH}) are indeed caused by the tight correlation between FWHM$_{H\beta}$ and M_{BH}. But $\Gamma_{2-10keV}$ has weak dependence on M_{BH} for Log(M_{BH}) $>$ 7.82, with a mean value of 1.84$\pm$0.21.

5.3.6 Other Strong Correlations

The diverse correlations found in small parameter groups imply more correlations among all these parameters. We show some significant correlations in Figure 5.12. These include decreasing λ_{Edd}, $\kappa_{2-10keV}$, κ_{5100} with increasing Hβ FWHM and M_{BH}. Binned data points are shown as cyan crosses. The dashed orange line in each panel is the bisector regression line.

The $\kappa_{2-10keV}$ vs. $L_{2-10keV}$ correlation

Marconi04 and Hopkins07 reported a strong positive correlation in $\kappa_{2-10keV}$ vs. $L_{2-10keV}$, based on a quasar SED template and the α_{ox} vs. L_{2500} correlation reported by Steffen et al. (2006). VF07 tested the same correlation in their low redshift AGN sample but found no correlation (see Figure 5.11). We tested this correlation in our sample and confirmed VF07's result (see Figure 5.11). A highly dispersed anti-correlation of $\kappa_{2-10keV}$ vs. $L_{2-10keV}$ is found in our study.

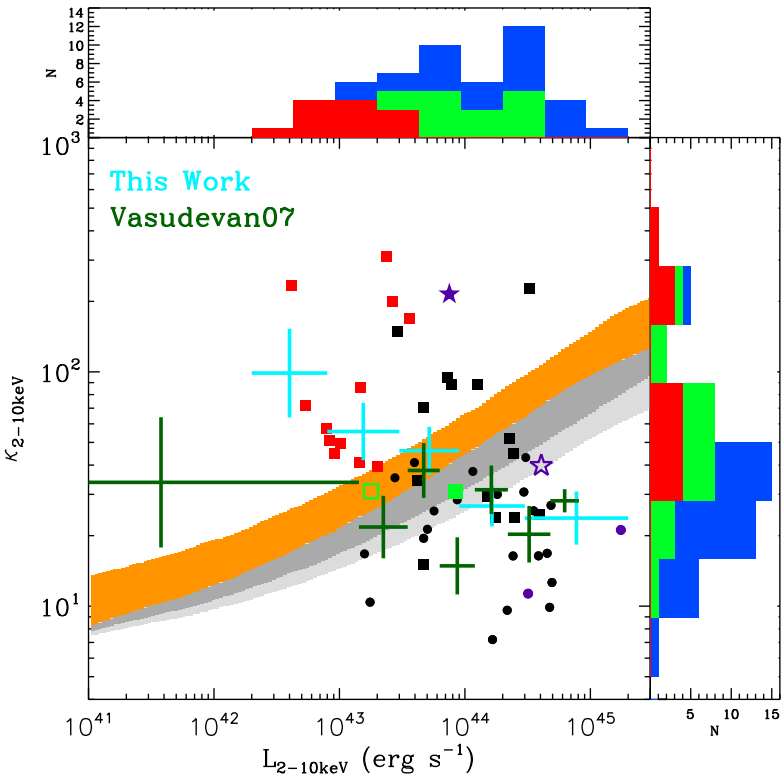

Figure 5.11: $\kappa_{2-10keV}$ vs. $L_{2-10keV}$. Different symbols represent the same type of sources as in Figure 5.2. The orange and gray shaded regions represent the theoretical $\kappa_{2-10keV}$ with $\pm 1\sigma$ scattering at each $L_{2-10keV}$ in Hopkins07 and Marconi04. The green data points are reproduced from Fig.3 in VF07.

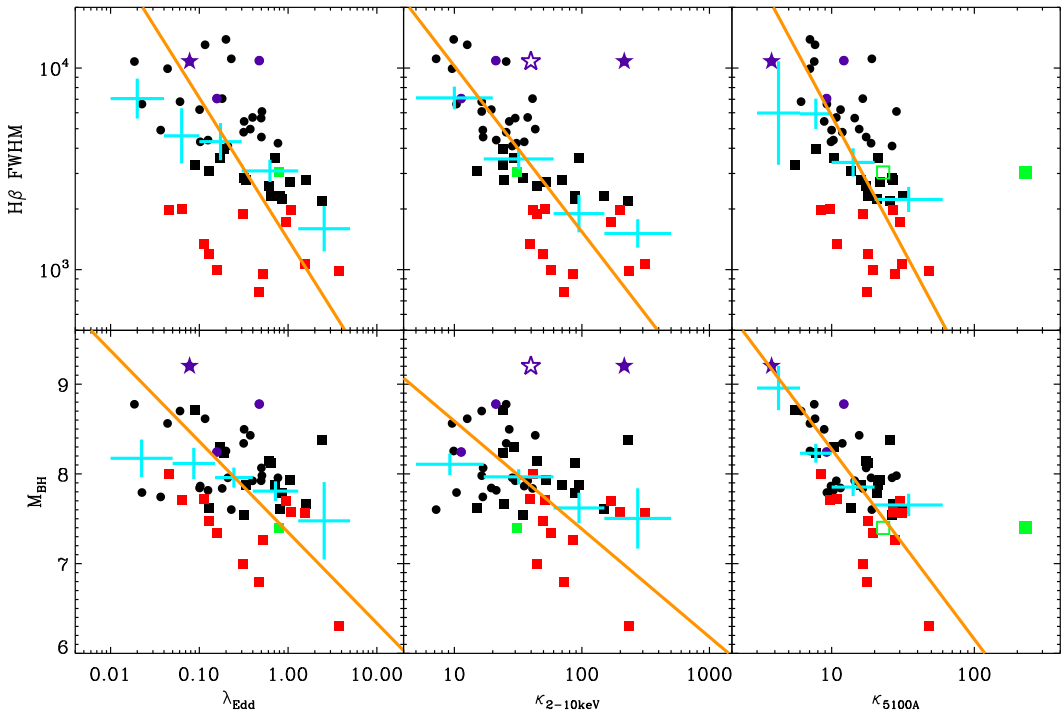

Figure 5.12: Examples of some good correlations not reported previously. In each panel the various symbols represent the same types of source as in Figure 5.2. The solid orange line is the bisector regression line. The cyan symbols are the binned data points over the X-axis with a 1 standard error on the Y-axis.

For the well sampled high X-ray luminosity region ($L_{2-10keV}$ >10^{43} erg s^{-1}), both VF07 and our samples show very similar distribution and dispersion. NLS1s in both samples mainly populate the regions of $\kappa_{2-10keV}$ >100 and 10^{42} erg s^{-1} <$L_{2-10keV}$ <10^{43} erg s^{-1}, and deviate from the correlation suggested by Marconi04 and Hopkins07. The main difference from VF07 is that our sample have more sources within the range of 3×10^{42} erg s^{-1} <$L_{2-10keV}$ <10^{43} erg s^{-1}, while VF07 sample contains three extraordinary weak X-ray sources whose $L_{2-10keV}$ < 2×10^{42} erg s^{-1}. Thus we think those intrinsically X-ray weak ($L_{2-10keV}$ ~10^{42} $ergs^{-1}$) sources may populate the low $L_{2-10keV}$, small $\kappa_{2-10keV}$ region, creating a scattered distribution in the $\kappa_{2-10keV}$ vs. $L_{2-10keV}$ plot. The correlations from Marconi04 and Hopkins07 may have underestimated the uncertainties in using α_{ox} vs. L_{2500} correlation (see discussion in Section 5.3.1) and the universal quasar SED template (e.g. Elvis et al. 1994; VF07; Chapter 3). However, we cannot rule out the possibility that the behavior of nearby

Table 5.4: The cross-correlation matrix of the 9 key SED parameters. ID 1∼9 are given to each parameter. ρ_s is the Spearman's rank coefficient. d_s is the logarithm of the significance level of being random distribution.

Parameters		$\Gamma_{2-10keV}$	$\kappa_{2-10keV}$	κ_{5100A}	λ_{Edd}	Hβ FWHM	M_{BH}	α_{ox}	L_{bol}	$L_{2-10keV}$
						$km\ s^{-1}$	$M_\odot$		10^{+44}	10^{+44}
			log	*log*	*log*	*log*	*log*		*log*	*log*
$\Gamma_{2-10keV}$	ρ_s	1	0.73	0.32	0.40	-0.72	-0.33	0.39	0.05	-0.38
	d_s	-∞	-8.	-2.	-2.	-8.	-2.	-2.	-0.	-2.
$\kappa_{2-10keV}$	ρ_s	—	1	0.64	0.60	-0.81	-0.45	0.74	0.12	-0.49
	d_s	—	-∞	—	-5.	-12.	-3.	-9.	-0.	-3.
κ_{5100A}	ρ_s	—	—	1	0.80	-0.56	-0.60	0.32	0.20	-0.24
	d_s	—	—	-∞	-11.	-5.	-5.	-2.	-1.	-1.
λ_{Edd}	ρ_s	—	—	—	1	-0.40	-0.24	0.38	0.62	0.16
	d_s	—	—	—	-∞	-2.	-1.	-2.	-6.	-1.
Hβ FWHM	ρ_s	—	—	—	—	1	0.64	-0.48	0.17	0.63
	d_s	—	—	—	—	-∞	-6.	-3.	-1.	-6.
M_{BH}	ρ_s	—	—	—	—	—	1	-0.03	0.55	0.78
	d_s	—	—	—	—	—	-∞	-0.	-4.	-10.
α_{ox}	ρ_s	—	—	—	—	—	—	1	0.33	-0.17
	d_s	—	—	—	—	—	—	-∞	-2.	-1.
L_{bol}	ρ_s	—	—	—	—	—	—	—	1	0.78
	d_s	—	—	—	—	—	—	—	-∞	-10.
$L_{2-10keV}$	ρ_s	—	—	—	—	—	—	—	—	1
	d_s	—	—	—	—	—	—	—	—	-∞

Seyfert AGNs are different from quasars at higher redshift.

5.4 A Study of Correlations between All The 9 Key SED Parameters

To summarize the various correlations discussed in the previous section, we performed a systematic correlation study of the following key SED parameters: $\Gamma_{2-10keV}$, $\kappa_{2-10keV}$, κ_{5100A}, λ_{Edd}, FWHM$_{H\beta}$, M_{BH}, α_{ox}, L_{bol} and $L_{2-10keV}$.

First, a correlation matrix was constructed as shown in Table 5.4. The Spearman's rank coefficient and probability of a null hypothesis are given. The table shows that there are some sub-groups of parameters which are strongly coupled with each other. For example, $\kappa_{2-10keV}$, κ_{5100A} and λ_{Edd} are coupled; $\Gamma_{2-10keV}$, Hβ

FWHM and $\kappa_{2-10keV}$ are also coupled with each other. The strong correlation between Hβ FWHM and $\kappa_{2-10keV}$ can be expressed by the following equation derived from a bisector regression analysis:

$$Log(\kappa_{2-10}) = (-1.22\pm0.12)Log(FWHM) + (5.88\pm0.45) \quad (5.18)$$

There also appears to be a sub-group consisting of M_{BH}, L_{bol} and $L_{2-10keV}$, and a sub-group consisting of M_{BH}, Hβ FWHM and $L_{2-10keV}$. However, correlations within these sub-groups are probably a result of selection effects arising from our sample selection criteria. Inclusion of extremely weak $L_{2-10keV}$ sources may weaken or eliminate the correlations between $L_{2-10keV}$ and other parameters.

The observed properties of AGN should be ultimately driven by the black hole mass, mass accretion rate, black hole spin and orientation angle. We have assumed the simplest Schwarzschild black hole in our model and so its spin is not considered. Uncertainties introduced by orientation angle should also be small since our sample only contains unobscured Type 1 AGNs. Therefore, the remaining intrinsic parameters are just the black hole mass and mass accretion rate (or equivalently, Eddington ratio)

We can examine the correlations further by performing a principal component analysis (PCA) on the correlation matrix formed by Pearson's correlation coefficient (Boroson & Green 1992). The dimension of this matrix is 9, so the outcome of the PCA must contain 9 normalized eigenvectors (principal components: PCs), each associated with a positive eigenvalue. Each PC is a linear combination of the 9 SED parameters, and is orthogonal to all the other PCs. The sum of the 9 eigenvalues equals 9. A higher eigenvalue would suggest a larger fraction of correlations contained in the direction of the corresponding eigenvector.

The *EIGENQL* program in `IDL` (Interactive Data Language) v6.2 was used to perform the PCA. We found that the first three eigenvectors contain 90% of the total correlations in the matrix, i.e. 50% in eigenvector 1 (PC1), 30% in eigenvector 2 (PC2) and 10% in eigenvector 3 (PC3). To determine the actual contributors of these eigenvectors, we cross-correlated them with the 9 SED parameters. Table 5.5 lists the Spearman's rank coefficients. It is clear that PC1 correlates/anti-correlates very

Table 5.5: The cross-correlation of the three principal eigenvectors with the 9 key SED parameters. The coefficients given are from the Spearman's rank test.

	Eigenvector 1	Eigenvector 2	Eigenvector 3
Property	50%	30%	10%
$\Gamma_{2-10keV}$	0.74	0.13	0.32
$\kappa_{2-10keV}$	0.92	0.25	0.26
κ_{5100A}	0.70	0.32	-0.43
λ_{Edd}	0.54	0.71	-0.33
Hβ FWHM	-0.92	0.08	-0.15
M_{BH}	-0.72	0.44	0.34
α_{ox}	0.55	0.44	0.56
L_{bol}	-0.13	0.98	0.03
$L_{2-10keV}$	-0.66	0.68	-0.13

well with most SED parameters, except for L_{bol}. The highest correlation strength is for Hβ FWHM and $\kappa_{2-10keV}$. These in turn are probably proxies for the physical variables of M_{BH} and λ_{Edd}. PC2 is dominated by L_{bol} which confirms that L_{bol} is a relatively independent variable. We have assumed that $L_{bol} = \mu \dot{M} c^2$, where μ is the standard accretion efficiency of 0.057 (see Chapter 3), so PC2 is in effect dominated by the mass accretion rate $\dot{M}$. PC3 is dominated by α_{ox}, but its contribution to the total set of correlations is small compared to PC1 and PC2. The other seven eigenvectors share the remaining 10% of correlations, and are therefore not important. It was also reported by Boroson (2002) that the PC1 from the correlation matrix of optical emission line parameters is driven predominantly by the Eddington ratio, while the PC2 from the same matrix is dominated by the luminosity. Therefore, the PC1 and PC2 from our correlation matrix of SED parameters have a similar basis to the two eigenvectors reported by Boroson (2002).

5.5 The Mean SEDs

5.5.1 Diversity of the Mean SEDs

In Chapter 3 we derived the mean SED for the 12 NLS1s in our sample, and compared this with the mean SEDs of another two groups of BLS1s. We showed that the SED shape changes dramatically as the Hβ FWHM increases. Since quasar SED are not uniform, modelling their spectra and evolution using a single template such as that of Elvis et al. (1994), will mask out a large dispersion in their intrinsic properties. In our study we aim to minimize this dispersion by grouping the SED based on each of the 9 SED parameters discussed in the previous section.

There are 51 AGNs in our sample. For each of the 9 SED parameters we sorted the sources according to the parameter value, and then classified the sample into three subsets so that each subset includes 17 sources. Then the BAL quasar PG 1004+130 was excluded from its subset. The SEDs constructed using Model-B in this chapter were first corrected for redshift, and then divided into 450 energy bins between 1 eV and 100 keV in the logarithm. Within each subset we calculated the average luminosity in every energy bin in logarithm, together with the 1σ deviation. Then we derived the mean SED for each group together with the 1σ dispersion. The same calculation was repeated for each of the 9 parameters, so that there are three mean SEDs for each parameter. No special note was made for the NLS1s because their defining parameter, Hβ FWHM, is one of the 9 parameters.

Figure 5.13 shows our results. Each row displays the three mean SEDs divided according to the parameter shown in the panel title. The SEDs have all been renormalized to the mean luminosity at 2500Å of each subset. To highlight the differences among these SEDs, we mark the locations of 2500Å and 2 keV by the vertical orange lines. The relative height of these two lines directly reflects the value of α_{ox}, and the height of the bar at 2 keV shows the dispersion in α_{ox} since the co-added SED's are all normalized at 2500Å. We also mark the energy peak for each mean SED by the vertical thick purple line. The mean values of other parameters are given in each plot for comparison.

We find that the mean SED changes in a similar way with all the parameters

except L_{bol}. The energy at which the disc emission peaks decreases along with the ratio of luminosity in the disc compared to the Comptonised components, and the 2-10 keV spectral slope. Our stringent sample selection means that these spectral differences are intrinsic rather than due to absorption/extinction.

If the SED changes are determined solely by one of the parameters considered here, then binning based on that parameter should result in the minimum dispersion within each individual binned SED, and maximal difference between the three SEDs spanning the range in that parameter. However, the SED changes should ultimately be physically dependent on changes in M_{BH} and λ_{Edd}. Since there are two dependent variables no single parameter will completely determine the behaviour. Hence the dispersion within each of the three binned SEDs is minimized (and the difference between them is maximized) for composite parameters which depend on both λ_{Edd} and M_{BH} such as $\kappa_{2-10keV}$, κ_{5100} and Hβ FWHM rather than the fundamental physical parameter λ_{Edd}. Future work with larger samples can improve on this study by selecting a subsample of AGN with different λ_{Edd} but similar M_{BH}. Such mass selected samples would give the best comparison to the SED changes in Black Hole Binaries (BHB), which all have the same mass to within a factor of ~ 2.

5.5.2 Discussion of the Mean SEDs

Since our SED fitting is based on a physical model, we can 'correct' for the mass dependence of the SED shape to get an estimate for the SED differences in AGN as a function solely of λ_{Edd}. This is shown in Done et al. (2011) for a $M_{BH} = 10^8 M_{\odot}$ and forms the basis of a direct comparison with the BHB spectral states seen for these $M_{BH} = 10 M_{\odot}$ systems as λ_{Edd} changes. This has many superficial similarities to the dramatic state change seen in BHB as their luminosity increases. The SED changes from a 'low/hard state' being dominated by Comptonisation, with a hard X-ray spectral index $\Gamma_{2-10keV} < 2$, and the disc component peaking at rather low temperature, to a 'high/soft state' where the disc dominates the luminosity and the X-ray spectral index is softer, $\Gamma_{2-10keV} \sim 2 - 2.2$ (see e.g. the review by Done, Gierliński & Kubota 2007). However, this occurs at $\lambda_{Edd} \sim 0.02$ for moderate

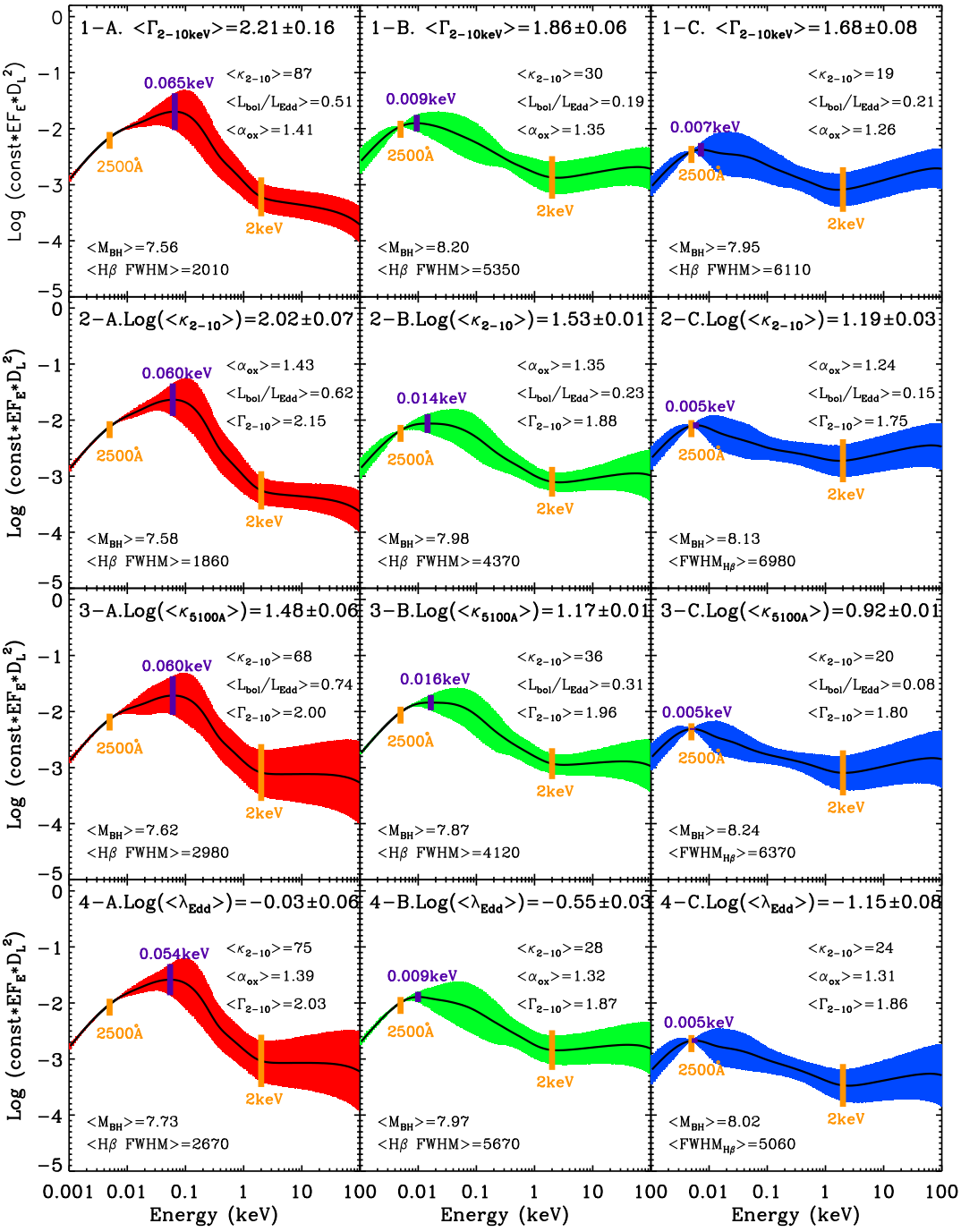

Figure 5.13: The AGN mean SEDs based on different values of the 9 key parameters from Model-B fitting (i.e. including the effect of a colour temperature correction). For each parameter, the 51 sources are sorted according to the parameter value, and then are divided into three equal subsets so that each contains 17 sources. PG 1004+130 is excluded from its subset. Finally, a mean SED is constructed for each of the three subsets after renormalizing each individual SED to the mean luminosity at 2500Å of that subset. The three panels (A, B, C) in each row show the mean SEDs for the subsets classified by the parameter shown in the panel title. In each panel the solid curve is the mean SED, while the shaded coloured region is the $\pm1\sigma$ deviation. The 2500 Å and 2 keV positions are marked by the vertical solid orange lines, whose relative height indicates the value of α_{ox}. The peak position of the SED is marked by the vertical solid purple line. The average values of some other parameters in that subset are also shown in the panel. Each mean SED has been rescaled by the same arbitrary constant on the Y-axis which is 1×10^{-46}. Note that the energy ranges E < 6 eV and 0.3 keV < E < 10 keV, are covered by SDSS, OM and EPIC data respectively, while the SED in the rest energy bands is determined from an extrapolation of the best-fit model.

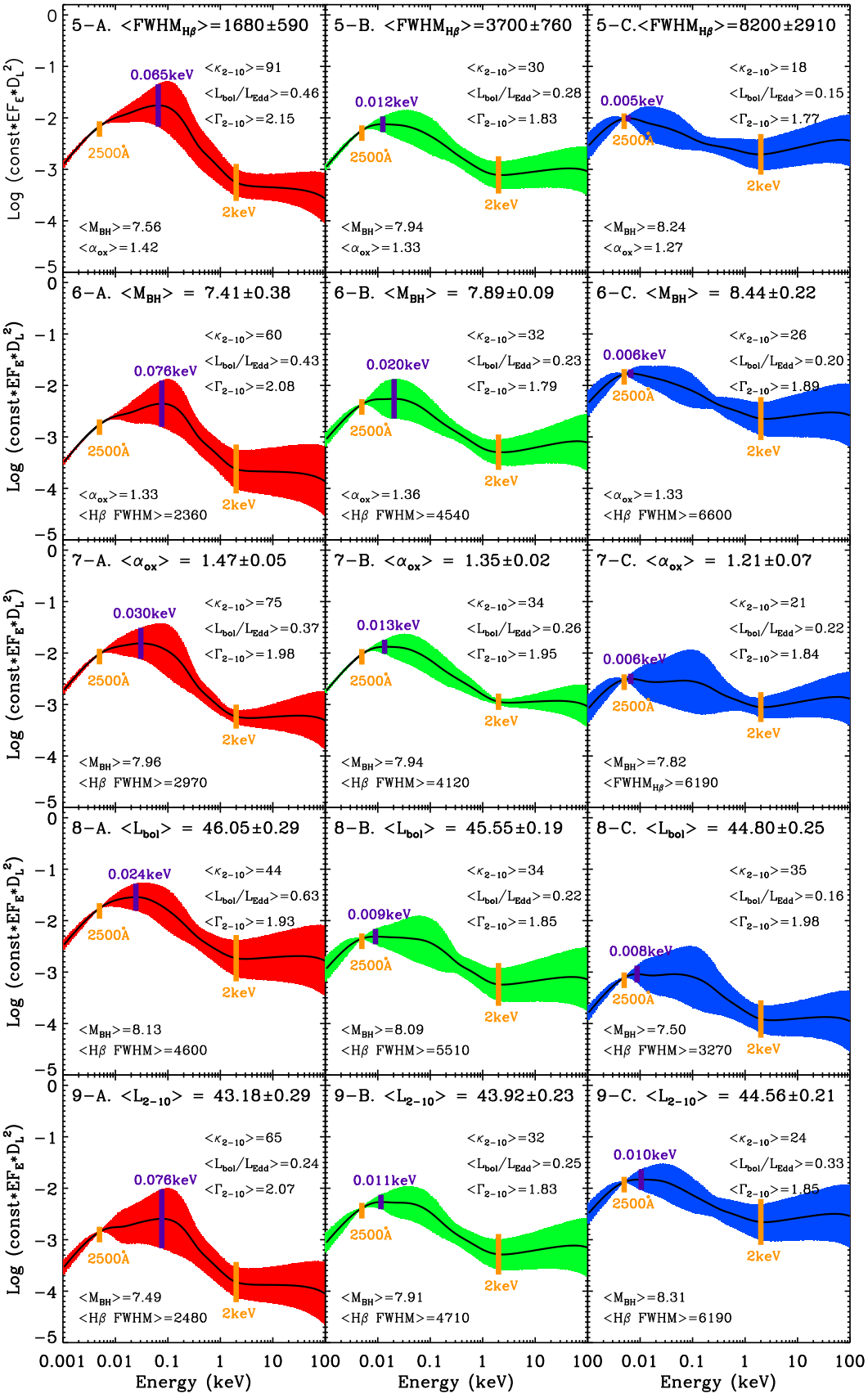

Figure 5.13: *continued*

changes in mass accretion rate (Maccarone 2003), an order of magnitude lower than the spectral differences seen here in the AGN (see also the discussion in Done et al. 2011). This could indicate some subtle differences in the transition due to the very different masses, but in BHB this transition is also associated with the radio jet switching off (Fender, Belloni & Gallo 2004). If the Compton dominated states in AGN correspond to the low/hard state in BHB then we would expect them to be radio loud. However, AGNs are radio-quiet by a factor of 10:1.

This makes unlikely an identification of the two lower λ_{Edd} AGN templates as analogs to the low/hard (or intermediate state) seen in BHB. Instead, there is another state in BHB called the 'very high' or 'steep power law state', where the disc also peaks at a lower temperature than expected, and where the Comptonised component contains a large fraction of the total luminosity (see e.g. the review by Done, Gierliński & Kubota 2007). However, this state has $\Gamma_{2-10keV} > 2.5$ i.e. the hard X-ray spectra are steep. Yet these AGN have $\Gamma_{2-10keV} < 2$, as well as a soft X-ray excess component. Therefore, to match the AGN with the very high state would require that reflection and/or complex absorption modify the spectrum, producing an apparent soft X-ray excess and a hard power law from an intrinsically steep spectrum. However, the time variability properties of individual objects make it clear that these high mass, relatively low Eddington ratio objects do indeed have two separate components. The intrinsically hard power law which is more variable on short timescales, and a soft X-ray excess which is relatively constant on these timescales but more variable over longer times (e.g. Mkn509: Mehdipour et al. 2011; Noda et al. 2012).

Therefore, the two lowest λ_{Edd} spectra shown in Figure 5.13 do not look similar to *any* state observed in BHB. Yet these sources span the typical QSO accretion rates (e.g. Steinhardt & Elvis 2010), and indeed our templates are very similar to the mean SED in Elvis et al. (1994). It seems that these most common QSO SED's are not simply analogous to BHB accretion flows. Only the very rare AGN SED's with the highest λ_{Edd} can be well matched to the BHB, as they are similar to the high/soft state (see also Done et al. 2011).

5.6 Analogy with Black Hole Binary Systems

BHB show (at least) three different states, variously termed the low/hard, high/soft (i.e. thermal dominant or disc dominant) and very high (a.k.a. steep power law state). Spectra from this latter state appear very similar to intermediate spectra seen as the source makes a transition from the low/hard to high/soft states (e.g. Belloni et al. 2005). It is plain from Figure 5.14b that the highest L/L_{Edd} spectrum of M3 (see caption of Figure 5.14) is very much like a disc dominated high/soft state spectrum with a small amount of additional soft Comptonisation. The lower luminosity spectra are more ambiguous, and could be either low/hard state spectra or intrinsically steeper very high state spectra which are modified by complex absorption/reflection. We explore each of these possibilities below, and then discuss how we can distinguish between the two scenarios.

5.6.1 AGN sequence as a low/hard to high/soft transition

The increasing dominance of the disc with increasing L/L_{Edd}, together with the switch from hard to soft 2-10 keV X-ray emission is initially very reminiscent of the spectral transition seen in stellar mass galactic black hole binary systems (BHB). These show a clear switch from a hard power law dominated low/hard state to disk dominated high/soft state with a steep tail to higher energies (see e.g. the reviews by McClintock & Remillard 2006 hereafter MR06; DGK07). This is generally interpreted as a decreasing transition radius between a cool disc and hot comptonised region (Esin, McClintock & Narayan 1997), matching the decreasing r_{corona} seen in our AGN fits.

The BHB in the low/hard state also often show a complex continuum, with a softer Comptonisation component from the outer parts of the flow which intercept more seed photons from the disc, together with a harder tail from the hotter central regions (Ibragimov et al. 2005; Takahashi et al. 2008; Makishima et al. 2008; Kawabata & Mineshige 2010). This inhomogeneous Comptonisation in BHB is also required to explain the time lags seen in the data (Kotov, Churazov & Gilfanov 2001; Arévalo & Uttley 2006). Thus the two component (soft and hard) Comptonisation

required to fit the X-ray spectra in M1 and M2 could be analogous to the two component Comptonisation spectra seen in the BHB low/hard state.

However, there are also some significant differences. The transition in BHB occurs at $L/_{Edd} \sim 0.02$ when the mass accretion rate is slowly declining, (Maccarone 2003). This is as expected for an advection dominated flow, which collapses when the energy transfer between the ions and electrons becomes efficient. The collapse depends only on optical depth of the flow rather than black hole mass, so should be the same for both AGN and BHB (Narayan & Yi 1995). Yet in these AGN the low/hard state must persist up to at least $L/L_{Edd} \sim 0.2$ to explain M2. Such high transition luminosities are only seen in BHB during the rapid rise during disc outbursts (see e.g. the compilation by Yu & Yan 2009) which drive the flow out of its equilibrium states (Gladstone, Done & Gierliński 2007). Our M2 spectrum would then be analogous to the intermediate state seen during this transition, but this transition is very rapid in BHB so these intermediate spectra are rare (Dunn et al. 2009). By contrast, M2 is very similar to the mean QSO spectral template of Elvis et al. (1994). and has similar mass and mass accretion rate as a typical QSO (Kollmeier et al. 2006; Steinhardt & Elvis 2010) so it must be a very common state. Thus it does not seem very likely that all these AGN are preferentially seen during a dramatic rise in mass accretion rate. The only real possibility for this AGN sequence to represent a low/hard to high/soft transition is if there is some weak mass dependence on the critical luminosity not predicted by the advective flow models (Narayan & Yi 1995).

5.6.2 AGN sequence as high mass accretion rate transition

This motivates us to explore the alternative possibility, that the AGN spectra seen here are above the low/hard state transition luminosity, so correspond to one of the high mass accretion states in BHB. The hard X-ray tail ($\Gamma < 2$) is incompatible with this, as these high mass accretion states in BHB almost always have $\Gamma > 2$ (MR06; DGK06). Hence the observed hard X-ray spectra in M1 and M2 would have to be distorted by complex absorption and/or reflection, whereas M3 already has

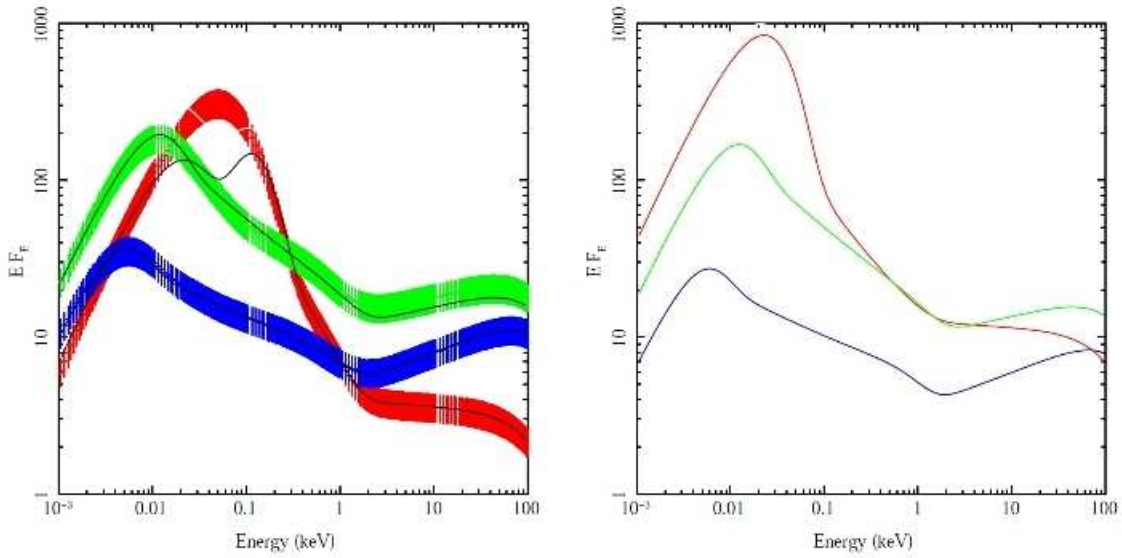

Figure 5.14: a) The three mean spectra from Figure 5.13, derived using $f_{col} = 1$, but we show the fit (excluding the unobservable 0.01-0.3 keV region) with $f_{col} = 2.5$ for the lowest mass/highest mass accretion rate spectrum, where the disc temperature exceeds $T_{scatt} = 105$ K. M1 (blue) has $L/L_{Edd} = 0.058$ and black hole mass of 1.4×10^8 $M_\odot$. M2 (green) has $L/L_{Edd} = 0.23$ and black hole mass of 1.1×10^8 $M_\odot$. M3 (red) has $L/L_{Edd} = 0.77$ and black hole mass of 2.6×10^7 $M_\odot$. b) shows the spectral evolution with L/L_{Edd} alone by redoing each model for a single black hole mass of 10^8 $M_\odot$ (and $f_{col} = 1$).

a soft 2-10 keV spectrum, so does not require complex absorption. This potential difference is supported by the behaviour of the soft X-ray excess. In the highest L/L_{Edd} spectra (M3 and REJ1034+396) the soft excess appears as a true excess over a $\Gamma = 2$-2.2 extrapolation of the 10 keV flux level down below 2 keV, unlike M2, M1 and PG 1048+231 where the vfv flux level at 0.1 keV is roughly similar to that at 10 keV. The soft excess seen in the highest L/L_{Edd} spectra could then represent a 'true' soft X-ray excess connected to the disc as its approaches Eddington (perhaps bulk motion Comptonisation from turbulence: Socrates et al 2004, or trapped radiation advected along with the flow which can then be released in the plunging region: Sadowski 2009), while the 'bend' seen in the lower L/L_{Edd} is a 'fake' soft excess, where the apparently hard 2-10 keV spectrum and steeper 0.3-2 keV excess are both distortions from complex absorption and/or reflection. Complex absorption seems quite likely in an AGN environment, as a UV bright disc is very efficient in producing a strong wind from UV line driving (Proga, Stone & Kallman 2000). The wind should become stronger as L/L_{Edd} increases, which is at first sight inconsistent with the requirement that the spectral distortion is larger in M1 and M2 than in M3. However, the wind also depends strongly on black hole mass as it is launched from the region where the disc temperature is around the energies of the strong UV resonance lines, as this is where the opacity peaks. The increase in UV opacity for a lower temperature (i.e. higher mass, lower L/L_{Edd}) disc may more than compensate for the lower L/L_{Edd}. The wind mass loss rate may even be substantial enough to modify the disk structure, significantly reducing the mass accretion rate below the wind launching point. We caution that this may require new disc models, which allow the mass accretion rate to change with radius. The fraction of luminosity emitted in the inferred $\Gamma \sim 2.2$ tail is substantial in both M1 and M2. These spectra would then correspond to the very high/steep power law state seen in BHB (e.g. DK06), whereas M3 would still be a disc dominated state with a small additional Comptonisation component. However, the M1/M2 spectra do not appear to be modified by complex X-ray absorption. While the signal-to-noise in PG 1048+213 is not overwhelming, its spectrum is very similar to the much better data from Mkn 509 which has similar mass and mass accretion rate (Mehdipour et

al 2011; Noda et al 2011). Here the 'soft excess' clearly has different variability to the 'power law', supporting a true two component interpretation of the spectrum (Noda et al 2011). It is the higher mass accretion rate, low mass objects (more like M3) for which the complex spectral variability is most often interpreted in terms of reflection and/or complex absorption (Fabian et al 2002; Fabian et al 2009; Ponti et al (2010); Miller et al 2007; 2009; 2010; 2011; Turner et al 2007).

5.6.3 Distinguishing between a low/hard and very high state

The shape of the power spectra of the rapid X-ray variability correlates with spectral state in BHB. However, both low/hard and very high states have variability power spectra which can be roughly characterised as band limited noise, i.e. have power spectra with both a low and high frequency break (see e.g. MR06; DGK07). Conversely, stationary high/soft states (in Cyg X-1) show only a high frequency break (e.g.MR06; DGK07). Thus both possibilities predict that the objects contributing to M2 should predominantly have power spectra which are band limited noise, while those which contribute to M3 should extend unbroken to low frequencies. Currently there are no objects in our samples with well defined variability power spectra, but objects with similar L/L_{Edd} to those in M2/M3 typically show only a high frequency break i.e. are more similar to the high/soft state in Cyg X-1 (see e.g. the review by McHardy et al. 2010). However, we caution that if M1 and M2 do indeed correspond to very high state spectra, distorted by complex absorption/reflection, then their variability will also be similarly distorted. Variable obscuration in a clumpy absorber will add to the intrinsic variability, changing the shape and/or normalisation of the power spectrum. Even in the reflection model there are differences in predicted variability from the more neutral reflection seen in AGN compared to the much higher ionisation expected for the hotter discs in BHB (Done & Gardner 2011, in preparation). The only clearcut distinction may be the high energy spectral shape since this should be much less affected by atomic processes. Low/hard state spectra are intrinsically hard up to a thermal Comptonisation rollover at a few hundred keV (e.g. Ibragimov et al. 2005; Takahashi et al. 2008; Makishima et al. 2008), while

the high/soft and very high states are soft and extend unbroken beyond 511 keV (Gierliński et al 1999; Zdziarski et al. 2001; Gierliński & Done 2003). We already know that local AGN do show hard spectra in the 20-200 keV band, with a clear high energy rollover (Zdziarski et al. 1995), but these have mean luminosity below M1, so clearly correspond to a low/hard state (Vasudevan et al. 2009). Currently there are no objects in our sample with well defined high energy spectra. Sensitive higher energy data from NuSTAr or ASTRO-H on the objects in the M1/M2 sample should give a clear test of their spectral state.

5.7 Discussion

5.7.1 Selection Effects

Biases and systematics inherent in this sample have already been discussed at length in Chapter 3 and Chapter 3I. The principal imposed selection effect is that sources in our sample are bright nearby AGN ($z < 0.4$). The luminosity of our sources is higher than the average among nearby sources, but only moderate with respect to samples containing higher redshift sources (e.g. Green09; Lusso10). Our sample contains very few sources with $L_{2-10keV} < 5{\times}10^{42}$ erg s^{-1} or $\lambda_{Edd} < 0.05$. As discussed in Section 5.3.2 and Section 5.3.6, those very low luminosity sources may not follow the linear regression line in the $\kappa_{2-10keV}$ vs. λ_{Edd} plot in Figure 5.6, and these sources may populate the low $L_{2-10keV}$, low $\kappa_{2-10keV}$ region in Figure 5.11. It is also possible that these sources may not follow other correlations reported in this chapter, thereby weakening the correlations between $L_{2-10keV}$ and M_{BH} and Hβ FWHM. Further studies of large samples are required to test such possibilities.

The weak anti-correlation found between λ_{Edd} and M_{BH} (Table 5.4) also implies some selection effect. Sources having both low black hole mass and low mass accretion rate are unlikely to be included in our sample as they would be too faint. Hence low mass sources in our sample will have relatively high λ_{Edd}. For higher mass sources, their luminosity will peak when there is a considerable supply of gas around them to be accreted. This occurs around redshift $\sim$2, and as the available

gas decreases, the mass accretion rate of high mass AGN in the local universe is suppressed (so-called downsizing, Fanidakis et al. 2010). Therefore, in the local universe high mass sources should have low λ_{Edd}, resulting in the weak anti-correlation found between M_{BH} and λ_{Edd} (Done et al. 2011).

There are also redshift selection effects. Although comparison of parameter correlations with previous work (based on larger samples) results in a general consistency, the question remains whether there could be a redshift dependence in the correlations we find. However, there are some evidences that redshift evolution in the spectral properties of AGN may not be strong (Fan 2006).

5.7.2 Limitations of the Model and Uncertainties

There is another underlying question, whether the correlations found might arise artificially as a result of our model assumptions. We will consider this point in two ways:

First, there are no direct constrains on the parameters in our SED model. Compared with some previous work (e.g. VF07, Lusso10, Grupe10), our spectral fitting employs the least external constraints on the values of its parameters. The only parameter that is directly constrained is M_{BH}, whose value is restricted by the FWHM of the intermediate and broad components of the Hβ emission line. However, this range often spans more than one order of magnitude, and the best-fit M_{BH} did not exceed the model limits for most sources (see Table C1 of Chapter 3). Therefore this constraint should not be strong enough to cause systematics.

Second, for previously known correlations such as λ_{Edd} vs. $\kappa_{2-10keV}$, λ_{Edd} vs. $\Gamma_{2-10keV}$ and Hβ FWHM vs. $\Gamma_{2-10keV}$, our results are all consistent with past studies based on a variety of AGN samples. This suggests that the reported correlations should be intrinsic, and that our results are not strongly contaminated by model assumptions. As discussed in the previous sections, the differences between our results and those previously reported are mainly due to two reasons. One is our exclusion of highly obscured sources, which reduces the non-intrinsic dispersion within these correlations. The other reason is that our parameter values are derived

Table 5.6: The average value of parameters from the best-fit SEDs using Model-A (without a colour temperature correction, Chapter 3) and Model-B (with colour temperature correction). The values and their standard deviations are calculated separately for NLS1s, BLS1s and for the whole sample.

	NLS1s	NLS1s	BLS1s	BLS1s	Whole Sample	Whole Sample
Model-	A	B	A	B	A	B
$< \kappa_{2-10keV} >$	127^{+197}_{-77}	86^{+96}_{-45}	29^{+44}_{-17}	30^{+38}_{-17}	41^{+85}_{-27}	38^{+58}_{-23}
$< \kappa_{5100A} >$	29^{+37}_{-16}	20^{+13}_{-8}	13^{+17}_{-8}	14^{+14}_{-7}	16^{+23}_{-9}	15^{+14}_{-7}
$< \lambda_{Edd} >$	$0.95^{+5.33}_{-0.80}$	$0.35^{+0.99}_{-0.26}$	$0.27^{+0.81}_{-0.20}$	$0.25^{+0.52}_{-0.17}$	$0.36^{+1.42}_{-0.29}$	$0.27^{+0.61}_{-0.19}$
$<M_{BH}>$	7.11±0.54	7.37±0.47	8.04±0.48	8.10±0.41	7.83±0.64	7.93±0.52
$< \alpha_{ox} >$	1.42±0.08	1.39±0.10	1.34±0.16	1.34±0.15	1.36±0.14	1.35±0.14
$<L_{bol}>$	45.19±0.54	45.02±0.49	45.59±0.52	45.61±0.53	45.49±0.55	45.47±0.57

from a detailed spectral fitting, rather than from simply applying scaling relations which will contain high uncertainties.

However, the range of values for each of the 9 SED parameters discussed previously could be dominated by model uncertainties, except for $\Gamma_{2-10keV}$, whose measurement is relatively model independent. For this reason we did not adopt the uncertainties returned by `Xspec`, because they must be negligible compared with the model uncertainties. Such model uncertainties are very difficult to estimate, and the values of the same parameter derived from different SED models, can be quite different. As an illustration, in the following paragraphs we will compare the parameter values before and after introducing a colour temperature correction into our broadband SED model.

5.7.3 The Effect of the Colour Temperature Correction

The colour temperature correction is only important for sources having both a low black hole mass and a high mass accretion rate (see Done et al. 2011 and references therein). So it only affects a small fraction of all the sources in our sample, mainly the NLS1s. The main consequences of introducing a colour temperature correction by using Model-B (i.e. *optxagnf* in `Xspec` v12) are that M_{BH} increases, L_{bol} decreases and so λ_{Edd} decreases. For example, the λ_{Edd} of PG 2233+134 decreases significantly from 14 to 2.4 after using Model-B, making it much less extreme. $\kappa_{2-10keV}$ and κ_{5100A}

also decrease due to the decrease of L_{bol}. α_{ox} changes slightly but not significantly, because the luminosity at 2500Å is mainly constrained by the OM data (Chapter 3). Figure 5.15 compares the distribution of these parameters between Model-A (Chapter 3) and Model-B fitting. Table 5.6 lists the average values of these parameters for NLS1s, BLS1s and the whole sample, for both Model-A and Model-B fitting. This confirms that the large differences in results from the Model-A and Model-B fittings are mostly restricted to the NLS1s, whose colour temperature corrections are significant.

In order to further investigate the differences between using Model-A and Model-B, we redo all of the above cross-correlation analysis by adopting Model-A parameter values from Chapter 3, and then we compare the statistical results in the appendices. Appendix E.1 shows all of the correlation plots that could in principle be modified by the differences between the Model-A and Model-B fittings. In each plot the dashed gray lines are for Model-B fitting (this chapter), compared with the solid orange lines for Model-A fitting. It is clear that there are no significant changes in any of these correlation plots. This is further confirmed by the correlation matrix for Model-A fitting in Appendix D.4. Performing a PCA on this matrix, very similar eigenvectors and eigenvalues are obtained. Appendix E.2 shows the mean SEDs based on the parameter values obtained from Model-A fitting, which does not include the colour temperature correction. Therefore, we conclude that use of the refined Model-B compared with the original Model-A, does not alter the main results reported in this chapter, although for individual sources such as the NLS1s, the refined model should be more realistic.

5.7.4 Correction for Radiation Pressure

Marconi et al. (2008) suggested that the virial mass estimates should be corrected for the effects of radiation pressure (RP), especially for those sources with high Eddington ratios, such as the NLS1s. In our study the M_{BH} was not derived directly from the virial mass, but was only constrained by the virial masses calculated from the FWHM of the intermediate and broad components of the Hβ line. The final

estimate of M_{BH} is derived from the best-fit SED, and so there is no need to correct for the RP effect. However, we may still choose to derive the virial mass from using the FWHM of Hβ profile (narrow component subtracted), and then correct these values for the RP effect. Chapter 3 has listed and compared these masses (M_{RP}) with the best-fit masses (M_{BF}) from the SED fitting using Model-A. The distributions of these two estimates of masses are very similar, except that the average M_{RP} is 0.4 dex higher compared with M_{BF}.

As discussed in previous section, the SED fittings including the colour temperature correction (Model-B) increases the average M_{BF} by 0.27 dex for NLS1s, and 0.05 dex for BLS1s (Table 5.6). So for the NLS1s using Model-B fitting, the average M_{BF} is just 0.05 dex smaller than the average M_{RP}, while for the BLS1s the difference is still 0.34 dex. Furthermore, no significant difference is found in Table 5.4 if we substitute M_{RP} for M_{BF}, and cross-correlate with the other 8 SED parameters. The coefficients in Equation 5.16, 5.17 only differ by less than 1 σ when using M_{RP} instead of M_{BF}. This suggests that the difference between M_{RP} and M_{BF} is far less than the intrinsic dispersion in any of the correlations, and so is not important in our correlation studies.

5.7.5 The 4000 km s^{-1} Hβ FWHM Break

The FWHM$_{H\beta}$ = 2000 km s^{-1} is the conventional, but arbitrary value to distinguish between NLS1 and BLS1 (Goodrich 1989). Recently, the limit of 4000 km s^{-1} for the FWHM$_{H\beta}$ was claimed to be of special interest. For example, when AGNs are divided into two populations based on FWHM$_{H\beta}$ = 4000 km s^{-1} (population A: FWHM$_{H\beta}$ $<$ 4000 km s^{-1} and B: FWHM$_{H\beta}$ $>$ 4000 km s^{-1}), it appeared that most radio loud sources are contained in population B (Sulentic et al. 2008). Compared with the RL-RQ and the NLS1-BLS1 divisions, this dividing line in FWHM also seems to be more effective in distinguishing the different SEDs (Sulentic et al. 2008). Furthermore, Zhou10a reported that in the FWHM$_{H\beta}$ vs. $\Gamma_{2-10keV}$ correlation plot, there is a change in the slope at $\sim$4000 km s^{-1}, as consistent with our results. They also showed that the the broadest iron Kα lines, those with intrinsic width $\sigma > 0.5$

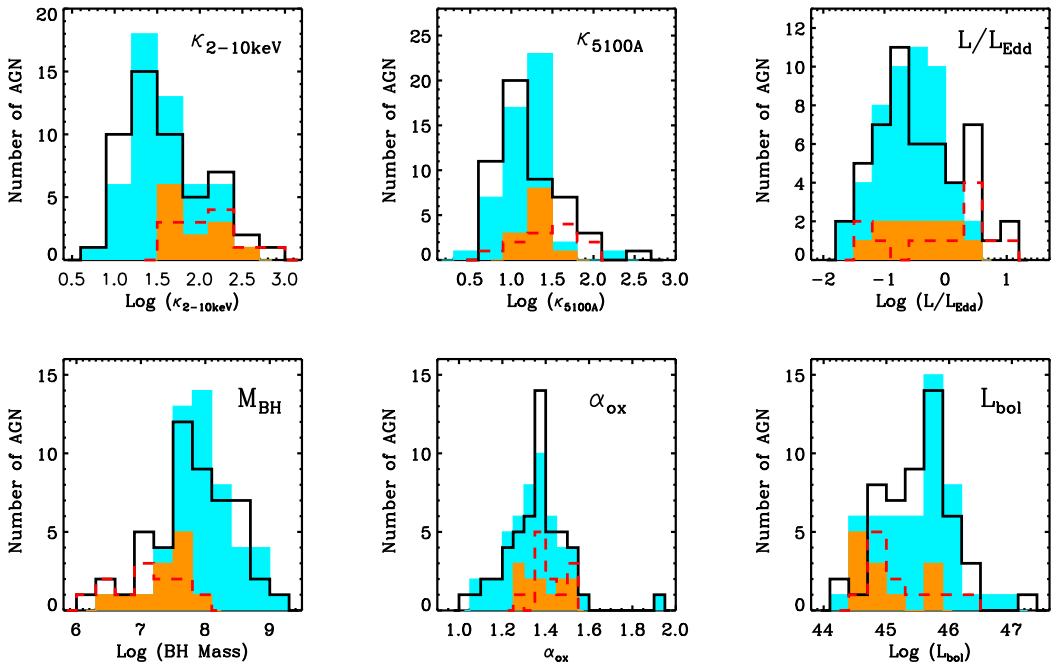

Figure 5.15: Comparison of parameter distributions between Model-A and Model-B SED fittings. In each panel the shaded cyan histogram is based on our modified SED fitting using Model-B (listed in Table D.3), with the 12 NLS1s highlighted by the shaded orange region. The solid black line shows the parameter histogram for Model-A fitting (listed in Table 3 of Chapter 3), with the dashed red line indicating the 12 NLS1s.

keV) have are all found in AGNs with FWHM$_{H\beta}$ < 4000 km s^{-1}.

In Section 5.3.5, we confirmed a slope change at FWHM$_{H\beta}$ = 4070±90 km s^{-1} in FWHM$_{H\beta}$ vs. $\Gamma_{2-10keV}$ correlation plot. All the three RL sources in our sample (purple symbols in Figure 5.9) have FWHM$_{H\beta}$ > 4000 km s^{-1}. To highlight the 27 population A sources in our sample, we use the square symbol to identify these sources in all correlation plots, and we show their distribution in the histograms as the green region. The 12 NLS1s among them are shown as the red region. The two-sided KS-Test was used to determine the significance of the difference between the distributions of the sub-samples for the NLS1-BLS1 division, and the population A-B division. Among the 9 SED parameters, the population A-B provides a slightly better division for the four parameters: $\kappa_{2-10keV}$, κ_{5100A}, λ_{Edd}, Hβ FWHM and

α_{ox}; while NLS1-BLS1 division is better for the other parameters (see Table 5.7). Therefore, the population A-B division for our RQ Type 1 AGN sample does not seem to be significantly better than the NLS1-BLS1 division.

5.8 Summary and Future Work

5.8.1 Summary of Principle Results

In this chapter, we have studied the SED properties of our Type 1 AGN sample. We employ a new broadband SED model (*optxagnf* in `Xspec` v12), which includes a colour temperature correction, to construct the SED for each source in the sample. Various parameters were obtained from the results of the SED fitting. A detailed statistical analysis was performed, which can be divided into three major parts:

• In the first part we studied the diverse correlations found among the SED parameters. We divided these parameters into five groups, according to previously reported correlations. Within each group we conducted a detailed cross-correlation analysis, and applied several regression methods. Our results are generally in good agreement with previous work. However, as a consequence of the unobscured nature of the sample and the more reliable parameter values that resulted from our refined spectral fitting, we were able to reduce the non-intrinsic dispersion and so obtain the intrinsic and better constrained correlations.

Table 5.7: The significance level of the difference in the NLS1-BLS1 pair and Population A-B pair for values of the 9 key SED parameters. The two-sided Kolmogorov-Smirnov test is applied. A smaller value suggests a greater difference within each sample division pair.

	$\Gamma_{2-10keV}$	$\kappa_{2-10keV}$	κ_{5100A}	λ_{Edd}	Hβ FWHM	M_{BH}	α_{ox}	L_{bol}	$L_{2-10keV}$
NLS1-BLS1	2×10^{-5}	5×10^{-5}	1×10^{-1}	5×10^{-1}	1×10^{-7}	1×10^{-5}	2×10^{-1}	4×10^{-3}	7×10^{-7}
Population A-B	1×10^{-4}	7×10^{-6}	5×10^{-3}	8×10^{-3}	4×10^{-11}	1×10^{-3}	1×10^{-2}	5×10^{-1}	1×10^{-2}

For example, we confirmed the linear correlation in Log(L_{2500}) vs. Log(L_{2keV}) with slope ∼1. The correlation of Log($\kappa_{2-10keV}$) vs. α_{ox} can be approximated using a second order polynomial. The correlation between α_{ox} and Log(λ_{Edd}) is weak and dominated by dispersion in intrinsic source properties. Some strong correlations have been confirmed e.g. Log($\kappa_{2-10keV}$) vs. Log(λ_{Edd}), Log(κ_{5100}) vs. Log(λ_{Edd}), Log(κ_{5100}) vs. Log($\kappa_{2-10keV}$), $\Gamma_{2-10keV}$ vs. Log(λ_{Edd}), $\Gamma_{2-10keV}$ vs. Log(κ_{5100}), Log(M_{BH}) vs. Log(FWHM$_{H\beta}$) and Log($\kappa_{2-10keV}$) vs. Log(M_{BH}). The correlations in both $\Gamma_{2-10keV}$ vs. Log(FWHM$_{H\beta}$) and $\Gamma_{2-10keV}$ vs. Log(M_{BH}) change slopes as $\Gamma_{2-10keV}$ decreases to ∼1.8. The break region is around FWHM$_{H\beta}$=4070±90 km s^{-1} and Log(M_{BH})=7.82±0.02. $\Gamma_{2-10keV}$ is almost independent of the FWHM$_{H\beta}$ after the break region, with a mean value of 1.8±0.2.

• In the second part of our work, we performed a systematic cross-correlation study by producing the correlation matrix of the 9 SED parameters: $\Gamma_{2-10keV}$, $\kappa_{2-10keV}$, κ_{5100A}, λ_{Edd}, FWHM$_{H\beta}$, M_{BH}, α_{ox}, L_{bol} and $L_{2-10keV}$. The PCA was performed on the correlation matrix to discover the principal eigenvectors that drive the most correlations. We found that the first two eigenvectors (PC1 and PC2) contain 80% of all correlations in the matrix. PC1 contains 50% of all correlations and strongly correlates with M_{BH}, while PC2 contains 30% of all correlations and is dominated by L_{bol}. In addition both PC1 and PC2 well correlate with λ_{Edd}. Thus the two principle eigenvectors are driven by M_{BH}, λ_{Edd} and L_{bol} (or equivalently $\dot{M}$). Our eigenvectors also have similar properties to the two principal eigenvectors derived by Boroson (2002) based on their optical emission line study.

• In the third part we produced various mean SEDs classified by each of the 9 parameters. The SED shapes are found to exhibit similar changes with most parameters except L_{bol}. This explains the strong correlations found among these SED parameters. A more detailed mean SED comparison suggests that the dispersion within each of the three binned SEDs is minimized (and the difference between them is maximized) for composite parameters which depend on both λ_{Edd} and M_{BH}, such as $\kappa_{2-10keV}$, κ_{5100} and Hβ FWHM. This is because the SED change is not determined solely by any one of the 9 parameters. It should ultimately depend on both λ_{Edd} and M_{BH}.

• To test the robustness of the main results from our correlation study, we looked at the black hole masses corrected for the effect of radiation pressure. We found no significant differences from using our best-fit black hole masses. We also compared the correlation results between Model-A (without a colour temperature correction) and Model-B (including a colour temperature correction) fitting, and found that they were all very similar.

• The population A-B division for AGNs was compared with the NLS1-BLS1 division, but it did not prove to be a better AGN classification method.

5.8.2 Future Work

Our sample is limited to relatively high λ_{Edd}, with few objects below $\lambda_{Edd} = 0.05$. These (predominantly LINER) objects are the ones expected to be the counterparts of the low/hard state in BHB. Another important extension would be to increase the sample size and include rare higher mass objects with high Eddington ratios. This would allow the SEDs to be co-added for different λ_{Edd} at a given (fixed) black hole mass, thus providing a direct comparison with the BHB states.

The major result of this study is that the SEDs of AGN exhibit a very wide range, most plausibly as a function of mass accretion rate for a given mass black hole. This clearly shows that so-called unified schemes, where AGN have intrinsically identical spectra which are modified by orientation dependent obscuration, are an over simplification of the actual situation. In fact, unobscured AGN can have quite different SED shapes depending on λ_{Edd}, and M_{BH}.

Although not widely appreciated, this is broadly expected by analogy of AGN with BHB. The stellar mass black holes clearly show a dramatic change in spectral shape with λ_{Edd}, but unlike AGN, these changes can be tracked in a single object because of the much shorter timescale for variability. However, while the highest λ_{Edd} spectra appear similar to the disc dominated 'high/soft state' seen in BHB, the more typical AGN (with an SED similar to the standard quasar SED template in Elvis et al. (1994)), do not appear to have SED properties which match with any spectral state known in BBB.

This might indicate a physical break in the properties of the accretion flow between stellar mass and supermassive black holes. The most obvious change in physical conditions between these two mass regimes is that AGN discs are strong in the UV, and so are capable of powering substantial mass loss via a UV line driven wind. A consequence of mass loss in the wind is that the accretion rate is no longer constant as a function of radius, causing an intrinsic change in the structure of the accretion flow (e.g. Proga, Stone & Kallman 2000). Emission/absorption/scattering processes in the wind can also change the observed properties of the spectrum (Sim et al. 2010). Further work on theoretical disc models including these effects will show whether standard AGN accretion flows are indeed sculpted by a wind.

Chapter 6 | *Conclusions*

In this thesis I have conducted a systematic study of AGN spectra from optical to hard X-ray wavelengths. New AGN SED models are described in Chapter 2 and applied to two extremely high Eddington ratio sources. An unobscured Type 1 AGN sample is selected from objects with high signal to noise SDSS and XMM-Newton data. The optical data are decomposed into multiple line and Balmer/FeII components in order to determine the continuum SED. This is combined with the X-ray continuum and fit with the new SED model. The correlation of this continuum SED with the line and continuum parameters are presented in Chapter 4. A complete cross-correlation is conducted between some key SED parameters in Chapter 5, and the sample is split into three to show how the mean SED changes when averaged over different parameters. Here, I conclude the thesis by summarizing the main results of each previous chapter, and suggest possible future research directions to extend this study which may finally lead to a more detailed understanding of the intrinsic emission in AGN.

6.1 Broadband SED Model And Super Eddington Accretion State

In this chapter we present the new broadband SED models (*optxagn(f)* in `Xspec` v12) which combine a standard accretion disc, a low temperature Comptonisation and a high temperature Comptonisation, constrained so that the total luminosity is set by the mass accretion rate through the outer disc which produces the optical

emission. The key parameter in these models is a coronal radius, the radium within which the accretion power is disspated in the Comptonised components rather than in the blackbody emission from a thin disc. Electron scattering is also considered in these models which results in colour temperature correction to the blackbody spectra for the highest temperature (predominantly NLS1) discs.

• We report that RX J0136.9-3510 is the only well observed, X-ray bright, variable AGN which has a similar energy dependence to its X-ray variability as the so far unique X-ray QPO AGN, RE J1034+396. After applying various SED models to their optical, UV and X-ray data, we find that both sources have similar Eddington ratios of around 3, although the larger mass of RX J0136.9-3510 means any QPO is undetectable in its lightcurve. The broad band SED of RX J0136.9-3510 is also remarkably similar to that of RE J1034+396, being well modelled by a multi-colour disc component, a low temperature, optically thick Comptonisation component, plus a high temperature, optically thin Comptonisation component. Such super Eddington flows may suggest a distinct spectral state related those seen in the ULX.

6.2 Type 1 AGN Study - I. Optical and Broadband SED Modeling

In this chapter, we presented a spectral study for 51 unobscured Type 1 AGNs, including 12 NLS1s. We assembled X-ray data from the EPIC cameras on board the XMM-Newton satellite, and optical data from the SDSS DR7. In addition we added optical/UV data from the XMM-Newton OM monitor when available. Our results confirm some previously known correlations. For example, NLS1s often have softer 2-10 keV power-laws, and lower 2-10 keV luminosities. Their Hα, Hβ and [OIII]λ5007 lines are also less luminous on average than found in BLS1s.

• We fit the $H\alpha$ and $H\beta$ line profiles with multi-components to deblend the narrow (NC), intermediate (IC) and broad (BC) components by means of simultaneous modeling of the FeII continuum and other blended lines. We then use the results from the $H\beta$ line fitting to constrain the black hole mass. The FWHM of

the intermediate and broad components give a lower and upper limit for the mass, respectively. Our results confirm previous studies which find that NLS1s tend to have lower black hole masses and higher Eddington ratios, although their bolometric luminosities are not significantly different from those of BLS1s.

• We include the Balmer continuum and permitted iron emission, and extend the modeling across the entire SDSS spectrum in order to isolate the intrinsic optical underlying continuum. However, this 'pure' optical continuum is often (in 32/51 objects) flatter than is predicted by the accretion disc continuum models. This could be due to host galaxy contamination, but the possibility of an additional component in the optical region related to the AGN cannot be ruled out.

• We also show that the Balmer continuum is not well modeled if the edge wavelength is fixed at its laboratory value of 3646Å. It is shifted redwards, and smoothed by more than predicted by the FWHM of the Balmer emission lines. These effects could both be produced by density broadening.

• A multi-component decomposition of the broadband continuum SED with *optxagn* model shows that relative contributions to the bolometric luminosity from the accretion disc, Compotonisation and power law components vary among sources with different luminosity and Hβ linewidth.

• Our study also supports the distinctiveness of the NLS1s among the whole sample. We find that NLS1s tend to have softer 2-10 keV spectrum, lower 2-10 keV luminosity, lower black hole mass, higher Eddington ratio and higher α_{ox} index. However NLS1s do not stand out from the whole sample in terms of their bolometric luminosity distribution. We estimate the corona radii for every AGN in our sample from the SED fitting. This shows that on average NLS1s have smaller corona radii, and correspondingly a smaller coronal component contribution. This means that NLS1 have the largest fraction of their luminosity emitted in the standard disc component.

• The SED fitting also gives constraints on black hole mass which are much tighter than the original limits from the Hβ IC and BC line widths, though these will be somewhat affected by the lack of inclination dependence in the model. We compare these derived masses with other mass estimates based on the R_{BLR}-L_{5100}

relation, including numerous options for measuring the velocity width of the Hβ emission line and corrections for radiation pressure. These results show that the black holes masses derived from the SED fitting are best correlated with the masses derived from the Hβ profiles corrected for radiation pressure effects, but with an offset to lower masses of 0.3 dex for both the NLS1 and BLS1 subsamples. This supports the use of the radiation pressure correction to the FWHM of the Hβ line, so that these objects may lie closer to the established M-σ_* relation.

• Finally, we form three broadband SED templates by co-adding SEDs in three subsamples (consisting of 12 objects in each) to examine how the broadband SED depends on $H\beta$ FWHM velocity width (roughly equivalent to the Eddington ratio). The results show that there is a marked change in the SED shape as the FWHM increases, with NLS1s being the most disc dominated, with the largest big blue bump in the extreme-UV region. Other important parameters such as $\Gamma_{2-10keV}$, $\kappa_{2-10keV}$ and α_{ox} also change as the Hβ FWHM increases.

6.3 Type 1 AGN Study - II. X-ray and Optical Spectral Relation

In this chapter, we made use of the detailed spectral fitting of the AGN sample reported in Chapter 3, to study their optical spectral properties using their hard X-ray luminosity as a diagnostic. Our study focussed on the Hβ, Hα and [OIII] λ5007 emissions lines and the underlying continuum. The main results are summarized below.

• We use the Correlation Spectral Technique to produce an optical 'spectrum', showing the strength of correlation of optical flux at each each wavelength against the hard X-ray luminosity, $L2-10keV$. This reveals that $L2-10keV$ drives correlations across the entire optical spectrum. Some were known previously, others are new. For example, the entire optical underlying continuum strongly correlates with $L_{2-10keV}$. [NeIII] $\lambda\lambda$3869/3967, [OI] $\lambda\lambda$6300/6364, [OII] $\lambda\lambda$3726/3729, [OIII] $\lambda\lambda$4959/5007 and the IC and BC in Balmer lines all well correlate with $L_{2-10keV}$, especially for BLS1s.

However, stellar absorption lines, FeII and the NC in the Balmer lines has much weaker or no correlation with $L_{2-10keV}$.

• A cross-correlation between the Hβ and Hα line component luminosities and the broadband SED component luminosities was performed. The results suggest that among the three SED components, the hard X-ray power law component correlates the best with Balmer line luminosity, and the correlations among different Balmer line components strengthen from NC, IC to BC. This supports the view that the BC has the closest link with AGN's central UV/X-ray continuum emission.

• Significant correlations were found between Hβ EWs and $L_{2-10keV}$, $\kappa^{-1}_{2-10keV}$, Hβ FWHM and black hole mass, although these correlations become weaker for the BLS1 subset alone. By cross-correlating Balmer line component EWs with L_{5100}, no evidence for the 'Baldwin Effect' was for Balmer line IC and BC, but such effect is weakly detected for the Balmer line NC.

• Our results suggest an exponential, rather than linear, dependence of Balmer line IC and BC luminosities on the underlying continuum (e.g. $L_{2-10keV}$ and L_{5100}), implying the presence of a second-order factor. We propose that this second-order effect could be the covering factor of the BLR and ILR seen by the central UV/X-ray continuum, so that higher $L_{2-10keV}$ and L_{5100} sources may also have larger ILR and BLR covering factors. The covering factor may be affected by the corona radius.

• We carried out detailed Balmer line shape studies in order to reveal the nature of ILR and BLR. We found that the Balmer Decrement value, defined by Hα/Hβ, peaks at the line centre and decreases towards both sides, with the red wing having a lower decrement than the blue side. This was also consistent with IC's average decrement value of 4.83±2.18 compared to the BC's 2.13±0.84. These results, along with the systematic inflow speed we found in the BC (mean velocity: 550 km s^{-1}), support the scenario that the inner region of BLR forms the red wing while the outer edge links with the ILR. Compared to the ILR, the BLR may have higher inflow speed, higher electron density, larger ionization parameter or higher Lyα optical depth, A weak correlation between the shape of Balmer line profile and Eddington ratio was confirmed. A higher Eddington ratio corresponds to a more extended wing relative to the overall Balmer line structure. This implies that the velocity width of

the Balmer line is not simply determined by the black hole mass, but also affected by local turbulence whose strength depends on the Eddington ratio. As for ILR, we could not find strong evidence to support its link with the dusty torus. A weak anti-correlation between the EW of Balmer line NC and black hole mass was found, suggesting relatively less NLR emission in higher black hole mass AGNs.

• In our study of [OIII] λ5007, we refined its tight correlation with $L_{2-10keV}$ and $L_{3-20keV}$. We found that the blue and central components of [OIII] λ5007 should be added together to provide the best correlation with hard X-rays. The mean outflow velocity of the blue component in [OIII] λ5007 is -130^{+80}_{-230} $km\ s^{-1}$. The strong correlation between the FWHM and velocity shift of the blue component in [OIII] λ5007 suggests that the outflow speed of [OIII] λ5007 clouds decreases from the central region outwards.

• Using our best-fit broadband SEDs from Chapter 3, we produced another correlation spectrum, with each wavelength of the entire continuum SED correlated against the luminosity in [OIII]. This showed strong correlations between [OIII] λ5007 luminosity and the continuum luminosities in both optical and hard X-ray bandpasses, but surprisingly there is less correlation with the EUVE-soft X-ray component. We split the sample into three subsamples depending on 2-10 keV spectral slope: S1, corresponding to the steepest slopes ($\Gamma_{2-10keV} \geq 2.0$, i.e. predominantly NLS1) S2 corresponding to the flattest ($\Gamma_{2-10keV} \leq 1.8$, predominantly BLS1), with S3 between these two. S1 and S2 both have highly significant correlations in the hard X-ray band, implying that the shapes of hard X-ray power law tail in these two subsets are intrinsic, in spite of their totally different spectral slopes. However, the 2-10 keV flux is much less strongly correlated with the [OIII] luminosity for the moderate $\Gamma_{2-10keV}$ sources in S3.

• In this chapter, we present well constrained equations which can be used to convert between the luminosity of Balmer line broad component and the intrinsic $L_{2-10keV}$ (Equation 1∼4), between the intrinsic L_{5100} and $L_{2-10keV}$ (Equation 5∼6), and between the [OIII] λ5007 luminosity and the intrinsic $L_{2-10keV}$ and $L_{3-20keV}$ (Equation 8∼11). We suggest that these equations be used for inferring the intrinsic optical and X-ray luminosities of obscured sources such as BAL-quasars or Type 2

AGNs, and for calculating the X-ray luminosity function. Considering the limited redshift range and size of our sample, similar studies should be carried out on larger samples to test the robustness of these relations.

6.4 Type 1 AGN Study - III. Broadband SED Properties

In this chapter, we have studied the SED properties of our Type 1 AGN sample. We employ a new broadband SED model (*optxagnf* in `Xspec` v12), which includes a colour temperature correction, to construct the SED for each source in the sample. Various parameters were obtained from the results of the SED fitting. A detailed statistical analysis was performed, which can be divided into three major parts:

• In the first part we studied the diverse correlations found among the SED parameters. We divided these parameters into five groups, according to previously reported correlations. Within each group we conducted a detailed cross-correlation analysis, and applied several regression methods. Our results are generally in good agreement with previous work. However, as a consequence of the unobscured nature of the sample and the more reliable parameter values that resulted from our refined spectral fitting, we were able to reduce the non-intrinsic dispersion and so obtain the intrinsic and better constrained correlations.

For example, we confirmed the linear correlation in Log(L_{2500}) vs. Log(L_{2keV}) with slope ∼1. The correlation of Log($\kappa_{2-10keV}$) vs. α_{ox} can be approximated using a second order polynomial. The correlation between α_{ox} and Log(λ_{Edd}) is weak and dominated by dispersion in intrinsic source properties. Some strong correlations have been confirmed e.g. Log($\kappa_{2-10keV}$) vs. Log(λ_{Edd}), Log(κ_{5100}) vs. Log(λ_{Edd}), Log(κ_{5100}) vs. Log($\kappa_{2-10keV}$), $\Gamma_{2-10keV}$ vs. Log(λ_{Edd}), $\Gamma_{2-10keV}$ vs. Log(κ_{5100}), Log(M_{BH}) vs. Log(FWHM$_{H\beta}$) and Log($\kappa_{2-10keV}$) vs. Log(M_{BH}). The correlations in both $\Gamma_{2-10keV}$ vs. Log(FWHM$_{H\beta}$) and $\Gamma_{2-10keV}$ vs. Log(M_{BH}) change slopes as $\Gamma_{2-10keV}$ decreases to ∼1.8. The break region is around FWHM$_{H\beta}$=4070±90 km s^{-1} and Log(M_{BH})=7.82±0.02. $\Gamma_{2-10keV}$ is almost independent of the FWHM$_{H\beta}$ after

the break region, with a mean value of 1.8±0.2.

• In the second part of our work, we performed a systematic cross-correlation study by producing the correlation matrix of the 9 SED parameters: $\Gamma_{2-10keV}$, $\kappa_{2-10keV}$, κ_{5100A}, λ_{Edd}, FWHM$_{H\beta}$, M$_{BH}$, α_{ox}, L$_{bol}$ and L$_{2-10keV}$. The PCA was performed on the correlation matrix to discover the principal eigenvectors that drive the most correlations. We found that the first two eigenvectors (PC1 and PC2) contain 80% of all correlations in the matrix. PC1 contains 50% of all correlations and strongly correlates with M$_{BH}$, while PC2 contains 30% of all correlations and is dominated by L$_{bol}$. In addition both PC1 and PC2 well correlate with λ_{Edd}. Thus the two principle eigenvectors are driven by M$_{BH}$, λ_{Edd} and L$_{bol}$ (or equivalently $\dot{M}$). Our eigenvectors also have similar properties to the two principal eigenvectors derived by Boroson (2002) based on their optical emission line study.

• In the third part we produced various mean SEDs classified by each of the 9 parameters. The SED shapes are found to exhibit similar changes with most parameters except L$_{bol}$. This explains the strong correlations found among these SED parameters. A more detailed mean SED comparison suggests that the dispersion within each of the three binned SEDs is minimized (and the difference between them is maximized) for composite parameters which depend on both λ_{Edd} and M$_{BH}$, such as $\kappa_{2-10keV}$, κ_{5100} and Hβ FWHM. This is because the SED change is not determined solely by any one of the 9 parameters. It should ultimately depend on both λ_{Edd} and M$_{BH}$.

• To test the robustness of the main results from our correlation study, we looked at the black hole masses corrected for the effect of radiation pressure. We found no significant differences from using our best-fit black hole masses. We also compared the correlation results between Model-A (without a colour temperature correction) and Model-B (including a colour temperature correction) fitting, and found that they were all very similar.

• The population A-B division for AGNs was compared with the NLS1-BLS1 division, but it did not prove to be a better AGN classification method.

6.5 Future Work, What Lies Ahead?

The work described in this thesis can be extended further and lead to a more detailed understanding of the intrinsic emission of AGN. I summarize a few possible topics below:

• In Chapter 2, we propose that the spectral state indicated by super Eddington accretion rate may be associated with the QPO. This speculation requires more sources in this subclass, and most crucially requires another AGN QPO to be detected. One good candidate is PG 1244+026, whose broadband SED is very similar as RE J1034+396 and probably has a super Eddington accretion flow. A 100 ks XMM-Newton observation of PG 1244+026 has just been taken (PI: Jin), from which we may obtain more evidence on the unique properties of this extreme spectral state. However, the higher mass of this AGN means that even 100ks is not enough to significantly detect a similar QPO even if it is present.

• The sample can be extended by relaxing the strict signal-to-noise selection criteria for the sample. A larger number of AGN enable us to better determine the correlation between the luminosity of Balmer line broader component and the luminosity of intrinsic 2-10 keV emission (see Chapter 4).

• An important extension of this work is to include more sources with intrinsic $L_{2-10keV} < 10^{42}\ ergs\ s^{-1}$. As discussed in Chapter 5 that the inclusion of these intrinsically X-ray weak sources may break the correlations between $L_{2-10keV}$ and other parameters. But the weakness of their X-ray emission also indicates that it is difficult to obtain high quality X-ray spectra from these sources. The very low Eddington ratio AGNs (e.g. $\lambda_{Edd} < 0.01$) may also have different properties from our luminous AGN sample, and so are worth more a detailed study.

• Another important extension of this work is to perform similar study for AGN samples at higher redshift, which we have already started to do. It is not clear whether AGN SEDs would evolve with redshift or not. However, strong evolution seems unlikely as the mean SED of moderate Eddington ratio sources (Panel 4-B in Figure 5.13) has similar shape as the mean RQ quasar SED in Elvis et al. (1994).

• The spectral variability analysis in Chapter 2 showed the importance of studing

the time dependent characteristics of the source as well as the time averaged SED. This would provide better evidence for the link between the emission in different wavebands. Currently, such multi-waveband spectral and temporal data is only available for very few sources, but more would be expected in the future.

• In Chapter 3, we reported the extended red wing of the edge of the Balmer continuum, and pointed out that this spectral characteristic requires more detailed study because it may provide information about the densest regions of the BLR.

• The Cross-correlation Spectra presented in Chapter 4 is a powerful tool for studying the link between different wavebands of AGN spectra. The next step is to use a bigger sample to refine these optical and X-ray cross-correlation spectra. We have also started to extend these spectra into the infrared wavebands.

• The nature of the optical spectral slope change at $\sim$5000Å remains unclear. More detailed investigation including reliable host galaxy subtraction and reddening correction is required to clarify this question. Optical reverberation mapping technique can also help to answer this question.

Consequently, the results presented in this thesis are just the first steps to understanding the intrinsic multi-waveband emission of AGN. However, this work provides a set of methods that is useful for further studies based on better data and more complete samples. There are more exciting discoveries coming in the years ahead!

Appendix A

The Spectral Modelling Results in Chapter 3

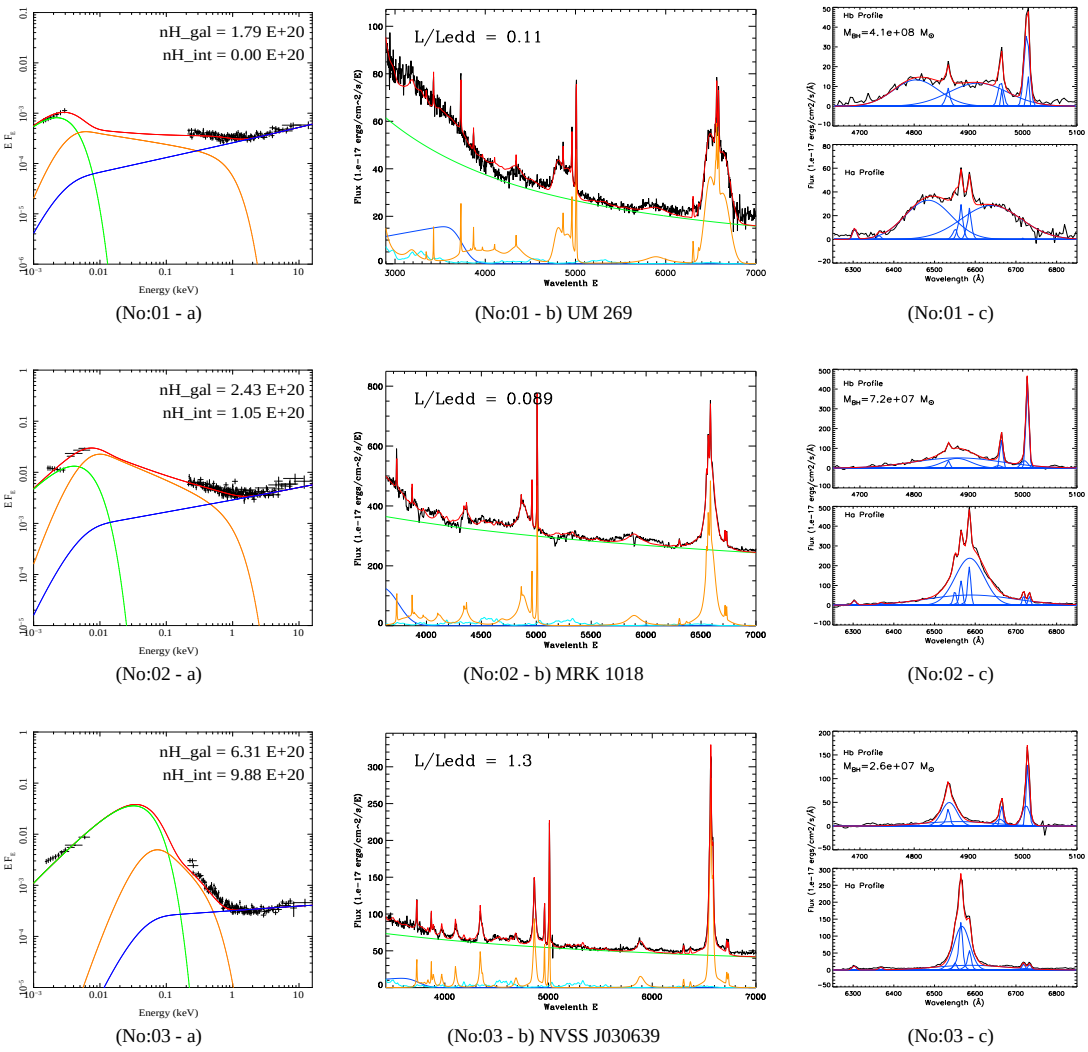

Figure A.1: The spectral fitting results. Object order follows all other tables in this paper as increasing RA and DEC. 1. Broadband SED fitting plot (panel-a): X-ray data has been rebinned for each object. Green solid line is the pure accretion disc component peaking at optical/UV region, orange line is Comptonisation component producing soft X-ray excess below 2 keV, blue line is the hard X-ray Comptonisation component dominating 2-10 keV spectrum, and red is the total broadband SED model. 2. SDSS spectrum fitting plot (panel-b): only the fitted spectrum below 7000Å is plotted. Green solid line is the best-fit underlying continuum from accretion disc. Orange line shows all best-fit emission lines, including the results from detailed Balmer line fitting in panel-c. FeII emission is plotted as light blue, while Balmer continuum being dark blue. The total best-fit model with reddening is drawn in red solid line. 3. Balmer emission line fitting plot(panel-c): spectral ranges containing Hα and Hβ profiles are plotted separately, with blue lines showing individual line components and red line showing the whole best-fit model. These are also the corresponding zoom-in plots of nearby regions of Hα and Hβ in panel-b. The given black hole mass is the broadband SED best-fit value, see Section 3.6.5 for detailed descriptions.

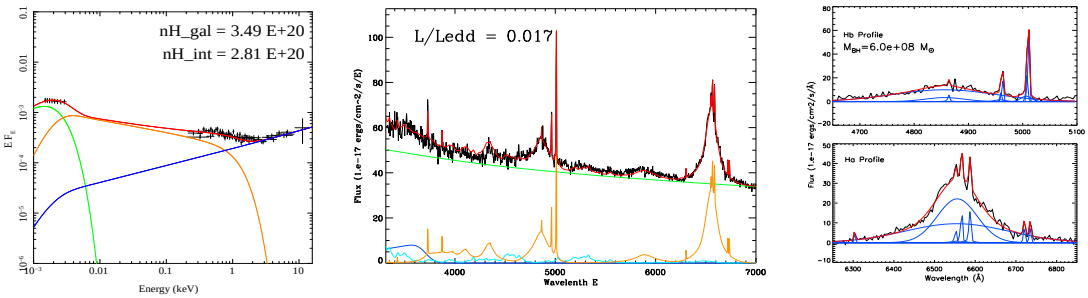

(No:04 - a) (No:04 - b) 2XMM J074601.2+280732 (No:04 - c)

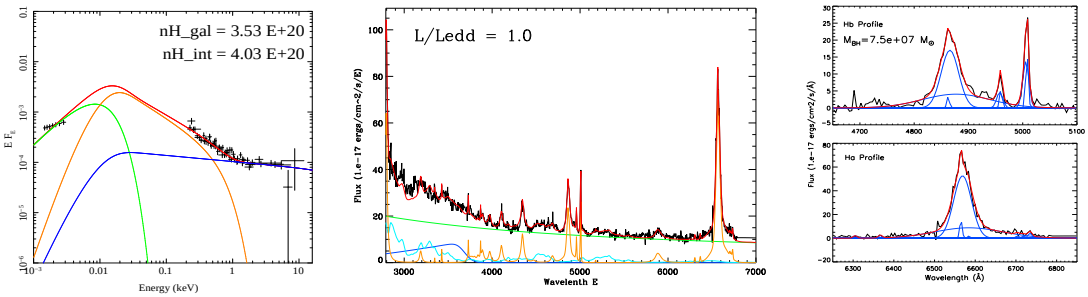

(No:05 - a) (No:05 - b) 2XMM J080608.0+244421 (No:05 - c)

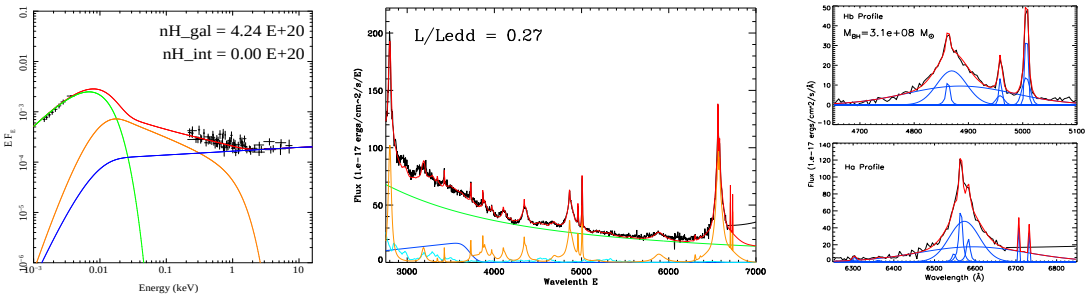

(No:06 - a) (No:06 - b) HS 0810+5157 (No:06 - c)

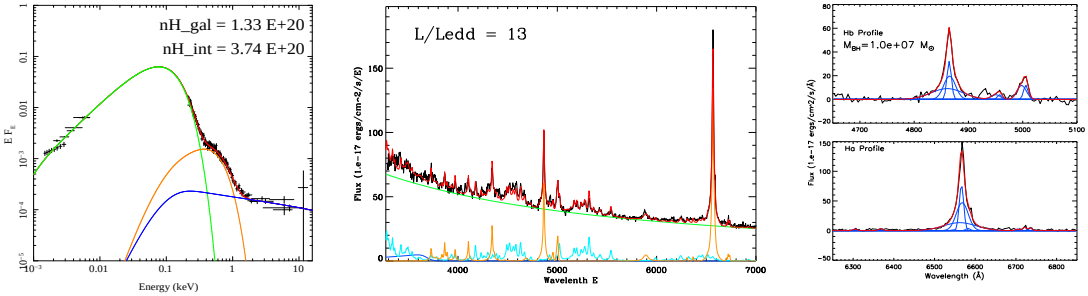

(No:07 - a) (No:07 - b) RBS 0769 (No:07 - c)

Figure A.1: *continued*

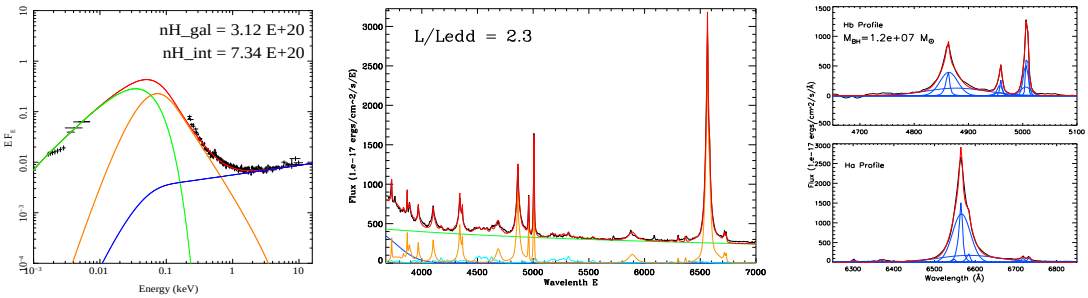

(No:08 - a) (No:08 - b) RBS 0770 (No:08 - c)

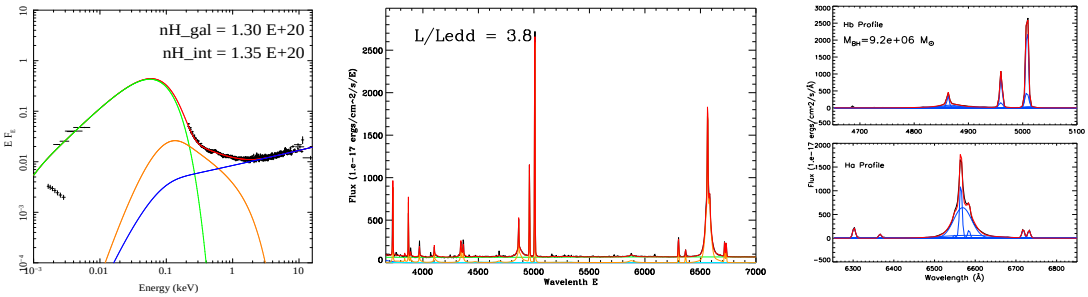

(No:09 - a) (No:09 - b) MRK 0110 (No:09 - c)

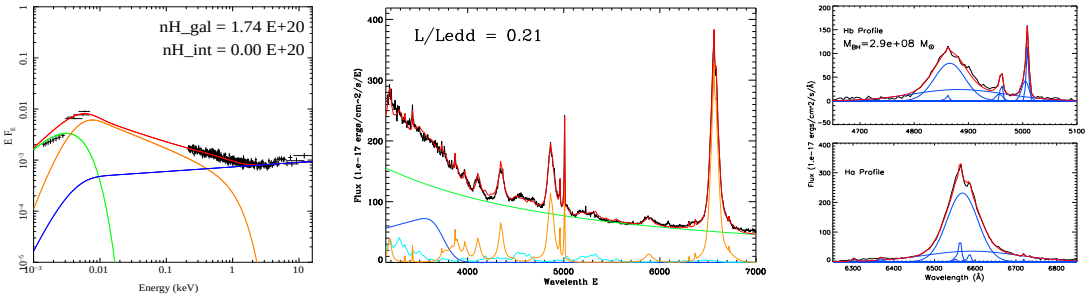

(No:10 - a) (No:10 - b) PG 0947+396 (No:10 - c)

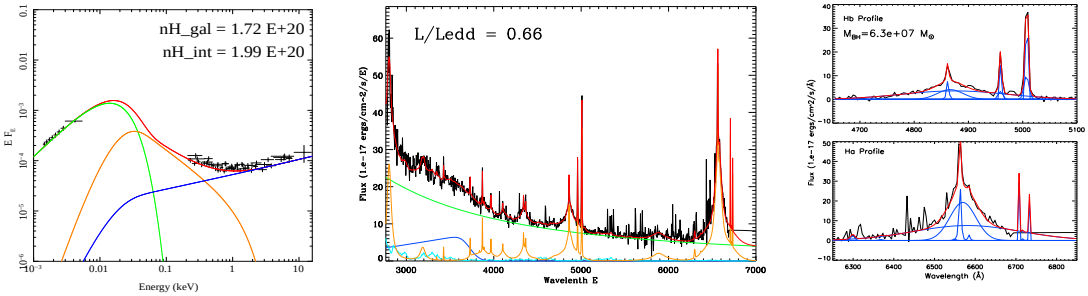

(No:11 - a) (No:11 - b) 2XMM J100025.2+015852 (No:11 - c)

Figure A.1: *continued*

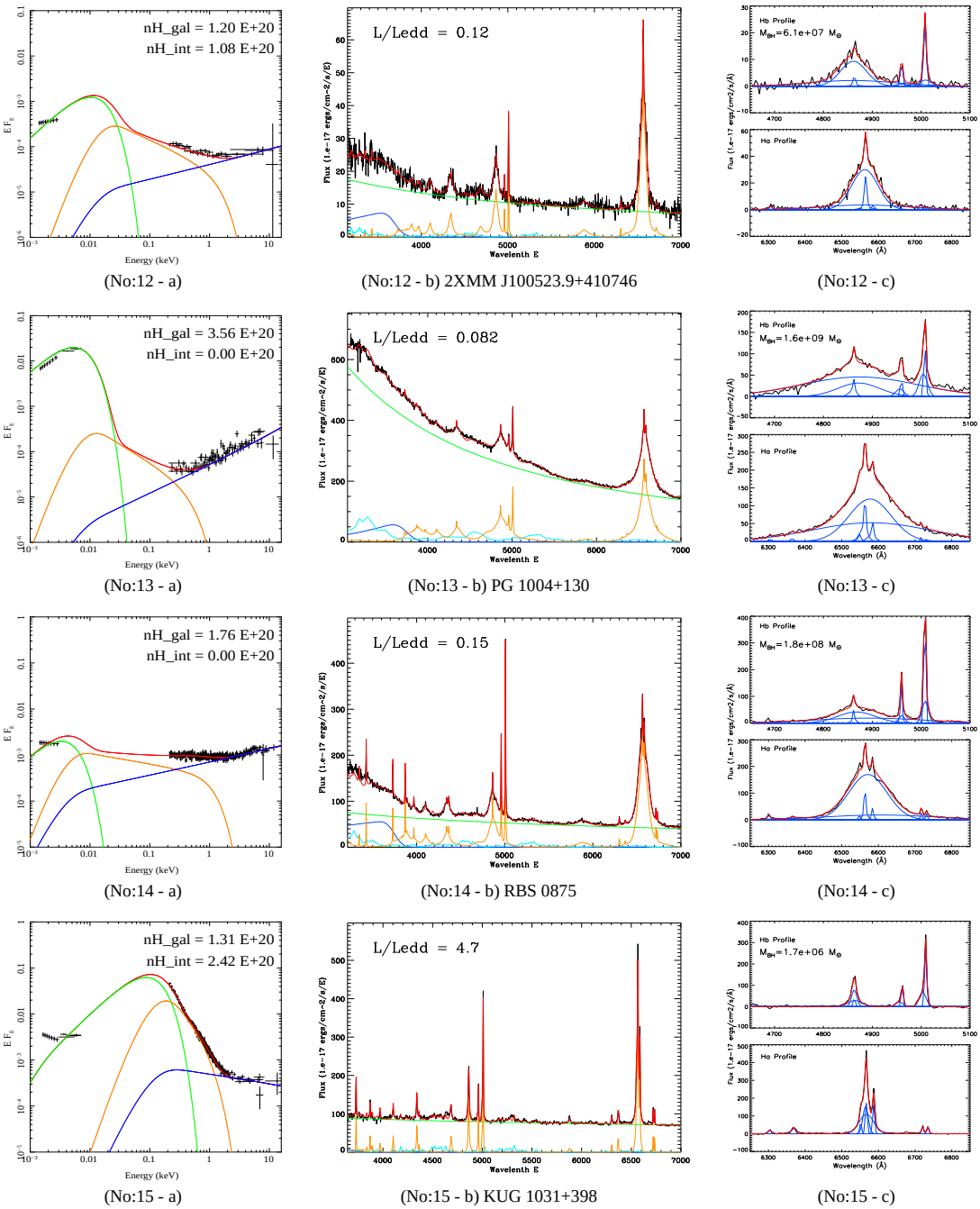

(No:12 - a) (No:12 - b) 2XMM J100523.9+410746 (No:12 - c)

(No:13 - a) (No:13 - b) PG 1004+130 (No:13 - c)

(No:14 - a) (No:14 - b) RBS 0875 (No:14 - c)

(No:15 - a) (No:15 - b) KUG 1031+398 (No:15 - c)

Figure A.1: *continued*

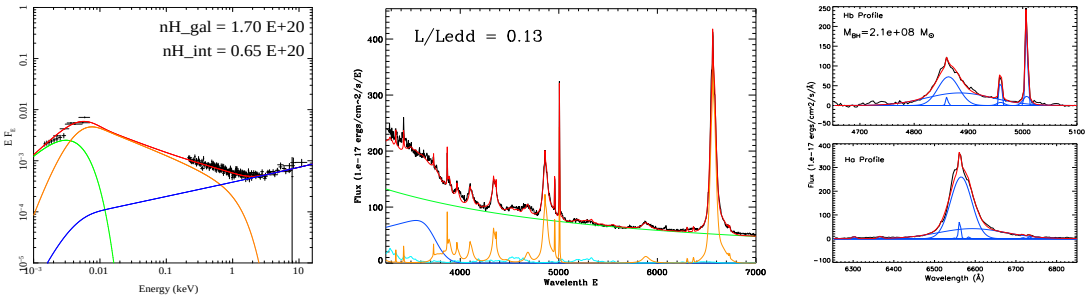

(No:16 - a) (No:16 - b) PG 1048+342 (No:16 - c)

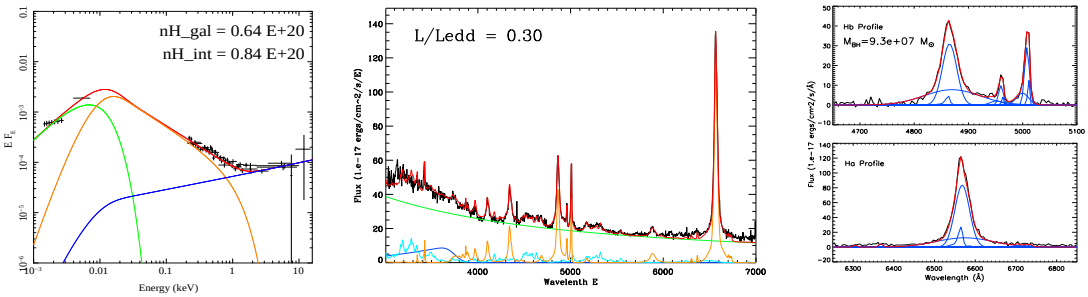

(No:17 - a) (No:17 - b) 1RXS J111007 (No:17 - c)

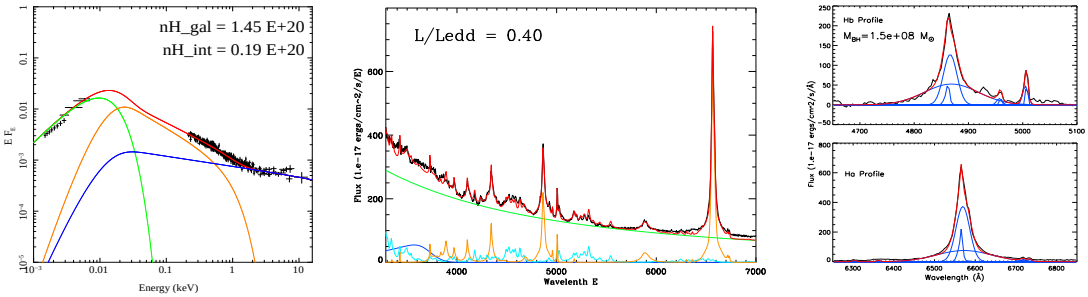

(No:18 - a) (No:18 - b) PG 1115+407 (No:18 - c)

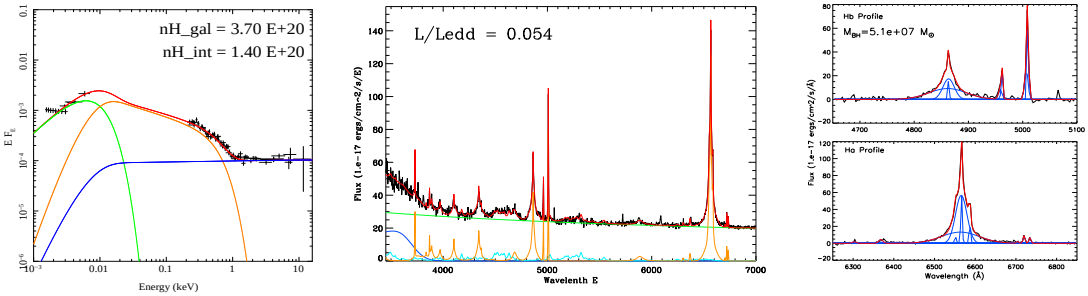

(No:19 - a) (No:19 - b) 2XMM J112328.0+052823 (No:19 - c)

Figure A.1: *continued*

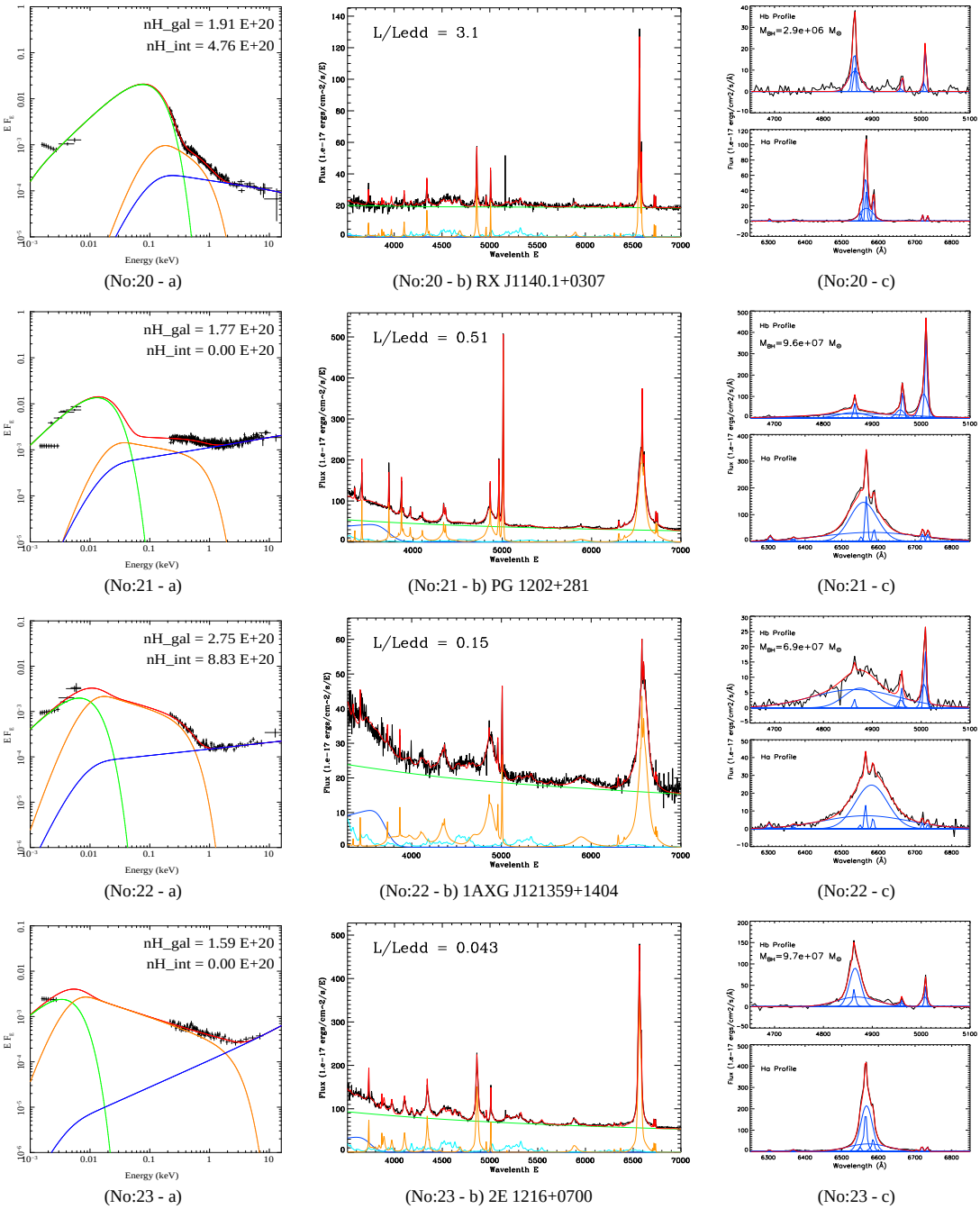

(No:20 - a) (No:20 - b) RX J1140.1+0307 (No:20 - c)

(No:21 - a) (No:21 - b) PG 1202+281 (No:21 - c)

(No:22 - a) (No:22 - b) 1AXG J121359+1404 (No:22 - c)

(No:23 - a) (No:23 - b) 2E 1216+0700 (No:23 - c)

Figure A.1: *continued*

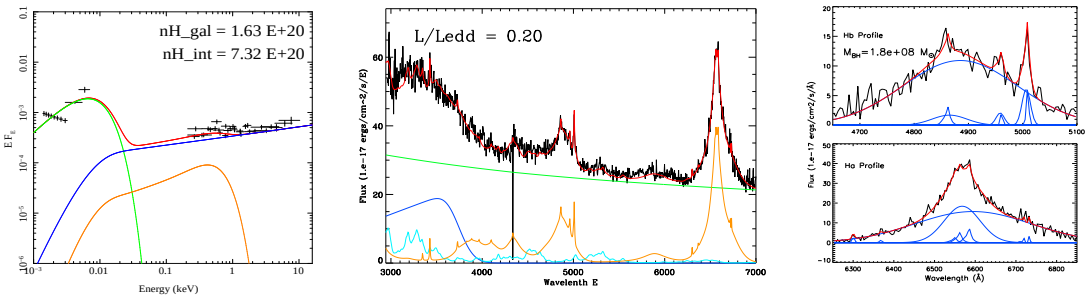

(No:24 - a) (No:24 - b) 1RXS J122019 (No:24 - c)

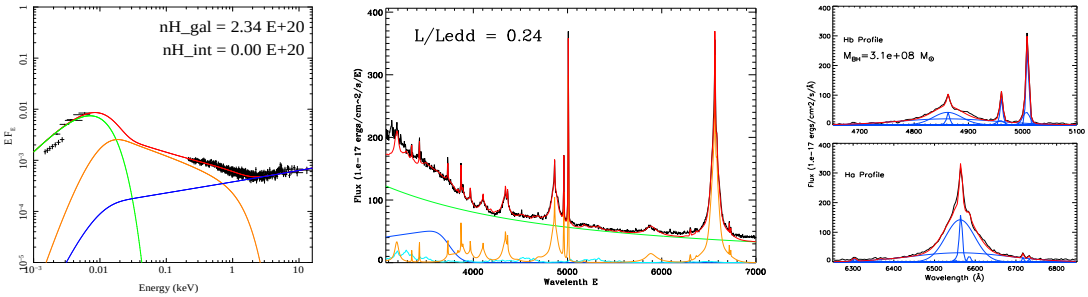

(No:25 - a) (No:25 - b) LBQS 1228+1116 (No:25 - c)

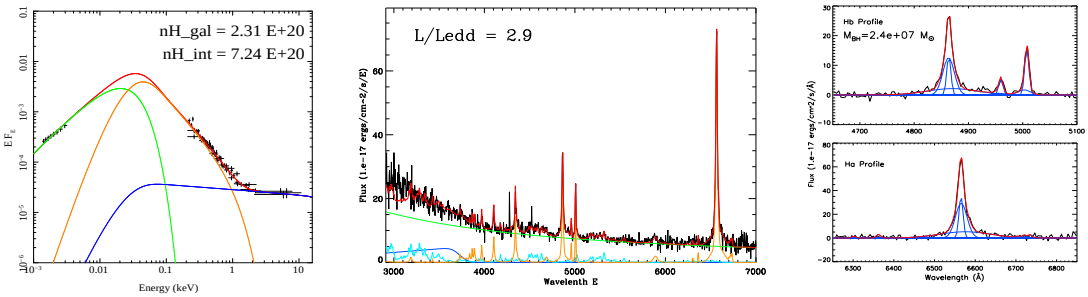

(No:26 - a) (No:26 - b) 2XMM J123126.4+105111 (No:26 - c)

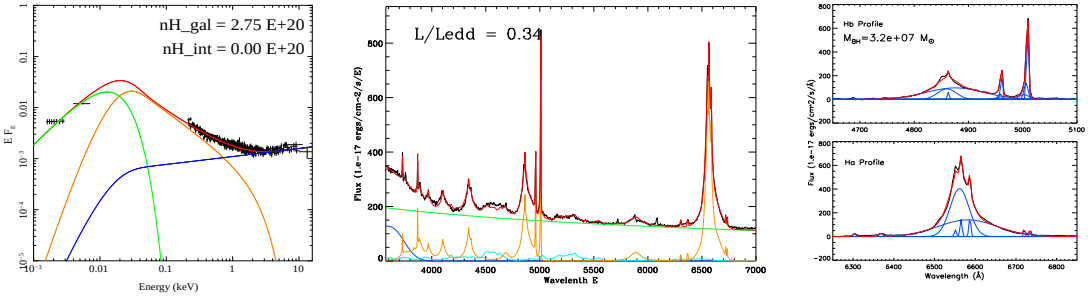

(No:27 - a) (No:27 - b) MRK 0771 (No:27 - c)

Figure A.1: *continued*

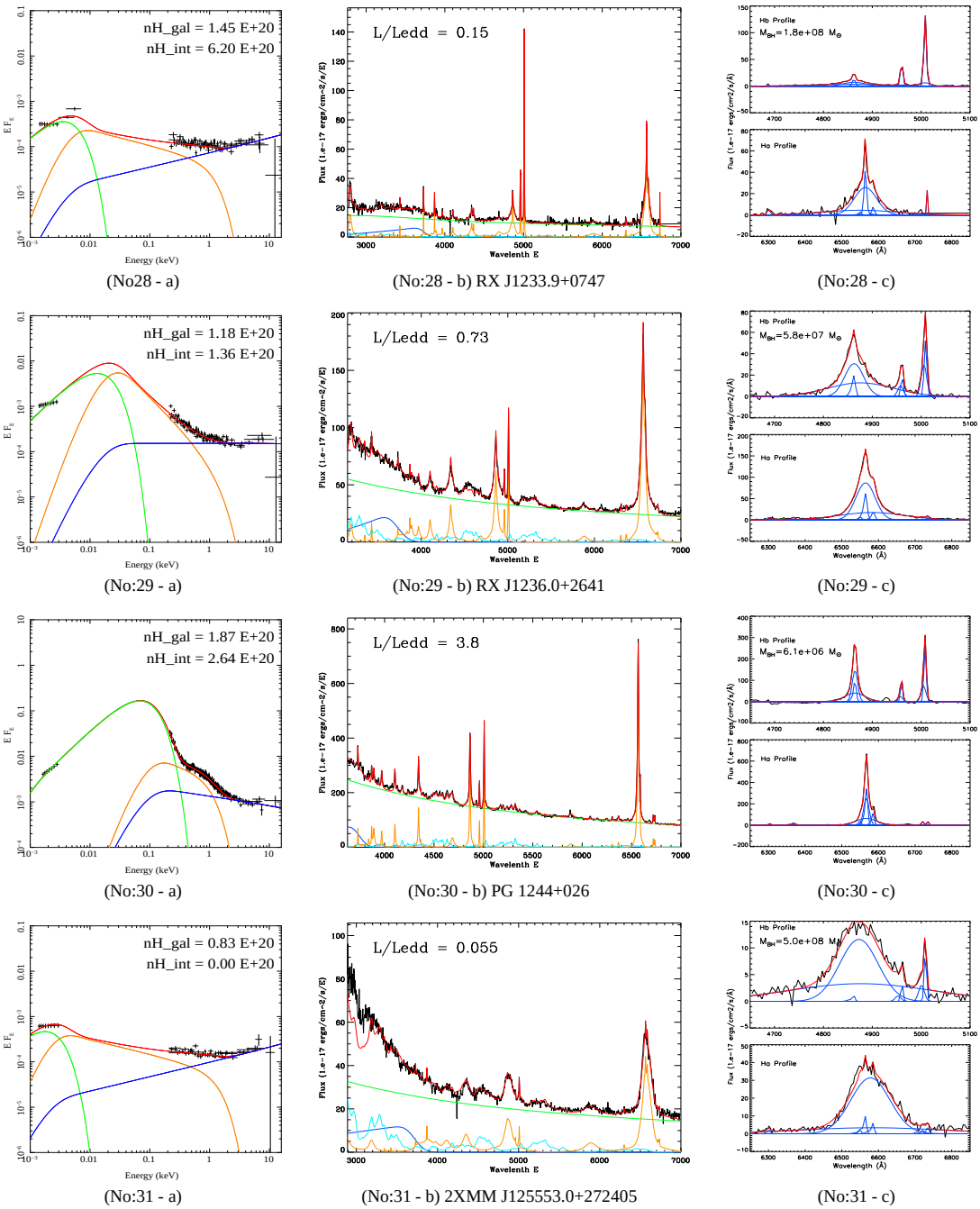

(No28 - a) (No:28 - b) RX J1233.9+0747 (No:28 - c)

(No:29 - a) (No:29 - b) RX J1236.0+2641 (No:29 - c)

(No:30 - a) (No:30 - b) PG 1244+026 (No:30 - c)

(No:31 - a) (No:31 - b) 2XMM J125553.0+272405 (No:31 - c)

Figure A.1: *continued*

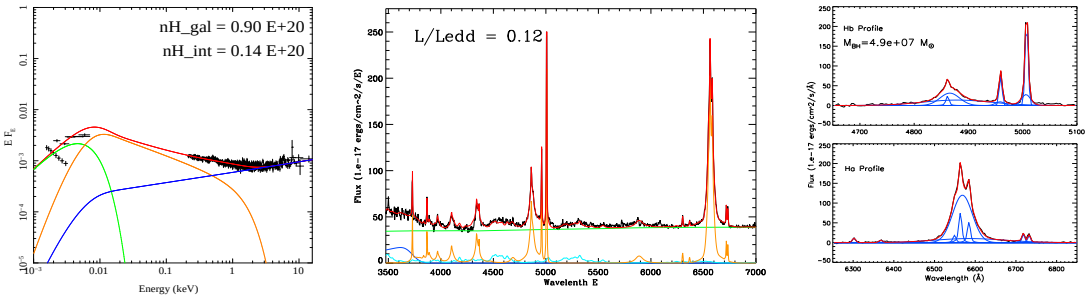

(No:32 - a) (No:32 - b) RBS 1201 (No:32 - c)

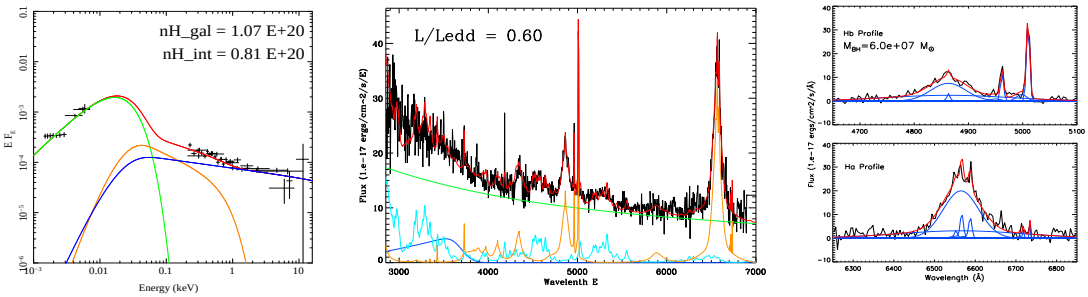

(No:33 - a) (No:33 - b) 2XMM J132101.4+340658 (No:33 - c)

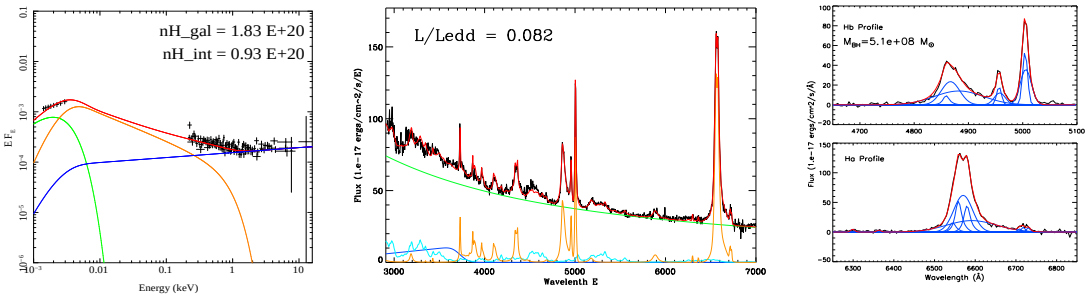

(No:34 - a) (No:34 - b) 1RXS J132447 (No:34 - c)

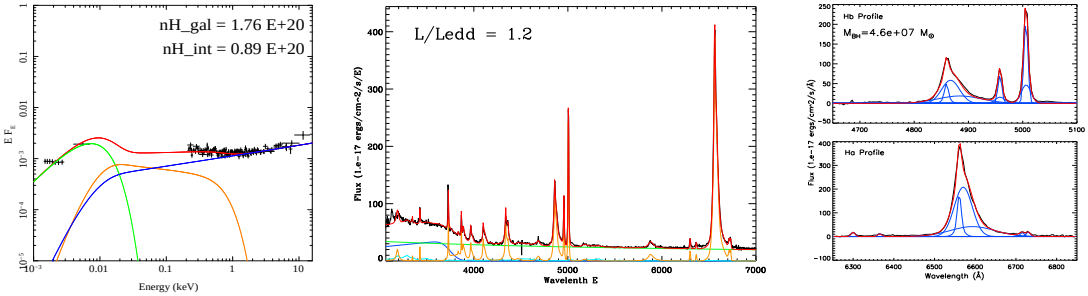

(No:35 - a) (No:35 - b) UM 602 (No:35 - c)

Figure A.1: *continued*

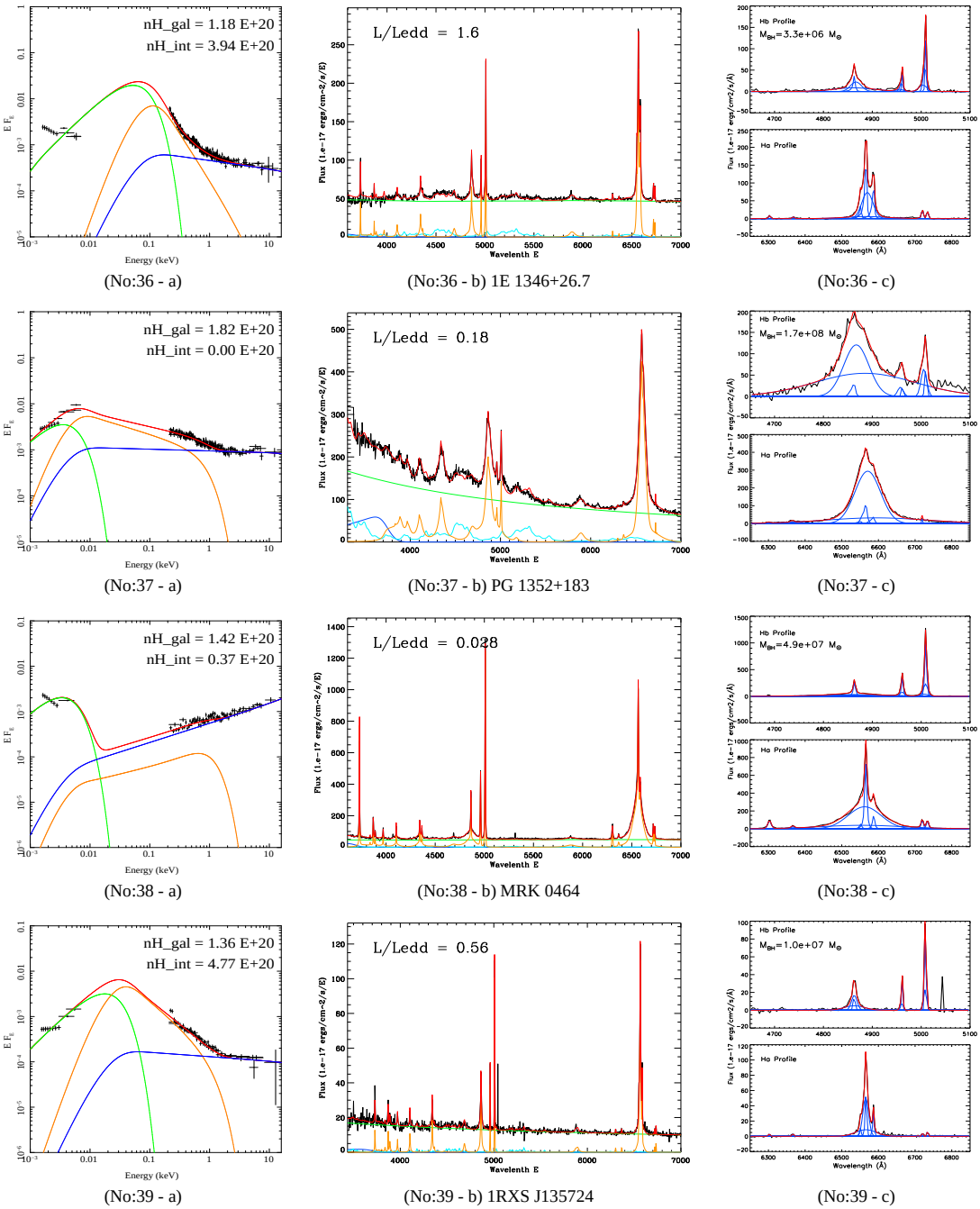

(No:36 - a) (No:36 - b) 1E 1346+26.7 (No:36 - c)

(No:37 - a) (No:37 - b) PG 1352+183 (No:37 - c)

(No:38 - a) (No:38 - b) MRK 0464 (No:38 - c)

(No:39 - a) (No:39 - b) 1RXS J135724 (No:39 - c)

Figure A.1: *continued*

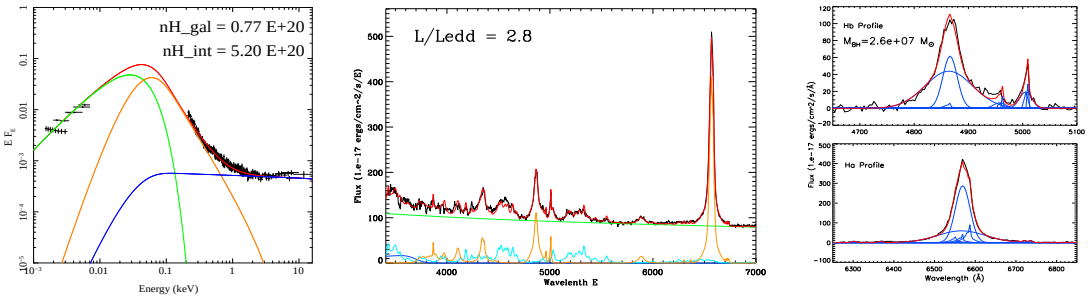

(No:40 - a) (No:40 - b) PG 1415+451 (No:40 - c)

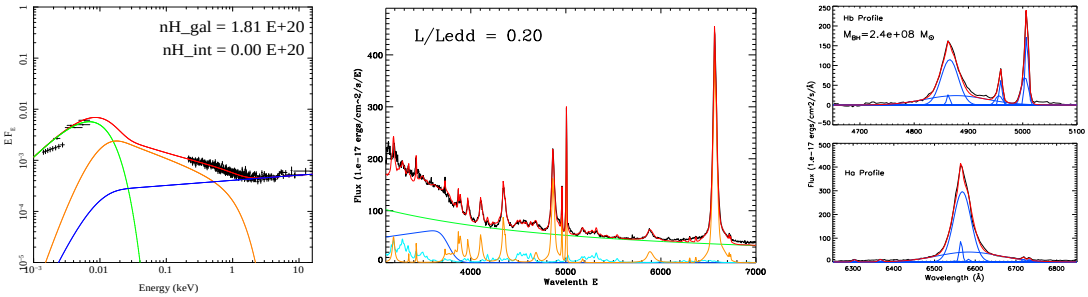

(No:41 - a) (No:41 - b) PG 1427+480 (No:41 - c)

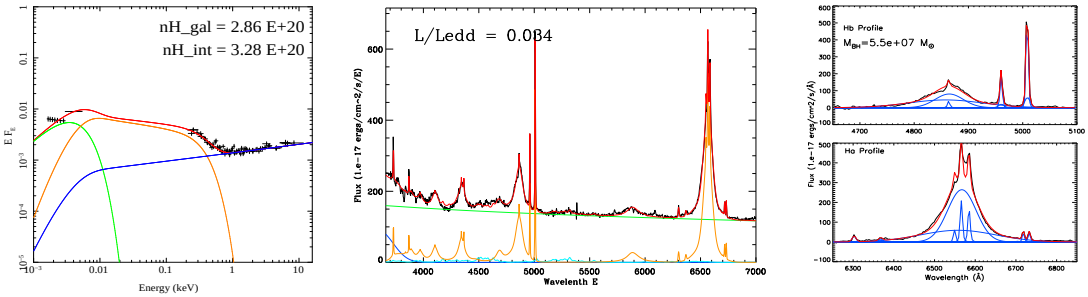

(No:42 - a) (No:42 - b) NGC 5683 (No:42 - c)

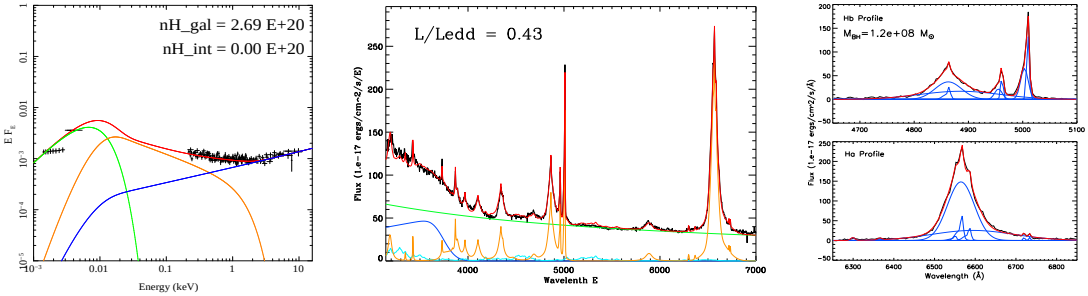

(No:43 - a) (No:43 - b) RBS 1423 (No:43 - c)

Figure A.1: *continued*

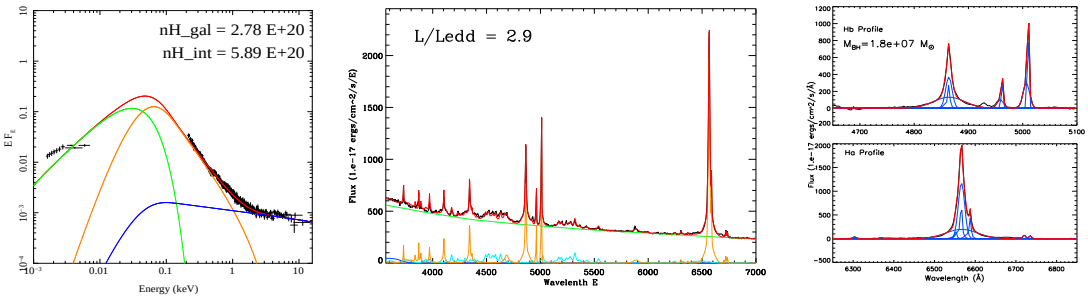

(No:44 - a) (No:44 - b) PG 1448+273 (No:44 - c)

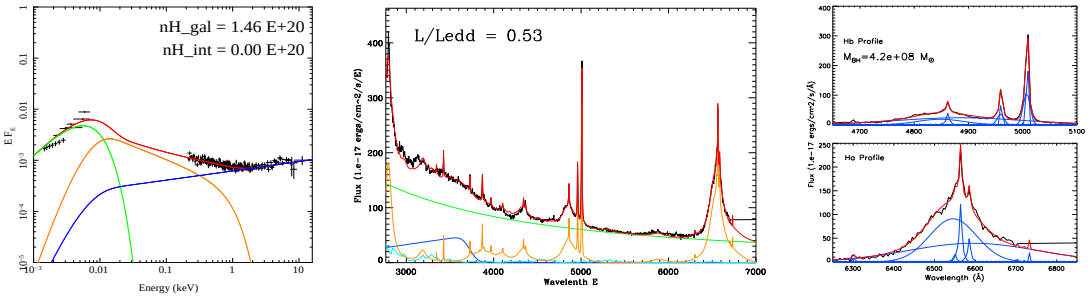

(No:45 - a) (No:45 - b) PG 1512+370 (No:45 - c)

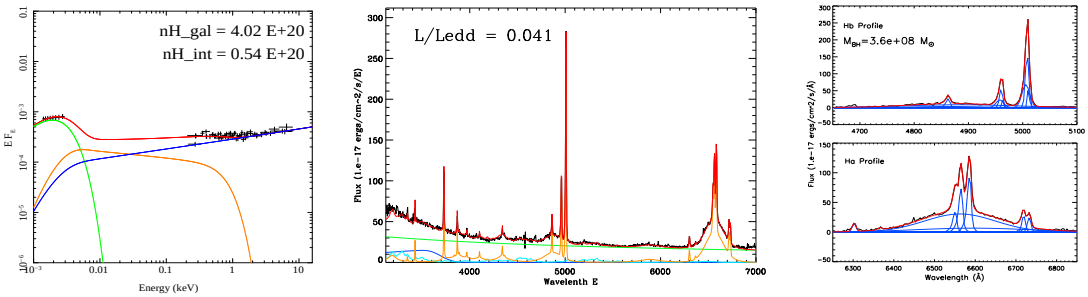

(No:46 - a) (No:46 - b) Q 1529+050 (No:46 - c)

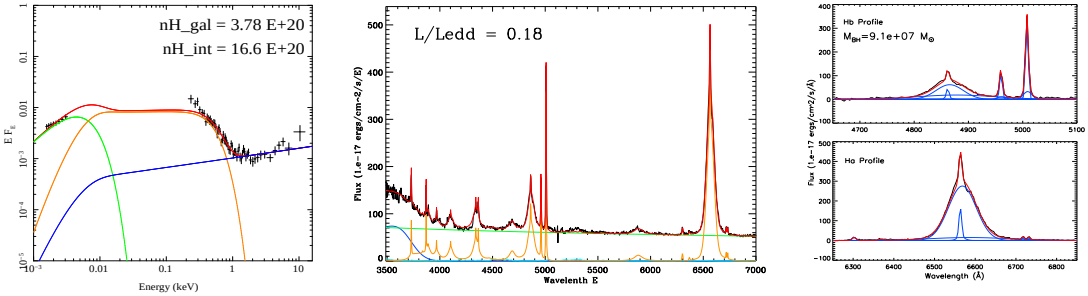

(No:47 - a) (No:47 - b) 1E 1556+27.4 (No:47 - c)

Figure A.1: *continued*

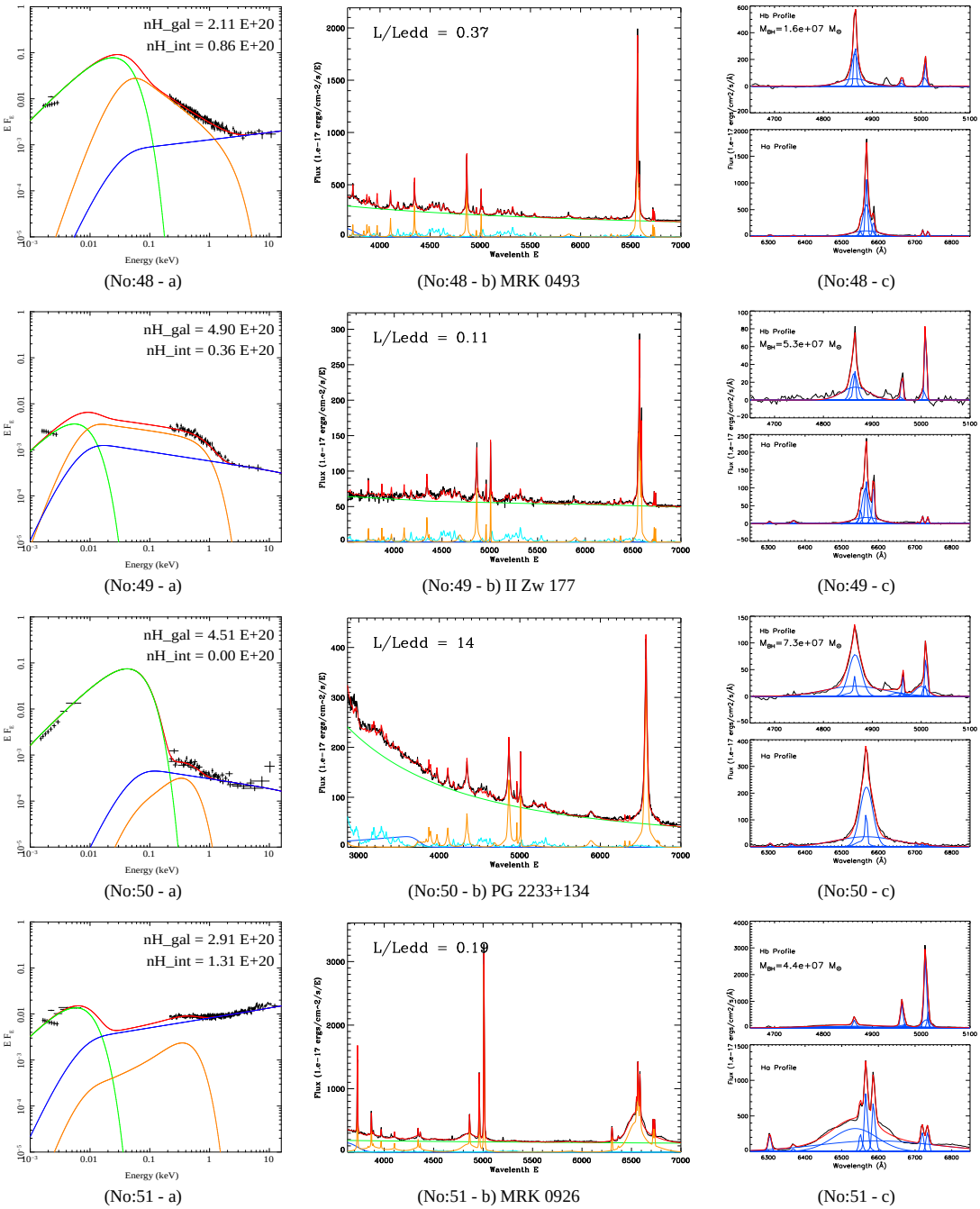

(No:48 - a) (No:48 - b) MRK 0493 (No:48 - c)

(No:49 - a) (No:49 - b) II Zw 177 (No:49 - c)

(No:50 - a) (No:50 - b) PG 2233+134 (No:50 - c)

(No:51 - a) (No:51 - b) MRK 0926 (No:51 - c)

Figure A.1: *continued*

Appendix B

The Complete Parameter Tables in Chapter 3

B.1 XMM-Newton and SDSS DR7 Source Position And Seperation of Our Sample

Table B.1: XMM-Newton and SDSS DR7 source position and separation of our sample. ID: object number, the same as Table 3.1; XMM_Ra and XMM_Dec: source's right ascension and declination in the corresponding XMM-Newton observation; XMM_PosErr: X-ray position uncertainty from XMM-Newton; SDSS_Ra and SDSS_Dec: source's right ascension and declination measured by SDSS; Separation: the angular separation between source's XMM-Newton and SDSS coordinates; Sep./XMM_PosErr: the ratio between coordinates separation and X-ray position uncertainty, showing the significance of coordinate separation.

ID	XMM_Ra	XMM_Dec	XMM_PosErr	SDSS_Ra	SDSS_Dec	Separation	Sep./XMM_PosErr
	degree	*degree*	*arcsec*	*degree*	*degree*	*arcsec*	
1	10.83216	0.85443	0.35	10.83227	0.85425	0.75	2.10
2	31.56642	-0.29178	1.03	31.56664	-0.29144	1.44	1.40
3	46.66479	0.06204	0.35	46.66487	0.06200	0.33	0.93
4	116.50527	28.12559	0.36	116.50530	28.12559	0.09	0.25
5	121.53373	24.73937	0.40	121.53390	24.73919	0.86	2.14
6	123.59218	51.81109	0.38	123.59217	51.81095	0.50	1.32
7	140.69583	51.34385	0.35	140.69595	51.34390	0.33	0.92
8	140.92903	22.90931	0.35	140.92918	22.90907	1.00	2.86
9	141.30347	52.28644	0.35	141.30355	52.28621	0.85	2.44
10	147.70155	39.44735	0.35	147.70161	39.44737	0.19	0.54
11	150.10520	1.98110	0.17	150.10519	1.98115	0.18	1.04
12	151.34968	41.12950	0.38	151.34980	41.12941	0.44	1.14
13	151.85868	12.81567	0.38	151.85876	12.81562	0.34	0.89
14	157.74620	31.04878	0.35	157.74623	31.04884	0.21	0.61
15	158.66084	39.64129	0.35	158.66082	39.64119	0.36	1.03
16	162.93283	33.99096	0.35	162.93290	33.99075	0.76	2.17
17	167.52841	61.42283	0.37	167.52898	61.42262	1.23	3.36
18	169.62621	40.43171	0.35	169.62619	40.43167	0.17	0.47
19	170.86692	5.47319	0.36	170.86718	5.47311	0.98	2.71
20	175.03644	3.11972	0.35	175.03633	3.11984	0.58	1.63
21	181.17565	27.90348	0.35	181.17545	27.90328	0.95	2.69
22	183.48412	14.07530	0.26	183.48415	14.07537	0.27	1.05
23	184.87880	6.72630	0.28	184.87863	6.72623	0.66	2.38
24	185.07680	6.68898	0.37	185.07683	6.68878	0.71	1.94
25	187.72544	11.00311	0.20	187.72550	11.00310	0.23	1.16
26	187.86003	10.85327	0.22	187.86020	10.85314	0.75	3.46
27	188.01513	20.15831	0.35	188.01511	20.15821	0.38	1.07
28	188.48376	7.79869	0.37	188.48381	7.79888	0.71	1.92
29	189.01670	26.69323	0.36	189.01677	26.69335	0.46	1.28
30	191.64732	2.36918	1.00	191.64687	2.36910	1.64	1.63

Table B.1: continued...

ID	XMM_Ra	XMM_Dec	XMM_PosErr	SDSS_Ra	SDSS_Dec	Separation	Sep./XMM_PosErr
	degree	*degree*	*arcsec*	*degree*	*degree*	*arcsec*	
31	193.97112	27.40152	0.27	193.97104	27.40146	0.33	1.23
32	195.09236	28.40082	0.13	195.09234	28.40073	0.32	2.45
33	200.25592	34.11620	0.38	200.25590	34.11609	0.38	1.00
34	201.19851	3.40888	0.37	201.19856	3.40908	0.71	1.92
35	205.30811	-0.88743	0.35	205.30807	-0.88755	0.45	1.26
36	207.14581	26.51932	0.25	207.14562	26.51943	0.72	2.90
37	208.64863	18.08835	0.35	208.64872	18.08820	0.64	1.80
38	208.97286	38.57458	0.36	208.97302	38.57464	0.49	1.37
39	209.35241	65.41847	0.25	209.35220	65.41831	0.67	2.69
40	214.25318	44.93513	0.35	214.25341	44.93510	0.60	1.69
41	217.42952	47.79076	0.35	217.42947	47.79061	0.54	1.52
42	218.71847	48.66196	0.25	218.71857	48.66188	0.38	1.50
43	221.06099	6.55192	0.35	221.06111	6.55188	0.47	1.32
44	222.78667	27.15737	0.35	222.78651	27.15748	0.64	1.82
45	228.67944	36.84746	0.35	228.67946	36.84734	0.46	1.29
46	233.12007	4.89952	0.37	233.11998	4.89956	0.34	0.93
47	239.62260	27.28773	0.37	239.62235	27.28729	1.80	4.86
48	239.79023	35.02983	0.35	239.79012	35.02986	0.35	1.00
49	334.82724	12.13148	0.35	334.82721	12.13144	0.18	0.52
50	339.03200	13.73203	0.37	339.03201	13.73205	0.11	0.29
51	346.18072	-8.68642	1.00	346.18116	-8.68573	2.95	2.95

B.2 Black Hole Masses from Different Methods

Table B.2: Black hole masses from different methods. $M_{BH,IC}$: black hole mass calculated from the FWHM of Hβ intermediate component in logarithm and solar mass; $M_{BH,BC}$: black hole mass calculated from the FWHM of Hβ broad component; $M_{BH,IC+BC}$: black hole masses calculated from the FWHM of superposing Hβ intermediate component (IC) and broad component (BC) (i.e. narrow component subtracted), using Equation 3.5; $M_{BH,\sigma}$: black hole mass calculated from the second momentum of the whole Hβ line profile, see Section 3.6.5 for details; $M_{BH,Fit}$: the best-fit black hole masses in logarithm, which is constrained by $M_{BH,IC}$ and $M_{BH,BC}$, but values within 0.5 lower than log($M_{BH,IC}$) were also adopted in the fitting, see Section 3.6.5; log($M_{BH,RP}$): the radiation pressure corrected black hole mass using Equation 9 in Marconi et al. (2008) with f=3.1 and log$g$=7.6; (*): note that $M_{BH,IC+BC}$ is always within the range of $M_{BH,IC}$ and $M_{BH,BC}$, except for UM269 whose Hβ shows double-peak profile.

ID	Common Name	$M_{BH,IC}$	$M_{BH,BC}$	$M_{BH,IC+BC}$	$M_{BH,\sigma}$	$M_{BH,Fit}$	$M_{BH,RP}$
		log, $M_\odot$	*log*, $M_\odot$	*log*, $M_\odot$	*log*, $M_\odot$	*log*, $M_\odot$	*log*, $M_\odot$
1	UM269	8.89	9.11	9.55*	8.26	8.61	9.26
2	MRK1018	7.77	8.75	8.20	7.79	7.85	8.14
3	NVSSJ030639	7.40	8.72	7.50	7.47	7.41	7.86
4	2XMMi/DR7	8.32	9.15	8.94	8.15	8.78	8.76
5	2XMMi/DR7	7.94	9.11	8.07	7.71	7.87	8.43
6	HS0810+5157	8.70	9.82	8.97	8.45	8.50	8.97
7	RBS0769	7.28	8.15	7.48	6.89	7.00	7.98
8	RBS0770	7.24	8.31	7.40	7.22	7.09	7.60
9	MRK0110	6.77	7.74	6.98	6.76	6.96	7.15
10	PG0947+396	8.52	9.48	8.66	8.13	8.47	8.70
11	2XMMi/DR7	8.16	9.39	8.59	8.18	7.80	8.53
12	2XMMi/DR7	7.86	8.90	7.98	7.64	7.79	8.01
13	PG1004+130	9.40	10.30	9.89	8.97	9.20	9.61
14	RBS0875	8.59	9.52	8.79	8.28	8.24	8.66
15	KUG1031+398	6.13	7.49	6.19	5.85	6.23	6.98
16	PG1048+342	8.02	9.02	8.23	7.80	8.33	8.40
17	1RXSJ111007	7.62	8.79	7.75	7.46	7.97	8.20
18	PG1115+407	7.75	8.95	7.96	7.69	8.17	8.45

Table B.2: continued...

ID	Common Name	$M_{BH,IC}$ *log*, $M_\odot$	$M_{BH,BC}$ *log*, $M_\odot$	$M_{BH,IC+BC}$ *log*, $M_\odot$	$M_{BH,\sigma}$ *log*, $M_\odot$	$M_{BH,Fit}$ *log*, $M_\odot$	$M_{BH,RP}$ *log*, $M_\odot$
19	2XMMi/DR7	6.79	7.83	7.04	6.82	7.71	7.41
20	RXJ1140.1+0307	5.74	6.80	5.99	5.83	6.46	6.97
21	PG1202+281	8.13	9.21	8.49	8.09	7.98	8.41
22	1AXGJ121359+1404	8.02	8.88	8.37	7.85	7.84	8.28
23	2E1216+0700	7.04	8.13	7.17	6.96	7.99	7.58
24	1RXSJ122019	8.60	9.63	9.54	8.51	8.26	9.26
25	LBQS1228+1116	8.50	9.54	8.73	8.23	8.49	8.75
26	2XMMi/DR7	7.27	8.56	7.37	7.13	7.37	7.97
27	MRK0771	7.48	8.46	7.95	7.49	7.50	7.98
28	RXJ1233.9+0747	8.19	9.24	8.41	7.90	8.24	8.50
29	RXJ1236.0+2641	7.94	9.02	8.14	7.78	7.76	8.30
30	PG1244+026	6.26	7.41	6.40	6.27	6.79	7.30
31	2XMMi/DR7	8.77	9.92	8.92	8.54	8.70	8.80
32	RBS1201	7.29	8.29	7.46	7.38	7.69	7.62
33	2XMMi/DR7	8.28	9.55	8.62	8.22	7.78	8.56
34	1RXSJ132447	8.19	9.04	8.45	7.71	8.71	8.73
35	UM602	7.82	8.61	7.96	7.29	7.67	8.28
36	1E1346+26.7	6.63	7.55	6.81	6.81	6.52	7.18
37	PG1352+183	8.27	9.20	8.39	8.33	8.23	8.52
38	MRK0464	7.56	8.36	7.83	7.39	7.69	7.83
39	1RXSJ135724	6.08	7.20	6.23	6.10	7.01	7.03
40	PG1415+451	7.47	8.51	7.79	7.42	7.41	8.07
41	PG1427+480	7.96	9.08	8.07	7.68	8.39	8.48
42	NGC5683	7.43	8.27	7.66	7.33	7.74	7.69
43	RBS1423	8.23	9.20	8.45	7.96	8.07	8.49
44	PG1448+273	6.81	8.19	7.00	7.01	7.26	8.00
45	PG1512+370	9.12	10.19	9.79	8.84	8.62	9.51
46	Q1529+050	8.70	8.86	9.01	8.26	8.56	8.81
47	1E1556+27.4	7.76	8.40	7.89	7.55	7.96	7.94
48	MRK0493	6.33	7.56	6.45	6.43	7.19	7.13
49	IIZw177	6.59	7.79	6.83	6.72	7.73	7.52
50	PG2233+134	8.26	9.62	8.39	8.10	7.86	9.10
51	MRK0926	8.15	9.01	8.63	8.06	7.65	8.51

B.3 Emission Line Fitting Parameters of The Whole Sample

Table B.3: Emission line parameters for the whole sample. Narrow component (NC), intermediate component (IC), broad component (BC) and intermediate plus broad component (I+B) are shown separately for Hα and Hβ. IC and BC are both Gaussian, while NC may have the same profile as the whole [OIII] λ5007 or only the narrowest Gaussian component in [OIII] λ5007. [OIII] λ5007 has two (or sometimes three) Gaussian components. In the case of [OIII] λ5007, 'I+B' raw shows the parameters for the whole emission line rather than having narrow component subtracted Only one Gaussian profile is used for HeII λ4686, [FeVII] λ6087 and [FeX] λ6374. Sometimes the S/N of our spectra is not high enough to resolve all these lines, or they are too week to be resolved, thus they do not have their line parameters measured. 'vel' means velocity of line center relative to the rest frame vacuum wavelength in kms^{-1}. The velocity of 'NC' is small and may come from the redshift uncertainty in Sloan's final redshift measurement, and thus should not be taken seriously. FWHMs of 'NC', 'IC' and 'BC' are directly from the Gaussian profile parameters. FWHM for 'I+B' is measured directly from the superposed model profile. The numbers are all in kms^{-1}. 'lum' and 'ew' means luminosity in $Log_{10}(ergss^{-1})$ and equivalent width in Å.

ID		Hα				Hβ				[OIII] 5007				HeII	FeVII	FeX
		vel	*fwhm*	*lum*	*ew*	*vel*	*fwhm*	*lum*	*ew*	*vel*	*fwhm*	*lum*	*ew*	*lum*	*lum*	*lum*
1[d]	*NC*	—	456	42.09	21	—	457	41.46	3.1	—	—	—	—	—	42.3	—
(1)[f]	*IC*	-3700	6080	43.18	270	-3700	6080	42.67	50	47	203	41.49	3.5	—	—	—
	BC	3400	7840	43.23	300	3400	7840	42.73	57	-47	720	42.19	18	—	—	—
	I+B	—	13000	43.51	570	—	13000	43.00	110	—	462	42.27	21	—	—	—
2	*NC*	—	405	40.77	5.0	—	401	40.13	0.94	—	—	—	—	41.1	41.0	—
(1)[f]	*IC*	1000	3810	41.98	83	1000	3810	41.19	11	21	386	41.15	10.0	—	—	—
	BC	1100	11700	41.81	55	1100	11700	41.70	34	-300	892	40.46	2.0	—	—	—
	I+B	—	4330	42.21	140	—	6220	41.82	45	—	401	41.23	12	—	—	—
3	*NC*	—	470	41.84	42	—	469	41.17	6.4	—	—	—	—	41.3	41.3	41.2
(1)[f]	*IC*	120	2040	42.36	140	120	2040	41.86	32	52	396	41.59	17	—	—	—
	BC	1100	9390	42.05	68	1100	9390	41.80	28	-130	1030	41.51	15	—	—	—
	I+B	—	2190	42.53	210	—	2310	42.14	59	—	468	41.85	32	—	—	—
4*	*NC*	—	251	40.89	3.5	—	249	40.35	0.81	-34	239	40.82	2.5	40.8	—	—
(1)[f]	*IC*	-400	5260	42.23	77	-400	5260	41.31	7.4	140	192	41.23	6.2	—	—	—
	BC	-450	13700	42.29	86	-450	13700	42.20	57	-110	1370	40.87	2.7	—	—	—
	I+B	—	6500	42.56	160	—	10800	42.25	64	—	248	41.49	11	—	—	—
5	*NC*	—	326	41.76	13	—	325	41.01	1.6	—	—	—	—	41.9	41.9	—
(2)[f]	*IC*	190	2360	43.15	320	190	2360	42.56	58	-23	325	41.71	8.4	—	—	—
	BC	900	9030	42.96	200	900	9030	42.52	53	-150	794	42.01	17	—	—	—
	I+B	—	2610	43.37	520	—	2720	42.84	110	—	474	42.19	25	—	—	—
6	*NC*	—	461	42.66	51	—	457	41.88	4.7	—	—	—	—	42.4	—	—
(1)[f]	*IC*	400	3980	43.40	280	400	3980	42.86	45	-76	387	42.25	12	—	—	—
	BC	1400	14400	43.53	370	1400	14400	43.16	90	-120	1020	42.19	10.	—	—	—
	I+B	—	4930	43.77	650	—	5430	43.34	140	—	462	42.52	22	—	—	—
7	*NC*	—	580	41.88	38	—	575	41.38	8.0	—	—	—	—	41.5	—	—
(2)[f]	*IC*	160	1570	42.10	62	160	1570	41.60	13	-160	580	40.96	3.2	—	—	—
	BC	-120	4300	41.99	48	-120	4300	41.70	17	-610	1200	41.27	6.5	—	—	—
	I+B	—	1820	42.35	110	—	1980	41.95	30	—	1030	41.45	9.7	—	—	—
8*	*NC*	—	442	41.75	78	—	445	41.08	12	-27	300	41.10	13	41.6	41.0	41.0
(1)[f]	*IC*	73	2360	42.28	260	73	2360	41.68	48	-160	663	41.26	19	—	—	—
	BC	920	8080	41.97	130	920	8080	41.72	53	-170	1390	41.03	11	—	—	—
	I+B	—	2580	42.45	390	—	2840	42.00	100	—	444	41.62	43	—	—	—
9*	*NC*	—	317	41.46	150	—	319	40.81	34	-10.	297	41.66	240	40.6	40.4	—
(1)[f]	*IC*	200	2360	42.02	530	200	2360	40.99	50	150	1450	40.44	14	—	—	—
	BC	840	7230	41.48	150	840	7230	41.14	72	-41	509	41.10	64	—	—	—
	I+B	—	2500	42.13	680	—	3030	41.37	120	—	316	41.79	320	—	—	—

Table B.3: continued

ID		Hα				Hβ				[OIII] 5007				HeII	FeVII	FeX
		vel	*fwhm*	*lum*	*ew*	*vel*	*fwhm*	*lum*	*ew*	*vel*	*fwhm*	*lum*	*ew*	*lum*	*lum*	*lum*
10	*NC*	—	405	42.06	18	—	401	41.13	1.3	—	—	—	—	41.9	42.0	41.2
(1)^f	*IC*	180	4060	43.45	430	180	4060	42.87	70	28	330	41.96	8.9	—	—	—
	BC	1200	12300	43.12	200	1200	12300	42.83	64	-210	934	41.97	9.2	—	—	—
	I+B	—	4440	43.62	630	—	4810	43.15	130	—	407	42.27	18	—	—	—
11	*NC*	—	279	42.03	47	—	281	41.38	5.8	—	—	—	—	41.7	—	—
(1)^f	*IC*	230	3440	42.89	340	230	3440	42.11	31	-43	249	42.06	29	—	—	—
	BC	730	14100	43.10	550	730	14100	42.66	110	-82	634	41.77	15	—	—	—
	I+B	—	4360	43.31	900	—	5640	42.77	140	—	279	42.24	44	—	—	—
12	*NC*	—	396	41.55	36	—	394	40.60	2.8	—	—	—	—	41.6	—	—
(1)^f	*IC*	-76	3850	42.53	350	-76	3850	41.90	57	36	1590	40.92	6.2	—	—	—
	BC	-140	12600	42.11	130	-140	12600	41.77	43	-23	372	41.33	16	—	—	—
	I+B	—	4130	42.67	480	—	4390	42.14	100	—	395	41.47	22	—	—	—
13	*NC*	—	396	42.50	10.	—	395	41.94	1.6	—	—	—	—	42.8	42.3	—
(1)^f	*IC*	580	6160	43.53	110	580	6160	42.85	13	-44	304	42.16	2.8	—	—	—
	BC	700	17200	43.62	140	700	17200	43.46	52	-250	1190	42.37	4.5	—	—	—
	I+B	—	7730	43.88	240	—	10800	43.55	65	—	395	42.58	7.3	—	—	—
14	*NC*	—	298	41.97	23	—	300	41.48	5.8	—	—	—	—	42.0	41.9	—
(1)^f	*IC*	300	5580	43.31	520	300	5580	42.59	74	6.0	893	42.10	25	—	—	—
	BC	1900	16300	42.81	160	1900	16300	42.70	96	-49	266	42.31	41	—	—	—
	I+B	—	5940	43.43	680	—	7060	42.95	170	—	297	42.52	65	—	—	—
15	*NC*	—	342	41.03	30	—	345	40.43	7.4	—	—	—	—	40.7	40.0	40.4
(2)^f	*IC*	58	918	41.22	46	58	918	40.73	15	53	299	40.84	19	—	—	—
	BC	-20	4400	40.97	26	-20	4400	40.48	8.3	-320	1000	40.74	15	—	—	—
	I+B	—	994	41.42	73	—	987	40.92	23	—	340	41.09	34	—	—	—
16	*NC*	—	279	41.62	9.9	—	281	40.98	1.5	—	—	—	—	42.1	41.4	—
(2)^f	*IC*	37	2810	43.14	330	37	2810	42.47	46	-55	968	41.53	5.4	—	—	—
	BC	1300	8860	42.85	170	1300	8860	42.61	63	-76	280	42.00	16	—	—	—
	I+B	—	3080	43.32	500	—	3560	42.84	110	—	297	42.13	22	—	—	—
17*	*NC*	—	608	42.00	37	—	607	41.08	2.9	-28	617	41.84	17	41.7	41.8	41.7
(3)^f	*IC*	160	1930	42.91	300	160	1930	42.35	53	140	235	41.14	3.4	—	—	—
	BC	430	7450	42.67	170	430	7450	42.34	51	-530	1600	41.57	9.2	—	—	—
	I+B	—	2120	43.10	470	—	2250	42.64	100	—	607	42.08	30	—	—	—
18	*NC*	—	400	42.23	32	—	401	41.53	3.6	—	—	—	—	42.1	—	41.9
(1)^f	*IC*	220	1810	43.02	200	220	1810	42.44	29	-60	260	41.28	2.1	—	—	—
	BC	360	7220	42.93	160	360	7220	42.66	48	-210	701	41.61	4.6	—	—	—
	I+B	—	2060	43.28	360	—	2310	42.86	76	—	401	41.78	6.7	—	—	—
19	*NC*	—	188	40.90	13	—	191	40.25	2.3	—	—	—	—	41.0	40.4	40.5
(2)^f	*IC*	46	1500	41.77	96	46	1500	41.16	19	75	186	40.93	11	—	—	—
	BC	-54	5010	41.66	74	-54	5010	41.40	33	-100	445	40.80	8.4	—	—	—
	I+B	—	1730	42.02	170	—	2000	41.60	51	—	223	41.17	20	—	—	—
20	*NC*	—	232	40.64	14	—	230	40.03	3.1	—	—	—	—	41.2	—	39.8
(2)^f	*IC*	29	578	41.12	40	29	578	40.51	9.5	43	234	40.29	5.8	—	—	—
	BC	120	1970	41.12	41	120	1970	40.76	17	-230	460	39.80	1.9	—	—	—
	I+B	—	686	41.42	82	—	774	40.95	27	—	254	40.41	7.6	—	—	—
21	*NC*	—	354	42.05	49	—	357	41.53	11	—	—	—	—	—	41.5	—
(2)^f	*IC*	-250	3990	43.03	470	-250	3990	42.14	44	110	357	42.29	64	—	—	—
	BC	730	13900	42.93	380	730	13900	42.58	120	-200	1160	42.27	63	—	—	—
	I+B	—	4570	43.29	840	—	6090	42.71	170	—	419	42.58	130	—	—	—
22	*NC*	—	317	40.86	6.5	—	319	40.08	0.86	—	—	—	—	41.5	—	—
(2)^f	*IC*	750	4700	42.28	170	750	4700	41.59	28	-19	316	40.92	6.0	—	—	—
	BC	59	12600	42.18	130	59	12600	41.98	68	-150	764	40.90	5.8	—	—	—
	I+B	—	5510	42.53	300	—	7050	42.13	96	—	389	41.21	12	—	—	—

Table B.3: continued

ID		Hα				Hβ				[OIII] 5007				HeII	FeVII	FeX
		vel	*fwhm*	*lum*	*ew*	*vel*	*fwhm*	*lum*	*ew*	*vel*	*fwhm*	*lum*	*ew*	*lum*	*lum*	*lum*
23	*NC*	—	340	41.56	39	—	344	40.79	5.0	—	—	—	—	41.0	—	41.0
(1)^f	*IC*	130	1700	42.15	150	130	1700	41.66	37	31	256	40.59	3.2	—	—	—
	BC	340	5970	41.92	89	340	5970	41.60	33	-79	930	40.81	5.4	—	—	—
	I+B	—	1890	42.35	240	—	1980	41.93	70	—	340	41.01	8.7	—	—	—
24	*NC*	—	576	41.37	3.9	—	575	41.04	1.6	—	—	—	—	42.3	42.2	—
(1)^f	*IC*	150	4700	42.74	91	150	4700	41.59	5.5	44	327	41.00	1.4	—	—	—
	BC	1400	15400	43.19	260	1400	15400	42.91	120	-110	1090	41.52	4.8	—	—	—
	I+B	—	7280	43.32	350	—	13900	42.93	120	—	577	41.64	6.2	—	—	—
25	*NC*	—	400	42.49	47	—	395	41.79	5.6	—	—	—	—	42.1	—	—
(1)^f	*IC*	-74	3820	43.36	350	-74	3820	42.72	47	29	365	42.51	31	—	—	—
	BC	-87	12700	43.22	250	-87	12700	42.92	75	-99	943	42.13	13	—	—	—
	I+B	—	4350	43.59	590	—	4980	43.13	120	—	395	42.66	43	—	—	—
26	*NC*	—	543	42.16	88	—	544	41.63	16	—	—	—	—	41.5	—	—
(2)^f	*IC*	44	1540	42.53	210	44	1540	42.05	43	-40	545	41.71	21	—	—	—
	BC	490	6770	42.42	160	490	6770	41.92	32	-330	1630	41.21	6.6	—	—	—
	I+B	—	1730	42.78	370	—	1720	42.29	76	—	577	41.83	27	—	—	—
27*	*NC*	—	255	40.98	7.6	—	256	40.48	1.8	49	254	41.53	20	41.5	40.9	40.9
(2)^f	*IC*	-150	2500	42.40	200	-150	2500	41.64	26	-130	504	41.15	8.6	—	—	—
	BC	780	7780	42.43	220	780	7780	42.17	86	-350	1240	41.00	6.1	—	—	—
	I+B	—	3030	42.72	420	—	4310	42.28	110	—	291	41.76	35	—	—	—
28	*NC*	—	368	42.31	55	—	369	41.74	11	—	—	—	—	42.7	—	—
(1)^f	*IC*	0	3260	42.99	260	0	3260	42.32	43	-9.0	356	42.62	88	—	—	—
	BC	-690	10900	42.75	150	-690	10900	42.52	68	-21	1530	41.94	18	—	—	—
	I+B	—	3610	43.19	420	—	4240	42.74	110	—	365	42.71	110	—	—	—
29	*NC*	—	497	42.03	34	—	494	41.40	5.6	—	—	—	—	41.8	41.5	41.0
(1)^f	*IC*	12	2810	42.87	240	12	2810	42.30	44	39	385	41.69	11	—	—	—
	BC	810	9770	42.71	170	810	9770	42.46	64	-160	789	41.75	13	—	—	—
	I+B	—	3170	43.10	400	—	3560	42.69	110	—	498	42.02	24	—	—	—
30	*NC*	—	386	41.31	39	—	388	40.66	5.1	—	—	—	—	41.1	39.8	40.3
(1)^f	*IC*	110	808	41.43	52	110	808	41.09	14	-19	336	40.97	11	—	—	—
	BC	110	3040	41.41	49	110	3040	41.10	14	-210	703	40.74	6.5	—	—	—
	I+B	—	943	41.72	100	—	953	41.39	28	—	389	41.17	17	—	—	—
31	*NC*	—	382	41.61	8.0	—	382	40.54	0.51	—	—	—	—	41.2	—	—
(3)^f	*IC*	610	5730	43.14	270	610	5730	42.59	57	20	333	41.29	3.0	—	—	—
	BC	850	21500	42.75	110	850	21500	42.62	61	-460	814	41.17	2.3	—	—	—
	I+B	—	6140	43.29	380	—	6810	42.90	120	—	377	41.54	5.2	—	—	—
32	*NC*	—	425	41.24	23	—	424	40.61	5.3	—	—	—	—	41.1	41.0	40.3
(1)^f	*IC*	140	2550	42.17	200	140	2550	41.48	39	-58	388	41.51	42	—	—	—
	BC	1000	8070	41.68	63	1000	8070	41.52	43	-130	1170	41.09	16	—	—	—
	I+B	—	2710	42.30	260	—	3100	41.80	82	—	419	41.65	58	—	—	—
33	*NC*	—	423	41.68	16	—	426	41.03	2.7	—	—	—	—	41.6	—	—
(1)^f	*IC*	17	4700	42.92	290	17	4700	42.37	59	100	412	41.99	25	—	—	—
	BC	23	16700	42.66	160	23	16700	42.44	68	-610	1370	41.42	6.8	—	—	—
	I+B	—	5170	43.11	450	—	5690	42.71	130	—	425	42.09	32	—	—	—
34	*NC*	—	838	42.57	44	—	836	41.70	4.0	—	—	—	—	41.8	—	—
(3)^f	*IC*	260	2470	43.06	130	260	2470	42.52	26	-150	1440	42.48	25	—	—	—
	BC	1200	6570	42.97	110	1200	6570	42.72	41	-240	634	42.30	16	—	—	—
	I+B	—	2910	43.32	250	—	3310	42.93	67	—	829	42.70	41	—	—	—
35	*NC*	—	572	42.67	130	—	576	42.01	22	—	—	—	—	42.0	41.8	42.1
(1)^f	*IC*	270	2380	43.31	560	270	2380	42.65	96	-120	1250	42.28	43	—	—	—
	BC	1300	5880	43.01	280	1300	5880	42.54	76	-140	512	42.55	79	—	—	—
	I+B	—	2640	43.49	840	—	2790	42.90	170	—	571	42.74	120	—	—	—

Table B.3: continued

ID		Hα				Hβ				[OIII] 5007				HeII	FeVII	FeX
		vel	*fwhm*	*lum*	*ew*	*vel*	*fwhm*	*lum*	*ew*	*vel*	*fwhm*	*lum*	*ew*	*lum*	*lum*	*lum*
36*	*NC*	—	274	41.15	36	—	271	40.32	5.1	54	175	40.54	8.6	41.1	40.2	39.6
(1)[f]	*IC*	210	1540	41.29	49	210	1540	40.69	12	-62	448	40.62	10.	—	—	—
	BC	-160	4450	40.98	24	-160	4450	40.75	14	-290	1150	40.42	6.5	—	—	—
	I+B	—	1690	41.47	73	—	1890	41.02	26	—	248	41.01	25	—	—	—
37	*NC*	—	567	41.92	13	—	566	41.17	2.2	—	—	—	—	42.5	41.7	41.0
(1)[f]	*IC*	220	3440	43.17	230	220	3440	42.68	72	72	294	41.37	3.7	—	—	—
	BC	870	10000	42.88	120	870	10000	42.55	53	-170	824	41.79	9.8	—	—	—
	I+B	—	3790	43.35	350	—	3960	42.92	130	—	558	41.93	13	—	—	—
38*	*NC*	—	326	41.61	140	—	325	41.05	38	38	635	41.22	56	41.1	—	—
(1)[f]	*IC*	-100	4830	42.23	580	-100	4830	41.25	60	60	286	41.51	110	—	—	—
	BC	-390	12200	41.83	230	-390	12200	41.51	110	-140	1280	40.77	20	—	—	—
	I+B	—	5250	42.38	800	—	6630	41.70	170	—	328	41.74	190	—	—	—
39	*NC*	—	212	41.00	32	—	217	40.44	6.9	—	—	—	—	40.8	40.0	40.1
(1)[f]	*IC*	29	829	41.47	93	29	829	40.87	19	33	193	41.06	29	—	—	—
	BC	50	3000	41.25	57	50	3000	40.90	20	-20	427	40.73	14	—	—	—
	I+B	—	925	41.67	150	—	990	41.19	38	—	216	41.22	43	—	—	—
40*	*NC*	—	446	41.34	8.0	—	451	40.45	0.88	-130	465	40.73	1.7	—	—	41.0
(3)[f]	*IC*	210	1930	42.64	160	210	1930	41.84	22	130	123	40.59	1.2	—	—	—
	BC	76	6350	42.47	110	76	6350	42.21	51	-160	1590	41.27	6.0	—	—	—
	I+B	—	2180	42.86	270	—	2790	42.37	73	—	450	41.45	8.9	—	—	—
41	*NC*	—	400	42.10	23	—	401	41.47	3.5	—	—	—	—	42.3	—	—
(2)[f]	*IC*	170	2300	43.38	440	170	2300	42.85	84	-52	401	42.32	25	—	—	—
	BC	890	8300	43.09	220	890	8300	42.73	62	-260	908	42.25	22	—	—	—
	I+B	—	2510	43.56	660	—	2610	43.10	150	—	486	42.59	47	—	—	—
42	*NC*	—	307	40.74	14	—	306	39.90	1.6	—	—	—	—	41.1	40.6	39.9
(1)[f]	*IC*	120	3760	41.89	190	120	3760	41.27	38	26	721	40.43	5.6	—	—	—
	BC	-300	9930	41.66	110	-300	9930	41.44	56	-3.0	287	41.02	22	—	—	—
	I+B	—	4240	42.09	300	—	4920	41.67	94	—	303	41.12	27	—	—	—
43	*NC*	—	414	42.10	29	—	419	41.60	6.5	—	—	—	—	42.0	—	41.0
(1)[f]	*IC*	12	3550	43.23	380	12	3550	42.51	53	79	324	42.07	20	—	—	—
	BC	1400	10900	42.95	200	1400	10900	42.67	75	-310	993	42.22	28	—	—	—
	I+B	—	3920	43.41	590	—	4550	42.90	130	—	419	42.45	47	—	—	—
44	*NC*	—	265	41.86	26	—	262	41.34	5.1	—	—	—	—	41.8	40.3	40.8
(1)[f]	*IC*	73	852	42.41	91	73	852	41.80	15	110	220	41.67	11	—	—	—
	BC	97	4190	42.32	74	97	4190	42.04	26	-98	852	41.72	13	—	—	—
	I+B	—	952	42.67	170	—	1070	42.24	40	—	260	41.99	24	—	—	—
45	*NC*	—	345	42.82	33	—	344	42.22	5.2	—	—	—	—	—	—	—
(1)[f]	*IC*	-870	6210	43.81	330	-870	6210	43.01	32	15	267	42.79	20	—	—	—
	BC	1400	17200	43.89	390	1400	17200	43.56	110	-62	880	42.93	28	—	—	—
	I+B	—	7740	44.16	720	—	10900	43.66	140	—	346	43.17	48	—	—	—
46*	*NC*	—	514	42.22	51	—	516	41.66	13	-11	432	42.32	63	41.4	41.9	—
(3)[f]	*IC*	3000	6960	42.54	110	3000	6960	41.99	29	150	223	41.66	14	—	—	—
	BC	-1400	8410	42.93	260	-1400	8410	42.09	36	-150	1010	42.30	60	—	—	—
	I+B	—	9970	43.08	370	—	9930	42.34	64	—	534	42.66	140	—	—	—
47	*NC*	—	391	41.58	27	—	391	40.93	5.7	—	—	—	—	41.7	—	—
(1)[f]	*IC*	160	3550	42.70	360	160	3550	41.94	58	50	1080	41.19	11	—	—	—
	BC	670	7400	42.02	74	670	7400	41.78	40	-24	355	41.70	34	—	—	—
	I+B	—	3730	42.78	430	—	4100	42.17	98	—	383	41.82	45	—	—	—
48	*NC*	—	302	41.27	51	—	306	40.67	8.7	—	—	—	—	40.4	—	40.2
(2)[f]	*IC*	110	1040	41.53	92	110	1040	41.03	20	28	306	40.37	4.6	—	—	—
	BC	33	4300	41.38	66	33	4300	41.00	19	-130	719	40.30	3.9	—	—	—
	I+B	—	1160	41.77	160	—	1190	41.32	39	—	365	40.64	8.4	—	—	—

Table B.3: continued

ID		Hα				Hβ				[OIII] 5007				HeII	FeVII	FeX
		vel	*fwhm*	*lum*	*ew*	*vel*	*fwhm*	*lum*	*ew*	*vel*	*fwhm*	*lum*	*ew*	*lum*	*lum*	*lum*
49	*NC*	—	284	41.27	19	—	281	40.65	3.8	—	—	—	—	41.5	—	40.5
(1)[f]	*IC*	16	1010	41.65	45	16	1010	41.05	9.4	44	268	40.98	8.1	—	—	—
	BC	160	4040	41.49	31	160	4040	41.33	18	-260	578	40.37	2.0	—	—	—
	I+B	—	1120	41.88	76	—	1340	41.51	27	—	285	41.07	10.	—	—	—
50*	*NC*	—	274	42.84	36	—	275	42.23	4.5	-73	402	41.87	2.1	42.3	42.2	41.9
(1)[f]	*IC*	120	1880	43.60	210	120	1880	43.06	30	130	224	42.34	6.2	—	—	—
	BC	91	8960	43.50	170	91	8960	43.12	35	-470	1770	42.42	7.4	—	—	—
	I+B	—	2090	43.86	370	—	2200	43.39	65	—	266	42.74	16	—	—	—
51*	*NC*	—	451	41.73	65	—	445	41.20	16	11	364	42.03	110	—	41.2	—
(1)[f]	*IC*	-1300	6490	42.44	330	-1300	6490	41.59	39	130	1150	41.57	39	—	—	—
	BC	1400	17200	42.53	410	1400	17200	42.10	130	340	247	41.23	18	—	—	—
	I+B	—	8170	42.79	750	—	11100	42.21	170	—	450	42.21	170	—	—	—

[f] : The final fitting method used for each object. see Section 3.3.1 for detailed description of each fitting methods.

* : Three gaussian profiles are used for these objects, in this case (I+B) means the total of all three components.

[d] : UM 269, the only object in our sample showing double-peak feature in Balmer lines. Two gaussian profiles are used for fitting the two peaks, thus the velocity shift of each component related to the line centre is huge.

Appendix C

The Cross-correlation Table and Figures in Chapter 4

C.1 Supplement of Balmer Component Correlation Plots

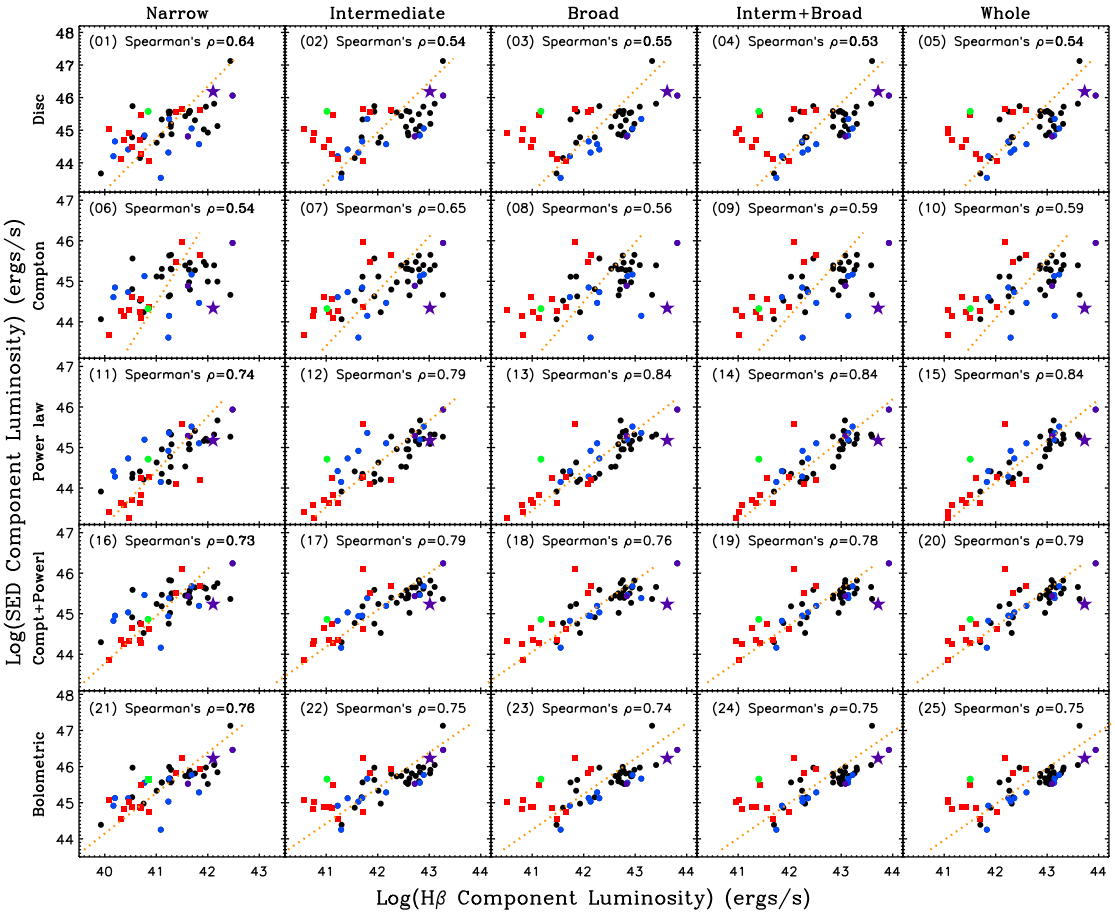

Figure C.1: The luminosity correlations between Hβ line components and SED components. Red points represent NLS1s; blue points represent the broadest Hβ line BLS1s; green point is Mrk 110; purple star is PG 1004+130; purple symbols indicate radio loud sources. The orange dotted line denotes the OLS regression line assuming the SED component luminosity is the independent variable. Spearman's rank correction coefficient ρ_s for the whole sample is also given in each panel.

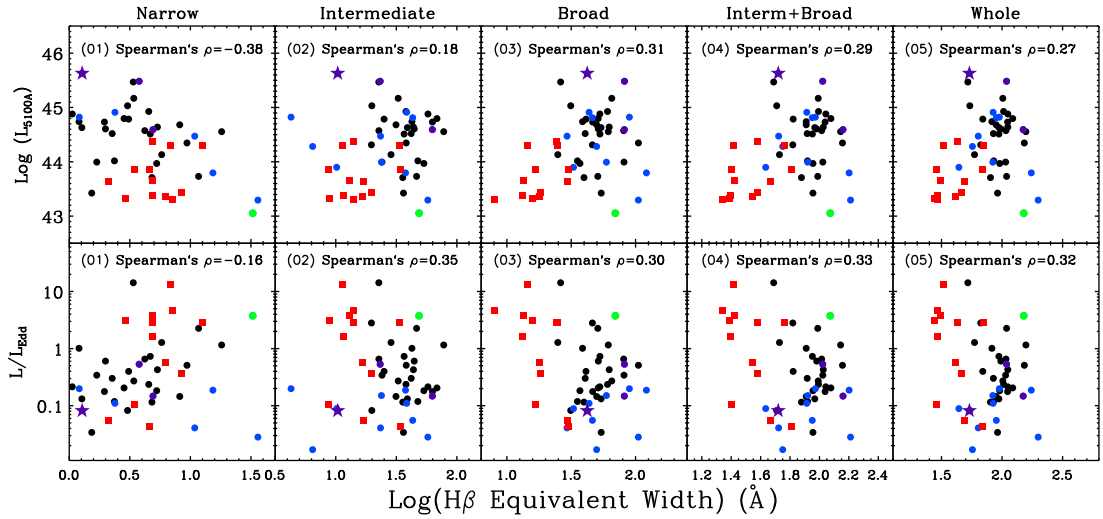

Figure C.2: The cross-correlation plots between Hβ line component EWs and L_{5100A} (the monochromatic luminosity at 5100Å) and L/L_{Edd} (the Eddington ratio) Different symbols have the same meaning as in Figure C.1. Spearman's ρ is given in each panel.

C.2 The Spearman's Rank Correlation Matrix between Hα, Hβ, [OIII] λ5007 Line Components and SED Components

Table C2. Spearman's Rank Correlation Coefficients of SED components vs. Hα, Hβ And [OIII]5007 Line Parameters. ρ_s is Spearman's rank correlation coefficient with 1 being perfect correlation and -1 being perfect anti-correlation. d_s is the logarithm of the significance level of being random distribution, i.e. a smaller d_s suggests a stronger correlation. 'NC, IC, BC, IC+BC, Whole' mean narrow component, intermediate component, broad component, intermediate plus broad component (i.e. narrow component subtracted) and the whole emission line, separately. For [OIII]5007, 'Centre, Blue, Whole' mean the central lower velocity shift component, higher velocity shift component (often shows blue shift) and the whole emission line. 'Compton' indicates the soft X-ray Comptonisation component. 'Power law' indicates the hard X-ray Comptonisation component. 'Com+Pow' indicates the sum of soft and hard X-ray Comptonisation emission (i.e. corona emission). The 'SED Component Fraction' indicates the fraction of each component in the bolometric luminosity. '$frac_{2-10keV}$'(i.e. $\kappa^{-1}_{2-10keV}$) is the fraction of 2-10 keV luminosity related to bolometric luminosity.

		SED Component Luminosity										SED Component Fraction								2-10 keV Energy Band					
		Disc		Compton		Power law		Com+Pow		Bolometric		Disc		Compton		Power law		Com+Pow		$\Gamma_{2-10keV}$		Lumin		$frac_{2-10keV}$	
		ρ_s	d_s	ρ_s	d_s	ρ_s	d_s	ρ_s	d_s	ρ_s	d_s	ρ_s	d_s	ρ_s	d_s	ρ_s	d_s	ρ_s	d_s	ρ_s	d_s	ρ_s	d_s	ρ_s	d_s
Hα	NC	0.63	-6	0.58	-5	0.72	-9	0.74	-9	0.76	-10	0.00	0	-0.16	0	0.15	0	-0.00	0	-0.09	0	0.75	-9	0.15	0
Lumin	IC	0.54	-4	0.60	-6	0.83	-13	0.78	-11	0.75	-10	-0.14	0	-0.07	0	0.29	-1	0.14	0	-0.26	-1	0.88	-17	0.31	-2
	BC	0.56	-5	0.55	-4	0.85	-14	0.77	-10	0.76	-10	-0.10	0	-0.15	0	0.32	-2	0.10	0	-0.22	0	0.89	-17	0.34	-2
	IC+BC	0.55	-5	0.58	-5	0.85	-15	0.79	-11	0.76	-10	-0.12	0	-0.11	0	0.30	-2	0.12	0	-0.26	-1	0.90	-18	0.33	-2
	Whole	0.56	-5	0.59	-5	0.85	-15	0.79	-11	0.77	-10	-0.12	0	-0.11	0	0.30	-2	0.12	0	-0.25	-1	0.90	-18	0.32	-2
Hα	NC	0.30	-1	0.36	-2	0.43	-3	0.48	-3	0.41	-3	-0.19	0	0.03	0	0.22	0	0.19	0	-0.12	0	0.41	-3	0.20	0
FWHM	IC	-0.05	0	0.02	0	0.56	-5	0.25	-1	0.12	0	-0.42	-3	-0.21	0	0.68	-7	0.42	-3	-0.73	-9	0.62	-6	0.74	-9
	BC	0.14	0	0.06	0	0.52	-4	0.24	-1	0.22	0	-0.16	0	-0.28	-1	0.47	-3	0.16	0	-0.62	-6	0.61	-6	0.58	-5
	IC+BC	-0.03	0	0.04	0	0.58	-5	0.28	-1	0.14	0	-0.41	-3	-0.22	0	0.68	-7	0.41	-3	-0.71	-8	0.64	-6	0.74	-9
	Whole	0.07	0	0.34	-2	0.54	-4	0.45	-3	0.30	-1	-0.39	-2	0.21	0	0.39	-2	0.39	-2	-0.42	-3	0.55	-5	0.39	-2
Hα	NC	0.13	0	-0.10	0	-0.08	0	-0.08	0	0.01	0	0.20	0	-0.31	-2	-0.08	0	-0.20	0	-0.01	0	-0.04	0	-0.05	0
EW	IC	0.13	0	0.25	-1	0.45	-3	0.36	-2	0.25	-1	-0.23	-1	-0.08	0	0.38	-2	0.23	-1	-0.54	-4	0.57	-5	0.46	-3
	BC	0.30	-1	0.26	-1	0.61	-6	0.49	-4	0.44	-3	-0.14	0	-0.28	-1	0.42	-3	0.14	0	-0.40	-2	0.72	-9	0.50	-4
	IC+BC	0.19	0	0.23	-1	0.53	-4	0.40	-2	0.32	-2	-0.21	0	-0.20	0	0.44	-3	0.21	0	-0.52	-4	0.66	-7	0.53	-4
	Whole	0.22	0	0.24	-1	0.51	-4	0.40	-2	0.33	-2	-0.18	0	-0.20	0	0.39	-2	0.18	0	-0.50	-4	0.65	-6	0.49	-4
Hβ	NC	0.64	-6	0.54	-4	0.74	-9	0.73	-9	0.76	-10	0.01	0	-0.21	0	0.18	0	-0.01	0	-0.08	0	0.75	-9	0.16	0
Lumin	IC	0.54	-4	0.65	-7	0.79	-11	0.79	-11	0.75	-10	-0.14	0	-0.01	0	0.24	-1	0.14	0	-0.19	0	0.83	-13	0.25	-1
	BC	0.55	-4	0.56	-5	0.84	-14	0.76	-10	0.74	-9	-0.11	0	-0.10	0	0.30	-2	0.11	0	-0.24	-1	0.88	-17	0.33	-2
	IC+BC	0.53	-4	0.59	-5	0.84	-14	0.78	-11	0.75	-9	-0.14	0	-0.07	0	0.30	-2	0.14	0	-0.21	0	0.88	-17	0.32	-2
	Whole	0.54	-4	0.59	-5	0.84	-14	0.79	-11	0.75	-10	-0.14	0	-0.08	0	0.30	-2	0.14	0	-0.21	0	0.88	-17	0.32	-2
Hβ	NC	0.32	-2	0.36	-2	0.43	-3	0.49	-4	0.42	-3	-0.18	0	0.02	0	0.21	0	0.18	0	-0.12	0	0.42	-3	0.19	0
FWHM	IC	-0.05	0	0.02	0	0.56	-5	0.25	-1	0.12	0	-0.42	-3	-0.21	0	0.68	-7	0.42	-3	-0.73	-9	0.62	-6	0.74	-9
	BC	0.14	0	0.06	0	0.52	-4	0.24	-1	0.22	0	-0.16	0	-0.28	-1	0.47	-3	0.16	0	-0.62	-6	0.61	-6	0.58	-5
	IC+BC	-0.05	0	0.01	0	0.55	-5	0.24	-1	0.11	0	-0.40	-2	-0.21	0	0.67	-7	0.40	-2	-0.73	-9	0.61	-6	0.74	-9
	Whole	0.05	0	0.30	-1	0.42	-3	0.37	-2	0.24	-1	-0.32	-2	0.24	-1	0.29	-1	0.32	-2	-0.32	-2	0.43	-3	0.30	-1
Hβ	NC	0.03	0	-0.18	0	-0.11	0	-0.13	0	-0.08	0	0.13	0	-0.31	-2	-0.02	0	-0.13	0	0.02	0	-0.12	0	-0.04	0
EW	IC	0.00	0	0.24	-1	0.32	-2	0.29	-1	0.13	0	-0.31	-2	0.04	0	0.34	-2	0.31	-2	-0.40	-2	0.42	-3	0.39	-2
	BC	0.11	0	0.11	0	0.50	-4	0.30	-1	0.21	0	-0.24	-1	-0.20	0	0.52	-4	0.24	-1	-0.56	-5	0.60	-5	0.60	-6
	IC+BC	0.10	0	0.18	0	0.49	-4	0.34	-2	0.22	0	-0.28	-1	-0.15	0	0.50	-4	0.28	-1	-0.53	-4	0.61	-6	0.58	-5
	Whole	0.11	0	0.18	0	0.49	-4	0.34	-2	0.22	0	-0.27	-1	-0.16	0	0.50	-4	0.27	-1	-0.53	-4	0.61	-6	0.57	-5
[OIII]5007	Centre	-0.09	0	-0.22	0	-0.12	0	-0.21	0	-0.12	0	0.03	0	-0.23	0	-0.03	0	-0.03	0	-0.04	0	-0.07	0	-0.03	0
Lumin	Blue	0.49	-4	0.52	-4	0.70	-8	0.66	-7	0.65	-7	-0.10	0	-0.14	0	0.27	-1	0.10	0	-0.19	0	0.77	-10	0.30	-1
	Whole	0.54	-4	0.55	-5	0.81	-12	0.75	-10	0.73	-9	-0.12	0	-0.10	0	0.28	-1	0.12	0	-0.24	-1	0.85	-15	0.30	-1
[OIII]5007	Centre	-0.13	0	-0.24	-1	-0.15	0	-0.24	-1	-0.17	0	0.02	0	-0.23	0	-0.01	0	-0.02	0	-0.08	0	-0.10	0	-0.01	0
EW	Blue	-0.09	0	-0.11	0	-0.04	0	-0.09	0	-0.12	0	-0.04	0	-0.19	0	0.16	0	0.04	0	-0.13	0	0.07	0	0.24	-1
	Whole	-0.05	0	0.02	0	0.22	0	0.14	0	0.02	0	-0.24	-1	-0.10	0	0.34	-2	0.24	-1	-0.35	-2	0.31	-2	0.42	-3

Appendix D | *Additional Tables in Chapter 5*

D.1 Summary of References for SED Parameter Correlations

Table D.1: A summary of references about the correlations among the most important AGN SED parameters. The upper right triangle shows some most recent works about each correlations pair, while the lower left triangle shows which cross-correlations are studied in this paper. '$\surd$' means this cross-correlation pair is studied in this paper, '$\times$' means not studied. The 'FWHM' is the FWHM of narrow component subtracted Hβ profile. (RM)*: the reverberation mapping studies, e.g. Kaspi et al. (2000), Peterson et al. (2004); Green09: Green et al. (2009); G99: Grupe et al. (1999); G10: Grupe et al. (2010); H07: Hopkins, Richards & Hernquist (2007); F10: Fanidakis et al. (2010); Jin11a: Jin et al. (2011); L10: Lusso et al. (2010); M04: Marconi et al. (2004); S06: Shemmer et al. (2006); S08: Shemmer et al. (2008); V07: Vasudevan & Fabian (2007); V09: Vasudevan & Fabian (2009); Woo02: Woo & Urry (2002); Zhou10a: Zhou & Zhang (2010); Zhou10b: Zhou & Zhao (2010).

	Γ_{2-10}	κ_{2-10}	κ_{5100}	λ_{Edd}	FWHM	M_{BH}	α_{ox}	L_{bol}	L_{2-10}	L_{2keV}	L_{2500}
Γ_{2-10}	—	Zhou10b	—	S08; S06	Zhou10a G10; S08 S06; G99	S06	Green09	—	—	Green09	—
κ_{2-10}	$\surd$	—	—	L10; V09 V07	—	—	L10	M04; H07	V07; H07 M04	—	—
κ_{5100}	$\surd$	$\surd$	—	V07; R06	—	—	—	—	—	—	—
λ_{Edd}	$\surd$	$\surd$	$\surd$	—	Jin11a G10	F10	L10; V09 S08; V07	—	—	—	—
FWHM	$\surd$	$\surd$	$\surd$	$\surd$	—	(RM)*	G10	Jin11a	Jin11a	—	—
M_{BH}	$\surd$	$\surd$	$\surd$	$\surd$	$\surd$	—	—	Woo02	—	—	—
α_{ox}	$\surd$	$\surd$	$\surd$	$\surd$	$\surd$	$\surd$	—	—	—	L10 Green09	L10; G10 S08; V07
L_{bol}	$\surd$	$\surd$	$\surd$	$\surd$	$\surd$	$\surd$	$\surd$	—	H07; M04	—	—
L_{2-10}	$\surd$	$\surd$	$\surd$	$\surd$	$\surd$	$\surd$	$\surd$	$\surd$	—	—	—
L_{2keV}	$\times$	$\times$	$\times$	$\times$	$\times$	$\times$	$\surd$	$\times$	$\times$	—	G10; L10 Green09 S08; V07
L_{2500}	$\times$	$\times$	$\times$	$\times$	$\times$	$\times$	$\surd$	$\times$	$\times$	$\surd$	—

D.2 SED Fitting Parameters Using Model-B (*optxagnf*) Fitting

D.3 Key SED Parameters Using Model-B (*optxagnf*) Fitting

Table D.2: Broadband SED fitting parameters using Model-B, and the fitting outputs (L_{bol}, f_d, f_c, f_p). ID: object number, the same as Table 1 in Jin11a; $N_{H,gal}$ and $N_{H,int}$: the fixed galactic and free intrinsic neutral hydrogen column densities in 10^{20} cm^{-2}; Γ_{pow}: the powerlaw component's slope in the SED fitting, (*) denotes the objects whose powerlaw slopes hit the uplimit of 2.2 and were fixed there; Fpl: the fraction of powerlaw component in the total reprocessed disc emission; R_{cor}: corona (truncation) radius in unit of Gravitational radii (r_g) within which all disc emission is reprocessed into the Comptonisation and powerlaw components; T_e: temperature of the Compton up-scattering electron population; Tau: optical depth of the Comptonisation component; $\log(M_{BH})$: the best-fit black hole mass; $\log(\dot{M})$: total mass accretion rate; L_{bol}: bolometric luminosity integrated from 0.001 keV to 100 keV; f_d, f_c, f_p: luminosity fractions of disc emission, soft Comptonisation and hard X-ray Compotonisation components in the bolometric luminosity; χ^2: the reduced χ^2 of the broadband SED fitting.

ID	$N_{H,gal}$ $\times 10^{20}$	$N_{H,int}$ $\times 10^{20}$	Γ_{pow}	Fpl	R_{cor} r_g	T_e keV	Tau	$log(M_{BH})$ $M_\odot$	$log(\dot{M})$ $g\ s^{-1}$	L_{bol} 10^{44}	f_d	f_c	f_p	χ^2 *reduced*
1	1.79	0.00	1.74	0.69	100.	0.246	17.4	8.61	26.08	62.2	0.19	0.25	0.56	1.00
2	2.43	1.28	1.78	0.39	100.	0.212	16.3	7.84	25.25	9.11	0.19	0.49	0.32	0.97
3	6.31	9.44	1.85	0.25	10.2	0.214	12.2	7.61	25.92	42.8	0.87	0.10	0.03	1.14
4	3.49	2.80	1.66	0.50	100.	0.317	15.2	8.78	25.45	14.4	0.19	0.41	0.40	1.16
5	3.53	5.08	2.20	0.36	69.0	0.202	14.4	7.94	26.37	119	0.32	0.44	0.24	1.04
6	4.24	0.00	1.90	0.46	20.6	0.348	12.2	8.50	26.41	130	0.59	0.22	0.19	1.09
7	1.33	0.00	2.20	0.29	10.5	0.149	33.4	7.58	26.01	52.9	0.26	0.53	0.21	1.16
8	3.12	3.94	1.79	0.15	23.7	0.598	6.91	7.54	25.44	14.3	0.58	0.35	0.06	1.42
9	1.30	0.59	1.72	0.71	16.5	0.267	15.0	7.40	25.70	25.9	0.84	0.05	0.11	20.7
10	1.74	0.46	1.90	0.32	100.	0.295	13.7	8.34	26.24	89.9	0.19	0.55	0.26	1.40
11	1.72	0.57	1.49	0.49	22.5	0.775	8.40	7.92	26.02	54.2	0.65	0.18	0.17	0.96
12	1.20	1.13	1.65	0.48	19.5	0.385	11.0	7.82	25.32	10.7	0.65	0.18	0.17	1.13
13	3.56	0.00	1.38	0.87	11.4	0.142	17.9	9.20	26.50	161	0.90	0.01	0.09	1.33
14	1.76	0.00	1.72	0.71	100.	0.294	16.0	8.24	25.85	36.0	0.19	0.23	0.58	1.07
15	1.31	3.71	2.20	0.09	100.	0.764	4.33	6.30	25.28	9.72	0.80	0.18	0.02	3.67
16	1.70	2.06	1.80	0.31	100.	0.242	15.1	8.30	25.93	43.9	0.19	0.56	0.25	1.40
17	0.65	2.51	1.68	0.14	88.9	0.474	8.27	7.79	26.12	68.4	0.35	0.56	0.09	1.06
18	1.45	0.00	2.20	0.24	11.9	0.260	13.6	8.12	26.33	110	0.51	0.37	0.12	1.48
19	3.70	1.63	1.98	0.19	31.4	0.144	20.6	7.71	24.92	4.28	0.37	0.52	0.12	1.03
20	1.91	3.14	2.20	0.36	12.1	0.186	22.7	6.80	24.87	3.81	0.94	0.04	0.02	1.55
21	1.77	0.00	1.78	0.75	23.1	0.205	19.5	7.98	26.09	63.0	0.61	0.10	0.29	3.45
22	2.75	7.95	1.85	0.21	47.7	0.116	22.1	7.84	25.50	16.2	0.34	0.52	0.14	1.09
23	1.59	0.00	1.39	0.45	95.8	0.628	9.70	8.00	25.06	5.92	0.22	0.43	0.35	0.99
24	1.63	0.66	1.86	0.94	30.8	0.144	54.9	8.26	25.96	46.7	0.48	0.03	0.49	1.89
25	2.34	0.51	1.79	0.40	16.8	0.354	12.4	8.43	26.41	131	0.56	0.27	0.17	1.88
26	2.31	6.32	2.09	0.03	13.5	0.291	10.6	7.70	26.08	61.0	0.46	0.52	0.02	1.14
27	2.75	0.00	2.03	0.22	36.8	0.194	17.0	7.86	25.28	9.75	0.43	0.45	0.12	1.13
28	1.45	5.52	1.73	0.60	72.8	0.315	11.5	7.96	26.25	90.4	0.26	0.30	0.45	1.16
29	1.18	4.24	2.11	0.12	17.8	0.363	7.33	7.87	26.13	68.8	0.49	0.45	0.06	1.19
30	1.87	1.94	2.20	0.36	12.1	0.228	17.9	7.27	25.39	12.5	0.94	0.04	0.02	1.03
31	0.84	0.00	1.66	0.54	100.	0.400	13.0	8.70	25.89	39.5	0.19	0.37	0.43	0.99
32	0.90	0.02	1.82	0.44	100.	0.361	12.9	7.62	25.14	7.00	0.19	0.46	0.35	1.42
33	1.07	0.00	2.17	0.57	12.9	0.244	16.1	7.92	25.93	43.4	0.78	0.10	0.13	1.20
34	1.83	0.85	1.90	0.33	100.	0.252	14.8	8.71	26.06	59.4	0.19	0.54	0.26	1.11
35	1.76	2.30	1.83	0.83	70.8	0.178	17.7	7.67	26.27	95.9	0.19	0.14	0.67	1.02
36	1.18	3.77	2.20	0.22	30.1	0.624	5.58	7.00	24.90	4.05	0.75	0.20	0.05	1.62
37	1.82	0.00	2.04	0.38	100.	0.219	17.2	8.23	25.91	42.1	0.19	0.50	0.31	1.33

Table D.2: continued...

ID	$N_{H,gal}$ $\times 10^{20}$	$N_{H,int}$ $\times 10^{20}$	Γ_{pow}	Fpl	R_{cor} r_g	T_e keV	Tau	$log(M_{BH})$ $M_\odot$	$log(\dot{M})$ $g\ s^{-1}$	L_{bol} 10^{44}	f_d	f_c	f_p	χ^2 *reduced*
38	1.42	0.26	1.61	0.97	100.	0.229	31.1	7.79	24.55	1.82	0.19	0.02	0.79	1.22
39	1.36	3.45	2.08	0.11	38.1	0.259	13.2	7.34	24.94	4.50	0.40	0.53	0.07	0.98
40	0.77	2.01	1.92	0.06	22.4	1.150	4.75	7.88	25.81	32.8	0.59	0.39	0.02	1.51
41	1.81	0.46	1.88	0.39	14.0	0.354	11.9	8.14	26.33	109	0.52	0.30	0.19	1.31
42	2.86	3.26	1.84	0.41	100.	0.083	31.2	7.74	24.71	2.64	0.19	0.47	0.33	1.01
43	2.69	0.93	1.71	0.58	100.	0.469	10.7	8.07	26.17	75.9	0.31	0.29	0.40	1.26
44	2.78	7.77	2.26	0.04	9.96	0.218	13.5	7.56	26.15	73.2	0.53	0.45	0.02	1.56
45	1.46	2.23	1.93	0.49	44.5	0.198	17.2	8.78	26.86	369	0.40	0.30	0.30	2.45
46	4.02	0.54	1.81	0.81	100.	0.207	20.2	8.56	25.61	20.8	0.19	0.15	0.66	1.12
47	3.78	16.5	1.85	0.25	85.8	0.115	29.0	7.96	25.68	24.6	0.19	0.61	0.20	0.97
48	2.11	0.72	1.84	0.19	31.2	0.475	9.28	7.47	24.99	5.01	0.70	0.24	0.06	1.18
49	4.90	0.35	2.20	0.33	71.0	0.211	19.6	7.73	25.18	7.85	0.25	0.50	0.25	1.15
50	4.51	0.00	2.20	0.80	9.10	0.590	7.57	8.38	27.17	750	0.98	0.00	0.01	2.21
51	2.91	1.45	1.77	0.95	100.	0.136	31.8	7.60	25.37	11.9	0.19	0.04	0.77	1.41

Table D.3: Broadband SED Key Parameters from Model-B fitting. ID: object number, the same as Table 1 in Jin11a; $\Gamma_{2-10keV}$: the slope of the single powerlaw fitted to 2-10 keV spectrum. $L_{2-10keV}$: 2-10 keV luminosity (in 10^{44} erg s^{-1}); $\kappa_{2-10keV}$: the 2-10keV bolometric correction coefficient; $\lambda L_{2500\mathring{A}}$: the monochromatic luminosity at 2500Å (in 10^{43} erg s^{-1}); νL_{2keV}: the monochromatic luminosity at 2keV (in 10^{43} erg s^{-1}); α_{ox}: the optical X-ray spectral index; λL_{5100}: the monochromatic luminosity at 5100Å (in 10^{44} erg s^{-1}); κ_{5100}: the 5100Å bolometric correction coefficient; $FWHM_{H\beta}$: the narrow component subtracted Hβ FWHM; L_{bol}/L_{Edd}: the Eddington Ratio.

ID	$\Gamma_{2-10keV}$	$L_{2-10keV}$ $\times 10^{44}$	$\kappa_{2-10keV}$	$\lambda L_{2500\mathring{A}}$ $\times 10^{43}$	νL_{2keV} $\times 10^{43}$	α_{ox}	λL_{5100} $\times 10^{44}$	κ_{5100}	$FWHM_{H\beta}$ $km\ s^{-1}$	L_{bol}/L_{Edd}
1	1.69±0.06	4.941	12.6	84.3	25.8	1.20	8.15	7.65	13000	0.12
2	1.67±0.10	0.469	19.5	18.9	2.48	1.34	0.791	11.5	6220	0.10
3	1.77±0.07	0.289	148	38.9	1.77	1.51	1.35	31.7	2310	0.80
4	1.80±0.11	0.567	25.5	13.3	3.15	1.24	1.91	7.55	10800	0.019
5	2.10±0.22	2.284	52.2	132	13.1	1.38	5.48	21.8	2720	1.1
6	1.93±0.18	4.855	26.9	281	27.4	1.39	14.8	8.87	5430	0.32
7	2.39±0.22	0.267	199	43.0	2.38	1.48	1.95	27.1	1980	1.1
8	1.84±0.04	0.418	34.3	16.4	2.82	1.29	0.539	26.6	2840	0.31
9	1.76±0.01	0.839	30.9	20.2	5.29	1.22	0.113	230	3030	0.80
10	1.92±0.05	3.532	25.5	199	23.0	1.36	7.59	11.9	4810	0.32
11	1.71±0.11	1.811	30.0	70.5	9.06	1.34	3.75	14.5	5640	0.50
12	1.68±0.23	0.502	21.3	19.4	1.58	1.42	1.04	10.3	4390	0.13
13	1.37±0.12	0.751	215	697	3.03	1.91	42.6	3.79	10800	0.078
14	1.69±0.04	3.189	11.3	50.1	17.0	1.18	3.91	9.22	7060	0.16
15	2.35±0.12	0.042	234	2.09	0.397	1.28	0.204	47.7	988	3.7
16	1.78±0.07	1.502	29.3	107	8.27	1.43	4.26	10.3	3560	0.17
17	1.80±0.20	0.779	88.0	82.7	3.70	1.52	3.31	20.7	2250	0.86
18	2.23±0.08	1.254	88.0	153	9.68	1.46	6.11	18.1	2310	0.64
19	1.98±0.18	0.084	51.0	8.66	0.496	1.48	0.443	9.69	2000	0.064
20	2.34±0.12	0.053	71.9	2.29	0.468	1.26	0.215	17.7	774	0.47
21	1.70±0.04	3.856	16.4	84.7	20.5	1.24	2.22	28.5	6090	0.51
22	1.70±0.09	0.396	41.0	27.3	2.15	1.42	0.983	16.5	7050	0.18
23	1.80±0.19	0.145	41.1	11.0	0.912	1.42	0.708	8.39	1980	0.046
24	1.83±0.18	4.735	9.88	94.9	24.4	1.23	6.64	7.05	13900	0.20
25	1.88±0.03	3.054	43.1	261	19.6	1.43	8.44	15.6	4980	0.37
26	2.09±0.25	0.362	169	56.0	2.57	1.51	2.04	30.0	1720	0.94
27	1.94±0.04	0.277	35.3	19.1	2.52	1.34	0.988	9.89	4310	0.10
28	1.71±0.14	2.951	30.7	115	13.4	1.36	4.80	18.9	4240	0.77
29	2.00±0.12	0.726	95.0	78.1	4.93	1.46	3.25	21.3	3560	0.71
30	2.46±0.09	0.146	85.5	10.2	1.26	1.35	0.452	27.7	954	0.52
31	1.69±0.14	2.420	16.4	53.2	11.9	1.25	6.49	6.10	6810	0.061
32	1.88±0.03	0.464	15.1	11.4	2.96	1.23	0.512	13.7	3100	0.13
33	2.14±0.21	1.157	37.6	60.5	7.50	1.35	4.03	10.8	5690	0.40
34	1.90±0.14	2.489	23.9	141	13.5	1.39	10.8	5.53	3310	0.089
35	1.76±0.07	3.918	24.5	72.9	52.7	1.05	3.59	26.8	2790	1.6
36	2.20±0.08	0.091	44.7	3.18	0.651	1.26	0.244	16.6	1890	0.31
37	1.95±0.08	1.768	23.9	88.7	12.3	1.33	5.39	7.82	3960	0.19
38	1.55±0.09	0.175	10.4	1.57	0.770	1.12	0.197	9.26	6630	0.023
39	2.17±0.20	0.079	57.4	5.55	0.726	1.34	0.233	19.4	991	0.16
40	2.02±0.06	0.468	70.3	46.6	3.46	1.43	2.05	16.0	2790	0.34
41	1.94±0.05	2.444	44.7	156	15.9	1.38	6.26	17.4	2610	0.60
42	1.76±0.11	0.158	16.7	4.96	0.803	1.30	0.265	9.99	4920	0.037
43	1.74±0.07	4.524	16.8	121	26.0	1.26	4.36	17.4	4550	0.50
44	2.25±0.05	0.236	311	52.5	2.08	1.54	2.36	31.1	1070	1.5
45	1.82±0.06	17.502	21.1	840	100.	1.35	30.4	12.2	10900	0.47
46	1.81±0.12	2.175	9.60	19.2	10.4	1.10	2.97	7.04	9930	0.044
47	1.45±0.25	0.868	28.4	40.8	4.39	1.37	0.931	26.5	4100	0.21
48	2.03±0.11	0.101	49.5	7.14	0.728	1.38	0.278	18.1	1190	0.13
49	2.40±0.22	0.200	39.4	14.4	1.69	1.36	0.719	10.9	1340	0.11
50	2.41±0.18	3.299	228	834	27.8	1.57	29.5	25.5	2200	2.4
51	1.67±0.03	1.659	7.20	13.2	8.22	1.08	0.624	19.1	11100	0.23

Table D.4: The cross-correlation matrix of the 9 key SED parameters based on Model-A data from Jin et al. (2011). ID 1∼9 are given to each parameter. ρ_s is the Spearman's rank coefficient. d_s is probability of random distribution in logarithm. α and β are the bisector regression line coefficients assuming Y=βX+α. The coefficients in the upper right triangle region assumes the vertical parameters to be X. The coefficients in the lower left triangle region assumes the horizontal parameters to be X.

		$\Gamma_{2-10keV}$	$\kappa_{2-10keV}$	κ_{5100A}	λ_{Edd}	Hβ FWHM $km\ s^{-1}$	M_{BH} $M_\odot$	α_{ox}	L_{bol} 10^{+44}	$L_{2-10keV}$ 10^{+44}
			log	*log*	*log*	*log*	*log*		*log*	*log*
ID		(1)	(2)	(3)	(4)	(5)	(6)	(7)	(8)	(9)
(1)	ρ_s	1	0.76	0.46	0.60	-0.72	-0.43	0.50	0.22	-0.38
	d_s	-∞	-10.	-3.	-5.	-8.	-3.	-4.	-1.	-2.
	β	1	1.93±0.17	1.26±0.11	2.61±0.27	-1.27±0.12	-2.19±0.30	0.56±0.06	1.42±0.37	-2.02±0.33
	α	0	-2.13±0.32	-1.24±0.21	-5.47±0.52	5.99±0.24	12.02±0.58	0.28±0.12	-1.26±0.70	3.77±0.65
(2)	ρ_s	0.76	1	0.72	0.72	-0.80	-0.62	0.76	0.17	-0.57
	d_s	-10.	-∞	-8.	-8.	-11.	-6.	-10.	-1.	-5.
	β	0.52±0.05	1	0.67±0.05	1.40±0.09	-0.66±0.06	-1.23±0.14	0.26±0.03	1.06±0.07	-1.24±0.13
	α	1.10±0.07	0	0.12±0.08	-2.69±0.18	4.60±0.09	9.76±0.21	0.94±0.04	-0.21±0.15	1.86±0.19
(3)	ρ_s	0.46	0.72	1	0.85	-0.59	-0.80	0.37	0.17	-0.41
	d_s	-3.	-8.	-∞	-14.	-5.	-11.	-2.	-1.	-3.
	β	0.79±0.07	1.49±0.10	1	2.11±0.15	-0.98±0.09	-1.84±0.17	0.49±0.09	1.23±0.19	-1.68±0.18
	α	0.98±0.09	-0.18±0.13	0	-2.96±0.19	4.71±0.11	10.01±0.19	0.76±0.11	0.02±0.24	1.88±0.23
(4)	ρ_s	0.60	0.72	0.85	1	-0.53	-0.58	0.42	0.51	-0.12
	d_s	-5.	-8.	-14.	-∞	-4.	-5.	-3.	-4.	-0.
	β	0.38±0.04	0.71±0.05	0.47±0.03	1	-0.51±0.06	-0.89±0.09	0.23±0.05	0.83±0.06	-0.97±0.04
	α	2.10±0.04	1.91±0.03	1.40±0.03	0	3.31±0.06	7.41±0.09	1.45±0.03	1.85±0.08	-0.56±0.12
(5)	ρ_s	-0.72	-0.80	-0.59	-0.53	1	0.65	-0.59	0.08	0.63
	d_s	-8.	-11.	-5.	-4.	-∞	-6.	-5.	-0.	-6.
	β	-0.79±0.07	-1.51±0.15	-1.02±0.09	-1.96±0.23	1	1.85±0.17	-0.43±0.06	1.11±0.15	1.89±0.14
	α	4.71±0.26	6.94±0.54	4.79±0.34	6.48±0.82	0	1.27±0.59	2.87±0.20	-2.46±0.55	-6.82±0.47
(6)	ρ_s	-0.43	-0.62	-0.80	-0.58	0.65	1	-0.25	0.31	0.76
	d_s	-3.	-6.	-11.	-5.	-6.	-∞	-1.	-2.	-10.
	β	-0.46±0.06	-0.82±0.09	-0.54±0.05	-1.12±0.11	0.54±0.05	1	-0.39±0.12	0.95±0.09	1.04±0.08
	α	5.50±0.50	7.97±0.73	5.43±0.41	8.33±0.91	-0.69±0.38	0	4.38±0.91	-5.93±0.70	-8.23±0.64
(7)	ρ_s	0.50	0.76	0.37	0.42	-0.59	-0.25	1	0.30	-0.32
	d_s	-4.	-10.	-2.	-3.	-5.	-1.	-∞	-1.	-2.
	β	1.79±0.20	3.87±0.40	2.03±0.37	4.42±1.00	-2.33±0.31	-2.58±0.78	1	2.81±0.96	-3.09±0.77
	α	-0.49±0.27	-3.64±0.54	-1.55±0.51	-6.43±1.36	6.70±0.42	11.30±1.07	0	-2.32±1.30	4.06±1.05
(8)	ρ_s	0.22	0.17	0.17	0.51	0.08	0.31	0.30	1	0.65
	d_s	-1.	-1.	-1.	-4.	-0.	-2.	-1.	-∞	-6.
	β	0.70±0.18	0.94±0.07	0.82±0.13	1.21±0.09	0.90±0.13	1.05±0.10	0.36±0.12	1	1.14±0.13
	α	0.89±0.26	0.20±0.13	-0.01±0.20	-2.24±0.15	2.21±0.20	6.26±0.18	0.83±0.18	0	-1.79±0.19
(9)	ρ_s	-0.38	-0.57	-0.41	-0.12	0.63	0.76	-0.32	0.65	1
	d_s	-2.	-5.	-3.	-0.	-6.	-10.	-2.	-6.	-∞
	β	-0.50±0.08	-0.81±0.08	-0.60±0.07	-1.03±0.04	0.53±0.04	0.96±0.08	-0.32±0.08	0.88±0.10	1
	α	1.87±0.04	1.50±0.06	1.12±0.05	-0.57±0.12	3.60±0.04	7.93±0.06	1.31±0.03	1.58±0.07	0

D.4 Parameter Correlations Matrix Using Values from Model-A (*optxagn*) Fitting

Appendix E | *Additional Figures in Chapter 5*

E.1 Parameter Cross-correlations Using Values from Model-A (*Optxagn*) Fitting

Similar cross-correlation plots as reported in previous sections but use parameter values from Model-A fitting in Jin et al. (2011). In each panel, the various point symbols show Model-A data. The solid orange line is the regression result for these Model-A data using the same regression methods as in previous sections. The dashed gray line is our result from previous sections based on Model-B data. All dotted lines are from the other literatures as indicated in previous sections.

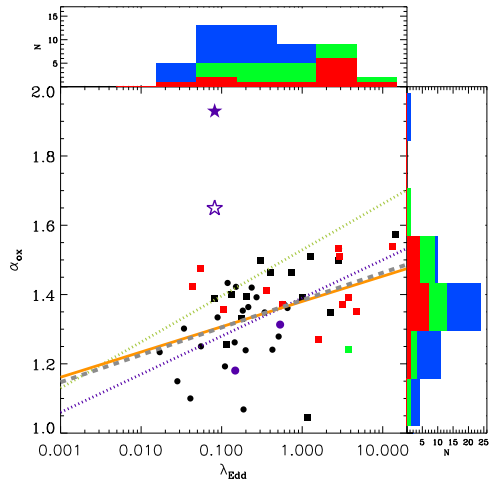

E.1-1

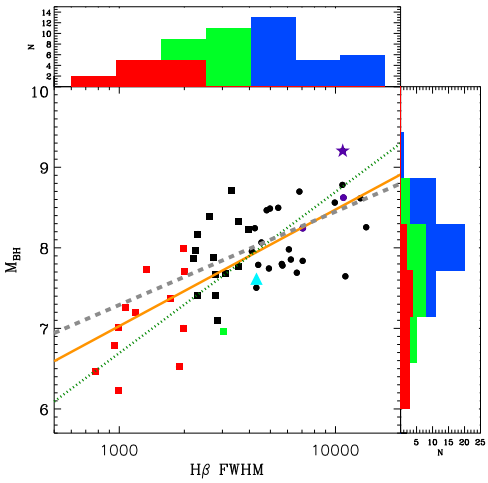

E.1-2

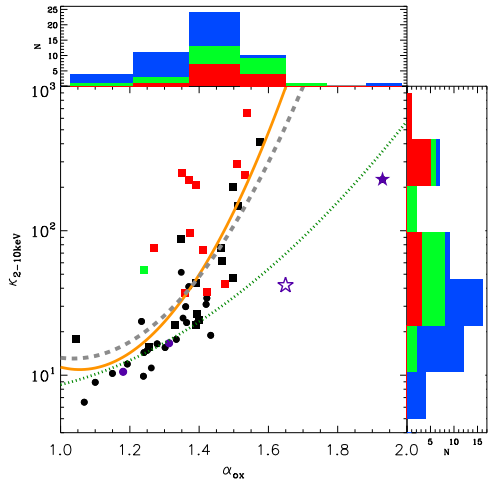

E.1-3

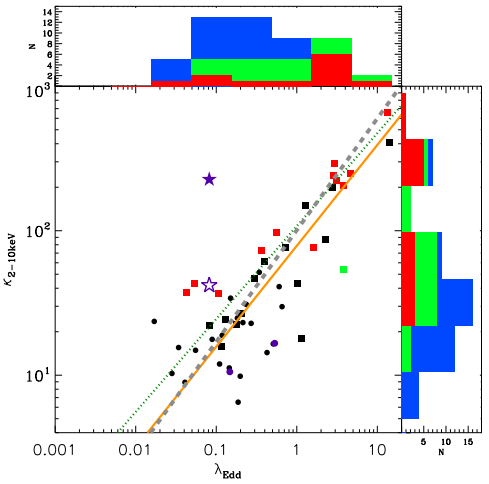

E.1-4

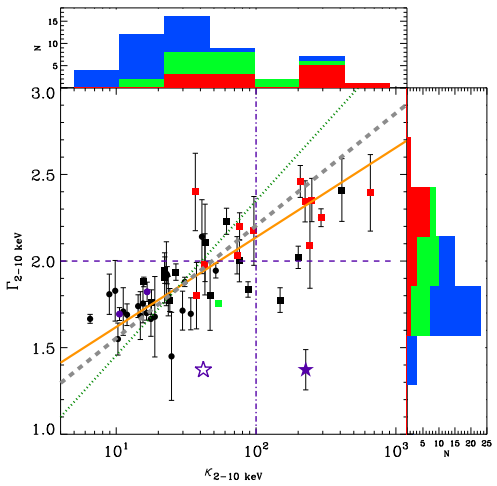

E.1-5

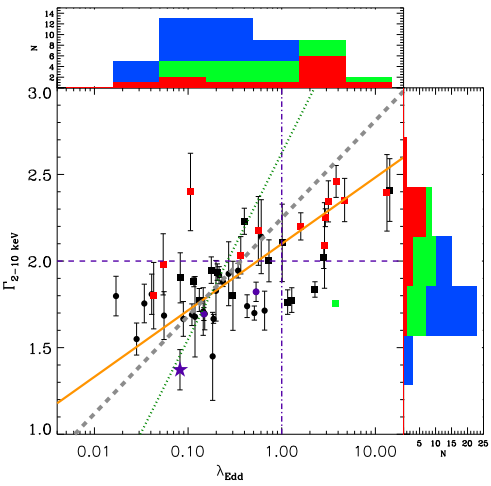

E.1-6

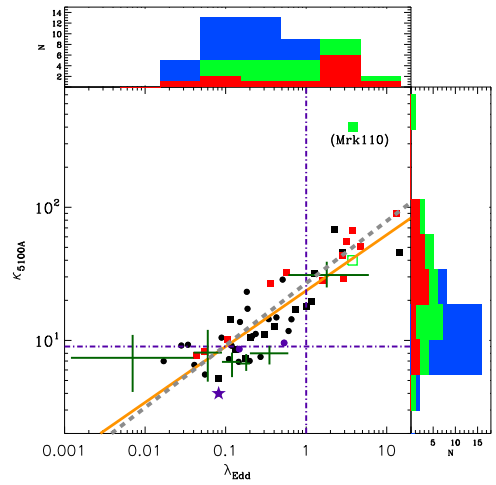
(Mrk110)
κ_{5100A}
λ_{Edd}
0.001
0.01
0.1
1
10
10^1
10^2

E.1-7

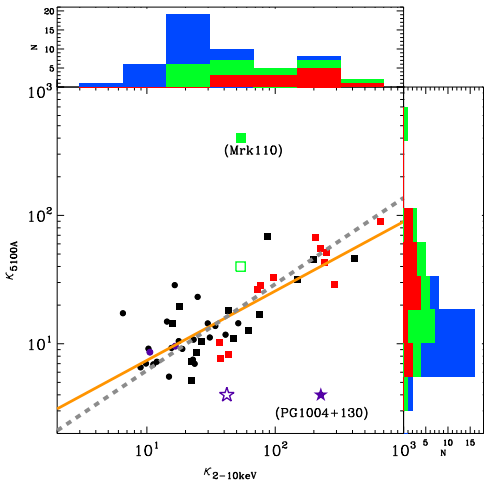
(Mrk110)
(PG1004+130)
κ_{5100A}
$\kappa_{2-10keV}$
10^1
10^2
10^3

E.1-8

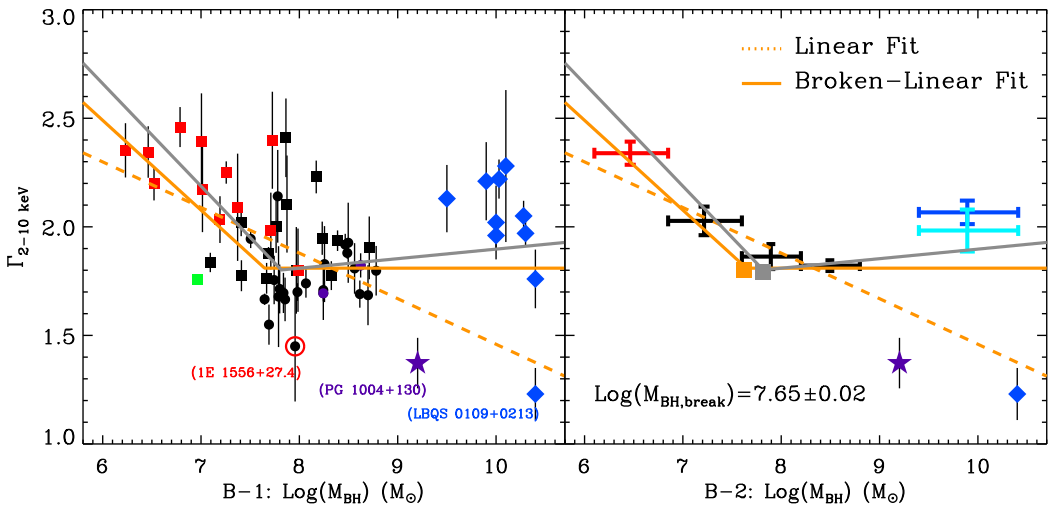
$\Gamma_{2-10\ keV}$
B−1: Log(M_{BH}) ($M_\odot$)
B−2: Log(M_{BH}) ($M_\odot$)
Linear Fit
Broken−Linear Fit
(1E 1556+27.4)
(PG 1004+130)
(LBQS 0109+0213)
Log($M_{BH,break}$)=7.65±0.02
3.0
2.5
2.0
1.5
1.0
6
7
8
9
10

E.1-9

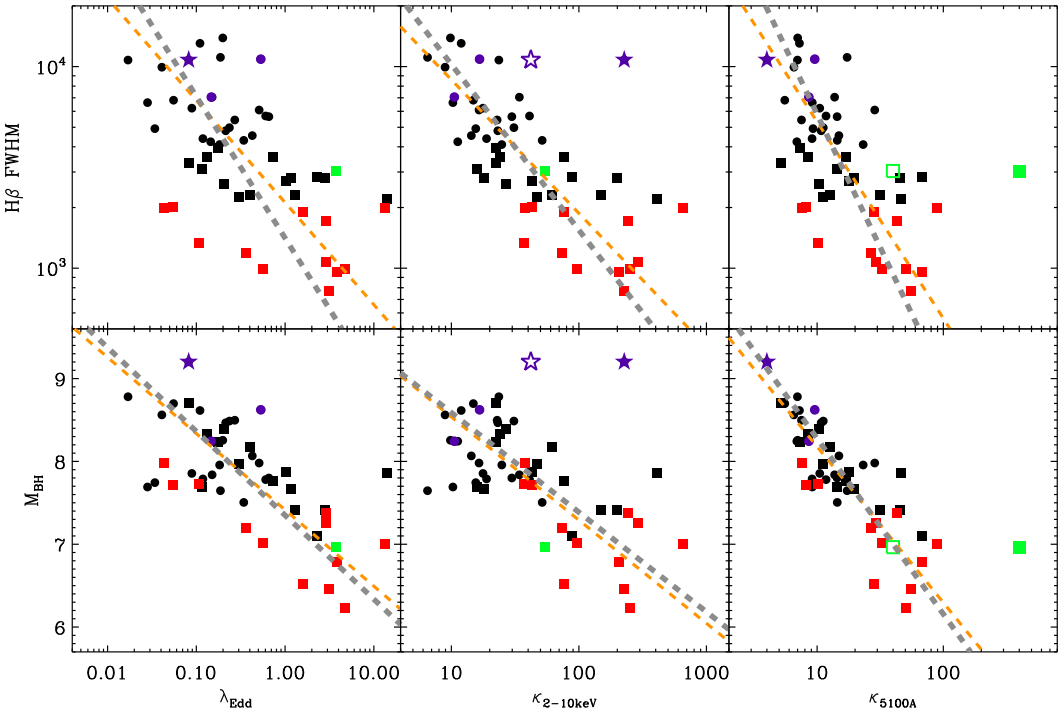
Hβ FWHM
10^4
10^3
M_{BH}
9
8
7
6
0.01
0.10
1.00
10.00
λ_{Edd}
10
100
1000
$\kappa_{2-10keV}$
10
100
κ_{5100A}

E.1-10

E.2 Mean AGN SEDs from Model-A (*Optxagn*) Fitting

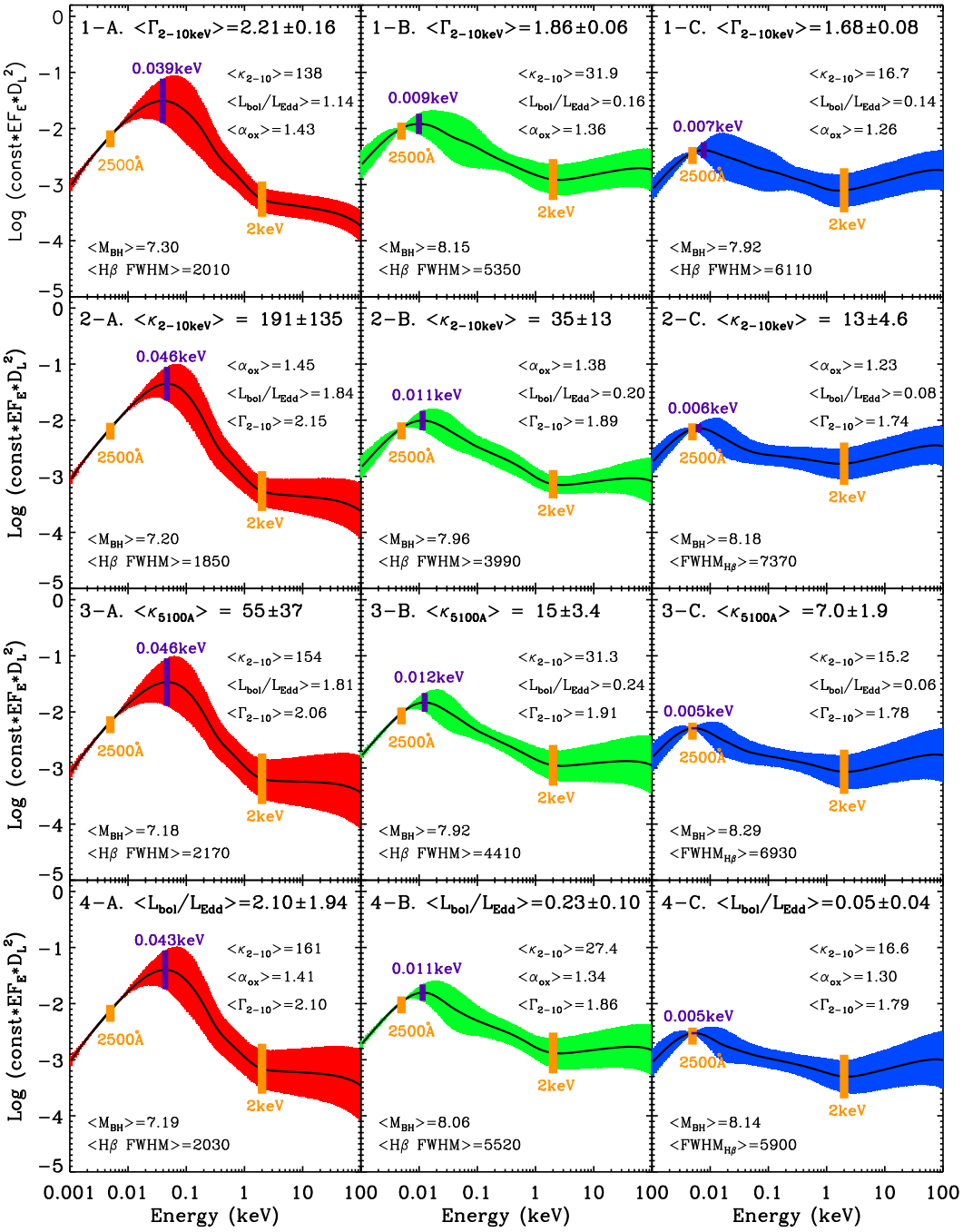

Figure E.2: The AGN mean SEDs based on different values of the 9 key parameters from Model-A fitting in Jin et al. (2011) (i.e. without effect of color temperature correction). For each parameter, the 51 sources are sorted according to the parameter value, and are then divided into three subsets evenly so that each subset contains 17 sources. PG 1004+130 is excluded from its subset. Finally, a mean SED is constructed for each of the three subsets after renormalizing each individual SED to the mean 2500Å luminosity of that subset. The three panels (A, B, C) in each row show the mean SEDs of the subsets classified by the parameter shown in the panel title. In each panel, the solid curve is the mean SED, while the color shaded region is the $\pm 1\sigma$ deviation. The 2500 Å and 2 keV positions are marked by the vertical solid orange lines, whose related height shows the value of α_{ox}, The SED peaking position is also marked by the vertical solid purple line. The average values of some other parameters in that subset are also shown in the panel. All the mean SEDs have been rescaled by the same arbitrary constant in the Y-axis which is 1.3×10^{-46}. Note that the energy ranges E < 6 eV and 0.3 keV < E < 10 keV are covered by SDSS, OM and EPIC data, while the SED in the rest energy bands is determined by the extrapolating of the best-fit model.

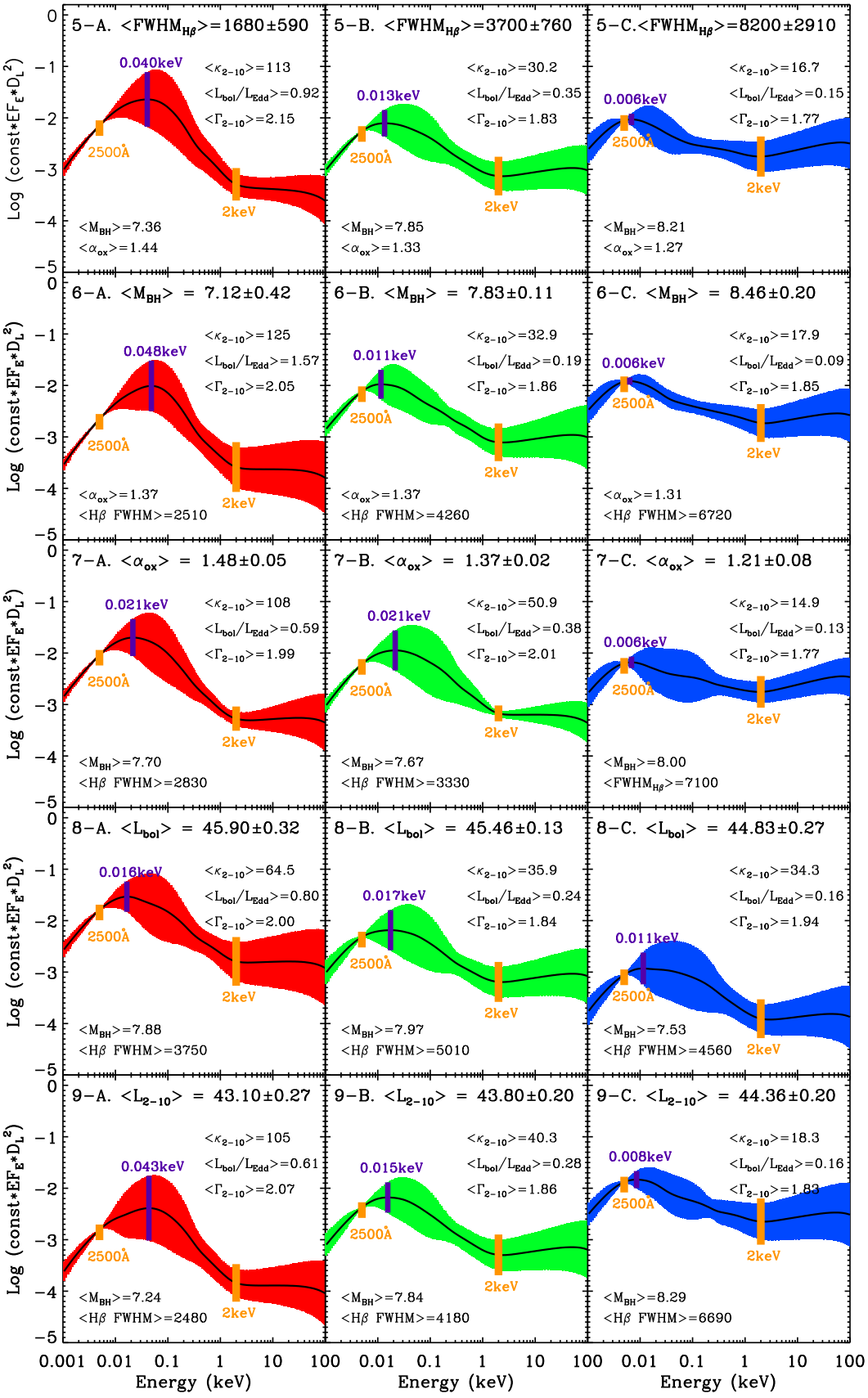

Figure E.2: *continued*

Bibliography

[1] Abramowicz M. A., Kato S., Matsumoto R., 1989, PASJ, 41, 1215

[2] Antonucci R., 1993, ARA&A, 31, 473

[3] Antonucci R. R. J., Miller J. S., 1985, ApJ, 297, 621

[4] Avni Y., Tananbaum H., 1982, ApJ, 262, L17

[5] Axelsson M., Church R. P., Davies M. B., Levan A. J., Ryde F., 2011, MNRAS, 412, 2260

[6] Baldwin J. A., Phillips M. M., Terlevich R., 1981, PASP, 93, 5

[7] Baldwin J., Ferland G., Korista K., Verner D., 1995, ApJ, 455, L119

[8] Baldwin J. A., Ferland G. J., Korista K. T., Hamann F., Dietrich M., 2003, ApJ, 582, 590

[9] Ballantyne D. R., 2010, ApJ, 708, L1

[10] Barth A. J., Ho L. C., Sargent W. L. W., 2002, AJ, 124, 2607

[11] Barth A. J., Greene J. E., Ho L. C., 2005, ApJ, 619, L151

[12] Barth A. J., Greene J. E., Ho L. C., 2008, AJ, 136, 1179

[13] Barth A. J., et al., 2011, ApJ, 743, L4

[14] Baskin A., Laor A., 2005, MNRAS, 356, 1029

[15] Bennert N., Jungwiert B., Komossa S., Haas M., Chini R., 2006, A&A, 459, 55

[16] Bentz M. C. et al., 2006, ApJ, 651, 775

[17] Bentz M. C. et al., 2010, ApJ, 716, 993

[18] Bessell M. S., 1991, A&A, 242, L17

[19] Bian Wei-Hao, 2005, ChJAS, 5, 289

[20] Bian W., Huang K., 2010, MNRAS, 401, 507

[21] Bian W., Zhao Y., 2004a, MNRAS, 347, 607

[22] Bian W., Zhao Y., 2004b, MNRAS, 352, 823

[23] Bian W., Yuan Q., Zhao Y., 2005, MNRAS, 364, 187

[24] Bian W., Chen Y., Gu Q., Wang J., 2007, ApJ, 668, 721

[25] Bian W., Hu C., Gu Q., Wang J., 2008, MNRAS, 390, 752

[26] Bian W., Gu Q., Zhao Y., Chao L., Cui Q., 2006, MNRAS, 372, 876

[27] Blandford R. D., McKee C. F., 1982, ApJ, 255, 419

[28] Blandford R. D., Rees M. J., 1978, PhyS, 17, 265

[29] Boisson C., Joly M., Moultaka J., Pelat D., Serote Roos M., 2000, A&A, 357, 850

[30] Boller T., Brandt W. N., Fink H., 1996, A&A, 305, 53

[31] Boroson T. A., 2002, ApJ, 565, 78

[32] Boroson T. A., 2003, ApJ, 585, 647

[33] Boroson T. A., 2005, AJ, 130, 381

[34] Boroson T. A., Green R. F., 1992, ApJS, 80, 109

[35] Bouchet P., Lequeux J., Maurice E., Prevot L., Prevot-Burnichon M. L., 1985, A&A, 149, 330

[36] Bradley J., et al., 2005, Science, 307, 244

[37] Brandt W. N., Mathur S., Elvis M., 1997, MNRAS, 285, L25

[38] Brinchmann J., Charlot S., White S. D. M., Tremonti C., Kauffmann G., Heckman T., Brinkmann J., 2004, MNRAS, 351, 1151

[39] Brocksopp C., Starling R. L. C., Schady P., Mason K. O., Romero-Colmenero E., Puchnarewicz E. M., 2006, MNRAS, 366, 953

[40] Cai W., Pradhan A. K., 1993, ApJS, 88, 329

[41] Calzetti D., Armus L., Bohlin R. C., Kinney A. L., Koornneef J., Storchi-Bergmann T., 2000, ApJ, 533, 682

[42] Canalizo G., Stockton A., 2001, ApJ, 555, 719

[43] Canfield R. C., Puetter R. C., 1981, ApJ, 243, 390

[44] Casebeer D. A., Leighly K. M., Baron E.,2006, ApJ, 637, 157

[45] Collin S., Dumont A. M., 1990, A&A, 229, 292

[46] Collin S., Huré J.-M., 2001, A&A, 372, 50

[47] Collin S., Kawaguchi T., 2004, A&A, 426, 797

[48] Collin S., Kawaguchi T., Peterson B. M., Vestergaard M., A&A, 456, 75

[49] Collin S., Boisson C., Mouchet M., Coupé S., Porquet D., Rokaki E., 2002, A&A, 388, 771

[50] Comastri A., 2000, NewAR, 44, 403

[51] Córdova F. A., Kartje, J. F., Thompson R. J. Jr., Mason K. O., Puchnarewicz E. M., Harnden F. R. Jr., 1992, ApJS, 81, 661

[52] Crenshaw D. M., Kraemer S. B., 1999, ApJ, 521, 572

[53] Crenshaw D. M., Kraemer S. B., George I. M., 2003, Ann.Rev.A&A, 41, 117

[54] Crenshaw D. M., Kraemer S. B., Bruhweiler F. C., Ruiz J. R., 2001, ApJ, 555, 633

[55] Crummy J., Fabian A. C., Gallo L., Ross R. R., 2006, MNRAS, 365, 1067

[56] Czerny B., Elvis M., 1987, ApJ, 321, 305

[57] Czerny B., Nikołajuk M., Różańska A, Dumont A.-M., Loska Z., Zycki P. T., 2003, A&A, 412, 317

[58] Davidson K., Netzer H.,1979, RvMP, 51, 715

[59] Davis S. W., Hubeny I., 2006, ApJS, 164, 530

[60] Davis S. W., Done C., Blaes O. M., 2006, ApJ, 647, 525

[61] Denney K. D. et al., 2010, ApJ, 721, 715

[62] Dickey J. M., Lockman F. J., 1990, ARA&A, 28, 215

[63] Done C., Gierliński M., 2005, Ap&SS, 300, 167

[64] Done C., Kubota A., 2006, MNRAS, 371, 1216

[65] Done C., Nayakshin S., 2007, MNRAS, 377, L59

[66] Done C., Gierliński M., Kubota A., 2007, A&ARv, 15, 1

[67] Done C., Davis S., Jin C., Blaes O., Ward M., 2011, MNRAS, preprint, (arXiv:1107.5429v2)

[68] Done C., Ward M. J., Fabian A. C., Kunieda H., Tsuruta S., Lawrence A., Smith M.G., Wamsteker W., 1990, MNRAS, 243, 713

[69] Edelson R., Vaughan S., Warwick R., Puchnarewicz E., George I., 1999, MNRAS, 307, 91

[70] Elvis M., Fassnacht C., Wilson A. S., Briel U., 1990, ApJ, 361, 459

[71] Elvis M., et al., 1994, ApJS, 95, 1

[72] Eracleous M., Halpern J. P., 2003, ApJ, 599, 886

[73] Evans I. N., Ford H. C., Kinney A. L., Antonucci R. R. J., Armus L., Caganoff S., 1991, ApJ, 369, 27

[74] Evans I. N., Tsvetanov Z., Kriss G. A., Ford H. C., Caganoff S., Koratkar A. P., 1993, ApJ, 417, 82

[75] Fan X., 2006, NewAR, 50, 665

[76] Fabian A. C., 2005, ESASP, 604, 463

[77] Fabian A. C., Rees M. J., Stella L., White N. E., 1989, MNRAS, 238,729

[78] Fabian A. C., Miniutti G., Gallo L., Boller Th., Tanaka Y., Vaughan S., Ross R. R., 2004, MNRAS, 353, 1071

[79] Fabian A. C., et al., 2002, MNRAS, 335, L1

[80] Fanidakis N., et al., 2010, (arXiv:1011.5222v1)

[81] Ferland G. J., Peterson B. M., Horne K., Welsh W. F., Nahar S. N., 1992, ApJ, 387, 95

[82] Ferrarese L., Merritt D., 2000, ApJ, 539, 9

[83] Fitzpatrick E. L., 1986, AJ, 92, 1068

[84] Gaskell C. M., 2009, NewAR, 53, 140

[85] Gaskell C. M., Klimek E. S., Nazarova L. S., 2007, ApJ, submitted, (arXiv:0711.1025v1)

[86] Gaskell C. M., Goosmann René W., Antonucci R. R. J., Whysong D. H., 2004, ApJ, 616, 147

[87] Gebhardt K., et al., 2000, ApJ, 539, L13

[88] Ghosh K. K., Swartz D. A., Tennant A. F., Wu J., Ramsey B., 2004, ApJ, 607, L111

[89] Gillessen S., Eisenhauer F., Trippe S., Alexander T., Genzel R., Martins F., Ott T., 2009a, ApJ, 692, 1075

[90] Gillessen S., Eisenhauer F., Fritz T. K., Bartko H., Dodds-Eden K., Pfuhl O., Ott T., Genzel R., 2009b, ApJ, 707, L114

[91] Giveon Uriel, Maoz D., Kaspi S., Netzer H., Smith P. S., 1999, MNRAS, 306 637

[92] Gierliński M., Done C., 2004, MNRAS, 349, L7

[93] Gierliński M., Done C., 2006, MNRAS, 371, L16

[94] Gierliński M., Middleton M., Ward M., Done C., 2008, Nature, 455, 369

[95] Gierliński M., Zdziarski A. A., Poutanen J., Coppi P. S., Ebisawa K., Johnson W. N., 1999, MNRAS, 309, 496

[96] Gladstone J., Roberts T., Done C., 2009, MNRAS, 397, 1836

[97] Gonzalez A. H., Faber S. M., 1997, ApJ, 485, 80

[98] Goodrich R. W., 1989, ApJ, 342, 224

[99] Grandi S. A., 1982, ApJ, 255, 25

[100] Green P. J., et al., 2009, ApJ, 690, 644

[101] Greene J. E., Ho L. C., 2005, ApJ, 627, 721

[102] Greene J. E., Ho L. C., 2006, ApJ, 641, L21

[103] Grupe D. 1996, Ph.D. Thesis, Univ. Göttingen

[104] Grupe D., Mathur S., ApJ, 606, L41

[105] Grupe D., Beuermann K., Mannheim K., Thomas H. C., 1999, A&A, 350, 805

[106] Grupe D., Komossa S., Leighly K. M., Page K. L., 2010, ApJS, 187, 64

[107] Grupe D., Beuermann K., Thomas H. C., Mannheim K., Fink H. H., 1998, A&A, 330, 25

[108] Haardt F., Maraschi L., 1991, ApJ, 380, L51

[109] Nagao T., Maiolino R., Marconi A., 2006a, A&A, 447, 863

[110] Nagao T., Maiolino R., Marconi A., 2006b, A&A, 459, 85

[111] Hamann F., Ferland G., 1999, ARA&A, 37, 487

[112] Hamann F., Korista K. T., Ferland G. J., Warner C., Baldwin J., 2002, ApJ, 564, 592

[113] Hao H. et al., 2010, ApJ, 724, L59

[114] Harms R. J., et al., 1994, ApJ, 435, L35

[115] Hasinger G., 2005, gbha.conf. 418

[116] Hawking S. W., 1971, MNRAS, 152, 75

[117] Hazard C., Mackey M. B., Shimmins A. J., 1963, Nature, 197, 1037

[118] Heckman T. M., 1980, A&A, 87, 152

[119] Heckman T. M., Kauffmann G., Brinchmann J., Charlot S., Tremonti C., White S., 2004, ApJ, 613, 109

[120] Heckman T. M., Ptak A., Hornschemeier A., Kauffmann G., ApJ, 634, 161

[121] Heinzeller D., Duschl W. J., 2007, MNRAS, 374, 1146

[122] Heisler C. A., Lumsden S. L., Bailey J. A., 1997, Nature, 385, 700

[123] Ho L. C., FilippenkoA.V., SargentW. L.W., 1997, ApJS, 112, 315

[124] Hopkins P. F., Richards G. T., Hernquist L., 2007, ApJ, 654, 731

[125] Hu C., Wang J., Ho L. C., Chen Y., Bian W., Xue S., 2008, ApJ, 683, L115

[126] Hubbard E. N., Puetter R. C., 1985, ApJ, 290, 394

[127] Ibragimov A., Poutanen J., Gilfanov M., Zdziarski A. A., Shrader C. R., 2005, MNRAS, 362, 1435

[128] Isobe T., Feigelson E. D., Akritas M. G., Babu G. J., 1990, ApJ, 364, 104

[129] Israel W., Event horizons in static vacuum space-times., 1967, Phys Rev, 164, 1776

[130] Iwasawa K., Fabian A. C., Young A. J., Inoue H., Matsumoto C., 1999, MNRAS, 306, L19

[131] Iwasawa K., et al., 1996, MNRAS, 282, 1038

[132] Jin C., Ward M., Done C., Gelbord J. M., 2011, MNRAS, preprint, (arXiv:1109.2069v2)

[133] Jin C., Done C., Ward M., Gierliński M., Mullaney J., 2009, MNRAS, 398, L16

[134] Just D. W., Brandt W. N., Shemmer O., Steffen A. T., Schneider D. P., Chartas G., Garmire G. P., 2007, ApJ, 665, 1004

[135] Kalberla P. M. W., Burton W. B., Hartmann Dap, Arnal E. M., Bajaja E., Morras R., Pöppel W. G. L., 2005, A&A, 440, 775

[136] Kalogera V., Baym G., 1996, ApJ, 470, L61

[137] Kaspi S., Smith P. S., Netzer H., Maoz D., Jannuzi B., Giveon U., 2000, ApJ, 533, 631

[138] Kaspi S., Maoz D., Netzer H., Peterson B. M., Vestergaard M., Jannuzi B. T., 2005, ApJ, 629, 61

[139] Kaspi S., et al., 2002, ApJ, 574, 643

[140] Kauffmann G., et al., 2003, MNRAS, 346, 1055

[141] Kawaguchi T., 2003, ApJ, 593, 69

[142] Kellermann K. I., Sramek R., Schmidt M., Shaffer D. B., Green R., 1989, AJ, 98, 1195

[143] Kerr R. P., 1963, Phys. Rev. Lett., 11, 237

[144] Kewley L. J., Dopita M. A., Sutherland R. S., Heisler C. A., Trevena J., 2001, ApJ, 556, 121

[145] Kewley L. J., Groves B., Kauffmannm G., Heckman T., 2006, MNRAS, 372, 961

[146] Khachikian E. Y., Weedman D. W., 1974, ApJ, 192, 581

[147] Kinney A. L., Antonucci R. R. J., Ward M. J., Wilson A. S., Whittle M., 1991, ApJ, 377, 100

[148] Kinney A. L., Calzetti D., Bohlin R. C., McQuade K., Storchi-Bergmann T., Schmitt H. R., 1996, ApJ, 467, 38

[149] Komossa S., 2008, RMxAC, 32, 86

[150] Komossa S., Mathur S., 2001, A&A, 374, 914

[151] Komossa S., Xu D., 2007, ApJ, 667, L33

[152] Komossa S., Xu D., Zhou H., Storchi-Bergmann T., Binette L., 2008, ApJ, 680, 926

[153] Koornneef J., 1983, A&A, 128, 84

[154] Koratkar A., Blaes O., 1999, PASP, 111, 1

[155] Krolik J. H., McKee C. F., 1979, ApJS, 37, 459

[156] Kubota A., Ebisawa K., Makishima K., Nakazawa K., 2005, ApJ, 631, 1062

[157] Kuraszkiewicz J., Wilkes B. J., Czerny B., Mathur S., 2000, ApJ, 542, 692

[158] Kwan J., 1984, ApJ, 283, 70

[159] Kwan J., Krolik J. H., 1979, ApJ, 233, L91

[160] Kwan J., Krolik J. H., 1981, ApJ, 250, 478

[161] La Franca F., Franceschini A., Cristiani S., Vio R., 1995, A&A, 299, 19

[162] Lacy M., Sajina A., Petric A. O., Seymour N., Canalizo G., Ridgway S. E., Armus L., Storrie-Lombardi L. J., 2007, ApJ, 669, L61

[163] Landt H., Elvis M., Ward M. J., Bentz M. C., Korista K. T., Karovska M., 2011, MNRAS, 414, 218

[164] Laor A., 1991, ApJ, 376, 90

[165] Laor A., Netzer H., 1989, MNRAS, 238, 897

[166] Laor A., Fiore F., Elvis M., Wilkes B. J., McDowell J. C., 1994, ApJ, 435, 611

[167] Larsson J., Miniutti G., Fabian A. C., Miller J. M., Reynolds C. S., Ponti G., 2008, MNRAS, 384, 1316

[168] Lawrence A., 1991, MNRAS, 252, 586

[169] Lebofsky M. J., Rieke G. H., 1980, Nature, 284, 410

[170] Lee J. C., Ogle P. M., Canizares C. R., Marshall H. L., Schulz N. S., Morales R., Fabian A. C., Iwasawa K., 2001, ApJ, 554, L13

[171] Leighly K. M., 1999, ApJS, 125, 297

[172] Leighly K. M., 1999, ApJS, 125, 317

[173] Levenson N. A., Weaver K. A., Heckman T. M., Awaki H., Terashima Y., 2004, ApJ, 602, 135

[174] Lu Y., Yu Q., 1999, ApJ, 526, L5

[175] Lusso E. et al., 2010, A&A, 512, 34

[176] MacAlpine G. M., 2003, RMxAC, 18, 63

[177] Magorrian J. et al., 1998, ApJ, 115, 2285

[178] Maiolino R., Marconi A., Salvati M., Risaliti G., Severgnini P., Oliva E., La Franca F., Vanzi L., 2001, A&A, 365, 28

[179] Mannucci F., Basile F., Poggianti B. M., Cimatti A., Daddi E., Pozzetti L., Vanzi L., 2001, MNRAS, 326, 745

[180] Maoz D. et al., 1993, ApJ, 404, 576

[181] Marconi A., Risaliti G., Gilli R., Hunt L. K., Maiolino R., Salvati M., 2004, MNRAS, 351, 169

[182] Marconi A., Axon D. J., Maiolino R., Nagao T., Pastorini G., Pietrini P., Robinson A., Torricelli G., 2008, ApJ, 678, 693

[183] Marziani P., Sulentic J. W., Stirpe G. M., Zamfir S., Calvani M., 2009, A&A, 495, 83

[184] Matsuoka K., Nagao T., Marconi A., Maiolino R., Taniguchi Y., 2011, A&A, 527, 100

[185] Mathews W. G., Blumenthal G. R., Grandi S. A., 1980, ApJ, 235, 971

[186] Mathis J. S., Rumpl W., Nordsieck K. H., 1977, ApJ, 217, 425

[187] Mathur S., 2000, MNRAS, 314, L17

[188] Mathur S., Kuraszkiewicz J.,Czerny B., 2001, NewA, 6, 321

[189] Matt G., Fabian A. C., Guainazzi M., Iwasawa K., Bassani L., Malaguti G., 2000, MNRAS, 318, 173

[190] Matthew T. A., Sandage A. R., 1963, ApJ, 138, 30

[191] McGill K. L., Woo J.-H., Treu T., Malkan M. A., 2008, ApJ, 673, 703

[192] McHardy I. M., Koerding E., Knigge C., Uttley P., Fender R. P., 2006, Nature, 444, 730

[193] Mehdipour M. et al., 2011, A&A, accepted, (arXiv:1107.0659v1)

[194] Mei L., Yuan W., Dong X., 2009, RAA, 9, 269

[195] Middleton M., Done C., 2010, MNRAS, 403, 9

[196] Middleton M., Done C., Gierliński M., 2007, MNRAS, 381, 1426

[197] Middleton M., Done C., Schurch N., 2008, MNRAS, 383, 1501

[198] Middleton M., Sutton A. D., Roberts T. P., 2011, MNRAS, 417, 464

[199] Middleton M., Uttley P., Done C., 2011, MNRAS, 417, 250

[200] Middleton M., Done C., Gierliński M., Davis S. W., 2006, MNRAS, 373, 1004

[201] Middleton M., Done C., Ward M., Gierliński M., Schurch N., 2009, MNRAS, 394,250

[202] Mihalas D., 1978, Stellar Atmospheres, (2nd ed.; San Francisco, CA: Freeman), 650

[203] Miller B. P., Brandt W. N., Gallagher S. C., Laor A., Wills B. J., Garmire G. P., Schneider D. P., 2006, ApJ, 652, 163

[204] Miller L., Turner T. J., Reeves J. N., 2008, A&A, 483, 437

[205] Mineshige S., Hirano A., Kitamoto S., Yamada T. T., Fukue J., 1994, ApJ, 426, 308

[206] Morgan E. H., Remillard R. A., Greiner J., 1997, ApJ, 482, 993

[207] Mullaney J. R., Ward M. J., 2008, MNRAS, 385,53

[208] Mullaney J. R., Ward M. J., Done C., Ferland G. J., Schurch N., 2009, MNRAS, 394, L16

[209] Mushotzky R. F., Marshall F. E., Boldt E. A., Holt S. S., Serlenmitsos P. J., 1980, ApJ, 235, 377

[210] Nandra K., Pounds K. A., 1994, MNRAS, 268, 405

[211] Nandra K., O'Neill P. M., George I. M., Reeves J. N., 2007, MNRAS, 382, 194

[212] Nandra K., Le T., George I. M., Edelson R. A., Mushotzky R. F., Peterson B. M., Turner T. J., 2000, ApJ, 544, 734

[213] Nelson C. H., Whittle M., 1995, ApJS, 99, 67

[214] Nelson C. H., Whittle M., 1996, ApJ, 465, 96

[215] Novikov I. D., Thorne K. S., 1973, blho.conf, 343

[216] Orosz, J. A., McClintock, J. E., Aufdenberg, J. P., Remillard R. A., Reid M. J., Narayan R., Gou L., 2011, ApJ, 742, 84

[217] Osterbrock D. E., 1978, PNAS, 75, 540

[218] Osterbrock D. E., 1981, ApJ, 249, 462

[219] Osterbrock D. E., 1989, Astrophysics of Gaseous Nebulae and Active Galacitc Nuclei (University Science Books, Mill Valley, California)

[220] Osterbrock D. E., Pogge R. W., 1985, ApJ, 297, 166

[221] Pei Y. C., 1992, ApJ, 395, 130

[222] Peterson B. M. et al., 2004, ApJ, 613, 682

[223] Petrucci P. O. et al., 2007, A&A, 470, 889

[224] Piconcelli E., Jimenez-Bailón E., Guainazzi M., Schartel N., Rodríguez-Pascual P. M., Santos-Lleó M., 2005, A&A, 432, 15

[225] Pierens A., Huré J. M., Kawagushi T., 2003, sf2a.conf., 489

[226] Pigarov A. Y., Terry J. L., Lipschultz B., 1998, Plasma Physics and Controlled Fusion, 40, 12

[227] Pogge R. W., 1988, ApJ, 328, 519

[228] Ponti G., Miniutti G., Cappi M., Maraschi L., Fabian A. C., Iwasawa K., 2006, MNRAS, 368, 903

[229] Porquet D., Reeves J. N., O'Brien P., Brinkmann W., 2004, A&A, 422, 85

[230] Pounds K. A., Done C., Osborne J. P., 1995, MNRAS, 277, L5

[231] Pounds K. A., Reeves J. N., King A. R., Page K. L., O'Brien P. T., Turner M. J. L., 2003, MNRAS, 345, 705

[232] Prevot M. L., Lequeux J., Prevot L., Maurice E., Rocca-Volmerange B., 1984, A&A, 132, 389

[233] Puchnarewicz E. M., Mason K. O., Siemiginowska A., Pounds, K. A., 1995, MNRAS, 276, 20

[234] Puchnarewicz E. M., Mason K. O., Siemiginowska A., Fruscione A., Comastri A., Fiore F., Cagnoni I., 2001, ApJ, 550, 644

[235] Puchnarewicz E. M., et al., 1992, MNRAS, 256, 589

[236] Puetter R. C., Levan P. D., 1982, ApJ, 260, 44

[237] Rees M. J., Silk J. I., Werner M. W., Wickramasinghe N. C., Nature, 223, 788

[238] Reeves J. N., Turner M. J. L., 2000, MNRAS, 316, 234

[239] Remillard R. A., McClintock J. E., ARA&A, 44, 49

[240] Reynolds C. S., 1997, MNRAS, 286, 513

[241] Reynolds C. S., 1999, ASPC, 161, 178

[242] Reynolds C. S., et al., 2009, ApJ, 691, 1159

[243] Richards G. T., et al., 2006, ApJS, 166, 470

[244] Rieke G. H., 1978, ApJ, 226, 550

[245] Roberts T. P., 2007, Ap&SS, 311, 203

[246] Ross R. R., Fabian A. C., 1993, MNRAS, 261, 74

[247] Ross R. R., Fabian A. C., Mineshige S., 1992, MNRAS, 258, 189

[248] Ross R. R., Fabian A. C., Young A. J., 1999, MNRAS, 306, 461

[249] Ruiz J. R., Crenshaw D. M., Kraemer S. B., Bower G. A., Gull T. R., Hutchings J. B., Kaiser M. E., Weistrop D., 2005, AJ, 129, 73

[250] Sanders D. B., Phinney E. S., Neugebauer G., Soifer B. T., Matthews K., 1989, ApJ, 347, 29

[251] Savage B. D., Mathis J. S., 1979, ARA&A, 17, 73

[252] Seyfert C. K., 1943, ApJ, 97, 28

[253] Schmidt M., 1963, Nature, 197, 1040

[254] Schmitt H. R., Donley J. L., Antonucci R. R. J., Hutchings J. B., Kinney A. L., 2003a, ApJS, 148, 327

[255] Schmitt H. R., Donley J. L., Antonucci R. R. J., Hutchings J. B., Kinney A. L., Pringle J. E., 2003b, ApJ, 597, 768

[256] Schödel R., et al., 2002, Nature, 419, 694

[257] Schwarzschild K., Über das Gravitationsfeld eines Massenpunktes nach der Einsteinschen Theorie Sitzber., Preuss Akad Wiss, 1916, 189

[258] Seaton M. J., 1979, MNRAS, 187, 73

[259] Shakura N. I., Sunyaev R. A., 1973, A&A, 24, 337

[260] Shang Z. et al., 2005, ApJ, 619, 41

[261] Shemmer O., Brandt W. N., Netzer H., Maiolino R., Kaspi S., 2006, ApJ, 646, L29

[262] Shemmer O., Brandt W. N., Netzer H., Maiolino R., Kaspi S., 2008, ApJ, 682, 81

[263] Shen Y., Greene J. E., Strauss M. A., Richards G. T., Schneider D. P., 2008, ApJ, 680, 169

[264] Shields G. A., 1978, Nature, 272, 706

[265] Shuder J. M., 1982, ApJ, 259, 48

[266] Shuder J. M., Osterbrock D. E., 1981, ApJ, 250, 55

[267] Sobolewska M. A., Done C., 2007, MNRAS, 374, 150

[268] Soria R., Puchnarewicz E. M., 2002, MNRAS, 329, 456

[269] Spitzer L. Jr., 1978, JRASC, 72, 349

[270] Steffen A. T., Strateva I., Brandt W. N., Alexander D. M., Koekemoer A. M., Lehmer B. D., Schneider D. P., Vignali C., 2006, AJ, 131, 2826

[271] Stephens S. A., 1989, AJ, 97, 10

[272] Strateva I. V., Brandt W. N., Schneider D. P., Vanden B., Daniel G., Vignali C., 2005, AJ, 130, 387

[273] Strateva I. V., et al. 2006, ApJ, 651, 749

[274] Sulentic J. W., Zwitter T., Marziani P., Dultzin-Hacyan D., 2000, ApJ, 536, L5

[275] Sulentic J. W., Zamfir S., Marziani P., Dultzin D., 2008, RMxAC, 32, 51

[276] Talavera A., 2009, Ap&SS, 320, 177

[277] Tananbaum H., Avni Y., Branduardi G., Elvis M., Fabbiano G., Feigelson E., Giacconi R., Henry J. P., Pye J. P., Soltan A., Zamorani G., 1979, ApJ, 234, L9

[278] Tang Su-Min, Zhang Shuang-Nan, Hopkins P. F., MNRAS, 377, 1113

[279] Thorne K. S., 1974, ApJ, 191, 507

[280] Tran H. D., 1995, ApJ, 440, 565

[281] Trippe M. L., Reynolds C. S., Koss M., Mushotzky R. F., Winter L. M., 2011, ApJ, 736, 81

[282] Tsuzuki Y., Kawara K., Yoshii Y., Oyabu S., Tanabé T., Matsuoka Y., 2006, ApJ, 650, 57

[283] Turner A. K., Fabian A. C., Lee J. C., Vaughan S., 2004, MNRAS, 353, 319

[284] Turner A. K., Miller L., Reeves J. N., Kraemer S. B., 2004, A&A, 475, 121

[285] Vanden Berk D.E., et al., 2001, ApJ, 122, 549

[286] Vasudevan R. V., Fabian A. C., 2007, MNRAS, 381, 1235

[287] Vasudevan R. V., Fabian A. C., 2009, MNRAS, 392, 1124

[288] Vaughan S., 2005, A&A, 431, 391

[289] Vaughan S., Fabian A. C., 2004, MNRAS, 348, 1415

[290] Vaughan S., Edelson R., Warwick R. S., Uttley P., 2003, MNRAS, 345, 1271

[291] Verner E., Bruhweiler F., Johansson S., Peterson B., 2009, Physica Scripta, 2009, T134

[292] Véron-Cetty M., P., Véron P., Goncalves A. C., 2001, A&A, 372, 730

[293] Véron-Cetty M. P., Joly M., Véron P., 2004, A&A, 417, 515

[294] Vierdayanti K., Done C., Roberts T. P., Mineshige S., 2010, MNRAS, 403, 1206

[295] Vignali C., Brandt W. N., Schneider D. P., 2003, AJ, 125, 433

[296] Walter R., Fink H. H., 1993, A&A, 274, 105

[297] Wandel A., Peterson B. M., Malkan M. A., 1999, ApJ, 526, 579

[298] Wang T., Lu Y., 2001, A&A, 377, 52

[299] Wang J.-M., Netzer H., 2003, A&A, 398, 927

[300] Wang Jian-Min, Watarai K., Mineshige S., 2004, ApJ, 607, L107

[301] Wang J.-M., et al., 2011, ApJ, 739, 3

[302] Ward M., Done C., Fabian A. C., Tennant A. F., Shafer R. A., 1988, ApJ, 324, 767

[303] Ward M., Elvis M., Fabbiano G., Carleton N. P., Willner S. P., Lawrence A., 1987, ApJ, 315, 74

[304] Warner C., Hamann F., Dietrich M., 2003, ApJ, 596, 72

[305] Wilkes B. J., Tananbaum H., Worrall D. M., Avni Y., Oey M. S., Flanagan J., 1994, ApJS, 92, 53

[306] Wills B. J., Netzer H., Wills D., 1985, ApJ, 288, 94

[307] Wills B. J., Laor, A., Brotherton M. S., Wills, D., Wilkes, B. J., Ferland, G. J., Shang Z., 1999, ApJ, 515, L53

[308] Winter L. M., Mushotzky R. F., Reynolds C. S., Tueller J., 2009, ApJ, 690, 1322

[309] Woo J., Urry C. M., 2002, ApJ, 579, 530

[310] Xiao T., Barth A. J., Greene J. E., Ho L. C., Bentz M. C., Ludwig R. R., Jiang Y., 2011, ApJ, 739, 28

[311] Yuan W., Siebert J., Brinkmann W., 1998, A&A, 334, 498

[312] Zel'Dovich Y. B., Novikov I. D., 1964, SPhD, 9, 246

[313] Zdziarski A. A., Poutanen J., Johnson W. N., 2000, ApJ, 542, 703

[314] Zdziarski A. A., Ghisellini G., George I. M., Fabian A. C., Svensson R., Done C., 1990, ApJ, 363, L1

[315] Zhang S.N., Cui W., Chen W., 1997, ApJ, 482, L155

[316] Zhou Xin-Lin, Zhang, Shuang-Nan, ApJ, 713, L11

[317] Zhou Xin-Lin, Zhao Yong-Heng, ApJ, 720, L206

[318] Zhou H., Wang T., Yuan W., Lu H., Dong X., Wang J., Lu J., 2006, ApJS, 166, 128

[319] Zhu L., Zhang S., Tang S., 2009, ApJ, 700, 1173